UNIVERSITÄT OSNABRÜCK

Traceable Imaging Spectrometer Calibration and Transformation of Geometric and Spectral Pixel Properties

Dissertation

Zur Erlangung
des Doktorgrades der Naturwissenschaften (Dr. rer. nat.)
des Fachbereichs Mathematik/Informatik
der Universität Osnabrück

Vorgelegt von

Andreas Baumgartner

Prüfer der Dissertation:

Prof. Dr. Peter Reinartz, Universität Osnabrück
Prof. Dr. Bernhard Mayer, Ludwig-Maximilians-Universität München

Osnabrück, 2021

To Isabell

ABSTRACT

Over the past several decades, push-broom imaging spectrometers have become a common Earth observation tool. Instruments of this type must be calibrated to convert the raw sensor data into units of spectral radiance. Calibration is in this case a two-step process: First, a sensor model is obtained by performing calibration measurements, which is then used to convert raw signals to spectral radiance data. Further processing steps can be performed to correct for optical image distortions.

In this work, we show the complete calibration process for push-broom imaging spectrometers, including uncertainty propagation. Although the focus is specifically on calibrating a HySpex VNIR-1600 airborne-imaging spectrometer, all methods can be adapted for other instruments.

We discuss the theory of push-broom imaging spectrometers by introducing a generic sensor model, which includes the main parameters and effects of such instruments.

Calibrating detector-related effects, such as dark signal, the noise as a function of the signal, and temperature effects is shown. Correcting temperature effects significantly reduces measurement errors. To determine the signal non-linearity, we built a setup based on the light-addition method and improved this method to allow smaller signal level distances of the sampling points of the non-linearity curve. In addition, we investigate the non-linearity of the integration time. The signal ($\leq$15 %) and the integration time ($\leq$0.5 %) non-linearities can be corrected with negligible errors. After correcting both non-linearity effects, a smearing effect is revealed, which is investigated in detail.

We use a collimator and monochromator setup for calibrating the geometric and spectral parameters, respectively. To accurately model the angular and spectral response functions, we propose using cubic splines, which leads to significant improvements compared to previously used Gaussian functions. We present a new method that allows interpolation of the cubic spline based response functions for pixels not measured. The results show that the spectral and geometric properties are non-uniform and change rapidly within a few pixels.

The absolute radiometric calibration is performed with a lamp-plaque setup and an integrating sphere is used for flat-fielding. To mitigate the influence of sphere non-uniformities, we rotate the instrument along the across-track angle to measure the same spot of the sphere with each pixel. We investigate potential systematic errors and use Monte Carlo simulations to determine the uncertainties of the radiometric calibration. In addition, we measure the polarization sensitivity with a wire-grid polarizer.

Finally, we propose a novel image transformation method that allows manipulation of geometric and spectral properties of each pixel individually. Image distortions can be corrected by changing a pixel's center angles, center wavelength, and response function shape. This is done by using a transformation matrix that maps each pixel of a target sensor B to the pixels of a source sensor A. This matrix is derived from two cross-correlation matrices: Sensor A and itself, and sensor B and sensor A. We provide the mathematical background and discuss the propagation of uncertainty. A case study shows that the method can significantly improve data quality.

ZUSAMMENFASSUNG

In den letzten Jahrzehnten sind abbildende Push-Broom-Spektrometer zu einem gängigen Werkzeug der Erdbeobachtung geworden. Derartige Messgeräte müssen kalibriert werden, um Sensorrohdaten in spektrale Strahldichte umrechnen zu können. Dabei ist die Kalibrierung ein zweistufiger Prozess: Zunächst wird durch Messungen ein Sensormodell erstellt, das dann zur Umwandlung der Rohsignale in spektrale Strahldichten verwendet wird. Danach können weitere Verarbeitungsschritte durchgeführt werden, um Abbildungsfehler zu korrigieren.

In dieser Arbeit wird der komplette Kalibrierungsprozess, inklusive der Fortpflanzung von Messunsicherheiten, von abbildenden Push-Broom-Spektrometern beschrieben. Obwohl der Schwerpunkt auf der Kalibrierung eines flugzeuggetragenen Sensors vom Typ HySpex VNIR-1600 liegt, sind alle Methoden auf andere Instrumente übertragbar.

Die wichtigsten Eigenschaften von abbildenden Push-Broom-Spektrometern werden durch die Einführung eines generischen Sensormodells dargestellt.

Es wird die Kalibrierung von Detektoreigenschaften gezeigt, wie z. B. das Dunkelsignal und das Rauschen als Funktion des Signals. Ebenso werden Temperatureffekte korrigiert, was Messfehler erheblich reduziert. Um signalabhängige Nichtlinearität zu korrigieren, wurde ein Aufbau basierend auf der Light-Addition-Methode entwickelt. Diese Methode wurde dahingehen weiterentwickelt, sodass Nichtlinearitätskurven beliebig hoch aufgelöst werden können. Darüber hinaus wird die Nichtlinearität der Integrationszeit untersucht. Die Nichtlinearitäten des Signals ($\leq$15 %) und der Integrationszeit ($\leq$0.5 %) können mit vernachlässigbaren Fehlern korrigiert werden. Nach der Korrektur der beiden Nichtlinearitätseffekte wird der Einfluss des Smear-Effects relevant, der ebenfalls im Detail untersucht wird.

Zur Kalibrierung von geometrischen und spektralen Eigenschaften wird ein Kollimator- bzw. Monochromatoraufbau verwendet. Die Ergebnisse zeigen, dass die geometrischen und spektralen Eigenschaften sich rapide innerhalb weniger Pixel ändern und inhomogen verteilt sind. Um die Winkel- und Spektralantwortfunktionen akkurat zu modellieren, werden kubische Splines verwendet, was zu signifikanten Verbesserungen im Vergleich zu bisher verwendeten Gauß-Funktionen führt. Zusätzlich wird eine neue Methode beschrieben, mit der diese Spline-basierten Funktionen für nicht gemessene Pixel interpoliert werden können.

Die radiometrische Kalibrierung wird mit einem Lampen-Paneel-Aufbau durchgeführt und für das Flat-Fielding eine Ulbrichtkugel verwendet. Es werden mögliche systematische Fehler untersucht und mittels Monte-Carlo-Simulationen die Unsicherheiten der radiometrischen Kalibrierung bestimmt. Zusätzlich wird die Polarisationsempfindlichkeit ermittelt.

Schließlich wird eine neuartige Bildtransformationsmethode vorgestellt, welche eine individuelle Manipulation der geometrischen und spektralen Eigenschaften jedes Detektor-Pixels ermöglicht. Bildverzerrungen können durch Änderung von Mittelpunktswinkel, Mittelpunktswellenlänge und Form der Antwortfunktion eines Pixels korrigiert werden. Dies geschieht mit Hilfe einer Transformationsmatrix, die jedes Pixel eines Zielsensors B auf die Pixel eines Quellensensors A abbildet. Eine Fallstudie zeigt, dass diese Methode die Datenqualität deutlich verbessern kann.

Acknowledgments

First of all, I would like to thank my supervisor Rupert Müller for all his support and encouragement. While he gave me great freedom in exploring the topic, he guided me where it was necessary.

Second, I am indebted to Dr. Peter Haschberger, who has supported me not only since the formulation of my desire to write a PHD thesis, but all my years at DLR. Without his feedback, guidance and support this work would not have been possible.

I would like to thank Prof. Dr. Peter Reinartz for giving me the opportunity to carry out this thesis at the University of Osnabrück. My gratitude also goes to Prof. Dr. Bernhard Mayer for reviewing this work.

This thesis would not have been possible without the help of many people. This is especially true for Dr. Karim Lenhard, who laid with his work the foundation for this thesis. No less important was the assistance provided by Dr. Claas Köhler and Thomas Schwarzmaier. All three were and are always great to work with.

I wish to express my appreciation to Dr. Peter Gege and Prof. Dr. Michael Schaepman, who supported me in the early phase of this work.

I want to extend my thanks to all the current and previous members of my department at DLR for the friendly and helpful atmosphere. Although they were not directly involved in this thesis, I want to thank the following people who made and make working here most enjoyable: Dr. Manfred Birk, Erich Bogner, Eva Fahrenschon, Dr. Anna Göritz, Dr. Martin Israel, Stefan Plattner, Charles Pope, Dr. Clemens Rammeloo, Sebastian Riedel, Christian Röske, Dr. Erwin Lindermeir, Dr. Georg Wagner, Andreas Wenisch and Jürgen Wörishofer.

Most importantly, none of this would have been possible without my parents Renate and Herbert, who have supported me throughout my life. I want to thank them and my siblings Carolin and Christian for being such a great family.

Last but not least, I would like to thank Isabell for her support, encouragement and love. She was always (mostly) patient and pushed me when needed.

Andreas Baumgartner
Munich, Germany, March 2021

Contents

1 Introduction **1**

1.1 Current State of Imaging Spectrometer Calibration . . . 3
1.1.1 Calibration of Detector-Related Parameters . . . 3
1.1.2 Calibration of Geometric and Spectral Instrument Properties . . . 5
1.1.3 Calibration of Radiometric Instrument Properties . . . 5
1.1.4 Transformation of Geometric and Spectral Pixel Properties . . . 6
1.2 Objectives and Scope of the Thesis . . . 7
1.3 Definition of Calibration . . . 9
1.4 DLR's Calibration Home Base for Imaging Spectrometers . . . 10
1.5 Airborne Imaging Spectrometer HySpex VNIR-1600 Operated by DLR . . . 10
1.6 Organization of the Thesis . . . 12

2 Theory of Push-broom Imaging Spectrometers **13**

2.1 Introduction . . . 14
2.2 Imaging Equation . . . 15
2.3 Focal Plane Array . . . 16
2.4 Point Spread Function . . . 18
2.5 Pixel Response Function . . . 19
2.6 Image Distortions . . . 21
2.7 Stray Light . . . 22
2.8 Radiometric Responsivity . . . 22
2.9 Polarization Sensitivity . . . 23
2.10 Non-Linearity . . . 24
2.11 Noise . . . 25
2.12 Summary . . . 26

3 Calibration of Detector Related Parameters **27**

3.1 Introduction . . . 28
3.2 Dark and Offset Signal . . . 28
3.2.1 Dark and Offset Signal Measurements . . . 28
3.2.2 Dark and Offset Signal Results . . . 28
3.2.3 Dark and Offset Signal Correction . . . 29
3.3 Signal-Dependent Noise . . . 29
3.3.1 Photon Transfer Curve Method . . . 30
3.3.2 Results . . . 30
3.4 Temperature Sensitivity . . . 32
3.4.1 HySpex VNIR-1600 Operational Environment . . . 32
3.4.2 Detector Temperature Measurements . . . 32
3.4.3 Detector Temperature Sensitivity Results . . . 32
3.4.4 Temperature Sensitivity Correction . . . 33
3.5 Signal-Dependent Non-linearity . . . 34
3.5.1 Light-Addition Method . . . 34
3.5.2 Signal Non-linearity Measurements . . . 38
3.5.3 Signal Non-linearity Results . . . 42

3.5.4 Signal Non-linearity Correction . . . 44
3.6 Integration Time Non-linearity . . . 44
3.6.1 Integration Time Non-linearity Measurements . . . 44
3.6.2 Integration Time Non-linearity Results . . . 45
3.6.3 Integration Time Non-linearity Correction . . . 45
3.7 Smear Effect . . . 46
3.7.1 Theory . . . 46
3.7.2 Impact of Smear on Halogen-Lamp Measurements . . . 48
3.7.3 Smear Measurements . . . 49
3.7.4 Results . . . 50
3.8 Validation of Non-linearity Correction . . . 51
3.9 Order of Corrections . . . 52
3.10 Summary . . . 53

4 Geometric and Spectral Calibration 55
4.1 Introduction . . . 56
4.2 Geometric Calibration Setup . . . 56
4.3 Spectral Calibration Setup . . . 57
4.3.1 Monochromator Center Wavelength Calibration . . . 59
4.3.2 Monochromator Bandwidth Calibration . . . 60
4.3.3 Relative Radiometric Monochromator Calibration . . . 61
4.4 Geometric Calibration Measurements . . . 63
4.5 Spectral Calibration Measurements . . . 63
4.6 Evaluation Methods . . . 65
4.6.1 Data Pre-Processing . . . 65
4.6.2 Response Function Model . . . 67
4.6.3 Interpolation of Spectral Response Functions . . . 67
4.7 Measurement Results . . . 68
4.7.1 Geometric Calibration Results . . . 68
4.7.2 Spectral Calibration Results . . . 68
4.8 Pixel Response Function Reconstruction . . . 72
4.9 Uncertainties and Errors . . . 73
4.9.1 Uncertainty of Response Function Models . . . 73
4.9.2 Errors Caused by Source Bandwidths and Line Widths . . . 75
4.9.3 Error of Spectral Response Function Interpolation . . . 76
4.9.4 Improvements over Gaussian Response Function Model . . . 79
4.9.5 Spatial and Spectral Calibration Uncertainty . . . 80
4.10 Summary . . . 81

5 Radiometric Calibration 83
5.1 Introduction . . . 84
5.2 Methods . . . 84
5.2.1 Radiometric Calibration using Spectral Response Functions . . . 85
5.2.2 Conventional Radiometric Calibration Approach . . . 85
5.2.3 Center Pixel Calibration . . . 85
5.2.4 Interpolation Method . . . 87

5.2.5 Flat Field Calibration . . . 88
5.2.6 Monte Carlo Simulation . . . 89
5.2.7 Polarization Sensitivity Measurements . . . 90
5.3 Results . . . 90
5.3.1 Potential Sampling Errors . . . 90
5.3.2 Radiometric Calibration Results . . . 90
5.3.3 Polarization Sensitivity Results . . . 93
5.4 Summary . . . 94

6 Transformation of Geometric and Spectral Pixel Properties 95
6.1 Introduction . . . 96
6.2 Pixel Response Function Transformation . . . 96
6.3 Transformation Matrix Constraints . . . 98
6.4 Uncertainty Propagation . . . 98
6.5 Regularization Matrix . . . 99
6.6 Virtual Sensors . . . 99
6.7 Generation of Transformation Matrices . . . 101
6.8 Performance Tests . . . 104
6.8.1 Results for Test Scene 1 . . . 105
6.8.2 Results for Test Scene 2 . . . 107
6.8.3 Overall Results . . . 109
6.8.4 Impact on Noise . . . 109
6.9 Summary . . . 111

7 Summary, Conclusion, and Outlook 113
7.1 Summary and Description of Calibration Chain . . . 114
7.2 Conclusion . . . 119
7.3 Outlook . . . 120

List of Symbols 121

List of Abbreviations 125

Bibliography 137

Appendices 145

A Test Scenes 145
A.1 Test Scene 1 . . . 146
A.2 Test Scene 2 . . . 147

B Spherical Coordinate System 149

C Related Publications 151

1

Introduction

Contents

1.1 Current State of Imaging Spectrometer Calibration 3
1.2 Objectives and Scope of the Thesis 7
1.3 Definition of Calibration 9
1.4 DLR's Calibration Home Base for Imaging Spectrometers 10
1.5 Airborne Imaging Spectrometer HySpex VNIR-1600 Operated by DLR 10
1.6 Organization of the Thesis 12

Over the past several decades imaging spectrometers have become a common Earth observation tool. These sensors offer an unprecedented combination of spectral and spatial resolution with simultaneous continuous coverage of the spectral range throughout the ultraviolet, visible and infrared electromagnetic spectrum. Supported by continuously increasing availability of computational power, memory, and storage space, the vast amount of data generated by such instruments has become manageable for an increasing number of remote sensing scientists.

Many space- and airborne-imaging spectrometer designs are based on the push-broom principle. These instruments are line scanners, where a single image consists of a spectral and a spatial axis. A second spatial axis is added by moving the instrument perpendicular to the first spatial axis and simultaneously acquiring images. In the case of Earth observation, these instruments measure the solar radiation absorbed, reflected, and scattered by the Earth's surface and atmosphere.

The range of fields of application extends from the remote sensing of vocational health and chemistry, mapping a wide range of minerals, monitoring atmospheric trace gasses to water constitutions and depth [1, 2]. This is just an example of possible applications; many others are conceivable, some of which have yet to be discovered. Some of these applications require that the imaging spectrometer data is of very high quality [3–6]. High quality data has in common that it is traceable to SI units. This includes, of course, that uncertainties are provided with the imaging spectrometer data.

Imaging spectrometers measure at-aperture radiance. Internally, though, these instruments record raw data, which consists of digital numbers with no obvious physical meaning. An instrument model is required to convert raw data to at-aperture radiance. Determining the instrument model is the purpose of calibration measurements. During calibration, many instrument properties have to be considered. This includes, for instance the spectral, angular response of each pixel, its radiometric responsivity, as well as the non-linearity of the measured signal compared to the radiance level.

It is desirable that a measured object generate the same radiance signal independent of detector location. [3–6]. Optical aberrations and distortions, however, can result in different appearances of the same measured object depending on the image location. This can be caused by different center wavelengths of pixels of the same spectral channel (smile), different center angles of pixels of the same spatial pixel (keystone), and by non-uniformities of response function shapes and resolutions. Although it is theoretically possible to generate an instrument model that describes these inhomogeneities, most algorithms cannot usually deal with such complexity. Especially after orthorectification—the mapping of imaging data on the Earth's surface—pixel individual information is lost [7]. Great efforts are therefore being made to build instruments with uniform angular and spectral pixel properties [8–10]. Calibration measurements show, however, that some imaging spectrometers significantly suffer from spatial and spectral non-uniformities [11–13].

This thesis addresses calibrating imaging spectrometers with highly non-uniform pixel parameters. We demonstrate methods where imaging spectrometers are treated as black boxes to derive traceable instrument models, and we show the calibration and correction of

non-linearity effects, temperature sensitivity, as well as spectral, spatial, and radiometric properties by simultaneously addressing uncertainties. In addition, we present a novel image transformation method that allows geometric and spectral properties of each pixel individually to be manipulated individually.

1.1 Current State of Imaging Spectrometer Calibration

As already mentioned, to convert the raw data of imaging spectrometers to radiance units, an instrument model derived using calibration measurements is required. Space instruments in particular are extensively calibrated, since after launch, possibilities of calibration measurements are limited. For many space- and airborne-instruments, calibration measurements are well documented [11, 12, 14–25]. However, gaps in research still exist, which we discuss in the following.

1.1.1 Calibration of Detector-Related Parameters

Many characteristics of imaging spectrometers are directly linked to the properties of the instrument detector. Of these properties, we discuss in this thesis dark and offset signal, noise, temperature sensitivity, non-linearity of the signal and the integration time, and smearing, an effect which is typical for Charge Coupled Device (CCD) detectors. The easiest way to calibrate the detector would be at subsystem level, i.e., with the naked chip. However, this is usually not possible with an integrated system. Removing the detector for calibration is not an option, as previous calibration data of the integrated system will then become invalid, which is why calibrating the detector has to be performed with the optical system in front of the detector.

Signal-Dependent Noise A common method for determining the noise depending on the signal is the Photon Transfer Curve (PTC) method [26, 27]. The PTC is a plot of noise as function of the signal. This method can also be used with imaging spectrometers to determine basic parameters such as gain and read noise.

Temperature Sensitivity The responsivity of semiconductor detectors depends on their temperature. Many imaging spectrometers have a thermally stabilized detector and therefore do not have this issue [14]. However, the detectors of some instruments are not thermally stabilized, [12, 13]. If the detector temperature can be measured, it is possible to correct this effect by applying a calibration curve. To determine such a calibration curve, the detector temperature must be changed by changing the temperature of the surrounding environment and simultaneously measuring a stable light source. Some authors wrapped silicon rubber tubing around a non-imaging field spectrometer to control the environmental temperature [28]. Others also conducted a similar experiment with a non-imaging field spectrometer with the instrument in a thermally controlled chamber [29]. Another possibility is to measure a stable light source, but utilize the temperature change between instrument start and thermal stabilization [30]. However, we could not find any publications about comparable experiments

using imaging spectrometers.

Signal-Dependent Non-linearity The measured detector signal can have a non-linear relationship with the photons that accumulate in the detector element during acquisition. The non-linearity can be separated in non-linearity depending on the signal level and non-linearity of the integration time, i.e., the difference between set and actual integration time.

The easiest approach for measuring these non-linearities is to change the integration time while measuring a constant light source [13]. Unfortunately, this has the disadvantage that integration time non-linearity and signal non-linearity are very difficult to separated.

Another approach is to compare an imaging spectrometer signal with calibrated reference sensor signal while the measured light level is adjusted [12, 31–33]. For imaging spectrometers, this generally involves using an integrating sphere, where both the imaging spectrometer and the reference radiometer monitor the sphere's radiance. Integrating spheres are hollow spheres with a diffuse inner white coating. Light emitted from several lamps is scattered many times on the white coated surface, creating a uniform radiance field on the exit port. Since the imaging spectrometer and the reference sensor do not usually measure the exact locations of the sphere, any change of the uniformity of the sphere's output would result in an error in the non-linearity measurement. Changing the light level without altering the light distribution is quite challenging, since changing the current of the illumination lamps changes their spectrum and using a mechanical shutter changes the sphere homogeneity. Using polarization filters to adjust the light level has the disadvantage that such filters have wavelength-dependent extinction ratios. Hence, the spectrum has to be limited to a small region with a bandpass filter [18]. Additionally, the linearity of the reference radiometer limits the measurement accuracy.

Another option for measuring signal non-linearity is the small signal linearity method [34]. We performed several experiments using this approach, which involves measuring discrete signal levels over a small signal range by tuning the light intensity of a small signal lamp. An offset signal is added to the small signal measurements and the small signal measurements are repeated for many different offset signals. Assuming that a detector is linear at the middle of its dynamic range, the entire dynamic range is calibrated. This assumption is unfortunately not always true, as the results in this thesis reveal. Additionally, since the small signal measurement series need to be matched at overlapping signal levels, initially, small systematic uncertainties accumulate with the number of overlaps.

The light-addition method involves measuring two identical light levels, each individually and then both combined. [28, 35, 36]. This means that , if a system is linear, the sum of the signals of the individual light levels must be identical to the signal of both light levels combined. Although this method was used in the past with non-imaging spectrometers, no publications involving imaging spectrometers are available to the best of our knowledge.

1.1.2 Calibration of Geometric and Spectral Instrument Properties

The most basic method used for performing a spectral instrument calibration is to illuminate an imaging spectrometer's Field of View (FoV) with a spectral line lamp [37]. Since the wavelength of the emission lines is only affected by the refractive index of air, these kinds of lamps are used as a primary standard. However, spectral calibration information can only be obtained where the emission lines are located. Furthermore, the possibility of accurately extracting the shapes of an instrument's Spectral Response Functions (SRFs) is limited. A SRF is a pixel's the wavelength dependent responsivity.

SRFs can be measured very accurately with a tunable laser light source whose light is coupled to an integration sphere [23, 38]. With such setups, the entire FoV of an instrument can be covered with monochromatic light of sufficient intensity. Unfortunately, such calibration systems are very expensive and therefore not available for most calibration laboratories.

A more cost-efficient method for measuring SRFs is to use a monochromator whose emitted light is used to scan an instrument's wavelength range [11–13, 39]. Since monochromators usually emit light with such low intensity that the entire FoV cannot be covered simultaneously, only a subset of instrument pixels is usually measured. Consequently, the spectral properties of the pixels not measured need to be interpolated. This is usually done by assuming that the instrument's SRF can be described using Gaussian functions. The extracted center wavelength and Full Width at Half Maximum (FWHM) are then interpolated.

Gaussian SRF models are utilized for many instruments [11, 12, 16, 25, 40]. However, for other instrument and applications, SRFs cannot be accurately described with Gaussian functions, so more complex SRF models must be used [13, 20, 23, 41, 42]. In cases of relevant differences between model and reality, this could lead to significant errors in processing spectroscopic data, especially when it comes to atmospheric correction or trace gas retrieval [3]. The OCO and OCO-2 SRFs are described with lookup tables of the laboratory calibration data, since no sufficiently accurate analytical function was found [20, 41, 42]. For the TROPOMI-SWIR instrument, a complex model was developed, where for each SRF eight parameters are fitted [23].

Similar to SRFs, spatial properties of imaging spectrometer in the form of the Angular Response Function (ARF) are measured by scanning the image of a spatially narrow source over the across-track FoV of an instrument. Typically, this is a slit in the focus of a collimator [11–13, 43, 44]. As with SRFs, Gaussian functions are commonly used to describe ARF.

1.1.3 Calibration of Radiometric Instrument Properties

The purpose of the radiometric calibration measurement is to determine the radiometric calibration coefficients that are used to convert raw sensor data to spectral radiance.

The most common radiometric calibration method involves using a calibrated integrating sphere as reference source, which has the advantage that a sphere can illuminate the entire aperture and FoV of an imaging spectrometer. Integrating spheres are either directly calibrated by a national metrological institute or with calibrated transfer radiometers,

i.e., spectroradiometers [16, 21, 45–48]. Transfer radiometers and spectroradiometers are calibrated using a primary standard by a metrological institute, such as The Physikalisch-Technische Bundesanstalt (PTB) or The National Institute of Standards and Technology (NIST), or by using a secondary standard that is traceable to a primary standard [49–52].

Another option for radiometrically calibrating an imaging spectrometer is to use monochromatic tunable high-power light sources. The light from this type of source is coupled into an integrating sphere and is simultaneously measured with an imaging spectrometer and a calibrated reference radiometer. One example of this type of setup is the NIST Spectral Irradiance and Radiance Responsivity Calibrations using Uniform Sources (SIRCUS) system, which uses tunable lasers as light sources [38]. Since radiometers are usually more stable than calibration lamps and spectroradiometers, this approach is more accurate. Another advantage to this approach is that the spectral calibration for all pixels is performed simultaneously. Unfortunately, setups of this kind are very expensive and therefore not available to most calibration laboratories.

In both cases, the spectral radiance of this standard needs to be sampled using the spectroradiometer SRFs. This is often simplified by interpolating the spectral radiance calibration at the SRF center wavelengths. The unknown spectrum of the integration sphere needs to be derived from the spectroradiometer calibration to transfer it. The sphere's radiance needs then to be sampled by the SRF of the imaging spectrometer. Again, this is usually done by interpolating the radiance value at the imaging spectrometer's SRF center wavelengths. The errors these assumptions cause have not yet been investigated.

1.1.4 Transformation of Geometric and Spectral Pixel Properties

Existing calibration measurements show that some imaging spectrometers significantly suffer from spatial and spectral non-uniformities [12, 13]. In other words, the Point Spread Functions (PSFs) of these instruments are not constant but change rapidly depending on detector location. Imaging transformation techniques are therefore required to correct these types of optical distortions and non-uniformities.

Although many methods exist for correcting pixel center angle and wavelength for imaging spectrometers, the number of techniques that also take the homogenizing image resolution into account is rather limited. One method involves homogenizing geometric response functions over all pixels of an imaging sensor with linear and nearest-neighbor interpolation [4]. This approach is based on a single parameter, FWHM, and neglects further information about the shape of the response function.

Another technique addresses this issue of varying resolution and center wavelength of the spectral response by sharpening the spectral bands after the center wavelengths are adjusted by cubic spline interpolation [53]. An iterative method exists that involves the creation of a super resolution image, which is subsequently convolved with the geometric and spectral model of a desired instrument [54, 55]. However, none of these publications discusses propagating uncertainties to the transformed images.

Besides the publications on imaging spectrometers discussed so far, there are several publications from other research fields that are relevant to our work. For array spectroradiometers (non-imaging spectrometers), an approach is reported that enables the simultaneous correction of stray light and bandpass effects [56]. In the paper, the authors present a Tikhonov regularized spectral deconvolution method. Unfortunately, the publication is hampered by the lack of mathematical detail provided by the authors. Similar techniques are also applied by astronomers, who typically refer to them as "PSF matching" or "PSF homogenization" methods. Within the field of astronomy, these techniques are usually applied before comparing images taken by two or more cameras with different optical properties. In this type of scenario, homogenization is necessary to suppress image differences caused solely by different camera properties and not by actual variations in the light emitted by a star or other target of interest. Notable approaches in this category can be found in [57–62]. While the homogenization techniques described therein are in principle the solution we are looking for, they require pixel-to-pixel variations of the responsivity to be either negligible or to be representable by a slowly varying function, e.g., low order polynomial as in [60].

However, none of the these methods addresses the simultaneous PSF transformation and resampling of distorted images on an individual pixel scale. Furthermore, all of them lack the treatment of uncertainty propagation.

1.2 Objectives and Scope of the Thesis

The objectives of this thesis are:

- Development of traceable calibration methods for imaging spectrometers.
- Development of a method that allows the pixel-specific correction of center wavelength, center angle, resolution, and response function shape non-uniformities.

To demonstrate these developments, we use a HySpex VNIR-1600 imaging spectrometer. With this thesis, we continue existing work where the same instrument was used [11, 12, 18, 19].

A major impact on the instrument performance is caused by the detector. Because it is integrated behind a spectrometer unit, we will need to make some additional efforts to derive its properties. Specifically, we determine dark and offset signal characteristics, noise, and gain of each pixel, non-linearity of the signal and integration time, temperature sensitivity of the radiometric response, and smear. Smear typically occurs during readout in CCD detectors and is the leakage of electronic charge carries that distort the signal of other pixels.

From the dark and offset signal characterization, we derive its distribution and the read noise. To derive the signal-dependent noise and the gain of each pixel, we us the well-established PTC method. The temperature dependence of the detector's radiometric response is determined by placing the switched-off instrument at the exit port of an illuminated integrating sphere. After turning on the imaging spectrometer, the signal change is monitored until thermal stabilization. To the best of our knowledge, this is the first time that this type of measurement

has been reported for this type of instrument class. To measure the signal-dependent non-linearity, we have built a setup that uses the light-addition method. Our setup was designed to achieve a high degree of accuracy while emitting high radiance levels. In contrast to other setups, we developed a layout that allows the calibration of all relevant sources of measurement errors related to the setup. We also enhanced the light-addition method so that the non-linearity curve can be retrieved with arbitrary sampling distances without the need to use polynomial functions. For the non-linearity of the integration time, i.e., the discrepancy of set and actual integration time, we measure a constant light source while the integration time is changed. Additionally, we investigate the smear effect with a high-power monochromatic light source and present a method to separate the smear effect from instrument stray light.

To calibrate spectral instrument properties, we use a monochromator setup, whose wavelength accuracy is of great importance for achieving an accurate calibration. To calibrate the monochromator, we utilize an echelle grating wavelength meter with a method we developed that determines the emitted center wavelength with arbitrary sampling distances. Due to the low output power of the monochromator, it is not possible to illuminate all pixels of typical imaging spectrometers while maintaining a sufficiently high signal to noise ratio. We therefore use a collimator to illuminate a limited number of pixels at discrete illumination angles. However, due to time constraints, it is not possible to measure the spectral properties of each pixel. Usually, analytical models are fitted on the acquired measurement data that describe the SRFs of a pixel. We were not able to find this type of function for the HySpex instrument. We therefore propose a method for modeling the SRF with a cubic spline and an approach to interpolate these models for unmeasured pixels.

To calibrate the geometric properties, i.e., the ARFs, we use a collimator setup with a slit as a target. By changing the incident angle of the collimator beam relative to the instrument's FoV, we measure the ARFs perpendicular to an instrument's movement direction (across-track) of each pixel. To model the ARFs, we use the same method as for the SRFs.

The SRF models are then used for the radiometric calibration by sampling the spectrum of a radiometric reference light source. The resampled spectrum is then used to link the raw signal to radiance. Since the reference light source can only illuminate a subset of pixels in a typical instrument's FoV, we also perform a relative calibration of the remaining pixels with an integrating sphere. The instrument is mounted on a rotary stage, which rotates the instrument in it's across-track axis. In this manner, the same location of an integrating sphere is measured with all pixels. This avoids systematic errors, which would be introduced by inhomogeneities in the integrating spheres radiance field. Finally, we use Monte Carlos simulations to determine the propagation of uncertainties during radiometric calibration. In addition, we determine the polarization sensitivity of each pixel with respect to an instrument's slit with a wire-grid polarizer.

After the previous steps, the raw data of each pixel can be converted into radiance values and the angular and spectral parameters can be provided. However, non-uniform pixel properties make this data complicated to use, so we perform a transformation of the ARFs and SRFs to obtain distortion and aberration free, homogeneous data. Since the pixel properties can change rapidly in push-broom imaging spectrometers, we developed a novel method with

which the response functions of each pixel can be individually transformed. This is done by applying a transformation matrix on sensor A images that maps every pixel of sensor B to the set of pixels of sensor A. Sensor B can either be a distortion-free version of sensor A or a different instrument that allows the comparison of images acquired with both sensors. The transformation matrix can also be used to calculate the covariances of transformed sensor A images from the covariances of the source images. The method is basically a generalization of the well-known Wiener deconvolution for sensors that exhibit a rapid pixel-to-pixel variation of geometric or spectral responsivity. Though developed for correcting image distortions in imaging spectrometers, the presented algorithm is very general in nature. In fact, it should be applicable to almost any ground-based, air-, and space-borne camera and imaging spectrometer.

It is important to note that we cannot address all aspects of the calibration of push-broom imaging spectrometers. Explicitly excluded is the treatment of stray light, which was already covered in [18].

1.3 Definition of Calibration

According to the International Vocabulary of Metrology (VIM) [63] calibration is defined as

"... operation that, under specified conditions, in a first step, establishes a relation between the quantity values with measurement uncertainties provided by measurement standards and corresponding indications with associated measurement uncertainties and, in a second step, uses this information to establish a relation for obtaining a measurement result from an indication."

In our case, the described first step is performed during the laboratory calibration where a model of the instrument is derived. The second step is performed when the instrument model is used to convert the Digital Numbers (DN) provided by the sensor into physical values. These values must be traceable to international standards to guarantee comparability, where traceability is defined as

"... property of a measurement result whereby the result can be related to a reference through a documented unbroken chain of calibrations, each contributing to the measurement uncertainty."

Of course, there is no perfect measurement. Every measurement is compromised by an error. Following the Guide to the Expression of Uncertainty in Measurement (GUM) [64], an error has two components, a random and a systematic component. Random errors can be reduced by increasing the number of observations. On the other hand, systematic errors can be reduced or eliminated by modeling the effects and applying corrections.

The term error must not be used as synonym for uncertainty. After correcting systematic errors, the random error cannot be known. The uncertainty reflects the expected spread of the measured value around the "true" value. This imperfection arises from the uncertainty due to random effects and the uncertainty of correcting systematic errors. Without uncertainties, measurement values are in principle worthless, as their trustworthiness is unknown.

1.4 DLR's Calibration Home Base for Imaging Spectrometers

The work presented here was carried out at Deutsches Zentrum für Luft- und Raumfahrt (DLR)'s Calibration Home Base (CHB) for imaging spectrometers at DLR Oberpfaffenhofen, Germany [43, 44]. Originally built for calibrating the European Space Agency (ESA) airborne-sensor Airborne Prism EXperiment (APEX) [17], it also serves as a calibration facility for DLR's HySpex imaging spectrometer suite [65] and other sensors [13]. The laboratory allows the characterization of spectral, spatial and radiometric instrument characteristics. An integrating sphere in combination with the Radiometric Standard (RASTA) allows PTB traceable radiometric measurements. A setup with a movable and rotatable mirror allows the characterization of geometric and, together with a monochromator, spectral instrument properties. The high level of automation of this measurement setup allows a high number of measurements to be carried out that would be impossible via manual control.

We modified and enhanced all existing setups and built new ones during the course of this thesis. In addition, we have completely redesigned the laboratory automation software to allow easy integration of new devices and further increase flexibility. However, this is not part of this thesis.

1.5 Airborne Imaging Spectrometer HySpex VNIR-1600 Operated by DLR

In this work, we use a Norsk Elektro Optikk A/S (NEO) HySpex VNIR-1600 imaging spectrometer as an experimental platform for developing and testing the proposed methods, see Table 1.1. This sensor has a silicon interline transfer CCD as detector, which is a Kodak KAI2020 packaged in an Adimec-1600mD [66] camera body. The HySpex VNIR-1600 can be combined with different optics to change to focal point. The HySpex is normally used with a FoV expander that doubles the FoV, but simultaneously reduces the angular resolution. We therefore calibrate the instrument in this configuration.

The sensor is in combination with a HySpex SWIR-320m-e part of the DLR operated airborne imaging spectrometer system HySpex [65], see Fig. 1.1. Therefore, the results of this work directly benefit the calibration and data quality of this sensor suite. A modular processor that is currently in operational use was developed as part of this work in order to calibrate both instruments. Since the algorithms, characterization and calibration methods are very similar for both instruments, we focus on the VNIR instrument in this work.

Detector technology	Si interline transfer CCD
Spectral range	416 - 992 nm
Spectral sampling interval	3.6 nm
FoV	34.5°
Instantaneous Field of View (IFoV) (across-track)	0.37 mrad
IFoV (along-track)	0.5 mrad
Spatial columns	1600
Spectral channels	160
Radiometric quantization	12 bit
Max. frame rate	135 Hz
Detector temperature	ambient

Table 1.1: Specifications of the HySpex VNIR-1600 airborne imaging spectrometer used in this work.

Figure 1.1: Imaging spectrometers HySpex VNIR-1600 (a) and HySpex SWIR-320m-e (b) installed on a gyro-stabilized mount in a DLR aircraft.

1.6 Organization of the Thesis

Calibrating certain parameters requires knowledge about other instrument effects. For instance, evaluating spectral and geometric calibration measurements requires data that is corrected for all effects that cause a non-linear relationship between the incident radiance and the measured signal. Radiometric calibration in turn additionally demands spectral instrument calibration. This thesis is therefore structured according to these requirements. We grouped the calibration processes logically in four chapters.

- Chapter 2 gives the theory behind push-broom imaging spectrometers and includes a detailed overview is given of the key parameters which determine instrument performance.
- Chapter 3 defines how parameters associated with the detector array are calibrated. These are, in particular dark and offset signal, signal-dependent noise, temperature sensitivity, signal and integration time non-linearities, and smear, an effect which is typical for CCD detectors.
- Chapter 4 discusses the calibration of geometric and spectral instrument parameters. These are in particular across-track ARFs and SRFs.
- Chapter 5 defines calibrating radiometric instrument response and polarization sensitivity.
- Chapter 6 focuses on a novel method that corrects image distortions by individually transforming the ARFs and SRFs of each pixel.
- Chapter 7 summarizes this work and provides a conclusion and an outlook.

2

Theory of Push-broom Imaging Spectrometers

Contents

2.1 Introduction 14
2.2 Imaging Equation 15
2.3 Focal Plane Array 16
2.4 Point Spread Function 18
2.5 Pixel Response Function 19
2.6 Image Distortions 21
2.7 Stray Light 22
2.8 Radiometric Responsivity 22
2.9 Polarization Sensitivity 23
2.10 Non-Linearity 24
2.11 Noise 25
2.12 Summary 26

2.1 Introduction

Imaging spectrometers, often referred to as hyperspectral cameras, are passive optical instruments that measure spectral radiance. One of the most common device concepts is the push-broom design, which requires no moving parts. The principle configuration of a push-broom imaging spectrometer is shown in Fig. 2.1. A telescope creates an intermediate image of the target scene. With a slit a narrow line is cut out from the image. The beam coming through the slit is then collimated and its spectral components are split into different angles by a dispersing element. The dispersing element is usually realized as diffraction grating or a prism. Finally, focusing optics generate an image from the collimated and spectrally dispersed beam on the FPA. Since angles in the beam in front of the focusing optics correspond to wavelengths, positions perpendicular to the slit on the detector correspond to wavelengths in the same way. One single image take therefore has spectral and one-dimensional spatial information. Two-dimensional spatial data is generated by moving the instrument perpendicular to its slit and simultaneously capturing images. The result is a three-dimensional data array.

In the object plane, the spatial dimension parallel to the slit (across-track) is denoted as y'-axis, while the x'-axis is in the direction of motion (along-track). The x-, y- and z-axes describe the dimensions of the three-dimensional data array. The y-axis corresponds to the y'-axis of the object plane. Similarly, the x-axis is linked to the object plane's x'-axis. The

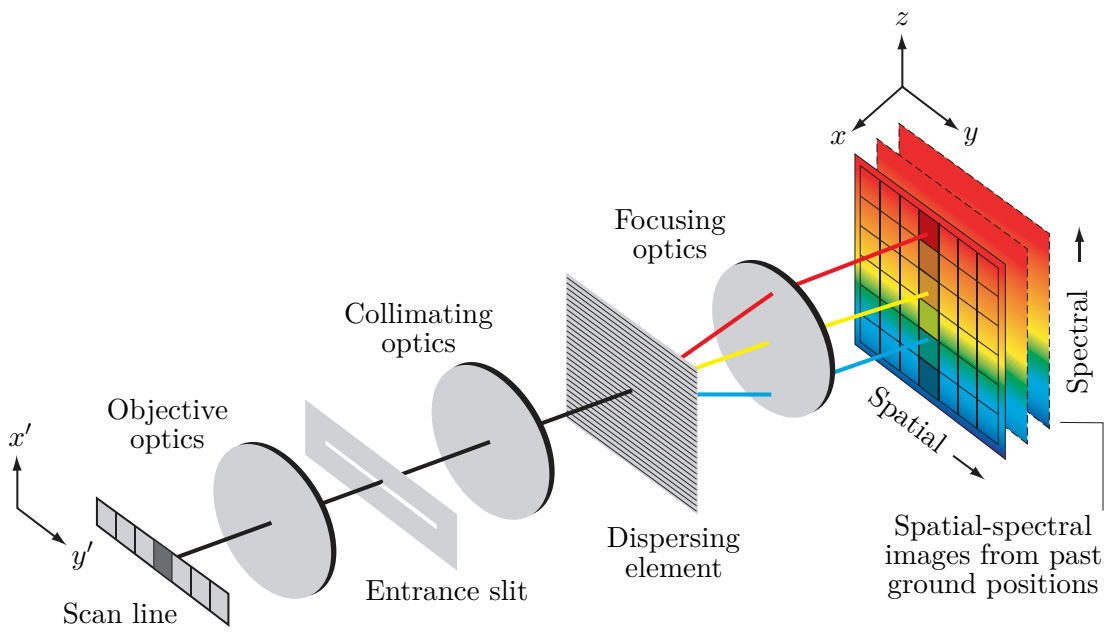

Figure 2.1: Principle setup of push-broom imaging spectrometers. An objective optics creates an intermediate image from which a slit cuts out a line. This line is a collimated and the spectral components are split perpendicularly to the slit by a dispersing element. Finally, a focusing optics images the collimated and spectrally dispersed beam a Focal Plane Array (FPA). By moving the instrument along x' and continuous data acquisition a three dimensional data array is generated. Figure taken from [67].

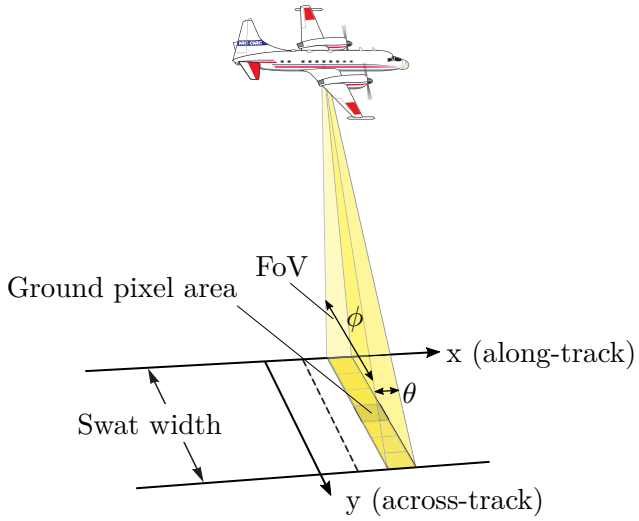

Figure 2.2: Push-broom imaging spectrometer geometry. A sensor platform, here represented by an aircraft, moves along the x'-axis in along-track direction. The instrument's Field of View (FoV) spans along the y'-axis in across-track direction, with α and β denoting the angular coordinates parallel and perpendicular to the FoV, respectively. The ground pixel area is the area of one geometric line covered during the acquisition of one frame. Please note that in reality the pixel footprints do not have a rectangular shape. Original figure taken from [67].

spectral dimension is referred to as the z-axis. The y- and z-axis are on the focal plane, where the FPA is located. The across-track angle is given as β and the along-track angle as α, see Fig. 2.2. The entire across-track viewing field is called FoV, while the IFoV is the viewing angle of discrete pixels. The IFoV distinguishes between along- and across-track.

In this work, we denote a single detector element as pixel, all pixels in one detector row which collect the same wavelength as spectral channel, and all pixels in one column on which light from the same across-track angle falls as spatial column. One data acquisition of all pixels is called a frame. The consecutive uninterrupted measurement of many frames is denoted as data take.

2.2 Imaging Equation

The optics O of an imaging spectrometer converts a spectral radiance field L_λ in units of $[\mathrm{W\,m^{-2}\,nm^{-1}\,sr^{-1}}]$ impinging on the sensor aperture into a two-dimensional irradiance image E $[\mathrm{W\,m^{-2}}]$ in the focal plane, where the detector is located. For L_λ, being a plane wave front of incoherent light the equation for this process can be written as

$$E(y,z) = \int_{A_\mathrm{e}} \int_{4\pi} \int_{0}^{\infty} O(y,z,A,\alpha,\beta,\lambda) L_\lambda(A,\alpha,\beta,\lambda)\,\mathrm{d}\lambda\,\mathrm{d}\alpha\,\mathrm{d}\beta\,\mathrm{d}^2A, \tag{2.1}$$

where A_e is the entrance aperture area and λ is the wavelength. A detailed description of the coordinate system can be found in Appendix B. It must be noted that here we assume an instrument that is focused on infinity. O describes all physical effects of the optical system, i.e., beam shaping and transmission depending on the wavelength λ, illuminated area on the

instrument aperture A, and the along-track α and across-track β incidence angles.

Since the instrument moves along its x-axis while a frame is recorded, the image is smeared along this axis. It can be assumed that scenes are homogeneous over the entrance pupil area A during one image take. Equation (2.1) simplifies then to

$$E(y,z) = A_\mathrm{e} \int_{4\pi} \int_{0}^{\infty} O(y,z,\alpha,\beta,\lambda) L_\lambda(\alpha,\beta,\lambda)\,\mathrm{d}\lambda\,\mathrm{d}\alpha\,\mathrm{d}\beta. \tag{2.2}$$

2.3 Focal Plane Array

A FPA is a semiconductor array of photosensitive pixels placed in the focal plane of the focusing optics, i.e., where we calculated the irradiance $E(y,z)$ in Eq. (2.2). The absorption of photons causes the generation of electrons in the pixels of the FPA. The rate with which electrons are generated is called photo current I_i^ph [e$^-$/s], calculated by

$$I_i^\mathrm{ph}(T) = A_\mathrm{e} \int_{A_\mathrm{d}} \int_{4\pi} \int_{0}^{\infty} D_i(\lambda,T,y,z) O(y,z,\alpha,\beta,\lambda) L_\lambda(\alpha,\beta,\lambda)\,\mathrm{d}\lambda\,\mathrm{d}\alpha\,\mathrm{d}\beta\,\mathrm{d}y\,\mathrm{d}z, \tag{2.3}$$

where T is the detector temperature, A_d is the detector area, and D_i is a model of the FPA. The index i denotes the pixel number, where the pixels of the two dimensional array are continuously numbered. Assuming that the pixels have a rectangular shape, the FPA D_i can be mathematically described by

$$D_i(\lambda,T,y,z) = \eta_i(\lambda,T)\frac{\lambda}{hc} \sqcap_{w_\mathrm{y}}(y - i\Delta y) \sqcap_{w_\mathrm{z}}(z - i\Delta z), \tag{2.4}$$

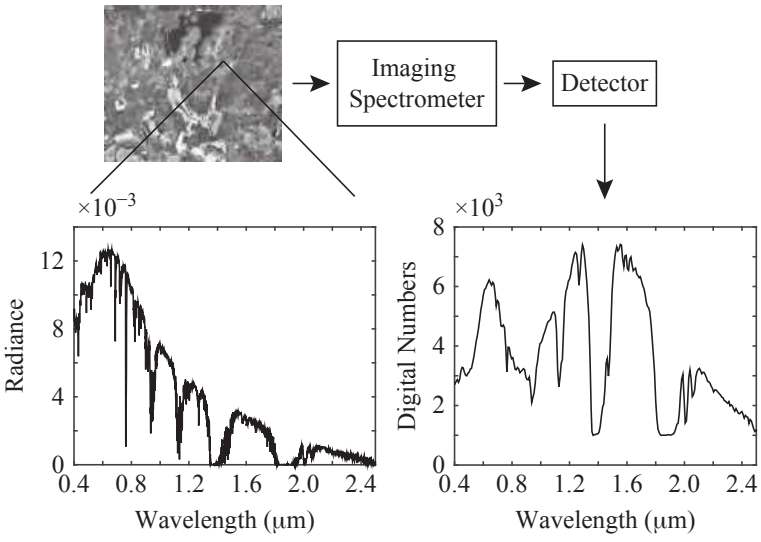

Figure 2.3: Conversion of radiance to digital numbers for a signal location in a scene. Figure taken from [2].

where η_i [e^-/photons] is the pixels wavelength and temperature T dependent quantum efficiency, h is Planck's constant, c is the speed of light, $\sqcap$ is the boxcar function defined as

$$\sqcap_w(x) = \begin{cases} 1 \text{ if } |x| > \frac{w}{2} \\ 0 \text{ if } |x| \leq \frac{w}{2} \end{cases}, \tag{2.5}$$

w_y and w_z are the widths of a pixels photosensitive area along the y-axis respectively z-axis, while Δy and Δz are the pixel pitches.

The ratio between the photosensitive area and the total area of a pixel is called the fill factor. The quantum efficiency is the chance of a photon hitting sensitive pixel area to be absorbed by an electron in the valance band of the semiconductor. By absorbing the energy of a photon, an electron is moved from the valance band to the higher energy conduction band, which causes the photo current. The energy difference between valence and conduction band is called the band gap. Photons with an energy smaller than the band gap cannot be absorbed. Thus, the quantum efficiency for them is zero. Both the band gap and the quantum efficiency depend on the temperature of the semiconductor [68, 69].

However, there is also a current $I_i^{\mathrm{d}}(T)$ when no photons are entering the instrument. It is denoted as Dark Current (DC) and is mainly caused by random thermal generation of electron hole pairs. The overall current is the sum of photo current and dark current:

$$I_i(T) = I_i^{\mathrm{ph}}(T) + I_i^{\mathrm{d}}(T). \tag{2.6}$$

The generated charge carriers in a pixel are accumulated in a pixels potential well during the integration time t_{int}, leading to an amount of N_i electrons, calculated by

$$N_i(T) = N_i^{\mathrm{ph}}(T) + N_i^{\mathrm{d}}(T) = t_{\mathrm{int}} \left(I_i^{\mathrm{ph}}(T) + I_i^{\mathrm{d}}(T) \right), \tag{2.7}$$

where N_i^{ph} and N_i^{d} are the electrons created by photo current and dark current, respectively. The stored electrons are then read out by an electronic circuit, which adds an offset equivalent to the amount of elections N^{o} to avoid negative signal levels. At the end of the readout process, the analog signal is digitized by an Analog Digital Converter (ADC). The digital signal S is then

$$S_i(T) = g\left(N_i(T) + N^{\mathrm{o}}\right), \tag{2.8}$$

where g is a constant factor called gain, which is the rate at which the electronic charge converts to DN. The signal is also affected by the quantization of the ADC. Since the quantization can be interpreted as noise, see Sec. 2.11, we ignore it here. Figure 2.3 shows an example of the conversion of radiance into a digital signal.

In the remainder of this work, we denote the signal of averaged frames by $S[\bar{x}yz]$. In the same manner, averaged spatial columns are denoted by $S[x\bar{y}z]$ and averaged spectral channels by $S[xy\bar{z}]$.

In a linear system, the signal is then the sum of the photo signal S_i^{ph} caused by photo current, the dark signal due to dark current S_i^{d}, and the offset signal S^{o}, which yields

$$S_i(T) = S_i^{\mathrm{ph}}(T) + S_i^{\mathrm{d}}(T) + S^{\mathrm{o}}, \tag{2.9}$$

with the photo signal as

$$S_i^{\mathrm{ph}}(T) = g t_{\mathrm{int}} A_{\mathrm{e}} \int\limits_{A_{\mathrm{d}}} \int\limits_{4\pi} \int\limits_{0}^{\infty} D_i(\lambda, T, y, z) O(y, z, \alpha, \beta, \lambda) L_\lambda(\alpha, \beta, \lambda) \,\mathrm{d}\lambda \,\mathrm{d}\alpha \,\mathrm{d}\beta \,\mathrm{d}y \,\mathrm{d}z, \tag{2.10}$$

the dark signal as

$$S_i^{\mathrm{d}}(T) = g t_{\mathrm{int}} I_i^{\mathrm{d}}(T), \tag{2.11}$$

and the offset signal as

$$S^{\mathrm{o}} = g N^{\mathrm{o}}. \tag{2.12}$$

2.4 Point Spread Function

The Point Spread Function (PSF) is the response of a spatial and spectral points source. It can be mathematically described by

$$\mathrm{PSF}(y, z, \alpha_0, \beta_0, \lambda_0) \propto A_{\mathrm{e}} \int\limits_{4\pi} \int\limits_{0}^{\infty} O(y, z, \alpha, \beta, \lambda) \delta(\alpha - \alpha_0, \beta - \beta_0, \lambda - \lambda_0) \,\mathrm{d}\lambda \,\mathrm{d}\alpha \,\mathrm{d}\beta \tag{2.13}$$

$$\propto A_{\mathrm{e}} \int\limits_{4\pi} \int\limits_{0}^{\infty} O(y, z, \alpha_0, \beta_0, \lambda_0) \,\mathrm{d}\lambda \,\mathrm{d}\alpha \,\mathrm{d}\beta, \tag{2.14}$$

where δ is the Dirac delta function denoting a point source at infinity at the angular position α_0 and β_0 emitting radiation with wavelength λ_0. The PSF is a relative spread function, hence its integral is normalized to unity:

$$\int\limits_{A_{\mathrm{d}}} \mathrm{PSF}(y, z) \,\mathrm{d}x \,\mathrm{d}y = 1. \tag{2.15}$$

We can now express the optical system function O as the product of the optical transmission function τ and the PSF by

$$O(y, z, \alpha, \beta, \lambda) = \tau(\alpha, \beta, \lambda) \mathrm{PSF}(y, z, \alpha, \beta, \lambda). \tag{2.16}$$

Since the PSF describes the relative signal spread in focal plain area, τ describes the signal attenuation.

However, since the image in the focal plane is sampled with an FPA, a PSF can only be determined with the finite resolution of the detector. Using Eq. (2.3) and (2.13) the sampled PSF is defined as

$$\mathrm{PSF}^{\mathrm{s}}_{\alpha_0\beta_0\lambda_0}(i) \propto \int\limits_{A_{\mathrm{d}}} D_i(\lambda_0, T, y, z) \mathrm{PSF}(y, z, \alpha_0, \beta_0, \lambda_0) \,\mathrm{d}x \,\mathrm{d}y. \tag{2.17}$$

Please observe that the PSF is independent of the detector temperature, since the point source is monochromatic and the temperature dependency of the quantum efficiency η of each pixel is assumed to be identical. Equivalent to Eq. (2.15) the sampled PSFs is normalized to

unity so that

$$\sum_i \mathrm{PSF}^{\mathrm{s}}_{\alpha_0\beta_0\lambda_0}(i) = 1. \tag{2.18}$$

2.5 Pixel Response Function

Equation 2.3 shows, that the combination of optical system and detector determine the conversion rate from incident photons to photo current. Another function, called PRF, can be derived from these functions, which describes a pixels relative sensitivity to the along-track and across-track angle as well as to the wavelength. The relationship between PRFs and PSFs is shown in Fig. 2.4.

Assuming that the slope change with temperature of the quantum efficiency is negligible for the wavelength range of the photons a pixel receives, a PRF is defined as

$$f_i(\alpha, \beta, \lambda) \propto \int_{A_\mathrm{d}} D_i(\lambda, T, y, z) O(y, z, \alpha, \beta, \lambda)\, \mathrm{d}y\, \mathrm{d}z, \tag{2.19}$$

and that the integral over wavelength and along-track and across-track angles is equal to one:

$$\int_{4\pi} \int_0^\infty f_i(\alpha, \beta, \lambda)\, \mathrm{d}\lambda\, \mathrm{d}\alpha\, \mathrm{d}\beta = 1 \tag{2.20}$$

Applying the PRF on spectral radiance L_λ yields the radiance sampled by the sensor L_i^{s}:

$$L_i^{\mathrm{s}} = \int_{4\pi} \int_0^\infty f_i(\alpha, \beta, \lambda) L_\lambda(\alpha, \beta, \lambda)\, \mathrm{d}\lambda\, \mathrm{d}\alpha\, \mathrm{d}\beta. \tag{2.21}$$

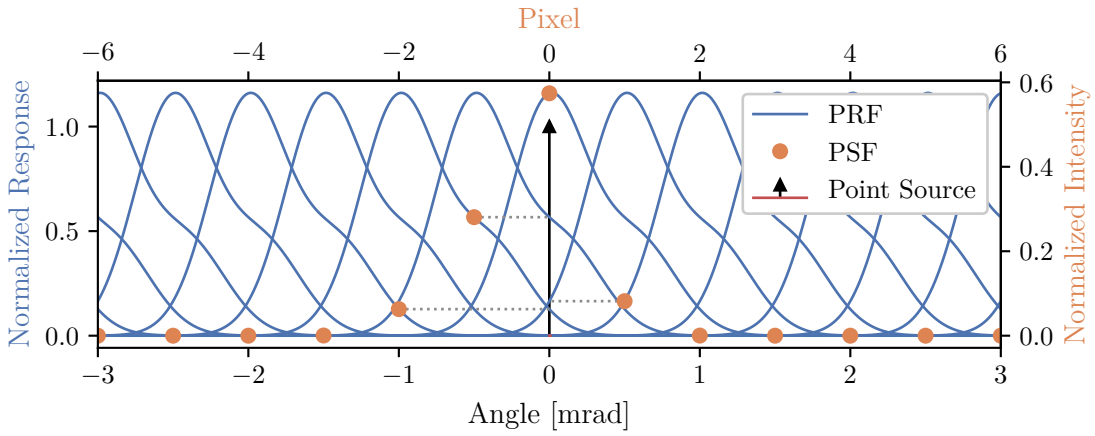

Figure 2.4: Slice through an angular axis of a PSF which is the signal created by a point source. The orange dots indicate the signal of each pixel while the blue curves are the Pixel Response Functions (PRFs). As it can be seen, the pixel signal corresponds to the value of the PRFs at the intersection which the point source.

From the PRF we can derive the SRF, the along-track ARF, and the across-track ARF. The SRF is the relative responsivity of a pixel to the wavelength of at-aperture radiance. It can be derived from a pixels PRF by integration of the geometric components:

$$\mathrm{SRF}_i(\lambda) = \int_0^\infty f_i(\alpha, \beta, \lambda)\,\mathrm{d}\alpha\,\mathrm{d}\beta. \tag{2.22}$$

The concept of the along-track ARF is analogous to the SRF. But instead of wavelength, it is a function of the along-track angle, yielding

$$\mathrm{ARF}_i(\alpha) = \int_0^\pi \int_0^\infty f_i(\alpha, \beta, \lambda)\,\mathrm{d}\lambda\,\mathrm{d}\beta. \tag{2.23}$$

In the same manner, the across-track ARF is defined as

$$\mathrm{ARF}_i(\beta) = \int_0^\pi \int_0^\infty f_i(\alpha, \beta, \lambda)\,\mathrm{d}\lambda\,\mathrm{d}\alpha. \tag{2.24}$$

This Response Function (RF) are often described by Gaussian functions. If this assumption is true, then center and resolution—defined as FWHM—can easily be derived from the function parameters. But this assumption is not always justified [23, 42]. In cases where response functions cannot be described by Gaussian functions, comparable metrics are required for the response function center and resolution. Therefore, here we use the approach we have published in [13] and which is described in this section.

The response function center is defined as the median x_c which is derived by

$$x_c = \arg\min_{\mathrm{x_c'}} \left\| \frac{1}{2} \int_{-\infty}^{\infty} \mathrm{RF}(x)\,\mathrm{d}x - \int_{-\infty}^{x_c'} \mathrm{RF}(x)\,\mathrm{d}x \right\|_2^2, \tag{2.25}$$

where $\|\cdot\|_2$ is the Euclidean norm.

In a similar way, the resolution is determined by the integral that is equally distant from the center, which equals the integral of the FWHM of a Gaussian function h, yielding

$$\int_{x_c-\Delta x/2}^{x_c+\Delta x/2} \mathrm{RF}(x)\,\mathrm{d}x = \frac{\int_{x_c-\mathrm{FWHM}/2}^{x_c+\mathrm{FWHM}/2} h(x)\,\mathrm{d}x}{\int_{-\infty}^{\infty} h(x)\,\mathrm{d}x} = 0.7610. \tag{2.26}$$

The sampling interval is defined as the distance between response function centers. This can be individual for each pixel pair, caused by e.g., non-constant dispersion. The sampling ratio can be derived from the sampling interval and resolution:

$$\text{Sampling Ratio} = \frac{\text{Resolution}}{\text{Sampling Interval}}. \tag{2.27}$$

The sampling ratio is an important measure for the resolvable of a system according the

Nyquist–Shannon sampling theorem [70, 71]. The width resolution can be interpreted as the band limit of the signal, while the sampling interval is the equal to the sampling rate. For a sampling ratio = 2, the sampling interval is equal to the Nyquist rate. A Sampling Ratio > 2 is therefore desirable to avoid aliasing of the image.

2.6 Image Distortions

In an ideal case, the y-position of a PSF in the focal plane is only dependent on the across-track angle β and the z-position only on the wavelength λ of an incident beam. If the z-coordinate changes with β as well, the distortion is called smile. In the same way, if y is dependent on the wavelength λ, then the effect is called keystone [9], see Fig. 2.5. However, besides these two effects, the shape of the PSF may not be constant for pixels of the same spectral channel or spatial column, either.

In the following, we define smile and keystone with respect to PRFs. Keystone is the difference of center angles of the across-track ARFs of a spatial column. Equivalently, smile is the difference of the center wavelengths of the SRFs of a spectral channel.

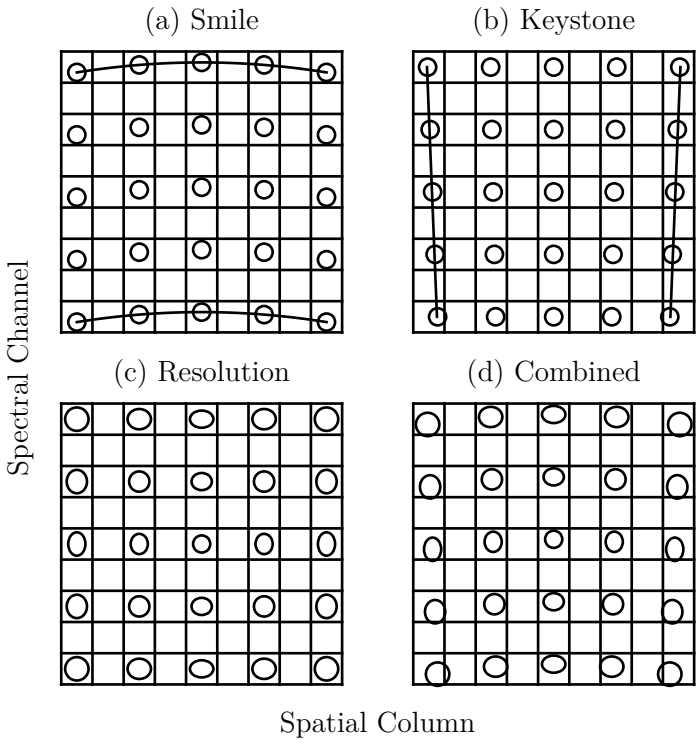

Figure 2.5: Smile and keystone distortions as well as change of PSF resolution shown on idealized FPA grids. Each circle is the FWHM of a PSF. (a) Smile: Change of center wavelength in one channel with spatial position. (b) Keystone: Change of center angle with wavelength. (c) Resolution: Change of spectral and spatial resolution with detector position. (d) Combination of these effects. Figure inspired by [2].

2.7 Stray Light

Although we do not deal with calibration of stray light in this thesis, it is discussed here for the sake of completeness. Stray light is light that hits a detector where it is not intended. Or, in other words, pixels are sensitive to light whose across-track angle and wavelength is several FWHMs away from the pixel's center angle and wavelength. Stray light manifests itself in longer tails of the PRF, see Fig. 2.6. While the sensitivity far from the PRF center is very low, the summation over a large area of the tails can cause a significant contribution to the overall signal of a pixel. This is especially the case, when more light is present in the area of the tails than around the center of a PRF. Stray light is caused by light scattering across imperfect optical components, such as mirrors, lenses, baffles, prisms and so forth.

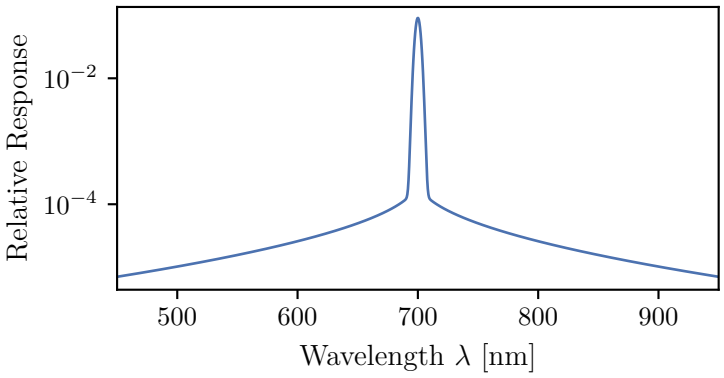

Figure 2.6: Example of a Spectral Response Function (SRF) with semi logarithmic representation. Although the response at three times of the FWHM from the center is below 0.01 %/nm, the sum of the response outside of these borders accounts for 2.5 % of the total response.

2.8 Radiometric Responsivity

Using the PRF representation from Eq. (2.21) we can rewrite Eq. (2.10) to

$$S_i^{\mathrm{ph}}(T) = t_{\mathrm{int}} g A_{\mathrm{e}} \int_{A_{\mathrm{d}}} \int_{4\pi} \int_{0}^{\infty} D_i(\lambda, T, y, z) O(y, z, \alpha, \beta, \lambda) \,\mathrm{d}\lambda \,\mathrm{d}\alpha \,\mathrm{d}\beta \,\mathrm{d}y \,\mathrm{d}z L_i^{\mathrm{s}} \tag{2.28}$$

$$= t_{\mathrm{int}} R_i(T) L_i^{\mathrm{s}} \tag{2.29}$$

$$= t_{\mathrm{int}} R_i(T) \int_{4\pi} \int_{0}^{\infty} f_i(\alpha, \beta, \lambda) L_\lambda(\alpha, \beta, \lambda) \,\mathrm{d}\lambda \,\mathrm{d}\alpha \,\mathrm{d}\beta, \tag{2.30}$$

where R is the radiometric coefficient, which is a measure for the radiometric responsivity. We have now separated the pixel responsivity into the normalized PRF f, which describes the relative spatial-spectral responsivity of a pixel, and into a constant scaling factor, namely the radiometric response R. The latter is usually determined by comparing a known radiance

with the measured signal, which is done during the radiometric instrument calibration by

$$R_i(T) = \frac{S_i^{\mathrm{ph}}(T)}{t_{\mathrm{int}} \int_{4\pi} \int_0^{\infty} f_i(\alpha, \beta, \lambda) L_\lambda(\alpha, \beta, \lambda)\, \mathrm{d}\lambda\, \mathrm{d}\alpha\, \mathrm{d}\beta}. \tag{2.31}$$

The sensor sampled radiance L_i^{s} is then obtained during calibration of the data using Eq. (2.29)

2.9 Polarization Sensitivity

Any optical surface in an optical instrument can exhibit polarization-dependent loss. Hence, the radiometric response R can be sensitive to linear polarization of measured light. The polarization-sensitivity can be determined by logically splitting the response in a polarization sensitive part $2R^{\mathrm{p}}$ and a polarization-insensitive part R^{up} so that the response for unpolarized light is $R = R^{\mathrm{p}} + R^{\mathrm{up}}$ [13], see Fig. 2.7. Following Magnus' law, the normalized polarization-dependent signal $S^{\mathrm{ph}}(\gamma)/t_{\mathrm{int}}$ of incoming measured radiance L^{s} with the degree of polarization p is

$$S^{\mathrm{ph}}(\gamma)/t_{\mathrm{int}} = 2R^{\mathrm{p}} \cdot L_{||}^{\mathrm{s}} + R^{\mathrm{up}} \cdot L^{\mathrm{s}} \tag{2.32}$$

$$= 2R^{\mathrm{p}} \left(p \cos^2(\gamma - \gamma_0) + \frac{1-p}{2} \right) L^{\mathrm{s}} + R^{\mathrm{up}} \cdot L^{\mathrm{s}}. \tag{2.33}$$

$L_{||}^{\mathrm{s}}$ is polarized light parallel to the entrance slit, γ is the polarization angle with respect to the entrance slit, and γ_0 is the polarization angle, for which $S^{\mathrm{ph}}(\gamma)$ is maximal. The

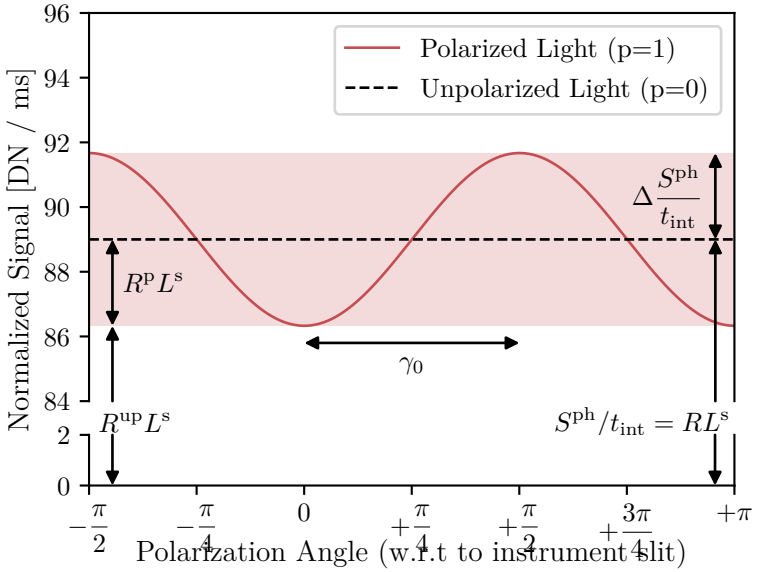

Figure 2.7: Example of signal normalized by integration time $S^{\mathrm{ph}}/t_{\mathrm{int}}$ dependent on the polarization angle of the measured radiance L^{s}. The radiometric response R is logically split in a polarization-dependent response R^{p} and polarization independent response R^{up}. γ_0 is the angle of the maximum sensitivity relative to the instrument slit. Figure inspired by [13].

polarization sensitivity P is defined as

$$P = \frac{R^{\mathrm{p}}}{R^{\mathrm{p}} + R^{\mathrm{up}}} \cdot 100\,\%. \tag{2.34}$$

The degree of polarization of measured radiance is often unknown. Hence, the maximum error due to polarization is equal to the polarization sensitivity P.

2.10 Non-Linearity

So far, we have assumed that the ratio of photo signal to at-aperture radiance and integration time is constant. If this is not the case and the ratio changes with radiance and integration time, respectively, then the instrument behaves in non-linear manner. This can have different causes. The first possibility is, that the set integration $t_{\mathrm{int}}^{\mathrm{set}}$ time differs from the actual integration time t_{int} by

$$t_{\mathrm{int}} = \frac{t_{\mathrm{int}}^{\mathrm{set}}}{\zeta_{\mathrm{t}}(t_{\mathrm{int}}^{\mathrm{set}})}. \tag{2.35}$$

The non-linearity is described here by the non-linearity function $\zeta_{\mathrm{t}}(t_{\mathrm{int}}^{\mathrm{set}})$, which depends on the set integration time. Another possibility is that the radiometric responsivity of a pixel changes with the fill level of the potential well, yielding

$$N^{\mathrm{nl}} = \zeta_{\mathrm{D}}\left(It_{\mathrm{int}}\right) It_{\mathrm{int}}, \tag{2.36}$$

where ζ_{D} is the potential well non-linearity function. Also, the ADC can exhibit non-linear behavior ζ_{g}, effectively resulting in a non-linear gain g described by

$$S^{\mathrm{nl}} = g\zeta_{\mathrm{g}}(N^{\mathrm{nl}})N^{\mathrm{nl}} + gN^{\mathrm{o}} \tag{2.37}$$

$$= g\zeta_{\mathrm{g}}\left(\zeta_{\mathrm{D}}\left(It_{\mathrm{int}}\right) It_{\mathrm{int}}\right)\zeta_{\mathrm{D}}\left(It_{\mathrm{int}}\right) It_{\mathrm{int}} + gN^{\mathrm{o}}. \tag{2.38}$$

Since the N^{o} is a constant offset, we assume here that it is independent of the potential fill value N. As we can see, the two non-linearity functions ζ_{g} and ζ_{D} depend on the same parameters I and t_{int}. Usually, these cannot be separated when the detector is not investigated at the subsystem level. However, it is possible to define a combined non-linearity function as

$$\zeta_{\mathrm{gD}}\left(It_{\mathrm{int}}\right) = \zeta_{\mathrm{g}}\left(\zeta_{\mathrm{D}}\left(It_{\mathrm{int}}\right) It_{\mathrm{int}}\right)\zeta_{\mathrm{D}}\left(It_{\mathrm{int}}\right). \tag{2.39}$$

Inserting Eq. (2.39) in Eq. (2.38) yields

$$S^{\mathrm{nl}} = g\zeta_{\mathrm{gD}}\left(It_{\mathrm{int}}\right) It_{\mathrm{int}} + gN^{\mathrm{o}}. \tag{2.40}$$

However, to correct the non-linearity of the signal S, we cannot use ζ_{gD} since it depends on a parameter we actually want to determine. Therefore, we need to express the non-linearity in terms of the non-linear signal S^{nl} as

$$S = \frac{S^{\mathrm{nl}}}{\zeta^{\mathrm{S}}(S^{\mathrm{nl}})} = \frac{S^{\mathrm{nl}}}{\zeta_{\mathrm{gD}}\left(It_{\mathrm{int}}\right)} = gIt_{\mathrm{int}} + gN^{\mathrm{o}}. \tag{2.41}$$

2.11 Noise

Noise is a random fluctuation of the signal from a the detector with contribution from several sources that contaminate a measurement. This includes the photon shot noise σ_{ph}, i.e., the random number of photons collected by the detector, dark noise σ_{d}, which is the random number of electrons generated by dark current, noise added during electronic readout σ_{r} including quantization noise σ_{Q}. The variance added due to quantization is fixed [27, 72]:

$$\sigma_{\mathrm{Q}}^2 = \frac{1}{12}\,[DN^2]. \tag{2.42}$$

Please note that this variance is independent on the ADC resolution and identical for every bit depth. This list is not exhaustive but does contain the most important sources of noise [2, 27]. Both the photon shot noise and the dark noise usually follow Poisson statistics. This means that the photon shot noise in $[e^-]$ is stated as

$$\sigma_{\mathrm{ph}} = \sqrt{N_{\mathrm{ph}}}, \tag{2.43}$$

and the dark noise as

$$\sigma_{\mathrm{d}} = \sqrt{N_{\mathrm{d}}}. \tag{2.44}$$

It follows then that we can determine the combination of photon shot noise and the dark noise from the total number of generate electrons N because

$$\sqrt{\sigma_{\mathrm{ph}}^2 + \sigma_{\mathrm{d}}^2} = \sqrt{N_{\mathrm{ph}} + N_{\mathrm{d}}} = \sqrt{N}. \tag{2.45}$$

In contrast to photon shot and dark noise, read noise σ_{r} is usually normally distributed. Assuming that the noise terms are independent, they can be added quadratically, yielding

$$\sigma_{\mathrm{tot}}(N) = \sqrt{N + \sigma_{\mathrm{r}}^2}\,[e^-]. \tag{2.46}$$

Equivalently, the noise as a function of the signal in DN can be modeled as

$$\sigma_{\mathrm{tot}}(S) = \sqrt{gS + g^2\sigma_{\mathrm{r}}^2}\,[DN], \tag{2.47}$$

assuming that the signal S has no fixed offset. A plot of the noise as a function of signal is called PTC [73]. Analyzing the PTC to determine detector parameters, such as gain and read noise, is called is called the PTC method.

2.12 Summary

- Imaging spectrometers are passive optical line scanners resolving many spectral channels, which can be converted to spectral radiance L_λ.
- In a detector, charge carriers are generated by the rate of the photo current I^{ph} and dark current I^{d} and accumulated over the integration time t_{int} in a potential well.
- An electronic readout electronics Analog Digital Converter (ADC) converts the amount of accumulated charge carriers N to a digital signal S. The conversion ratio is called gain g.
- Each pixel has a responsivity that depends on wavelength λ and incident along-track angle α, and across-track angle β.
- The responsivity of a pixel normalized to the integral over these three dimensions is called Pixel Response Function (PRF) f, while the integral is referred to as radiometric response R.
- The relative spectral responsivity of a pixel is called Spectral Response Function (SRF).
- The across-track and along-track angular responsivity is referred to as across-track Angular Response Function (ARF) and along-track Angular Response Function (ARF), respectively.
- The radiometric response R is temperature dependent.
- Imaging spectrometers can suffer from different kinds of image distortions:
  - The change in the center wavelength of SRFs of a channel with spatial column is called smile.
  - The change in across-track center angle with spectral channel is referred to as keystone.
  - The width and shape of response function can also change, depending on the detector location.
- Imaging spectrometers can be sensitive to the polarization of the measured radiance.
- We distinguish between two possible different kind of non-linearity effects. The non-linearity that depends on the measured signal level ζ_{S} and the non-linearity that depends on the set integration time ζ_{t}.
- Signal dependent noise $\sigma(S)$ can be modeled by the read noise σ_{r} and gain g.
- We denote a single detector element as a pixel; all pixels in one detector row that collect the same wavelength are called a spectral channel, and all pixels in one column on which light from the same across-track angle falls are called a spatial column. One data acquisition of all pixels is called a frame. The consecutive uninterrupted measurement of many frames is denoted as data take. The signal of averaged frames is denoted by $S[\bar{x}yz]$. In the same manner, averaged spatial columns are denoted by $S[x\bar{y}z]$, and averaged spectral channels by $S[xy\bar{z}]$.

3

Calibration of Detector Related Parameters

Contents

3.1 Introduction 28
3.2 Dark and Offset Signal 28
3.3 Signal-Dependent Noise 29
3.4 Temperature Sensitivity 32
3.5 Signal-Dependent Non-linearity 34
3.6 Integration Time Non-linearity 44
3.7 Smear Effect 46
3.8 Validation of Non-linearity Correction 51
3.9 Order of Corrections 52
3.10 Summary 53

3.1 Introduction

Many characteristics of imaging spectrometers are directly related to the properties of the instrument detector. Of these properties, we discuss in this chapter the dark and offset signal, the noise, the temperature sensitivity of radiometric response, the non-linearity of the signal and the integration time, and the smearing, an effect which is typical for CCD detectors. The easiest way of performing the calibration of the detector would be at subsystem level, i.e., at the naked chip. However, the HySpex instrument was purchased as a integrated system. Removing the detector for calibration is not an option, as previous calibration data of the integrated system will then become invalid. With the exception of offset and dark signal, the manufacturer has not characterized any of the effects discussed in this chapter, which is why characterizing the detector has to be performed with the optical system in front of the detector.

3.2 Dark and Offset Signal

When no photons enter the instrument a background signal, which is the sum of dark and offset signal, is measured, see Sec. 2.3. The first one is caused by the dark current while the second one is the result of an electronic offset. In addition to these parameters, we also derive the read noise in this section.

3.2.1 Dark and Offset Signal Measurements

To characterize the dark and offset signal, we acquire 1000 frames with closed instrument shutter and integration times ranging from 5 ms to 340 ms with a step width of 5 ms. This is the typical integration time range in which the instrument is used in the laboratory and in the field.

We average the background signal of each pixel ($S[\bar{x}yz]$) and calculate the appropriate standard deviation.

3.2.2 Dark and Offset Signal Results

The results show that the background signal does not significantly change (<0.1 DN) for integration times of up to 340 ms. The changes are actually so small that no trend is visible. This means that there is no relevant dark current if the instrument is used in this integration time range and the background signal is entirely caused by an constant electronic offset, see Fig. 3.1. Hence, we expect that the background signal is not temperature dependent, which we validate in Sec. 3.4.

The offset signal differs between the “left” (spatial column 0 - 799) and the “right” detector half (spatial column 800 - 1599). This is explained by the separate readout electronics of the two halves, which obviously add different offsets [66].

The read noise σ_r, which is the standard deviation of the offset signal, is approximately on the order of 3.2 DN, see Fig. 3.2. Here, too, a different behavior of the two halves can be seen. But with a difference of 0.1 DN, this is also negligible.

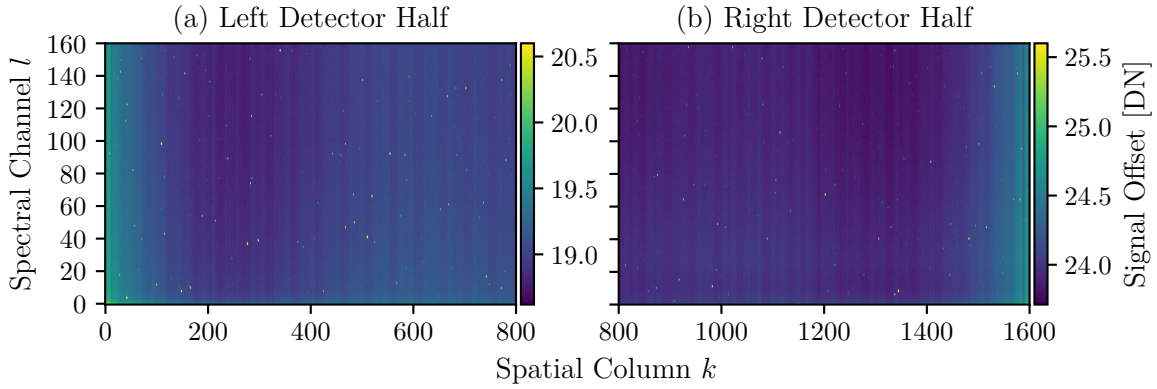

Figure 3.1: Offset signal of all pixels for the left (a) and right (b) detector halves. It can be seen that the offset signal level on the right side is with approximately 24 DN 5 DN higher than on the left detector half with 19 DN. The offset signal increases towards the left and right detector edges.

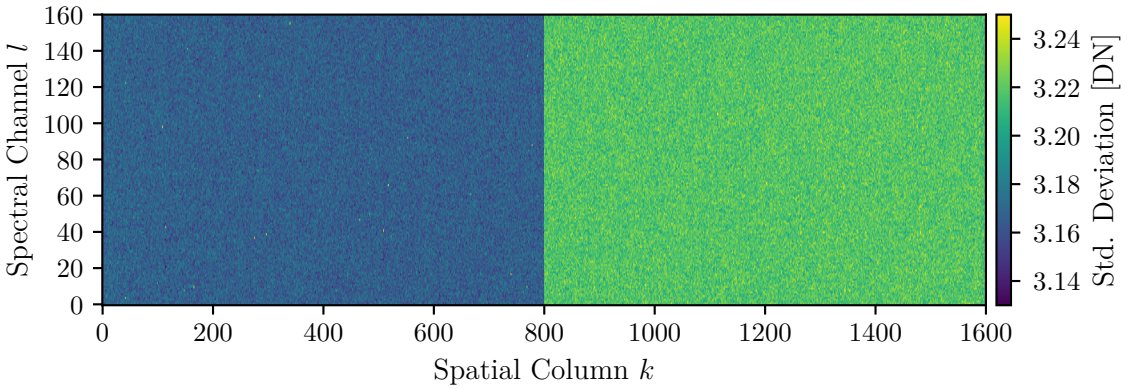

Figure 3.2: Read noise, which is the standard deviation of the offset signal. A minor difference between the left and the right detector halves is visible.

3.2.3 Dark and Offset Signal Correction

The correction of the dark and offset signal is straightforward by changing Eq. (2.9) to

$$S_i^{\mathrm{ph}} = S_i - S_i^{\mathrm{d}} - S^{\mathrm{o}}, \tag{3.1}$$

where $S_i^{\mathrm{d}} = 0$ in our case.

3.3 Signal-Dependent Noise

The signal dependent noise of DLR's HySpex VNIR-1600 was published in [12] to be described as

$$\sigma_{\mathrm{tot}}(S) = 0.35\sqrt{S + 51.4} + 0.56\,[DN]. \tag{3.2}$$

However, the published equation is not based on a physical model. Therefore we use the PTC method [26, 27] and the data measured for the signal non-linearity calibration to obtain addition information about the instrument, such as gain and read noise.

3.3.1 Photon Transfer Curve Method

To measure the PTC, we place the instrument in front of an integrating sphere whose light level can be controlled by iris shutters. We tune the light level over the entire dynamic range of the instrument and record 1000 frames at each of 541 different signal levels. More details regarding how the measurements were actually conducted can be found in Sec. 3.5.2. From each data take we subtract the offset signal, see Sec. 3.2, and calculate the average signal ($S[\bar{x}yz]$) and standard deviation.

To determine the signal-dependent noise $\sigma_{\mathrm{tot}}(S)$, we use the PTC method [26] by plotting the averaged signal against the standard deviation. Considering Eq. (2.47), the gain g and the read noise σ_{r} are the only parameters required to describe this relationship. Since we have already determined the read noise σ_{r}, see. 3.2, we optimize only the gain parameter for each pixel and fit Eq. (2.47) on the PTCs by

$$\hat{g} = \arg\min_{\mathrm{g}} \left\| \sqrt{gS + \sigma_{\mathrm{r}}^2[DN]} - \sigma_{\mathrm{tot}}(S) \right\|_2^2, \tag{3.3}$$

where $\hat{g}$ is the estimation of the gain value and $\|\cdot\|_2$ is the Euclidean norm. Optimizing only the gain value and deriving the read noise independently gives a more stable solution since the solution of read noise would only depend on a few measured signal levels close to zero.

3.3.2 Results

An example of a PTC fit is shown in Fig. 3.3. The noise drops to 0 after 4000 DN, which is caused by the fact that the random signal is limited to the maximum of the dynamic range. The closer the signal gets to saturation, the smaller the noise becomes. Random signals which would be above the maximum of 4095 DN are cropped at the saturation limit, limiting the spread of the standard distribution.

The gain is different between the two detector halves and changes with the channel, see Fig. 3.4. The determined gains of a channel of a detector half have a standard distribution of 6×10^{-4} DN. This is also the limit of the fit accuracy. Hence, we cannot identify other systematic patterns in the gain distribution.

The read noise also deviates between the left (3.174 ± 0.006) DN and right (3.231 ± 0.005) DN detector half. No other pattern is visible besides this difference. Calculating the read noise in units of [e^-] as

$$\sigma_{\mathrm{r}}[\mathrm{e}^-] = \frac{\sigma_{\mathrm{r}}[\mathrm{DN}]}{g}, \tag{3.4}$$

leads to values of 24 e^- to 25 e^-.

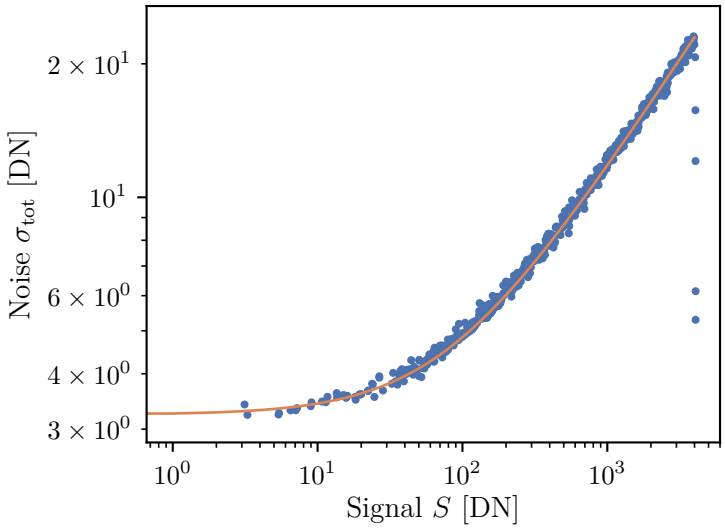

Figure 3.3: PTC of pixel in column 1200 channel 110. (blue) Standard deviation as function of wavelength. For signals over 4000 DN, the noise starts dropping to 0, since more and more of the random signals are saturated. (orange) Fit of Eq. (2.47) on values below 4000 DN.

We refer in other parts of this thesis to the noise of the instrument. In this case, we use the average instrument noise with an average read noise of 3.2 DN and an average gain of 0.13 DN/e^-.

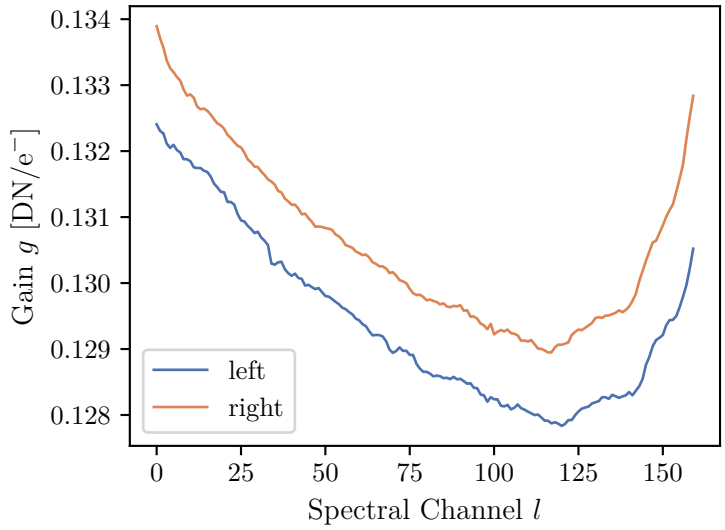

Figure 3.4: Average gain over each channel of the left and right detector half. The standard deviation over the averaged gain values is below 6×10^{-4} DN.

3.4 Temperature Sensitivity

The HySpex detector is not thermally stabilized. Consequently, it's radiometric response is sensitivity to the temperature of the detector, see Sec. 2.3. Many airborne sensors have a thermally stabilized detector and therefore do not have this issue [14]. Fortunately the detector temperature of the HySpex instrument is measured and stored with each data take, which enables characterization and correction of the temperature dependence of the radiometric response. To determine the detector's calibration curve, the temperature needs to be changed. To measure the temperature sensitivity, we use a approach similar to Hemmer and Westphal [30] and place the instrument on top of a thermally stabilized integrating sphere and measure its radiance unit once the instrument reaches thermal equilibrium, see Sec. 3.4.

3.4.1 HySpex VNIR-1600 Operational Environment

The HySpex instrument is usually operated in non-pressurized aircraft and thus in a thermally unstable environment. A temperature sensor reading close to the instrument detector is logged with each data take with a resolution of 1 K, which allows us to analyze the in-flight conditions. During the years of 2013 and 2020 for 748 flight tracks, i.e. contiguous acquisition, the measured detector temperatures range from 9 °C to 42 °C with an average temperature of 28 °C. A majority of 186 measurements fall within a temperature range of 20 °C to 40 °C. The average recording time for one of these data takes was 3 min, with a maximum of 7.5 min. Using the temperatures logged between consecutive flight tracks, we are able to determine the mean temperature change, which is 0.05 K/min with an maximum change of 0.30 K/min. These figures indicate that in most cases, the temperature changes are below the resolution of the temperature sensor, which therefore limits the accuracy of temperature effect corrections.

3.4.2 Detector Temperature Measurements

The temperature dependence is measured by having the instrument placed in front of an integrating sphere that is illuminated by lamps installed in its upper hemisphere. The lamps are thermally stabilized, while the sensor itself is turned off. By switching on the instrument, datasets with 200 bright and 200 dark frames are continuously recorded along with the detector temperature. This is done until the instrument reaches thermal equilibrium. For each dataset, we calculate the average of bright and dark data over all frames and all pixels for each channel ($S[\bar{x}\bar{y}z]$) and subtract the dark from the bright data.

3.4.3 Detector Temperature Sensitivity Results

The temperature recorded by the instruments temperature sensor that is close to the detector ranges from 24 °C to 33 °C. As we discussed in Sec. 3.2, there is no relevant dark current. This is still true for temperatures of up to 33 °C. The instrument response and the temperature shows a linear relationship within the measurement range. We therefore fit an offset and a

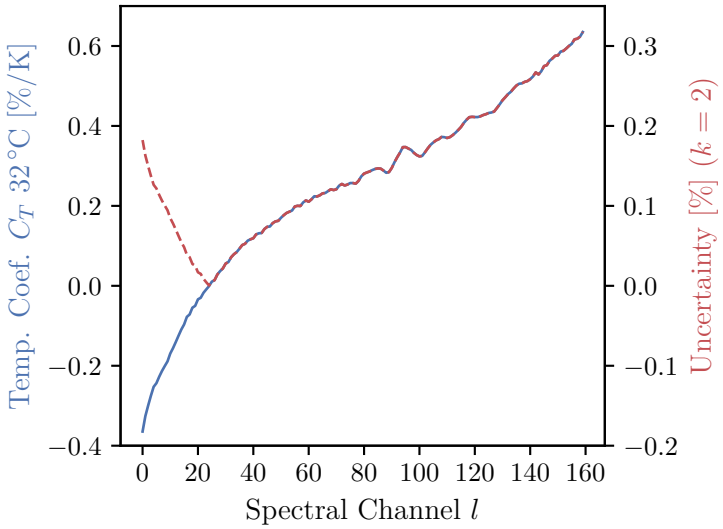

Figure 3.5: (blue) Change of detector sensitivity with temperature. The sensitivity ranges from -0.4 to 0.6 %/K. (red) The uncertainty of the temperature correction is the absolute value of the half coefficient, since the temperature only resolved at a 1 K resolution.

gradient to the data. Using this fit, we calculate signal levels at the reference temperature T_{ref} and temperature T to determine the temperature coefficient C_T of channel l:

$$C_{T,l} = \left(\frac{S_l(T)}{S_l(T_{\text{ref}})} - 1 \right) / \left(T - T_{\text{ref}} \right). \tag{3.5}$$

The reference temperature T_{ref} can be freely chose. However, we set it to the same temperature as present during the radiometric calibration, see chapter 5.

The temperature coefficient for a reference temperature of $T_{\text{ref}} = 32\,°\text{C}$ is depicted in Fig. 3.5. Between channels 20 and 30, the temperature sensitivity is close to zero. For higher channel numbers, the sensitivity increases up to 0.6 %/K, while for lower channel numbers, it decreases to almost −0.4 %/K. The curve can be used to correct the temperature dependency. Since the temperature is only resolved at a 1 K resolution, the uncertainty is not normally but rectangular distributed. The uncertainty with a coverage factor of $k = 2$ after correction is half of the absolute value temperature coefficient. Please note that a coverage factor of $k = \sqrt{3} = 1.73$ already covers 100 % of a rectangularly distribution. We use a coverage factor of $k = 2$ for consistency for the rest of this work.

3.4.4 Temperature Sensitivity Correction

To correct for temperature effects, we define a reference temperature T_{ref} and correct the signal S_{kl} of spatial column k and spectral channel l as

$$S_{kl}(T_{\text{ref}}) = \frac{S_{kl}(T)}{1 + C_{T,l}\,(T - T_{\text{ref}})}. \tag{3.6}$$

3.5 Signal-Dependent Non-linearity

The signal-dependent non-linearity of DLR's HySpex VNIR-1600 instrument was investigated and habe been published [18]. It is reported that the non-linearity has different characteristics for the "left" (spatial column 0 - 799) and the "right" detector half (spatial column 800 - 1599). This is mainly caused by the individual readout electronics of both detector halves. The calibration approach used is based on a common method, where the instrument signal is compared to the signal of a calibrated reference sensor while the measured light level is tuned [31–33]. For the HySpex calibration, a calibrated radiometer that monitored the relative light intensity in an integrating sphere was used as a reference. The amount of light coupled into the sphere was changed with the help of two polarization filters. In order to avoid errors induced by different wavelength-dependent extinction ratios of the polarization filters, a bandpass filter was used to allow only a narrow band of light to enter the sphere. Therefore, the non-linearity was measured for only a few channels. Since the HySpex and the radiometer were measuring different locations of the sphere, any change in uniformity involving the integrating spheres output would result in an error in the non-linearity measurement. Additionally, the linearity of the reference radiometer limited the measurement accuracy. It is specified to be 0.2 % over most of the dynamic range. Our goal is to derive the non-linearity of each pixel with an uncertainty introduced by the measurement and evaluation method of smaller than 0.1 % of the signal level. Non-linearity errors with such low uncertainty would be negligible.

To achieve this goal, we use the light-addition method, also called double aperture or superposition method [28, 35, 36]. We have built a setup for this purpose and conducted calibration measurements with our HySpex VNIR-1600 instrument. In addition, we have developed a method for retrieving non-linearity values using the light-addition method with signal level distances much smaller than the usual exponential spacing. To the best of our knowledge, this is a novel approach.

3.5.1 Light-Addition Method

The light-addition method is based on the fact that in a linear system, the sum of the individual signals $S(L_\mathrm{a})$ and $S(L_\mathrm{b})$ caused by the excitations L_a and L_b is equal to the signal of the sum of the excitations $S(L_\mathrm{a} + L_\mathrm{b})$ [28, 35, 36]. This behavior is described as

$$\frac{S(L_\mathrm{a} + L_\mathrm{b})}{S(L_\mathrm{a}) + S(L_\mathrm{b})} = 1 + \varepsilon, \tag{3.7}$$

where value ε represents the deviation from linearity. For any linear system, ε is therefore zero. To determine the linearity between two signal levels, excitations L_a and L_b must be of equal intensity:

$$S(L_\mathrm{a}) \approx S(L_\mathrm{b}). \tag{3.8}$$

Hence, this approach describes the relation between the signal levels $[S(L_\mathrm{a}) + S(L_\mathrm{b})]/2$ and $S(L_\mathrm{a} + L_\mathrm{b})$. The deviation of linearity between more than two signal levels can be expressed by creating a chain of ε values, see Fig. 3.6. The signal levels depicted are always—except

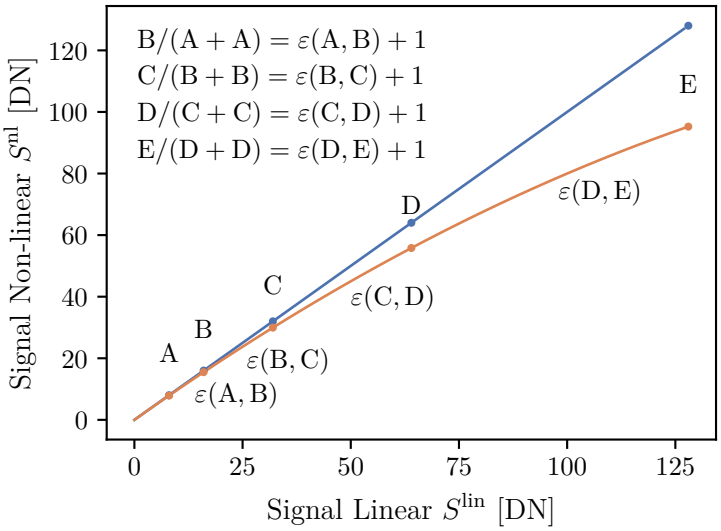

Figure 3.6: Example of a perfect linear (blue) and a non-linear response (orange). The deviation from linearity ε is determined between dedicated signal levels. While, for instance, $\varepsilon(\mathrm{C},\mathrm{D})$ describes the relation between levels C and D, a statement about the relation between the levels B and D can be derived from the combination of $\varepsilon(\mathrm{B},\mathrm{C})$ and $\varepsilon(\mathrm{C},\mathrm{D})$.

for the end levels A and E—once in the numerator in Eq. (3.7) $S(L_\mathrm{a}+L_\mathrm{b})$ when connected to the previous level and once in the denominator $S(L_\mathrm{a})$ $(=S(L_\mathrm{b}))$ when connected to the next level. This means that the radiances L_a and L_b are doubled for each consecutive measurement. Hence, the ε values are determined between intensities, which successively double. Combining several ε values makes it possible to describe the relationship of more than two levels. For instance, $\varepsilon(\mathrm{C},\mathrm{D})$ describes the relation between levels C and D in Fig. 3.6. The relation between the levels B and D is then derived by combining $\varepsilon(\mathrm{B},\mathrm{C})$ and $\varepsilon(\mathrm{C},\mathrm{D})$.

The goal is now to derive from all ε values the non-linearity factors ζ_i^S, which can be directly applied to the signal levels S_i^nl to correct them for their non-linearity as

$$S_i^\mathrm{lin} = \frac{S_i^\mathrm{nl}}{\zeta_i^\mathrm{S}}, \qquad i = 0,\ldots,n-1, \tag{3.9}$$

where n is the number of signal levels, see Fig. 3.7. By combining all ε values, we can derive the non-linearity factor ζ_i^S of all signal levels S_i^nl:

$$\zeta_i^\mathrm{S} = \zeta_{i-1}^\mathrm{S}\varepsilon_i, \qquad \zeta_0^\mathrm{S} = 1, \qquad i = 1,\ldots,n-1. \tag{3.10}$$

Arbitrary sampled data In the previous section, we discussed the derivation of the non-linearity factor ζ^S from exponentially spaced signal levels. In reality, this kind of data is very difficult to obtain compared to data measured at arbitrary signal levels. We can use data with arbitrary signal levels L_a and L_b by linearly interpolating between the signal levels $S(L_\mathrm{a}+L_\mathrm{b})$ and $\left[S(L_\mathrm{a})+S(L_\mathrm{b})\right]/2$. For this purpose, we define the linear interpolation

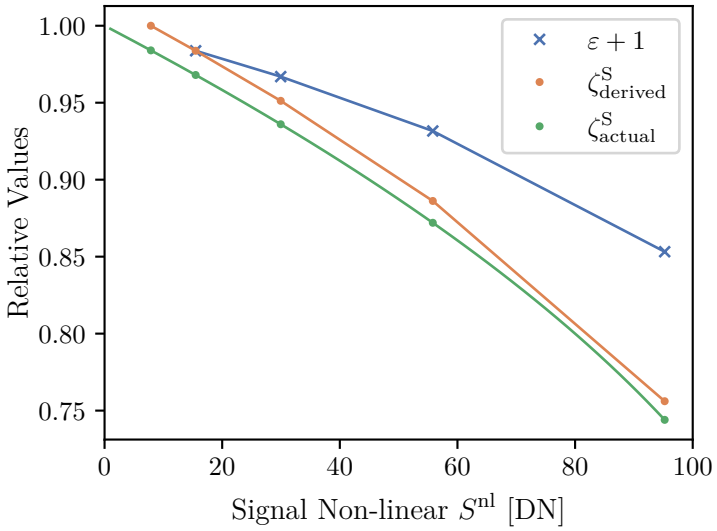

Figure 3.7: Deviation from non-linearity ε (blue) and from these derived the non-linearity factors ζ^{S} (orange). The actual non-linearity function ζ_{actual} (green) is shown for comparison.

function f_ε:

$$f_\varepsilon\left(\frac{S(L_\mathrm{a}) + S(L_\mathrm{b})}{2}\right) = S(L_\mathrm{a} + L_\mathrm{b}). \tag{3.11}$$

Please note that Eq. (3.8) still applies. With help of f_ε, we can then generate a contiguous set of exponentially spaced signal levels:

$$S^{\mathrm{nl}}_{i+1} = f_\varepsilon(S^{\mathrm{nl}}_i), \qquad S^{\mathrm{nl}}_i \in \left[\frac{S(L_{\mathrm{a,min}}) + S(L_{\mathrm{b,min}})}{2}, \frac{S(L_{\mathrm{a,max}}) + S(L_{\mathrm{b,max}})}{2}\right]. \tag{3.12}$$

The linearity deviations ε_i can now be calculated using Eq. (3.7) as

$$\varepsilon_{i+1} = \frac{S^{\mathrm{nl}}_{i+1}}{2S^{\mathrm{nl}}_i} - 1, \qquad i = 0, \ldots, n-1. \tag{3.13}$$

Finally, we use Eq. (3.10) to calculate the non-linearity factors ζ^{S}_i.

Filling the Gaps The large gaps between the signal levels, caused by the exponential distance, do not allow the evaluation of complex shapes of non-linearity curves. In fact, the upper half of the signal range is covered by only one value, while the lower half is covered by all others. Note, we have two sampling points in the upper half of the signal range in Fig. 3.7 due to the high non-linearity. The smaller the signal values compared to the total range, the more sampling points exist on an absolute scale. Also, the position of the sampling points can be choose with Eq. (3.12). This means that we can create many data sets with sampling points that describe the non-linearity on an exponential scale. These data sets j with signal levels S^{nl}_{ij} are generated by changing the start values S^{nl}_{0j} of Eq. (3.12) as

$$S^{\mathrm{nl}}_{i=0,j} = S^{\mathrm{nl}}_{i=0,j=0} v_j, \qquad v_j \in [1, 2), \qquad v_0 = 1, \tag{3.14}$$

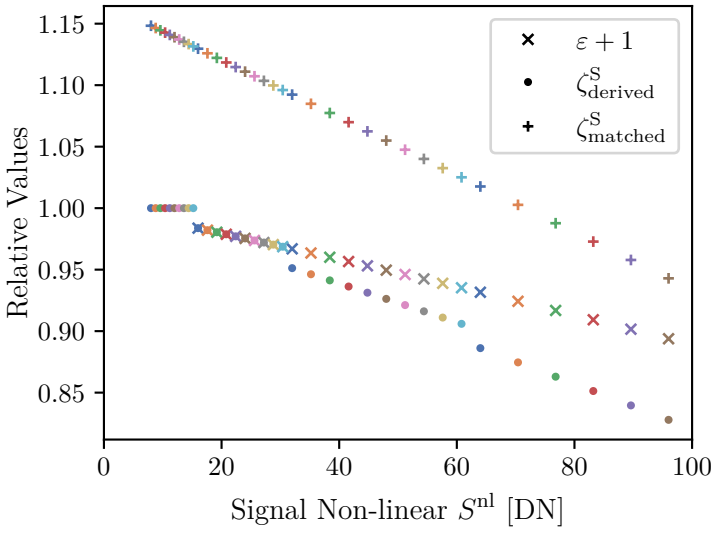

Figure 3.8: Additional data sets are added to fill the gaps shown in Fig. 3.7. Same colors correspond to the same data set. The initially from the ε values derived non-linearity factors ζ^{S} are not matched to each other. By matching these data sets $\zeta^{\mathrm{S,matched}}$ is derived.

where S^{nl}_{00} is the initial start value of data set $j = 0$. As an example, ten additional data sets that are generated in this manner are shown in Fig. 3.8. From each data set j, the non-linearity values ζ^{S}_{ij} are derived according to Eqs. 3.13 and 3.10. Therefore, the start value ζ^{S}_{0j} is always equal to 1.

Although each data set describes the non-linearity of certain exponentially spaced signal levels, the signal levels of different data sets cannot be directly compared. To make the individual data sets comparable, we need to match them. This is done by defining linear interpolation functions $f_{\zeta j}$ of the non-linearity values ζ^{S}_{ij}. The idea is to minimize the differences of the results of the interpolation functions $f_{\zeta j}$. We do this by calculating the mean over the interval $[S^{\mathrm{nl}}_{0\,\mathrm{max}}, S^{\mathrm{nl}}_{n-1\,\mathrm{min}}]$ for each function $f_{\zeta j}$ and normalize each data set with the corresponding result, yielding

$$\zeta^{\mathrm{S,matched}}_{ij} = \frac{\zeta^{\mathrm{S}}_{ij}}{\frac{1}{m}\sum_{q=1}^{m} f_{\zeta j}(s_q)}, \qquad s_q = S^{\mathrm{nl}}_{0\,\mathrm{max}}, \ldots, S^{\mathrm{nl}}_{n-1\,\mathrm{min}}, \qquad q = 1, \ldots, m, \tag{3.15}$$

where m is the number of matching values and the matching values s_q are constantly spaced. The number of matching points m can be freely chosen but the result of the matching approaches a stable solution with increasing number of matching points. We use at least the amount of digital numbers between s_{min} and s_{max} as a value for m.

Finally, by sorting all signal levels S^{nl}_{ij} and the corresponding non-linearity values $\zeta^{\mathrm{S,matched}}_{ij}$ by the signal levels S^{nl}_{ij}, we can collapse both to signal levels S^{nl}_{i} and to non-linearity values ζ^{S}_{i}. Using linear interpolation all signal values in the interval $[S^{\mathrm{nl}}_{\mathrm{min}}, S^{\mathrm{nl}}_{\mathrm{max}}]$ can be corrected for non-linearity.

3.5.2 Signal Non-linearity Measurements

Measurement Setup Figure 3.9 shows the Broadband Attenuable LIght Source (BALIS) that we have built for non-linearity measurements. The setup design is based on the light-addition method. The light of two identical lamp configurations a and b is coupled into an integrating sphere. Each configuration consists of a collimating lens, a beam shutter, an adjustable iris shutter, and a focusing lens. The iris shutters are used to adjust the light intensity of each configuration. The beam shutters allow the light of each lamp to be completely blocked and enable single and combined radiance measurements according to Eq. (3.7). The separate beam shutters are necessary, since the irises cannot be closed completely. Additionally, repeatability errors of the iris shutter positions are avoided.

By shaping the parallel beams with focusing lenses, the entrance ports of the integrating sphere can be smaller, resulting in a higher light intensity. We place the instrument under investigation in front of a third port. It is ensured that the sphere surface covered by the FoV of the instrument is illuminated only by light that is diffusely scattered at least once. Otherwise, some pixels might receive very different amounts of light, which must be avoided.

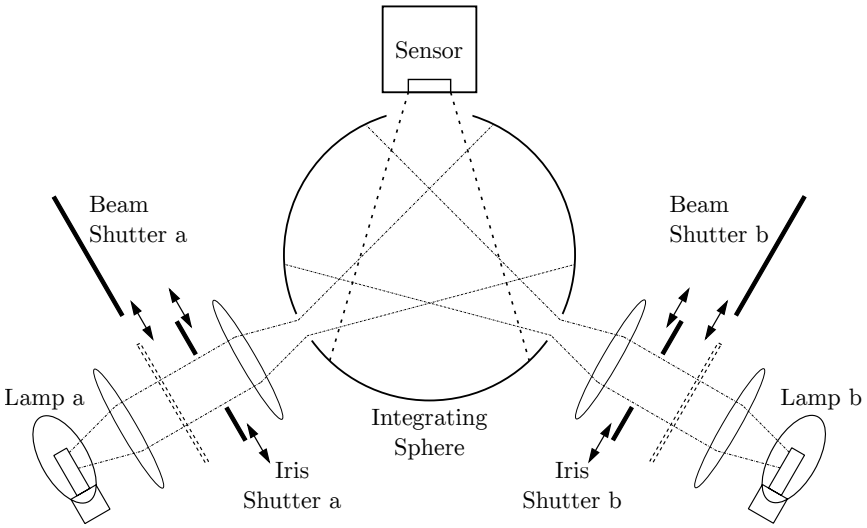

Figure 3.9: Broadband Attenuable LIght Source (BALIS) for non-linearity measurements. The light of two identical lamp configurations is coupled into an integrating sphere. Each lamp configuration consists of a collimating lens, a beam shutter, an adjustable iris shutter, and a focusing lens. The sensor under investigation is placed in front of a third port. We make sure that the area in the FoV is illuminated with light that is diffusely scattered at least once from other parts of the sphere.

Lamp intensities calibration Before the non-linearity measurement can be started, the measurement setup itself must be calibrated. The used light addition method requires that signal cause by both lamp configurations is similar to a certain degree. Of course perfect similarity is not achievable. We try to achieve a deviation of less than 3 %. Bigger differences may cause significant errors in the derived non-linearity. However, we made no particular investigations of the deviation at which the error becomes significant. The maximum allowed difference depends of course on the shape of the non-linearity curve and the desired accuracy of the calibration. The goal of a deviation of less than 3 % of both lamp configurations is based on experience and can be achieved with reasonable effort.

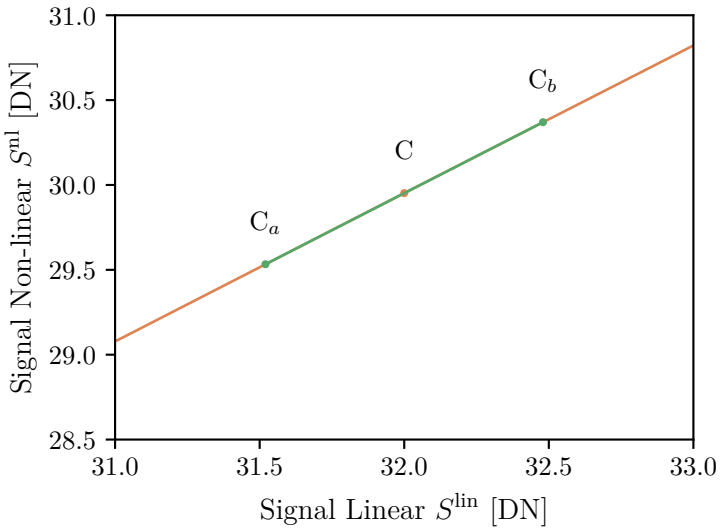

Figure 3.10: Closeup of signal level C of Fig. 3.6, which is the mean of signal levels C_a and C_b. Hence, the sum of C_a and C_b is the signal level D. As it can be seen, although both values diff by 1.5 % from C, no significant error between actual and calculated signal level is introduced.

Please note, that the deviation between both lamp configurations does not directly translate in errors of the non-linearity curve. To illustrate this a close up of signal level C of Fig. 3.6 is depicted in Fig. 3.10. The close-up shows an example of the calculation of the signal level C, which is the average of the two signal levels C_a and C_b. It follows that the sum of C_a and C_b is equal to signal level D. Although both signal levels differ by 1.5 % from C, no significant error is visible, since the instrument can be assumed to be linear at this small scale.

Adjusting the lamp intensities is a two-step process. First, we adjust the spectra of both lamps relative to each other so that they are as similar as possible. The goal of this step is to match the shape of the spectra, not the absolute intensity. This is done by changing the lamp current and measuring the spectrum with the sensor to be calibrated. We tested several different lamps, and found that both lamps should be of the same type. Although the output intensities of different lamps of the same type can differ considerably, the spectra could always be adjusted within the target deviation.

After the lamp spectra are relatively matched, the intensity levels of both lamp configurations are calibrated. Again, we use the sensor which is to be calibrated. Sequentially, we tune the iris shutter of one lamp configuration while the other lamp is blocked (beam shutter closed). In our particular case, the iris shutter is driven by a stepping motor that allows 3500 discrete positions to be set from minimum to maximum diameter. We measure the intensity in this range every 100 steps. This data is then used to convert a relative power setting to stepper motor positions, resulting in similar light levels from both lamp configurations.

Beam shutter calibration A possible relevant source of systematic errors is the influence of the beam shutters. Since we measure the superposition of the light coming from lamp a and b, the position of beam shutter a must not have a significant influence on light level in the sphere caused by lamp b and vice versa. A systematic error would lead to an over-

or underestimation of the linearity deviation ε. Since we chain these values together using Eq. (3.10), systematic errors would add up accordingly.

An influence of the beam shutter setting is possible, since light from lamp b is also coupled into the optical configuration of lamp a. Light from lamp b can then be reflected back by the optical configuration of lamp a. If the amount of back-reflected light differs between the closed and open position of beam shutter a, a systematic error is introduced. Of course, this is also true for light coming from lamp a. To minimize this potential error, the beam shutters are positioned between the lamps and the irises, reducing the effect for smaller iris apertures.

To measure this effect for beam shutter a, we switch lamp a off, lamp b on, and open iris b completely. We linearly tune the iris diameter from maximum to minimum with 21 measurement points. At each measurement point, we record 400 frames with the HySpex instrument with beam shutter a open respectively closed. These measurements are repeated for beam shutter b. We average the signal of all frames and pixels ($S[\bar{x}\bar{y}\bar{z}]$) to get one value per data take and beam shutter setting.

The influence of the beam shutters on the measurement is depicted in Fig. 3.11. It can be seen that a maximum systematic error of 0.03 % is introduced, which rapidly drops to irrelevant values of less than 0.015 % at relative intensities below 0.95. Below this intensity, the visible error is in the range of the lamp and instrument stability. We expect the error to increases with larger iris diameters, since the effective area blocked by the beam shutters is larger. However, since the errors at higher relative intensities have different signs, they compensate each other. We therefore consider the total error to be negligible.

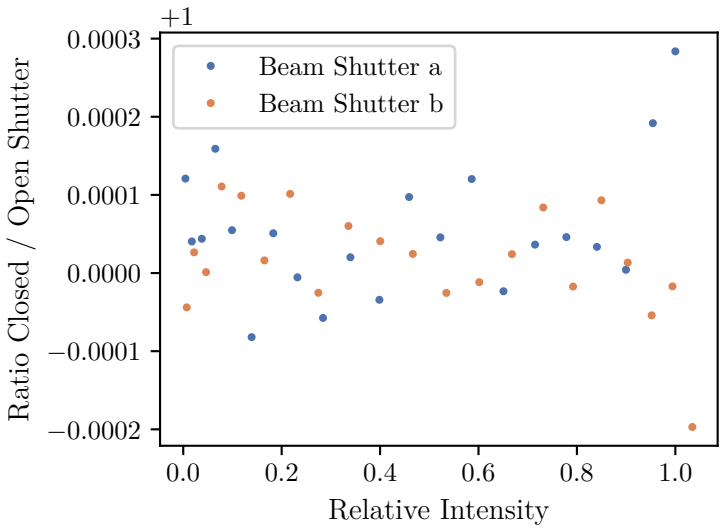

Figure 3.11: Error caused by signal level change due beam shutter position of the other lamp configuration. The relative intensity is related to the iris setting. No significant error is introduced for relative intensities below 0.95.

Measurement procedure We set the integration time to 10 ms, so that the center channels would be in saturation when both irises and the shutters are fully open. Both iris

Table 3.1: Relative output intensities of both lamp configurations. The values are adjusted by tuning the iris shutter.

Range	Start [%]	Stop [%]	Step [%]
1	0.8	19.8	0.5
2	20	39	1
3	40	100	2

Table 3.2: Measurement sequence for each linearity deviation ε. The background is acquired with the first measurement step. Steps 2 and 3 are used to measure the radiance emitted by lamps a and b, respectively. In the last step the sum of both lamp radiances is measured.

Step	Shutter a	Shutter b	Parameter Measured
1	Closed	Closed	$S(0)$
2	Open	Closed	$S(L_\mathrm{a})$
3	Closed	Open	$S(L_\mathrm{b})$
4	Open	Open	$S(L_\mathrm{a} + L_\mathrm{b})$

shutters allow adjustment of the light intensities in the range of 0.8 % to 100 %, where 100 % corresponds to the intensity when a iris shutter is completely open. We set the relative intensities given in Table 3.1 for both lamp configurations and execute for each intensity the measurement steps specified in Table 3.2 by recording 1000 frames at each step. To cover the low signal range of the instrument, we lower the current of both lamps and calibrate lamp intensities as described above. We choose both lamp currents so that each channel has a higher signal than the lowest signal of the previously recorded data sets. Then we repeat the measurement sequence from Table 3.2.

To process the data, we average the frames of each measurement ($S[\bar{x}yz]$). For background correction, for each sequence we subtract the background signal data of the first step from the data of the three other steps. Subtracting the background signal before non-linearity evaluation is possible, since it only consists of a constant offset, see Sec. 3.2. From the averaged frames of the second and third measurement step we determine the medium signal by

$$\overline{AB} = \frac{S(L_\mathrm{a}) + S(L_\mathrm{b})}{2}, \tag{3.16}$$

while the result of the forth measurement step we denote now as

$$\widehat{AB} = S(L_\mathrm{a} + L_\mathrm{b}). \tag{3.17}$$

To reduce the noise in the ε values we filter the data with a Gaussian function h, which is defined as

$$h(x, x_\mathrm{c}, \Delta x) = a \exp\left(-\frac{(x - x_\mathrm{c})^2}{2c^2}\right), \qquad c = \frac{\Delta x}{2\sqrt{2\ln 2}}, \qquad a = \frac{1}{\sqrt{2}\,|c|\,\sqrt{\pi}}, \tag{3.18}$$

where x_c is the function center and Δx is the FWHM. Since the data points are not equally

spaced, the weights w_{si} at the fixed signal levels s are given by

$$w_{si} = h(\widehat{AB}_i, s, f_{\mathrm{FWHM}}(s)), \qquad s = 1, \ldots, 4095, \tag{3.19}$$

where s is equally spaced over the detectors dynamic range. The FWHM of the Gaussian function h is returned by the function f_{FWHM} which is defined as

$$f_{\mathrm{FWHM}}(s) = 0.01s + 3. \tag{3.20}$$

Using the weights we calculate the filtered version $\overline{\overline{AB}}_s$ of $\overline{AB}_i$ by

$$\overline{\overline{AB}}_s = \frac{\frac{1}{n}\sum_{i=0}^{n-1} w_{si}\overline{AB}_i}{\sum_{i=0}^{n-1} w_{si}}, \tag{3.21}$$

and the filtered version $\overline{\widehat{AB}}_s$ of $\widehat{AB}_i$ by

$$\overline{\widehat{AB}}_s = \frac{\frac{1}{n}\sum_{i=0}^{n-1} w_{si}\widehat{AB}_i}{\sum_{i=0}^{n-1} w_{si}}. \tag{3.22}$$

The filtered values are then used to derive the beta values according to Eqs. (3.10) to (3.15).

Measurement stability The stability of the two lamps in combination with the stability of the sensor over the period of four measurement steps can have a significant impact on the measurement uncertainty. To determine this uncertainty, we open one shutter and acquire 20000 frames with a frame period of 10 ms, resulting in a total measurement time of 200 s. This measurement is repeated with the other lamp. All pixels for an individual frame are then averaged ($S[x\bar{y}\bar{z}]$). The averaged signal is within a range of $\pm 0.05\,\%$ over the measurement period of 200 s, while staying within $\pm 0.03\,\%$ for 100 s. These values are in the range of the noise of 1000 averaged frames, see Sec. 3.3. We therefore consider the influence on the measurement result is insignificant.

3.5.3 Signal Non-linearity Results

The non-linearity deviation values ε indicate that each channel of each detector half has an individual non-linearity. While ε values of pixels of a channel of one detector half are equal with respect to their noise level, they can differ significantly from the values of other channels. Therefore, we combined ε values of each channel of each detector half and filtered the data again accordingly to Eqs. (3.19) to (3.22). As an example, the unfiltered and filtered ε values of channel 80 are depicted in Fig. 3.12.

The derived non-linearity factors ζ^{S} of selected channels are depicted in Fig. 3.13. It can clearly be seen that the non-linearity changes with the channel number and that the non-linearity curves start to deviate from each other with higher signal levels. The “right” half of the detector has a significantly higher non-linearity with more than 15 % compared to the “left” half with non-linearities lower than 3 % over the full dynamic range.

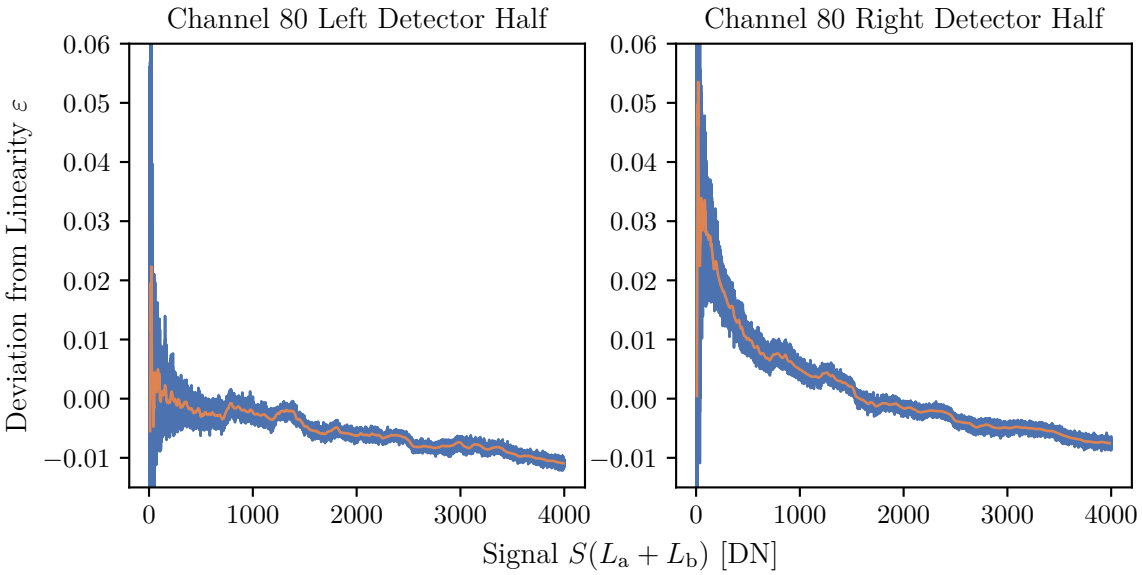

Figure 3.12: Deviation from linearity values ε of channel 80 of the left and right detector half. The in general larger values of the right side indicate a higher non-linearity.

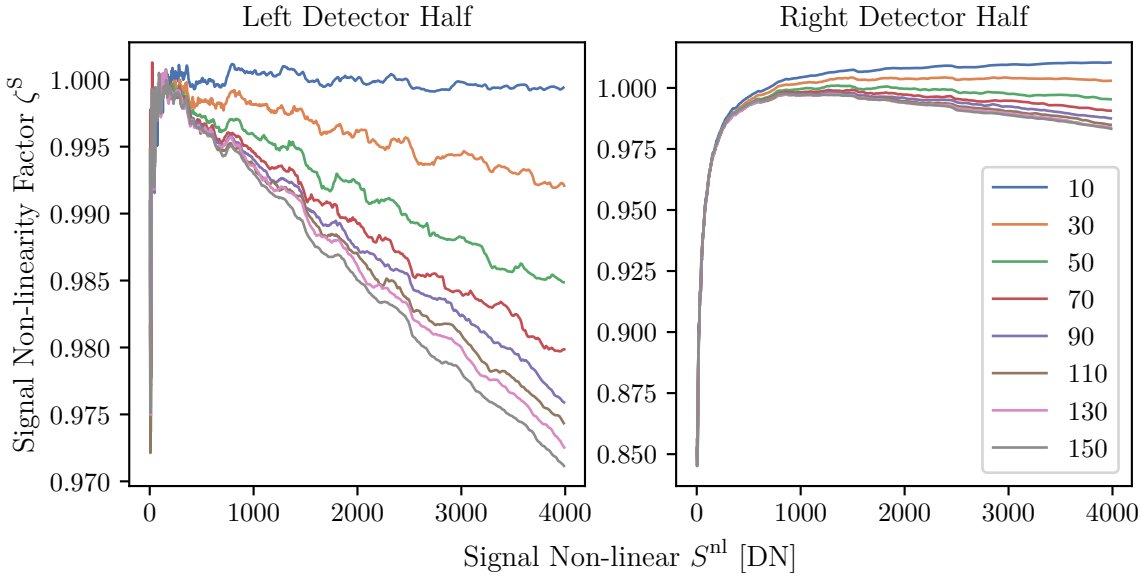

Figure 3.13: Deviations from linearity for both detector halves of selected channels and the averaged values. The legend indicates the channel number. A clear dependence of the non-linearity on the channel number is observable. Please note that both plots are differently scaled, since the non-linearity is on the right detector side much higher.

3.5.4 Signal Non-linearity Correction

We use then Eq. (3.9) to correct non-linear signal levels. Any signal values in the covered range can be corrected using linear interpolation of the derived non-linearity factors ζ^{S}. We expect that the uncertainty of the correction is negligible. This is validated by the results in Sec. 3.8.

3.6 Integration Time Non-linearity

For airborne operations, integration times between 5000 μs and 22 000 ms are typically used with the HySpex VNIR-1600 instrument. The non-linearity of the integration time is independently investigated for this imaging spectrometer for the first time. To measure the linearity between the set and the actual integration time, we use a stable light source while changing the integration time, see Sec. 3.6. Additionally, we use this method to verify the correction of the signal non-linearity.

As we have discussed in Sec. 2.10, for a linear system, it is expected that the ratio between the integration time and the measured signal of a stable light source be constant. In Sec. 3.5, we have found that the signal response of the HySpex instrument is non-linear. In this section, we will now check whether there is a difference between the set and the actual integration time.

3.6.1 Integration Time Non-linearity Measurements

The measurement setup for linearity measurements of the integration time is similar to the setup described in Sec. 3.5.2, but instead of both lamps, only one is switched on. The light source is kept stable while we perform measurements with different integration times. To cover the integration time range of the instrument, which is typically used during operation and calibration, we set the integration time to the values given in Table 3.3. For each set integration time, we record 1000 frames with open and closed beam shutter. To ensure that the light source is stable, we perform reference measurements with a fixed integration time between integration time changes. Since the integration time scan 3 was performed immediately after scan 2 with the same light source, we will consider both as one scan in the following.

Table 3.3: Integration time settings for measuring integration time-dependent non-linearity. The light sources is kept stable during each scan and between scan 2 and 3. Between each measurement step, a data take with an integration time of $t_{\mathrm{int,ref}}$ is performed.

Scan	$t_{\mathrm{int,min}}$ $[\mu s]$	$t_{\mathrm{int,max}}$ $[\mu s]$	Δt_{int} $[\mu s]$	$t_{\mathrm{int,ref}}$ $[\mu s]$
1	100	9900	100	9000
2	5000	95000	5000	30000
3	100000	340000	10000	30000

3.6.2 Integration Time Non-linearity Results

At first, we calculate the average over all frames ($S[\bar{x}yz]$) and correct this data for background signal and for signal non-linearity, see Sec. 3.2 and 3.5. After calculating the average of all pixels ($S[\bar{x}y\bar{z}]$), we determine the ratio between average signal level and set the integration time.

The results indicate that there is a constant integration time offset. Consulting the manual for the Adimec-1600mD camera body [66] reveals that the actual integration time is 25 μs longer than the set one, see Fig 3.14a. Since we can define integration times in the HySpex software as low as to 10 μs, we assume that this offset is not taken into account by the manufacturer.

However, the observed offset is bigger than the 25 μs stated in the manual. A closer look on the data shows that this is caused by a smear effect, which we discuss in detail in Sec. 3.7. To continue the investigation, we remove the remaining offset from the data. This reveals that there are further differences between the set and actual integration time of up to 0.5 % in the range of 3500 to 8900 μs, see Fig 3.14b.

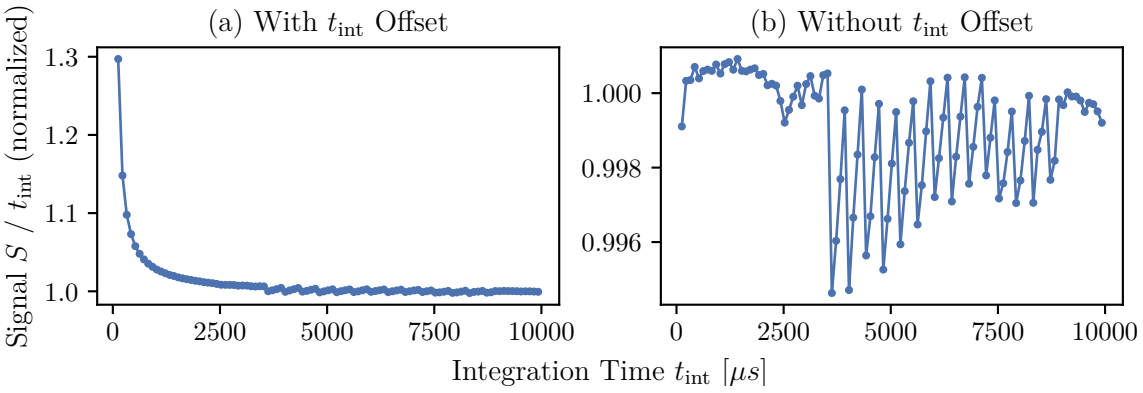

Figure 3.14: Normalized ratios for integration time and signal. (a) A constant integration time offset and smear causes a non-linear relation ship between integration time and signal. The smaller the integration time, the bigger the error. (b) With removed integration time offset and smear effect, systematic differences between set and actual integration times are visible in the range of 3500 to 8900 μs.

3.6.3 Integration Time Non-linearity Correction

To correct for the constant offset of 25 μs we add this value to the integration time given by meta data of the recorded instrument data. In the same manner, we correct the integration time error between 3500 and 8900 μs. Further processing steps will then use the corrected integration time. We assume that the remaining error is below 0.1 % and therefore negligible.

3.7 Smear Effect

We found another effect during the investigations of the integration time non-linearity, which appears like a signal-dependent offset of the integration time. More detailed investigations show, however, that the offset is independent of the signal level, and only depends on the shape of the spectrum. The phenomenon is similar to the smear effect that occurs during electronic readout [74]. It needs to be distinguished between different kind of smear effects dependent on the CCD detector type. The HySpex VNIR-1600 has interline transfer CCD. We could not find any reported measurements of smearing of such a detector installed in an imaging spectrometer. Since the readout time is fixed, the error is more pronounced at lower integration times where the readout time becomes comparably significant. Hence, the effects is at best characterized at low integration times. This requires of course a high radiance source to gain sufficient signal. We therefore use a high-power monochromatic light source to characterize the effect, see Sec. 3.7. In addition, we propose a method for separate the stray light from the smear signal.

3.7.1 Theory

The HySpex VNIR-1600 has an interline transfer CCDs, where each second column is a masked vertical shift register [66]. Since this reduces the fill factor, micro lenses are mounted on the uncovered pixels. To read out the stored charges, electrons are transfered from the uncovered pixels to the masked vertical shift register. From the vertical shift register, the electrons are then transfered to the horizontal shift register. They are then shifted to the electronic amplifier and then converted to digital values. In contrast to the integration time, the time for reading a pixel's charge is constant. During readout, the so-called smear effect can occur that causes electrons to be wrongly added to the charges of a pixel. The number of added electrons can usually directly be liked to the photo current of the other pixels in the same vertical shift register. The smear effect can have various causes [74, 75]:

- Remaining transmittance of the shift register mask
- Scattering of photons on the edge of the micro lenses into the masked pixels
- Scattering of photons within the uncovered pixels into the masked pixels
- Diffusion of electrons into the masked pixels

In the following, we assume that the smear effect adds up linearly, its relative distribution is independent of signal level, and occurs only along one axis of the detector. To keep the equations short, we assume that the signal S is dark and offset signal corrected.

The signal S_i of a pixel i consists of the photo signal S_i^{ph} and the smear signal S_i^{smear}:

$$S_l = S_l^{\mathrm{ph}} + S_l^{\mathrm{smear}} \tag{3.23}$$

As we already know, the photo signal is proportional to the integration time, while the smear

signal depends on the photo current of all other pixels by

$$S_l = g t_{\mathrm{int}} I_l^{\mathrm{ph}} + g t_{\mathrm{r}} \sum_{l'} V_{ll'}^{\mathrm{smear}} I_{l'}^{\mathrm{ph}}, \tag{3.24}$$

where l' is the index of all pixels in the same vertical shift register as pixel l and $V_{ll'}^{\mathrm{smear}}$ is the smear matrix. In the case of the HySpex VNIR-1600, the vertical shift registers are along the spectral axis and therefore corresponds to the spatial columns. Hence, the channel index l is equivalent to the vertical shift register index. This relationship can be swapped for other instruments. As we can see, the relative smear error becomes smaller with longer integration times. Using Eqs. (3.23) and (3.24), we can express the smear signal S_l^{smear} with the photo signal S_l^{ph} as

$$S_l = S_l^{\mathrm{ph}} + S_l^{\mathrm{smear}} = S_l^{\mathrm{ph}} + g \frac{t_{\mathrm{r}}}{t_{\mathrm{int}}} \sum_{l'} V_{ll'}^{\mathrm{smear}} S_{l'}^{\mathrm{ph}}. \tag{3.25}$$

For further formalism we introduce the vectors

$$\boldsymbol{S}_l := (S_1, \ldots, S_{M_{\mathrm{z}}})^T \tag{3.26}$$

$$\boldsymbol{S}_l^{\mathrm{ph}} := \left(S_1^{\mathrm{ph}}, \ldots, S_{M_{\mathrm{z}}}^{\mathrm{ph}}\right)^T, \tag{3.27}$$

where M_{z} is the number of channels, i.e., the length of the vertical shift register. We can express Eq. (3.25) in matrix form as

$$\boldsymbol{S} = \boldsymbol{S}^{\mathrm{ph}} + \frac{t_{\mathrm{r}}}{t_{\mathrm{int}}} \boldsymbol{V}^{\mathrm{smear}} \boldsymbol{S}^{\mathrm{ph}} \tag{3.28}$$

$$= \left[\boldsymbol{I}_M + \frac{t_{\mathrm{r}}}{t_{\mathrm{int}}} \boldsymbol{V}^{\mathrm{smear}}\right] \boldsymbol{S}^{\mathrm{ph}} \tag{3.29}$$

$$= \boldsymbol{A} \boldsymbol{S}^{\mathrm{ph}}, \tag{3.30}$$

where $\boldsymbol{I}_M$ is the identity matrix with $M \times M$ elements. If we compare Eq. (3.29) with stray light equations [76], we observe that the smear matrix can be interpreted as a stray light matrix that is scaled by the ratio $t_{\mathrm{r}}/t_{\mathrm{int}}$. We can therefore use the same methods to correct for smearing. Following [76] this can be done by inverting $\boldsymbol{A}$, which yields

$$\boldsymbol{A}^{-1} \boldsymbol{S} = \boldsymbol{S}^{\mathrm{ph}}. \tag{3.31}$$

Usually, the smear effect is measured by illuminating one pixel and determining the signal of the other pixels in the same column. However, in an integrated system, stray light is also present, which has a similar effect on the data. The photo signal caused by stray light is proportional to the photo signal of the illuminated pixel. To describe this relationship, we introduce the photo signal matrix $\boldsymbol{V}^{\mathrm{ph}}$. This allow us to model the signal S_l of a not directly illuminated pixel l dependent on an illuminated pixel $l = \nu$ as

$$S_l = g \left(t_{\mathrm{r}} V_{l\nu}^{\mathrm{smear}} + t_{\mathrm{int}} V_{l\nu}^{\mathrm{ph}}\right) I_\nu^{\mathrm{ph}}. \tag{3.32}$$

We can assume that the photo current due to stray light is comparably small and that

therefore the smear signal caused by stray light is negligible. Hence, if we illuminate only one pixel, then this pixel is not affected by smear of the other pixels, leading to

$$S_\nu = g t_{\mathrm{int}} I_\nu^{\mathrm{ph}}. \tag{3.33}$$

Inserting this into Eq. (3.32) yields

$$S_l = \left(\frac{t_{\mathrm{r}}}{t_{\mathrm{int}}} V_{l\nu}^{\mathrm{smear}} + V_{l\nu}^{\mathrm{ph}} \right) S_\nu. \tag{3.34}$$

Since the readout time is fixed, this equation allows us two separate the effect of smear and photo signal, when two or more images are recorded of the same peak illumination with different integration times.

3.7.2 Impact of Smear on Halogen-Lamp Measurements

To check the error the smear effect causes, we use scan 1 of the integration time non-linearity measurements, see Sec. 3.6.1. We calculate the average of all frames ($S[\bar{x}yz]$) for each data take and correct the data for the background signal as well as signal and integration time non-linearity, see Sec. 3.2, 3.5 and 3.6. Assuming that the smear effect only occurs along the spectral z-axis, we calculate the average signal ($S[\bar{x}\bar{y}z]$) along the spatial y-axis. As Eq. (3.24) reveals, if we keep the illumination constant and only change the integration time, we get a linear equation, where the smear signal is the constant offset. The gradient is then the signal normalized for the integration time, see Fig. 3.15a. With this functions, we can determine the signal for any integration time with or without constant smear offset. We use this to calculate the smear error for selected integration times, see Fig. 3.15b. For this particular measurement and for an integration time of 5 ms, the smear error is up to 1.25 % and, as expected, becomes smaller with longer integration times.

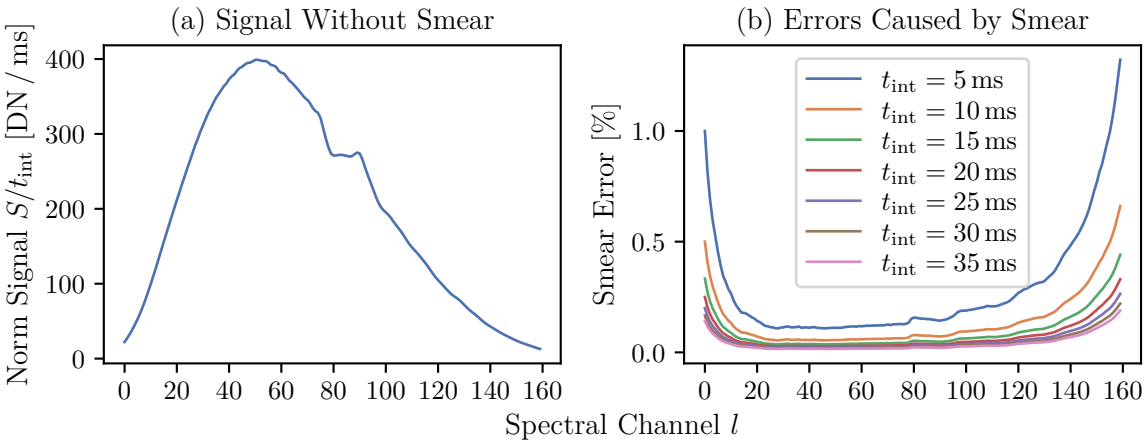

Figure 3.15: (a) Signal of a lamp measurement normalized to the integration time. (b) Errors caused by the smear effect for different integration times. Since the smear effect changes randomly after restarting the HySpex software, the errors cannot be corrected.

3.7.3 Smear Measurements

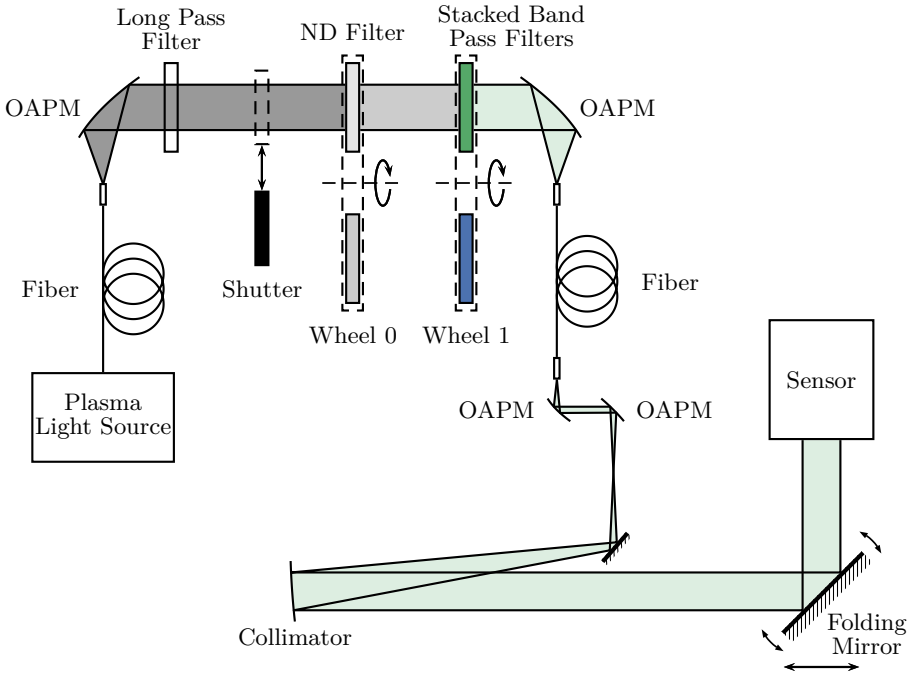

Figure 3.16: Stray Light Test Source (SLTS) and CHB collimator setup: Light from a plasma light source is guided via an optical fiber to a collimating Off-Axis Parabolic Mirror (OAPM). For safety reasons, a long pass filter suppresses light below 350 nm. A set of Neutral Density (ND) filters and a set of bandpass filters are used to control the output power and output wavelength of the SLTS, respectively. Each filter set is arranged in a filter wheel. From here, the beam is coupled into another optical fiber. Two OAPM and a collimator guide the beam over a folding mirror to the sensor. Moving and rotating the folding mirror changes the across-track illumination angle and allows illumination of different spatial columns.

From Eq. (3.34), it follow that the influence of the smear matrix $\boldsymbol{V}^{\text{smear}}$ is bigger with lower integration times. Hence, it is easier to measure the effect at short integration times. The readout time per horizontal line of the HySpex CCD is $t_{\text{r}} = 21.1\,\mu\text{s}$ [66]. To achieve a high Signal to Noise Ratio (SNR) a bright monochromatic light source is required. We therefore use a high-radiance plasma light source whose light we filter with stacked bandpass filters, see Fig. 3.16. This light source was originally designed for stray light measurement, hence its name Stray Light Test Source (SLTS). The filters are stacked to achieve step gradients at the flanks of the transmission bands and high suppression outside of the bandpass. The latter feature is not of great importance for smear measurements but rather for stray light investigations [77, 78]. A set of ND filters is used to control the power output, while a mechanical shutter allows any output to be blocked. To enable automated measurements, both the ND and bandpass filters are arranged in filter wheels. The filtered beam is guided with an optical fiber to the CHB's collimator setup. After the fiber, the beam is shaped so that the aperture of the HySpex instrument is overfilled as well as the along-track FoV. With the chosen configuration, several spatial columns in across-track direction are illuminated simultaneously.

We use 14 different bandpass filter types to measure the smear effect, 13 of which have a

bandwidth of 10 nm and one a bandwidth of 900 nm, see Table 3.4. For the 10 nm filters, 10000 frames at three different integration times are recorded, while the same is done with the 40 nm bandwidth filter at two integration times. Along with each measurement, with the same settings, the background signal is recorded by closing the SLTS shutter.

We calculate the average for all frames ($S[\bar{x}yz]$) for each data take and correct the data for background signal as well as signal and integration time non-linearity, see Sec. 3.2, 3.5 and 3.6. For each measurement series which are conducted with the same filters but different integration times, we take the sum of the peak signal as reference signal S_ν. Finally, by optimizing Eq. (3.34) on the data we determine the parameters $V_{l\nu}^{\text{smear}}$ and $V_{l\nu}^{\text{ph}}$.

Table 3.4: SLTS measurement settings.

λ_c [nm]	$\Delta\lambda$ [nm]	Stacked filter	Integration time [μs]
450	10	4	40, 100, 160
488	10	4	50, 120, 200
532	10	4	70, 170, 270
590	10	4	90, 210, 330
635	10	4	60, 140, 230
660	10	4	70, 170, 270
730	10	4	70, 160, 250
780	10	4	150, 320, 500
810	10	4	40, 100, 170
850	10	4	50, 120, 200
905	10	4	80, 190, 300
950	10	3	70, 170, 270
980	10	3	80, 190, 300
900	40	1	30, 130

3.7.4 Results

Figure 3.17 shows the results of the determined smear and photo signal factors. We set the smear factor to zero in the region of the peak signal. The fit does not work well here, since the smear signal is orders of magnitude lower than the photo signal. Between channel 78 and 80, a jump of the smear factor is visible. Outside of the peak area, the photo or stray light signal is negligible. This is especially visible in Fig. 3.18, which shows measurements for the 900 nm filter. Here, three different data takes are shown, conducted at different times with the same SLTS and instrument settings, each after a HySpex software restart. Three different smear offsets at the left side of the peak are visible. At the time this thesis was written, its seems to be completely random as to which pattern occurs. While the smear pattern is constant as long the acquisition software is running, it may change after a software restart. Therefore, it is currently not possible to generate a reliable correction method for the smear effect. Further research is needed to find an explanation and perhaps a correction method for this phenomenon. However, the proposed methods can still be used to separate smear and photo signal during laboratory measurements. Since the influence of the lubrication effect decreases with longer integration times, this can be taken into account for airborne

measurements.

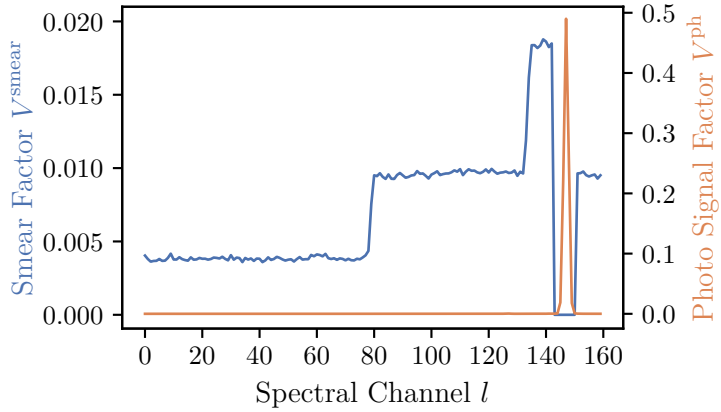

Figure 3.17: The Smear V^{smear} and photo signal factor V^{ph} for channel 147. A jump of the smear factor is visible between channel 78 and 80. Another jump is visible in front of the illuminated area, which has a smear factor of zero. The photo signal factor shows the peak at the illuminated pixels.

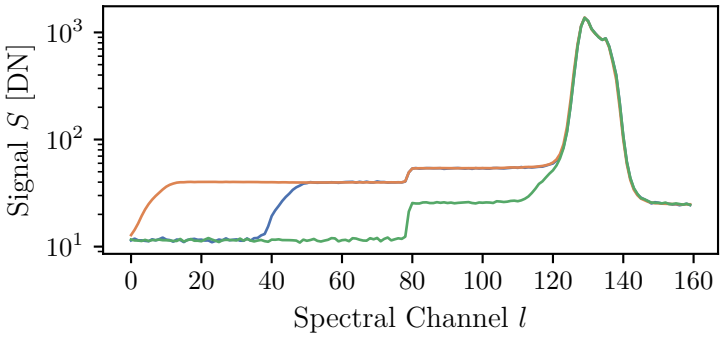

Figure 3.18: Measurements for a bandpass filter with a center wavelength of 900 nm and a bandwidth of 40 nm. Although the measurements are performed with the same instrument settings and illumination level, three different smear pattern occur after restarting the HySpex software.

3.8 Validation of Non-linearity Correction

In Fig. 3.19a, the normalized ratios between integration time and signal before non-linearity and smear offset correction are shown, while in Fig. 3.19b, the results after correction are depicted. After correction, the normalized ratios are within the target uncertainty of

$$e_{\text{nl}}(S) \leq \frac{\sigma_{\text{tot}}(S)}{\sqrt{1000}} + 0.001S, \tag{3.35}$$

where $e_{\text{nl}}(S)$ is the non-linearity error in units of [DN]. The first term of the equation is the noise of 1000 averaged frames. The second term accounts for an acceptable error of 0.1 % due to the stability of the lamp and expected accuracy of the signal-dependent non-linearity model. We expect that systematic errors of ≤0.1 % are negligible.

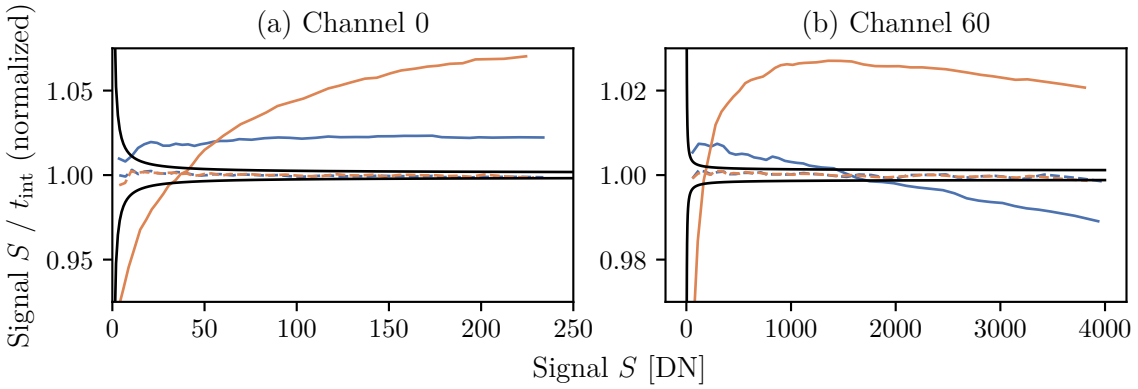

Figure 3.19: Non-linearities for integration times ranging from 5000 to 340 000 μs. The uncorrected (solid) ratios of the left (blue) and right (orange) detector halves show strong non-linearities. The for non-linearity corrected results (dashed) are within the specified target uncertainty (black). (a) Results for channel 0. For better visibility, we shifted the blue curve upwards. (b) Results for channel 60. The signal levels are higher than for channel 0 due to the lamp spectrum and the instrument responsivity. Please note the different axes scales.

3.9 Order of Corrections

The corrections of the detector effects are applied in the following order:

1. Offset signal
2. Signal non-linearity
3. Integration time non-linearity
4. Smear effect
5. Temperature sensitivity

The first two steps need to be performed in the order given, as they depend on the absolute signal level. Since the last three steps do not have such a dependency, their order can be changed. Because we could not find a deterministic behavior of the smear effect, this correction is actually not applied.

3.10 Summary

- The detector has two separate readout electronics that separates the detector into a "left" (spatial column 0 - 799) and the "right" half (spatial column 800 - 1599).
- The detector has negligible dark current (<0.1 DN at 340 ms) and a constant signal offset that differs between both detector halves.
- We analyzed the noise characteristics using the Photon Transfer Curve (PTC) method. The derived gain levels differ between channels and between the two detector halves.
- The average read noise is 3.2 DN and the average gain is 0.13 DN/e^-.
- The detector is not thermally stabilized, which causes a temperature-dependent radiometric responsivity change of up to 0.6 %/K. The detector temperature is monitored by a built-in temperature sensor at a resolution of 1 K, which limits the calibration accuracy.
- We built a setup for the signal non-linearity calibration using the light-addition method. The uncertainties caused by the setup are below 0.1 %.
- An unique feature of the setup is that it uses two separate lamp configurations compared to existing setups, which use one lamp. This allows to generate high radiance levels and to characterize error sources of the setup.
- This is the first time this type of a setup is used to calibrate an integrated imaging spectrometers.
- We have improved the light-addition method to allow smaller signal level distances of the sampling points of the non-linearity curve.
- The detector is non-linear depending on the signal level. This signal-dependent non-linearity differs between spectral channels and both detector halves and is up to 15 % for the right detector half.
- There is a constant offset between the set and the actual integration time of 25 μs. Additionally, there are integration time errors between 3500 μs and 8900 μs of up to 0.5 %.
- We discovered a smear effect which occurs along the spectral channel of the HySpex instrument. The smear effect occurs during the fixed readout time.
- The relative error cause by smear is inversely proportional to the integration time and depends on the shape of the spectrum. For a halogen-lamp and an integration time of 5000 μs the error is up to 1.25 % of the signal level.
- We developed a method for measuring the effect in an integrated system.
- The smear effect randomly alternates among at least three different patterns each the HySpex software is restarted, which is why we cannot correct it for the HySpex VNIR-1600. Further research is needed to find out whether the pattern is predictable.

4

Geometric and Spectral Calibration

Contents

4.1 Introduction 56
4.2 Geometric Calibration Setup 56
4.3 Spectral Calibration Setup 57
4.4 Geometric Calibration Measurements 63
4.5 Spectral Calibration Measurements 63
4.6 Evaluation Methods 65
4.7 Measurement Results 68
4.8 Pixel Response Function Reconstruction 72
4.9 Uncertainties and Errors 73
4.10 Summary 81

4.1 Introduction

In this chapter we discuss the determination of the Spectral Response Function (SRF) and across-track Angular Response Function (ARF) of each detector element of an push-broom imaging spectrometer.

The response functions of DLR's HySpex VNIR-1600 were also modeled in the past with Gaussian functions [11, 12]. However, in this chapter we show that this model does not describe the response functions accurately enough and can cause relevant errors. We therefore use a lookup table based method as it was published by Ewald et. al. [13], where the sampling points are interpolated with a cubic spline.

The ARF and the SRF measurements are based on the same principle. We scan with a point source, either spatially or spectrally narrow, over the responsive range of a pixel. For the ARF measurements, we use a slit in front of a collimator as a spatially narrow target while we perform the SRF measurements with a monochromator. We calibrate the monochromator center wavelength with an echelle grating Wavelength Meter (WM) and a method developed by us for this purpose [79]. We also investigate the other relevant monochromator parameters, such as bandwidth, relative wavelength dependent intensity and stability.

While we measure the ARF of each detector element individually, limitations in the optical output power of the monochromator and time constraints allow us to measure only a subset of an instrument's SRFs. To determine the missing SRFs, we interpolate their entire shape from the cubic spline-based SRFs we measured. From the ARFs and SRFs we then derive the across-track angular and spectral PRFs by assuming that the ARFs and the SRFs are orthogonal. In addition, we investigate the accuracy of the cubic spline-based response function model and the interpolation error of the SRFs. To quantify the error caused by a Gaussian based PRF model, we use this and the cubic spline-based PRFs model to sample two test scenes and compare the results. Due to the bandwidth of the monochromator, the SRFs' width is always overestimated. Again, we use the same two test scenes to evaluate possibles errors cause by the bandwidth of the monochromator.

4.2 Geometric Calibration Setup

To measure an imaging spectrometer's across-track ARFs, we use the setup shown in Fig. 4.1. A slit oriented perpendicular to the instruments across-track FoV is illuminated by a lamp. This slit is in the object plane of a collimator from which a collimated beam is guided to the aperture of the sensor under investigation. The optics of the instrument then creates an image of the slit on the detector. By changing the angular across-track orientation (β-angle) of the beam relative to the imaging spectrometer, we can scan the across-track ARFs with sub-pixel resolution. This is done by rotating (β-angle) the folding mirror and moving (y-axis) it.

The focal length of the collimator used is $f_{\text{collimator}} = 750\,\text{mm}$, while the slit width is

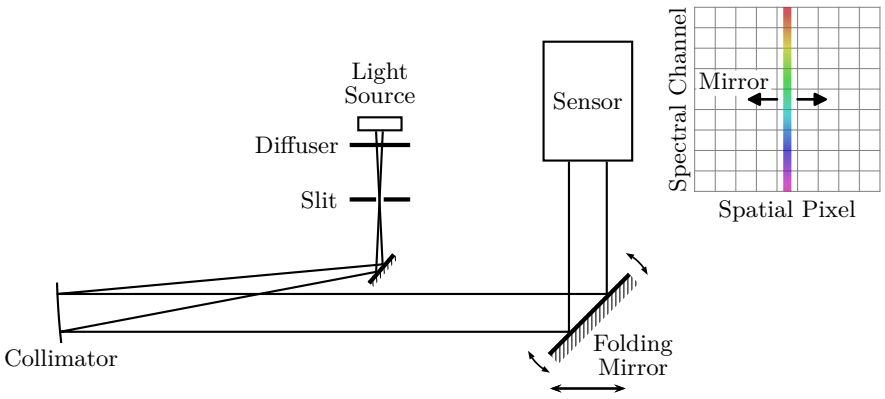

Figure 4.1: Geometric characterization setup. A lamp illuminates a slit from which the optical beam is guided via a collimator and a folding mirror to the aperture of an imaging spectrometer. The result is an image of the slit on the detector array. Moving and rotating the mirror changes the angle of incidence, the slit image on the detector to be displaced.

$w_{\text{slit}} = 20\,\mu\text{m}$. This results in a divergence angle of

$$\frac{w_{\text{slit}}}{f_{\text{collimator}}} = 0.027\,\text{mrad}. \tag{4.1}$$

The accuracy of the folding mirror angle is $\pm 0.006\,\text{mrad}$, which was determined by calibration measurements made by the manufacturer. Since the angular accuracy is based on the encoder pattern in the folding mirror's rotating wheel and since this pattern does not change, we assume that this is stable over time and does not require regular recalibration.

4.3 Spectral Calibration Setup

The setup we use for the spectral calibration of imaging spectrometers is shown in Fig. 4.2. A halogen lamp is placed in front of the entrance port of the monochromator. Between both, an order sorting filter is installed to suppress diffraction orders greater one. Without the filter, more than one wavelengths could be emitted by the monochromator. Four order filters installed in a filter wheel are available, from which one filter is selected depending on the output wavelength. The light coming from the monochromator is then coupled into a multi-mode fiber. A mode scrambler, which creates small radius bends of the fiber, is used to mix all modes in the fiber. This produces a spatially and angularly uniform output beam, independent of the input geometry. The end of the fiber is located in the focal plane of an off-axis parabolic mirror, which creates a collimated beam that is guided via a folding mirror to the aperture of the imaging spectrometer. An image of the fiber core is then generated on the FPA by the optics of the imaging spectrometer. By translating the mirror (y-axis) and rotating it (β-angle), the imaging spectrometer is illuminated under different across-track angles β, leading to the illumination of different locations on the FPA. An illumination of the whole across-track FoV is not possible because the output power of the monochromator is too low to obtain a reasonable SNR. Tuning the monochromator wavelength allows then to measure the SRFs of pixels at the selected spatial position.

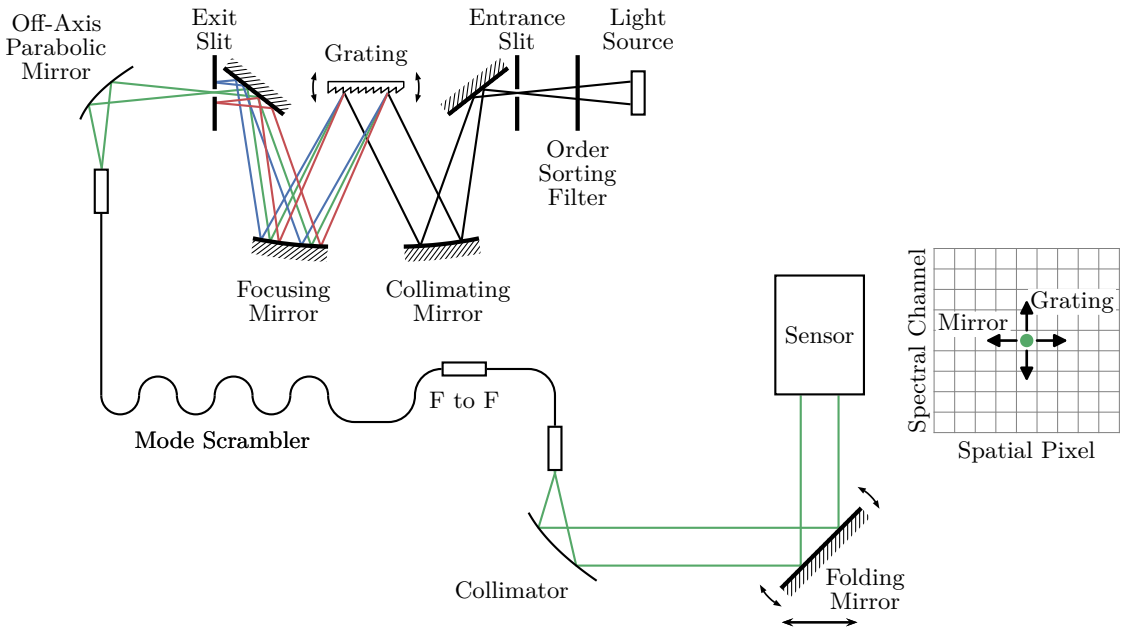

Figure 4.2: Setup for calibrating spectral properties of imaging spectrometers. The emitted light from a monochromator is coupled into a multi-mode fiber. Since the light has a certain bandwidth with changing wavelength over the exit port, a mode scrambler is used to mix the modes in the fiber to create an uniform output spectrum. A fiber-to-fiber (F to F) coupler provides a modular interface to which a second fiber is connected that leads to a collimating mirror. The collimated beam is guided over a folding mirror to the imaging spectrometer.

It is important that the beam coming from the calibration setup overfills the aperture area of the imaging spectrometer as well as the along-track FoV to get proper measurement results. If the aperture and the along-track acceptance angle are only partly filled, the measured SRFs potentially have a different shape than they would have if both dimensions were filled. An underfilling of the aperture area results in a smaller illuminated area on the dispersing element as well as on the collimating and focusing optics, see chapter 2. Similarly, underfilling the along-track acceptance angle means that the instrument slit is not fully illuminated. In this case, the slit of the instrument would have no or only partial functionality. This would lead to smaller divergence angles after the collimating optics and the dispersing element, with the consequence that the image of the beam would also be smaller along the spectral dimension.

The monochromator used (asymmetrical Czerny-Turner design) is a MS257 from Oriel, distributed by Newport. It is equipped with three different gratings, optimized for the wavelength range of 400 to 2500 nm, see Table 4.1. For a 1200 l/mm grating at 553 nm the accuracy is specified with 0.1 nm, <0.15 nm max; the repeatability is 0.015 nm, <0.03 nm max. With 600 l/mm gratings, these values approximately double.

The relevant parameters of the calibration setup are the center wavelength, the relatively emitted intensity with its stability, and the spectral bandwidth. In the following, the calibration of these parameters is discussed in this order. Note that the accuracy of the proposed method for center wavelength calibration is independent of the radiometric stability.

Table 4.1: Specifications of the three installed gratings and the corresponding measurement parameters. $\lambda_{\min}$, $\lambda_{\max}$ and $\delta\lambda$ are the start, the end and the step width of the measurements, respectively.

Grating	Line Density [l/mm]	Blaze Wavelength [nm]	$\lambda_{\min}$ [nm]	$\lambda_{\max}$ [nm]	$\delta\lambda$ [nm]
1	1200	350	370	1100	1
2	1200	750	400	1200	1
3	600	1600	900	2600	2

4.3.1 Monochromator Center Wavelength Calibration

To calibrate the center wavelength of the monochromator we use an echelle grating WM of LambdaScan-usb type distributed by GWU-Lasertechnik Vertriebsges.mbH (GWU). We apply the WM and the monochromator calibration methods published in [79]. The WM itself is calibrated with spectral line lamps. Unlike direct monochromator calibration with spectral line lamps, the position of the sampling points is not limited to the wavelengths of the emission lines of the lamps. Hence, a monochromator can be traceably calibrated at any wavelength setting, given that the wavelength is in the sensitive range of the WM. Additionally, it is possible to calibrate a monochromator at wavelengths which are longer than the maximum wavelength of the WM used.

We calibrated the monochromator for all three gratings over the wavelength range from 370 to 2600 nm according to Table 4.1. The spectrum of a halogen lamp is coupled into the monochromator and the WM is connected to the optical fiber via a fiber-to-fiber coupler.

We generated calibration tables for each grating from these measurements. By linearly interpolating between the sampling points, we corrected systematic monochromator errors of the second measurements. In this manner, we repeated the calibration measurements after four days to validate the correction of systematic errors and to investigate the monochromator's stability.

Figure 4.3 shows the results of the calibration and validation measurements. The uncertainties of the WM measurements are negligible, since for a wavelength of 1000 nm the uncertainty is 0.005 nm [79].

In the residuals of the calibration measurements a sinusoidal pattern can be seen, which is caused by the worm drive turning the grating turret. Since this is not a statistical but rather a systematic error, it must be corrected. It is important to note that the monochromator under investigation is more than 20 years old. Therefore, these results should not be misunderstood as a performance evaluation for this device series.

On the other hand, the residuals of the validation measurements are within a range of ± 0.1 nm. The original sinusoidal pattern vanished, but a short-term periodic fluctuation with small amplitudes remains. Since the remaining pattern does not correlate with the original one, we assume that this is related to the repeatability of the stepper motor of the monochromator. A linear trend is visible in the residuals of grating 1, where the error decreases with increasing wavelengths. It seems that we started the measurements before the

monochromator was completely thermally stabilized. However, all residuals are within the desired uncertainty of ±0.1 nm, even for grating 3, where the target uncertainty is ±0.2 nm.

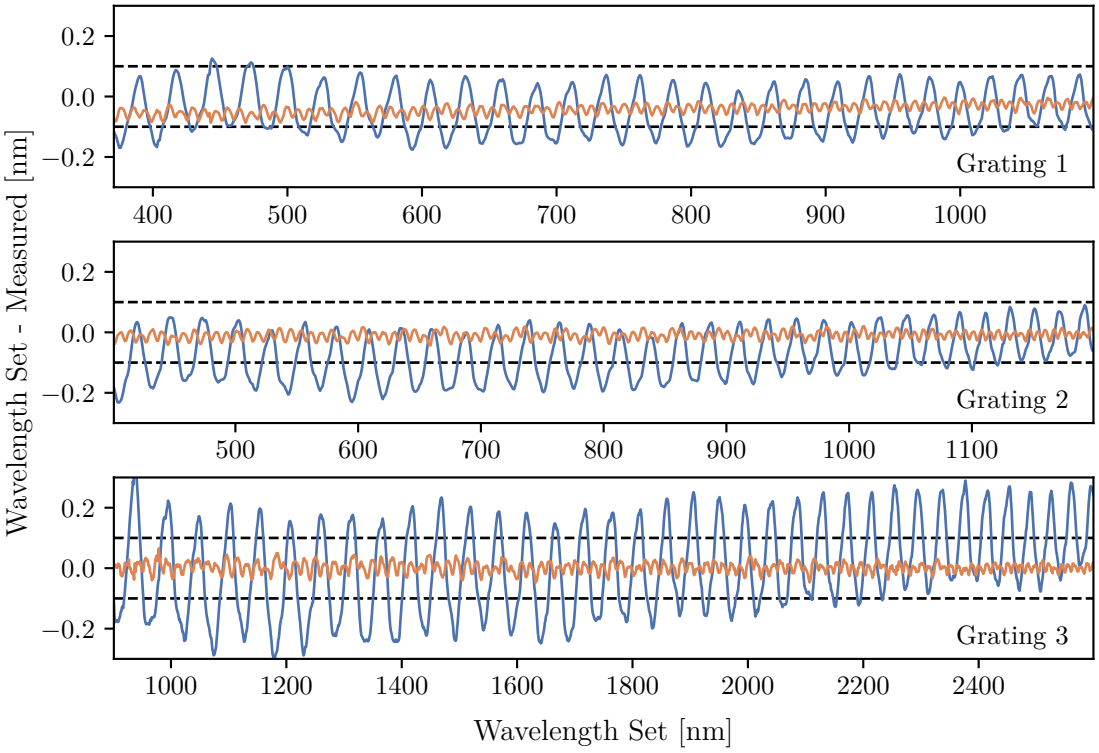

Figure 4.3: Residuals of monochromator calibration (blue) and validation measurements utilizing the former calibration (orange) for all three gratings. A sinusoidal pattern can be seen in the calibration measurements, caused by the worm gear of the grating turret. The pattern vanishes completely in the validation measurements.

4.3.2 Monochromator Bandwidth Calibration

The spectral bandwidth of the light emitted by the monochromator has a direct influence on the outcome of SRF calibration measurements. The width of an SRF can be significantly overestimated if the bandwidth of the calibration light source is too large. Assuming Gaussian shaped response functions and bandwidths, the effective influence can be estimated as

$$\Delta x_{\mathrm{RF,meas}} = \sqrt{\Delta x_{\mathrm{source}}^2 + \Delta x_{\mathrm{RF}}^2}, \tag{4.2}$$

where $\Delta x_{\mathrm{source}}$ is the bandwidth of the calibration source, Δx_{RF} is the FWHM of real instrument response function, and $\Delta x_{\mathrm{RF,meas}}$ is the FWHM of the measured response function. The bandwidth of the monochromator is determined by the focal length, the grating constant, and the slit width. The slit width setting of the monochromator must be carefully chosen, since it is usually a trade-off of the signal throughput and the bandwidth.

For bandwidth measurements, we connect a radiometer to the optical fiber via the fiber-to-fiber coupler and place a spectral line lamp as light source at the entrance of the monochromator, see Fig. 4.2. We set the same slit width for the entrance and exit slit

as it will be used for the imaging spectrometer calibration measurements, in this case to 0.15 mm. This value is based on a trade of between the instruments spectral resolution and its radiometric sensitivity in combination with the output intensity of the calibration setup, see Sec. 4.9.2.

Since the widths of the spectral lines of the spectral line lamp are infinitesimally small in comparison to the bandwidth of the monochromator, the influence on the measurement result is negligible. The bandwidth is measured with 4 mercury lines and 17 neon lines by scanning the monochromator wavelength in 0.1 nm steps over a range of ±1.5 nm at each peak wavelength. To the data generate by this way we fit a Gaussian functions, whose FWHMs are then the measure for the bandwidths $\Delta\lambda_{\text{mono}}$ of the output spectrum, see Fig. 4.4. For grating 1, the bandwidth $\Delta\lambda_{\text{mono}}$ declines from approximately 0.54 nm at an emitted wavelength of 404 nm to 0.48 nm at a wavelength of 600 nm. For grating 2, the bandwidth $\Delta\lambda_{\text{mono}}$ changes from 0.51 nm at a wavelength of 550 nm to 0.43 nm for wavelengths longer than 900 nm.

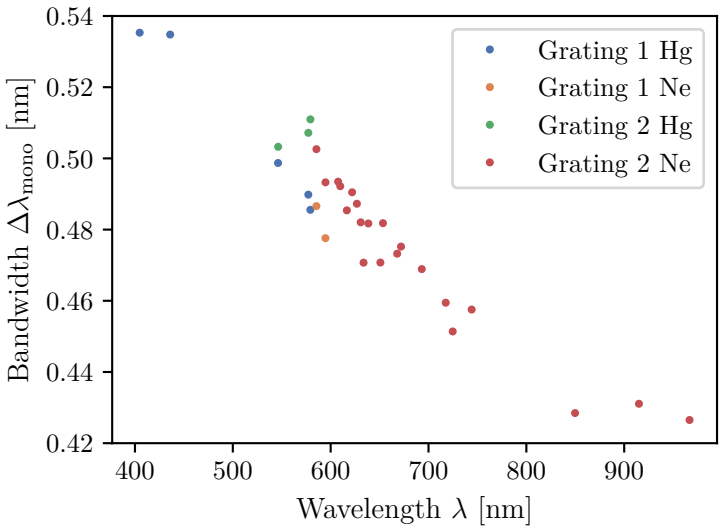

Figure 4.4: Results of bandwidth measurements for a monochromator slit width of 0.15 mm. Only the wavelength ranges of the grating that are used for the instrument characterization are given. For grating 1, the bandwidth declines from approx. 0.54 nm at an emitted wavelength 404 nm to 0.48 nm at 600 nm. For grating 2, the bandwidth changes from 0.51 nm at 550 nm to 0.43 nm for wavelengths longer than 900 nm.

4.3.3 Relative Radiometric Monochromator Calibration

The radiance of the spectral calibration setup at the aperture of the imaging spectrometer, see Fig. 4.2, is wavelength dependent. This is caused by the spectral emission curve of the lamp, the reflectance of the mirrors and the grating as well as the transmittance of the optical fiber. The wavelength dependency influences directly the shape of the measured SRFs and must therefore be corrected during data evaluation. For this reason, the relative spectral output of the measurement setup must be calibrated.

To measure the relative spectral radiance $L_{\text{mono}}^{\text{rel}}$ of the measurement setup, we mount a radiometer at the position where the imaging spectrometer is normally positioned. We set the folding mirror to a reflection angle of 90°, which corresponds to an illumination of the center pixels of an imaging spectrometer. We assume that the change of reflectance with the angle of the folding mirror has a negligible impact on the relative radiometric calibration. The radiometer is calibrated by the PTB. Figure 4.5 shows calibration data of the radiometer with the associated uncertainties. In the spectral sensitive range of the HySpex instrument these uncertainties are below 0.7 % ($k = 2$).

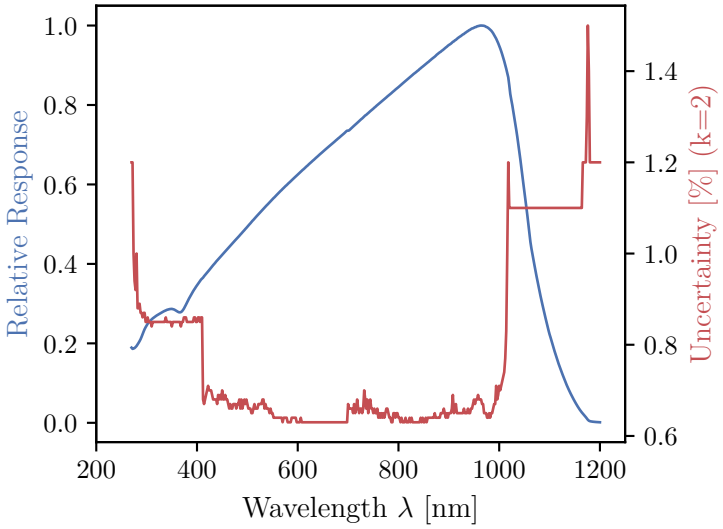

Figure 4.5: Calibrated radiometric response (blue) and uncertainties (red) of the radiometer used for the radiometric calibration of the spectral characterization setup.

We measure the relative intensity in the range of 370 nm to 601 nm with grating 1 and order sorting filter 1 (cut-on wavelength 305 nm). With grating 2 and order sorting filter 2 (cut-on wavelength 550 nm), the measurement range is from 550 nm to 1110 nm. The step width is 1 nm for both ranges.

To measure the stability of the measurement setup, we set the wavelength to 550 nm and monitor the output power with the radiometer. This measurement includes in the end the stability of the light source and of the radiometer.

We correct the data of the relative intensity measurements for the spectral response of the radiometer, see Fig. 4.5. From the stability of the radiometer and light source $u_{\text{stab}}(S)^2$ and the radiometric calibration uncertainty of the radiometer $u_{\text{calib}}(S)^2$ we calculate the measurement uncertainty $u(S)$ by

$$u(S) = \sqrt{u_{\text{calib}}(S)^2 + \sigma_{\text{tot}}(S)^2}. \tag{4.3}$$

The relative intensity measurements take less than 5 min for each grating. Over this period, at a wavelength of 550 nm, the monochromator output power is stable within a limit of ±0.02 %. Figure 4.6 illustrates the results of the relative radiometric calibration measurements. It can

be seen that filter 2 partially blocks up to a wavelength of 600 nm. At 660 nm, a ditch in the emitted spectrum is visible which is caused by the diffraction grating.

The derived uncertainties are in the specified spectral range of the HySpex instrument, which is 410 nm to 1000 nm below 0.8 % ($k = 2$). At shorter wavelengths the uncertainty rises to more than 1.8 %. This is due to the low sensitivity of the radiometer and at the same time low lamp power in this region, resulting in a small SNR. However, this region is outside the spectral range of the HySpex instrument and is therefore irrelevant here.

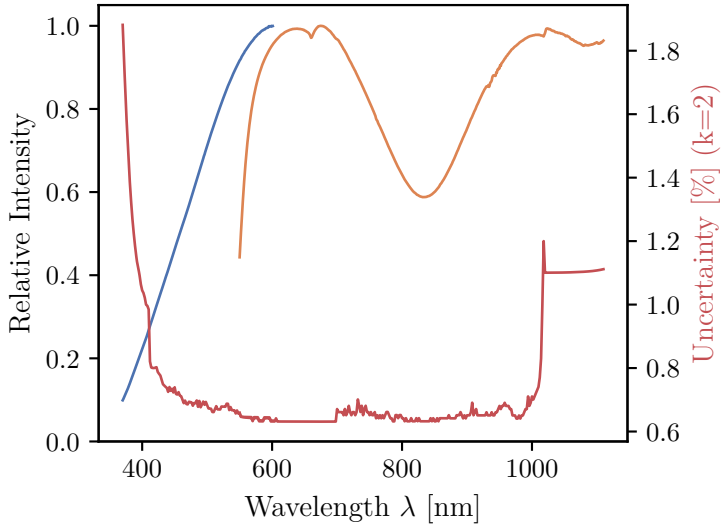

Figure 4.6: Radiometric calibration results of the spectral characterization setup. (blue) Relative spectral intensity for grating 1 with order sorting filter 1. (orange) Relative spectral intensity for grating 2 with order sorting filter 2. (red) Uncertainties for both data sets.

4.4 Geometric Calibration Measurements

We measure the ARFs by changing the incident angle from −0.297 rad to 0.332 rad with increments of 0.06 mrad, resulting in 5538 angular positions. At each position we record 50 frames. The asymmetric angle range is caused by an asymmetric FoV of the instrument.

4.5 Spectral Calibration Measurements

Due to the limited output power of the spectral calibration setup, only a subset of spatial columns can be illuminated simultaneously. Therefore we have to repeat the SRF scanning several times with different incident angles. We chose the number of spatial positions at which we perform the wavelength scans, so that the SRFs can be accurately interpolated later. Regions where the SRFs change quicker with the spatial column are therefore scanned with higher spatial density. This is an iterative process, since only after evaluating measurement data it is possible to determine whether the density of reference points is sufficient for proper interpolations. The approach described in the following is the result of such a process.

Table 4.2: Wavelength settings for the SRF measurements. We chose the number of spatial positions at which we perform the wavelength scans, so that the SRFs can be accurately interpolated later. Regions where the SRFs change quicker with the spatial column are therefore scanned with higher spatial density. For this reason, scan 4 is performed at 117 spatial positions which all other scans are performed at 15 positions.

Scan	λ_{min} [nm]	λ_{max} [nm]	$\delta\lambda$ [nm]	Spatial Positions
1	400	475	0.8	15
2	430	570	0.8	15
3	550	720	0.8	15
4	680	800	0.8	117
5	780	960	0.8	15
6	940	1010	0.8	15

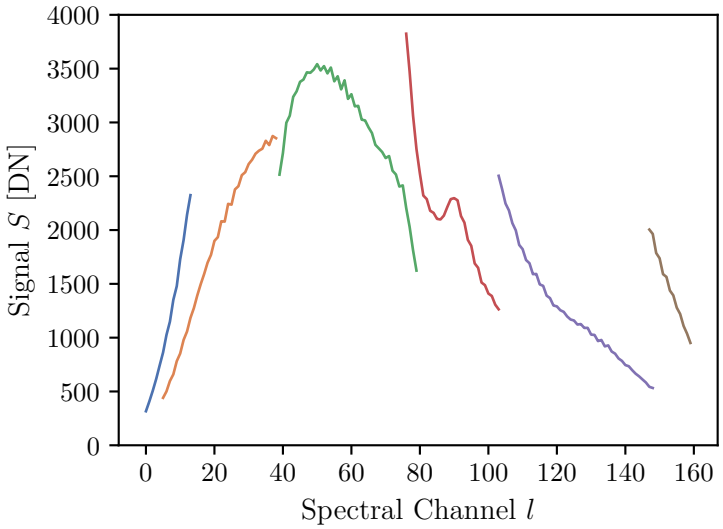

Figure 4.7: Maximum intensities of each channel of geometric line 755 for each wavelength scan. Different scans are necessary to either optimize the SNR or to address the change of the monochromator's order sorting filter between scan 2 (orange) and 3 (green).

We choose the combinations of monochromator grating and order filter together with the integration time so that a sufficiently high SNR is achieved. Whenever integration time of HySpex, the grating or spectral filter of the monochromator are changed, we start a new wavelength scan. We do this to guarantee that each SRF is measured without abrupt changes in the signal level. The ranges are chosen so that they overlap along the spectral axis at least for one complete SRF measurement. A SRF measurement is complete, when the curve has reached the noise level on the shorter and the longer wavelength side of an SRF.

We select the across-track angles so that the whole spatial dimension of the detector is covered with equal spacing. The most outer spatial columns are measured to avoid extrapolation. At positions where SRFs change too fast to be properly interpolated, further spatial positions are added.

We end up with six overlapping wavelength scans that cover the whole spectral range of the instrument at 15 spatial positions for four scans and 117 spatial position for the scan from 680 nm to 800 nm. These settings are given with Table 4.2 and the detector locations of the measured pixels are shown in Fig. 4.8 based on 28028 individual measurements. 50 frames are recorded with each measurement.

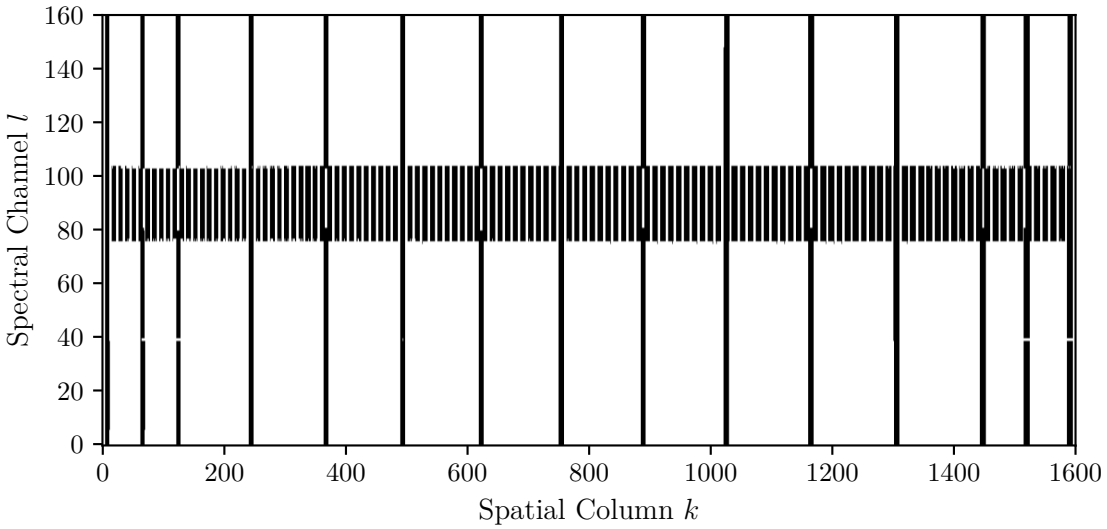

Figure 4.8: Coordinates of pixels from which the SRF is measured. Missing SRFs are later interpolated.

4.6 Evaluation Methods

4.6.1 Data Pre-Processing

The frames for each scan are averaged ($S[\bar{x}yz]$) to achieve a higher SNR. The frames are corrected for background signal and non-linearity, see chapter 3. Since the instrument is thermally stabilized and we perform relative measurements, correcting temperature effects is not necessary. All averaged frames of the ARF scan are stacked to get a contiguous data set.

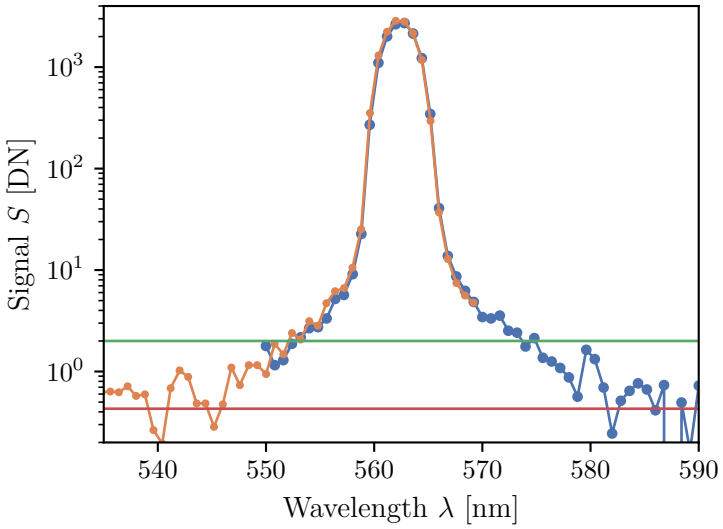

Figure 4.9: SRF measurement of column 755 channel 40. The response curves from scan range 2 (orange) and scan range 3 (blue) the 2 DN line (green) and the noise level (red) are depicted. The range 2 scan is not complete for this pixel as it did not go below the 2 DN line at the right side of the maximum.

The same is done with the data for each SRF scan.

Since during a scan several pixels are illuminated, we extract the SRFs of these pixels. Pixels that reached a minimum photo signal of 200 DN (SNR $\approx$ 230) have potentially received enough light for a complete SRF measurement. We exclude pixels that do not meet this condition from further processing. For these potential measured SRFs, we check whether the three most right and the most left data points are below 2 DN, i.e., 1 % of the minimum peak signal, see Fig. 4.9. We do this to ensure that an SRF is completely measured. This value is chosen since the background signal noise respectively read noise σ_r of 50 averaged data points is

$$\sigma_\mathrm{tot}(0\,\mathrm{DN}) = \frac{\sigma_\mathrm{r}}{\sqrt{n_\mathrm{frames}}} = \frac{3.2\,\mathrm{DN}}{\sqrt{50}} = 0.45\,\mathrm{DN}. \tag{4.4}$$

A threshold of 2 DN is robust enough so that less than 0.01 % pixels are erroneously excluded. This means that the sampling points reached zero at both sides of the peak with some noise included. Again, all pixels for which this condition is not met are excluded from further processing. Depending on the chosen filters and grating, the data from pixels selected for further processing are corrected for the relative output spectrum of the monochromator, see Sec. 4.3.3, written as

$$S^\mathrm{corr} = \frac{S}{L^\mathrm{rel}_\mathrm{mono}(\lambda)}, \tag{4.5}$$

with S as the measured photo signal and $L_\mathrm{mono}(\lambda)^\mathrm{rel}$ as the relative output radiance of the spectral calibration setup for monochromator wavelength λ, see Sec. 4.3.3.

4.6.2 Response Function Model

We found no analytical function that describes the shapes of the ARFs and SRFs properly. Therefore, we decide to model the RFs by interpolating the data points with cubic splines in order to have continuously differentiable curves. Since the integral of RFs is defined to be equal to unity we do the same with the cubic spline based RFs:

$$\mathrm{RF} = \frac{\mathrm{RF}^{\mathrm{raw}}}{\int \mathrm{RF}^{\mathrm{raw}}(x)\,\mathrm{d}x} \tag{4.6}$$

Here $\mathrm{RF}^{\mathrm{raw}}$ is the cubic spline interpolation of the data points and x is the incident angle β respectively wavelength λ.

4.6.3 Interpolation of Spectral Response Functions

As we have discussed before, we cannot measure all SRFs with the spectral calibration setup. This means that the missing SRFs have to be interpolated. We do this by linearly interpolating the center wavelengths λ_{c} and then interpolating the shapes of the reference SRFs.

For each missing SRF $\mathrm{SRF}^{\mathrm{m}}$ in spatial column y^{m} we search for the nearest measured SRFs left $\mathrm{SRF}^{\mathrm{l}}$ and right $\mathrm{SRF}^{\mathrm{r}}$ of $\mathrm{SRF}^{\mathrm{m}}$ that are in the same channel. These reference SRFs are located in the spatial columns y^{l} and y^{r}, respectively. The center wavelength λ_c^{m} of the interpolated SRF $\mathrm{SRF}^{\mathrm{m}}$ is calculated by linear interpolation, yielding

$$\lambda_{\mathrm{c}}^{\mathrm{m}} = \frac{\lambda_{\mathrm{c}}^{\mathrm{r}} - \lambda_{\mathrm{c}}^{\mathrm{l}}}{y^{\mathrm{r}} - y^{\mathrm{l}}}(y^{\mathrm{m}} - y^{\mathrm{l}}) + \lambda_{\mathrm{c}}^{\mathrm{l}}, \tag{4.7}$$

where $\lambda_{\mathrm{c}}^{\mathrm{l}}$ and $\lambda_{\mathrm{c}}^{\mathrm{r}}$ are the center wavelengths of the left and right reference SRFs, respectively.

For the sake of interpolation, we shift the left and the right SRFs so that their center wavelengths are equal to $\lambda_{\mathrm{c}}^{\mathrm{m}}$. Both functions are then weighted with the inverse distance to the interpolation positions, resulting in the interpolated SRF $\mathrm{SRF}^{\mathrm{m}}$ in spatial column y^{m}, yielding

$$\mathrm{SRF}^{\mathrm{m}}(\lambda) = \frac{\mathrm{SRF}^{\mathrm{l}}\left(\lambda - (\lambda_{\mathrm{c}}^{\mathrm{m}} - \lambda_{\mathrm{c}}^{\mathrm{l}})\right) w^{\mathrm{l}} + \mathrm{SRF}^{\mathrm{r}}\left(\lambda - (\lambda_{\mathrm{c}}^{\mathrm{m}} - \lambda_{\mathrm{c}}^{\mathrm{r}})\right) w^{\mathrm{r}}}{w^{\mathrm{l}} + w^{\mathrm{r}}}, \tag{4.8}$$

where w^{l} and w^{r} are the weights, which are given by

$$w^{\mathrm{l}} = \frac{1}{y^{\mathrm{l}} - y^{\mathrm{m}} + 1} \tag{4.9}$$

and

$$w^{\mathrm{r}} = \frac{1}{y^{\mathrm{m}} - y^{\mathrm{r}} + 1}. \tag{4.10}$$

The result is an interpolated SRF whose shape is based on the surrounding SRFs that are in the same spectral channel.

4.7 Measurement Results

4.7.1 Geometric Calibration Results

Figure 4.10 shows the results of the geometric calibration for each pixel. The difference between the center angles $\beta_{c,kl}$ of each pixel of one spatial column and their mean value $\bar{\beta}_{c,l}$ is shown in Fig. 4.10a, which illustrates the keystone effect. At the center pixels, the effect is almost absent, while the displacements of the center angles are up to 0.16 mrad (∼0.33 pixels) at the detector edges.

The across-track resolution is the highest in the center of the detector with values ranging between 0.28 mrad and 0.50 mrad, see Fig. 4.10b. At the left detector side, the resolution decreases to 0.77 mrad.

In Fig. 4.10c the Angular Sampling Interval (ASI) is depicted. As can be seen, the sampling interval is asymmetric and changes from 0.43 to 0.34 mrad along the geometric axis. This also means that the FoV is asymmetric, with a shift of 17.0 mrad of the center pixels from the FoV center.

The angular sampling ratio, which is the angular resolution divided by the ASI, is depicted in Fig. 4.10d. In the center of the detector, the sampling ratio is below 1 and reaches a maximum of 1.7 at the left detector edge.

The ARFs of selected pixels from different detector locations are depicted in Fig. 4.11. Figures 4.11a and 4.11b show the ARFs of spatial columns 755 to 758 of spectral channels 50 and 80, respectively. They overlap at levels below 50 % of their maximum, which indicates that the image sharpness in this area of the detector is not limited by the optical systems but rather by the pixel pitch and size, namely the fill factor.

This also applies to the ARFs in spatial columns 1390 to 1393 of channel 85, see Fig. 4.11c. The ARFs between spatial column 100 and 103 of spectral channel 140 are less sharp, with an overlapping value above 50 % of their maximum, see Fig. 4.11d. This is also indicated by the lower maximum values of these ARFs in comparison to the previously discussed ones, since all ARFs are normalized to their integral, see Eq. (4.6).

4.7.2 Spectral Calibration Results

The smile effect is visualized by referencing the center wavelengths $\lambda_{c,kl}$ of each channel to their mean value $\bar{\lambda}_{c,l}$, see Fig. 4.12a. Clearly visible is that the effect increases to the edges of the spatial axis. Between spectral channel 75 and 90 (∼690 nm and ∼745 nm), the spectral shift changes within a few pixels. According to the instrument manufacturer NEO, this is caused by a spectral filter—suppressing higher orders of the diffraction grating—which covers the upper detector half.

The spectral resolution is for most regions between 3.2 and 5 nm while it decreases to 10 nm on the right detector side, see Fig. 4.12b. As the center wavelength, the resolution is negatively affected over the whole area because they are distorted by the filter edge. As for the center wavelengths, the resolution changes within a few pixels in this detector area.

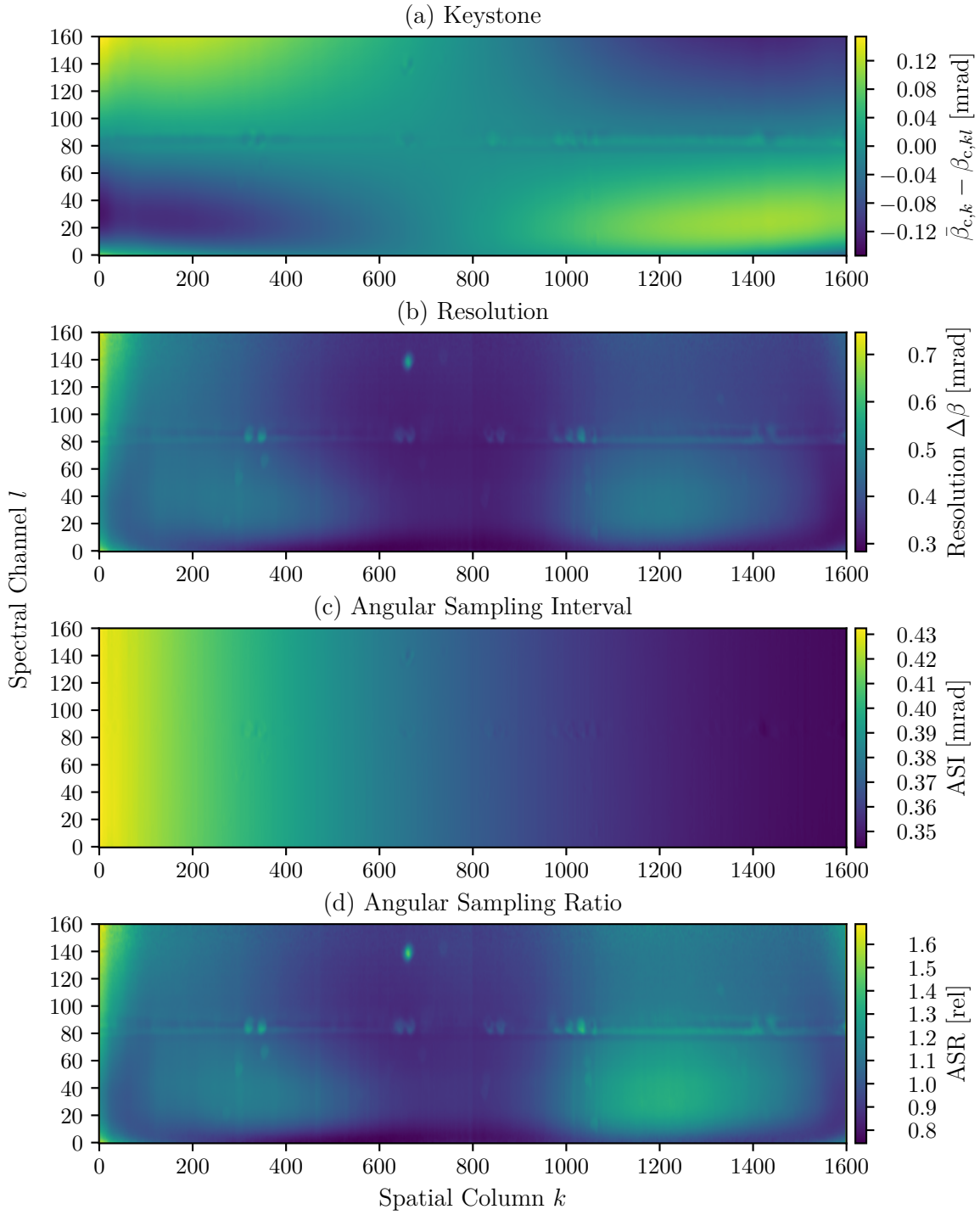

Figure 4.10: Results of the across-track geometric calibration of the HySpex instrument: (a) Center angles of each pixel referenced on the mean angle of each spatial column, illustrating the keystone effect. The effect is almost non-existent for the center pixels while it increases to displacements of up to 0.17 mrad. (b) Across-track resolution of each pixel. (c) Across-track Angular Sampling Interval (ASI), which is the distance of the center angles of adjacent pixels along the geometric axis. While the resolution of most pixels is approximately 0.50 mrad and better, it decreases to 0.77 mrad at the upper left of the detector. (d) Across-track Angular Sampling Ration (ASR), which is the resolution divided by the sampling interval.

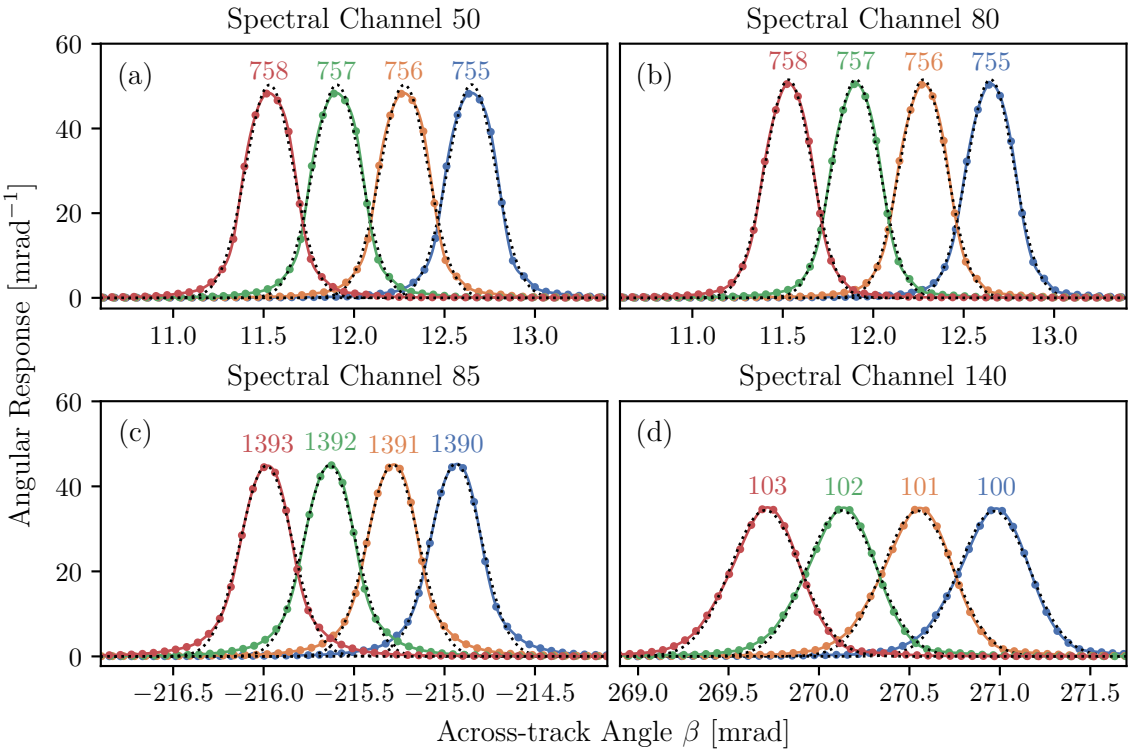

Figure 4.11: ARFs of selected pixels of the HySpex instrument. For comparison, the dotted lines represent Gaussian functions that are fitted to the data points. (a) and (b) ARFs in column 755 to 758 of channel 50 and channel 80 respectively. They overlap at levels below 50 % of their maximum, which indicates a fill factor below 100 % and that the image sharpness is not limited by the optical system but by the detector. (c) ARFs in columns 1390 to 1393 of channel 85. Although less sharp compared to the ARFs of (a) and (b) the overlapping values are also below 50 %. (d) ARFs in column 100 to 103 of channel 140. The overlapping values are above 50 %, indicating that the image sharpness is limited by the optical system.

The SSI is stable with a value of 3.6 nm over most parts of the detector, see Fig. 4.12c. Again, the area affected by the filter edge is an exception. Here, the SSI changes from 3.2 nm to 4.0 nm.

The spectral sampling ratio, i.e., the spectral resolution divided by the SSI ranges from 0.9 nm to 2.6 nm, see Fig. 4.12d.

The measured SRFs of selected pixels are shown in Fig. 4.13. It can be seen that they resemble a symmetric shape for most parts of the detector, see Fig. 4.13a. However, from approximately channel 75 to channel 90 (∼690 nm to ∼745 nm) the SRFs are highly asymmetric, see Fig. 4.13b and 4.13c. The shapes of the SRF change with each pixel along the spectral axis and within a few pixels along the spatial axis.

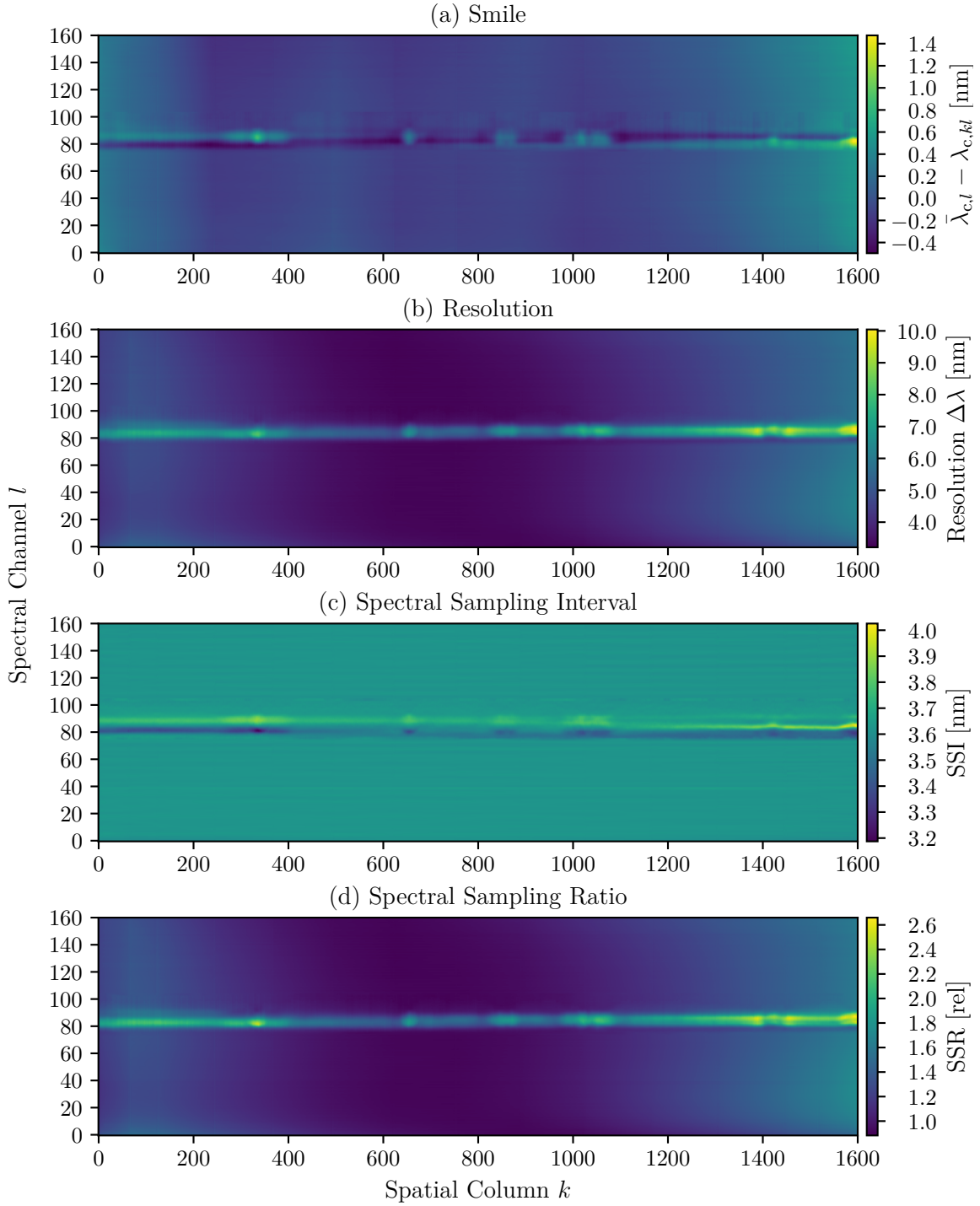

Figure 4.12: Results of the HySpex wavelength calibration. (a) Center wavelength of each spatial column in a spectral channel referenced on the mean of all channels of one spatial column, illustrating the Smile effect. (b) Spectral resolution of each detector pixel. (c) Spectral Sampling Interval (SSI), which is the distance of the center wavelengths of adjacent pixels. (d) Spectral Sampling Ration (SSR), which is the resolution divided by the sampling ratio. In all Figures the effect of the edge of a spectral filter placed at the upper detector half is visible between channel 70 and 90.

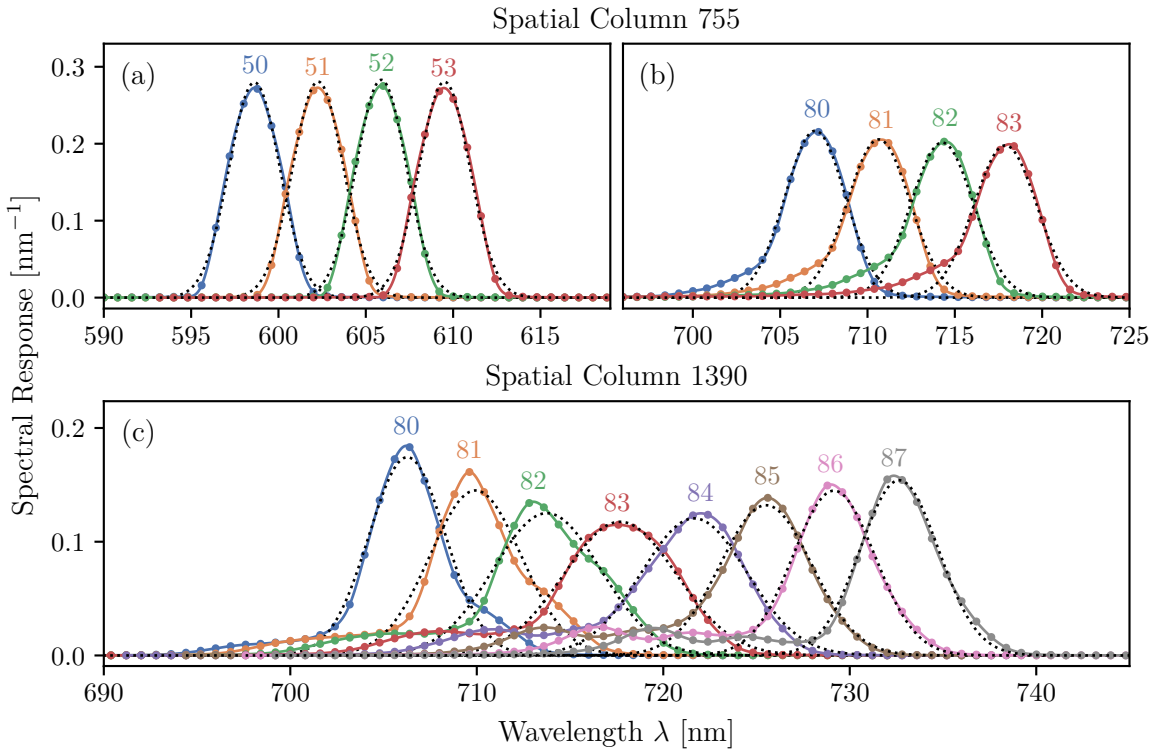

Figure 4.13: SRFs of selected pixels of the HySpex instrument. For comparison, the dotted lines represent Gaussian functions that are fitted to the data points. (a) SRFs of channels 50 to 53 of spatial column 755. The SRFs have a triangular shape and a 3.2 nm resolution. (b) SRFs of channels 80 to 83 of spatial column 755. The edge of the spectral filter causes distortions which leads to a asymmetric SRFs shape. (c) SRFs of channels 80 to 87 of spatial column 1390.

4.8 Pixel Response Function Reconstruction

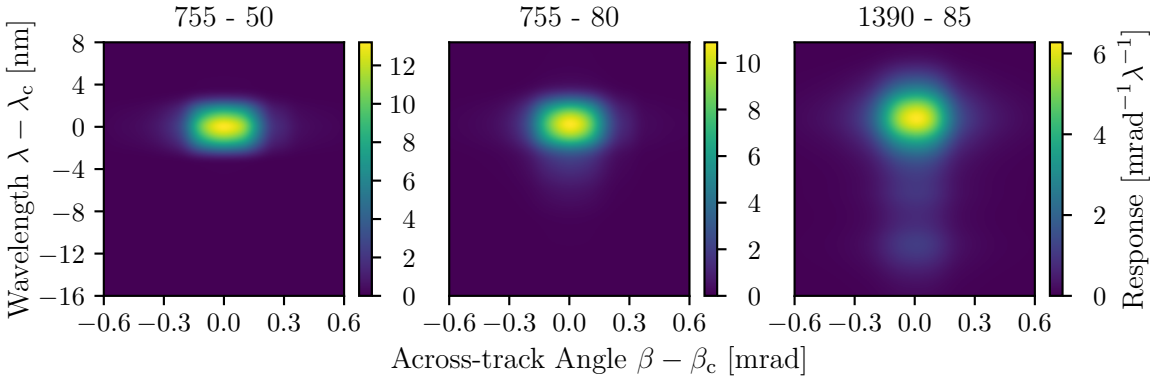

Figure 4.14: Examples of three PRFs constructed from the ARFs and SRFs measurement results. (left) PRF of pixel 755 channel 50. (center) PRF of pixel 755 channel 80. (right) PRF of pixel 1390 channel 80. Please note the different scales on the color axis. Since the integral of PRFs are normalized to one, higher values of the two-dimensional curves correspond to a high resolution.

As we have written in Sec. 2.5, across-track angle and spectral components of a PRF are described by the SRF and ARF, respectively. We assume that the SRFs and ARFs are orthogonally independent. Therefore, the instrument PRFs P_i can be reconstructed by

calculating the product of the ARFs and SRFs, yielding

$$f_i(\beta, \lambda) = \mathrm{ARF}_i(\beta)\,\mathrm{SRF}_i(\lambda). \tag{4.11}$$

Three PRFs reconstructed in this way from different detector locations are shown in Fig. 4.14. As expected, the PRF at the detector center below the filter edge is rather narrow. At the filter edge at spatial column 755 and spectral channel 80, distortions of the filter edge become visible. The depicted PRF at spatial column 1390 and spectral channel 80 shows a strongly asymmetric distribution due to the filter edge.

4.9 Uncertainties and Errors

4.9.1 Uncertainty of Response Function Models

RF models that interpolate between the sampling points have the advantage that any kind of RF can be approximated, which is why we use a cubic spline to describe the RF of the HySpex instrument. Unlike analytical functions, each measurement point with its uncertainty is part of the response model. The sampling distance of the response function is of course crucial for the accuracy of such a model.

The other possibility is to fit an analytical model, such as a Gaussian function, to the measurement points. This has the benefit that the influence of noise can be drastically reduced. But if the differences between the model and the measurement points are larger than the measurement uncertainty, a systematic error is introduced.

Since only the measurement points are fixed in the cubic spline model and the interpolation value between these points can deviate from the actual RF, we investigate the expected uncertainty here. For this purpose, we use a Gaussian normal distribution function as reference RF. Although the RFs of the HySpex instrument cannot be represent accurately with this model, it is very similar to the actual shape and will allow us to identify possible errors.

We choose a Gaussian normal distribution function with a FWHM of 3.2 nm and an amplitude of 1. This FWHM is equal to the lowest measured resolution value of the HySpex instrument, see Sec. 4.7.2. The Gaussian function h, compare Eq. (3.18), is sampled with the wavelengths $\lambda^{\mathrm{sampling}}$ ranging from -10 nm to 10 nm with a step width of 0.8 nm. The step width is equal to the sampling distance we have chosen for the SRF measurements, see Sec. 4.5. This results in 4 sampling points per FWHM. With this approach, we also evaluate the ARF model, which is at least sampled with 4.7 points per FWHM, due to the minimum resolution width of 0.28 mrad and the measurement increment of 0.06 mrad.

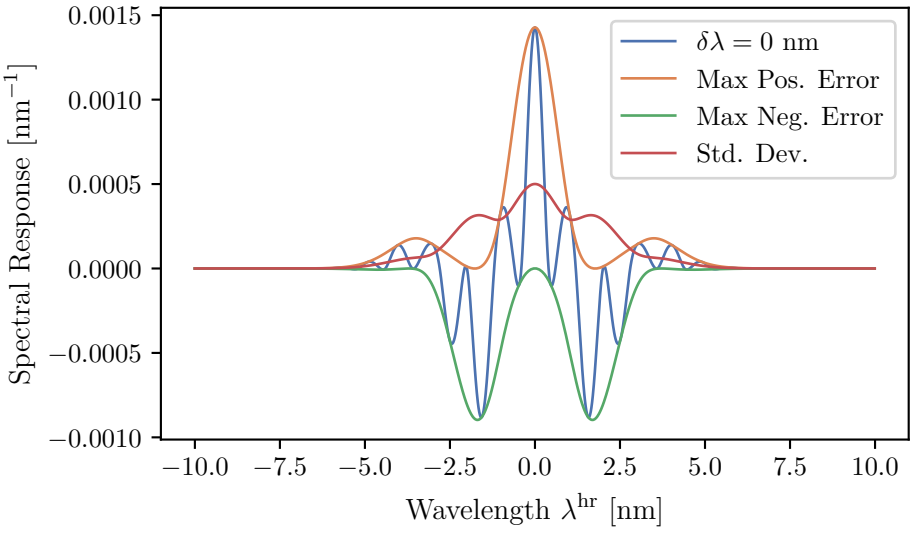

Figure 4.15: Error between cubic spline interpolation and Gaussian function with a FWHM of 3.2 nm when the function is sampled with 0.8 nm. (blue) Residuals when sampling function is not shifted. (orange and green) Range of errors. (red) Standard deviation.

The response r_i for a wavelength shift of $\delta\lambda_i$ is then

$$r_i = h(\lambda^{\mathrm{sampling}} + \delta\lambda_i, 0\,\mathrm{nm}, 3.2\,\mathrm{nm})/h(0\,\mathrm{nm}, 0\,\mathrm{nm}, 3.2\,\mathrm{nm}) \tag{4.12}$$

$$\lambda^{\mathrm{sampling}} = -10.0\,\mathrm{nm}, -9.2\,\mathrm{nm}, \ldots, 10.0\,\mathrm{nm} \tag{4.13}$$

$$\delta\lambda_i = i \cdot 0.01\,\mathrm{nm} \tag{4.14}$$

$$i = 0, 1, \ldots, 80. \tag{4.15}$$

The shift $\delta\lambda_i$ ranges therefore from 0 nm to 0.79 nm with a step with of 0.01 nm. For each response r_i with wavelengths $\lambda^{\mathrm{sampling}} + \Delta\lambda_i$ we get a spline interpolation function r_i^{spline}.

The difference between the spline models and the Gaussian function h is determined by defining wavelengths λ^{hr} ranging from −10 nm to 10 nm with a step width of 0.01 nm. We sample all splines and the Gaussian function h with λ^{hr} and determine for each wavelength λ^{hr} the errors e_i by

$$e_i^{\mathrm{spline}} = r_i^{\mathrm{spline}}(\lambda^{\mathrm{hr}}) - h(\lambda^{\mathrm{hr}}, 0\,\mathrm{nm}, 3.2\,\mathrm{nm})/h(0\,\mathrm{nm}, 0\,\mathrm{nm}, 3.2\,\mathrm{nm}), \tag{4.16}$$

$$\lambda^{\mathrm{hr}} = -10.00\,\mathrm{nm}, -9.99\,\mathrm{nm}, \ldots, 10.00\,\mathrm{nm}. \tag{4.17}$$

For each wavelength λ^{hr}, we determine the maximum positive $\max_i(e_i^{\mathrm{spline}})$ and maximum negative error $\min_i(e_i^{\mathrm{spline}})$ as well as standard deviation of e_i^{spline}. The results are show in Fig. 4.15. The maximum error is about 0.14 % of the amplitude with an standard deviation of maximum 0.05 %. We consider these errors as negligible.

4.9.2 Errors Caused by Source Bandwidths and Line Widths

We measure the ARFs with help of an illuminated slit which is in the focal point of a collimating mirror. From the mirror, a collimated beam is guided to the aperture of the imaging spectrometer, where the instrument optics creates an image of the slit on the detector. The slit image is the convolution of the collimator optics with the imaging spectrometer optics. Since the slit has a finite width, the image is always broader than that of a perfect point source, which leads to an overestimation of the resolution width of the ARFs. The same applies to the spectral bandwidth of a narrow spectral source used to measure SRFs.

The amount of overestimation can be approximated by assuming that both the instrument and collimator function, are Gaussian functions. Using Eq. (4.2), we can estimate the maximum error $e(\Delta\beta)$ caused by the width of the collimator slit target as

$$e(\Delta\beta) = \Delta\beta_{\text{meas}} - \sqrt{\Delta\beta_{\text{meas}}^2 - \Delta\beta_{\text{colli}}^2} \tag{4.18}$$

$$= 0.28\,\text{mrad} - \sqrt{(0.28\,\text{mrad})^2 - \left(\frac{0.02\,\text{mm}}{750\,\text{mm}}\right)^2} \tag{4.19}$$

$$= 0.001\,\text{mrad}, \tag{4.20}$$

where $\Delta\beta_{\text{meas}}$ is the measured angular resolution. We use the smallest resolution width here, as the relative overestimation error for this is the largest. However, the angular accuracy of the folding mirror setup is 0.006 mrad, which is larger than the line width error. We conclude that the line width error is negligible.

The error $e(\Delta\lambda)$ caused by the monochromator bandwidth $\Delta\lambda_{\text{mono}}$ is approximated again with the help of Eq. (4.2) and the results from the spectral bandwidth measurements, see Sec. 4.3.2, as

$$e(\Delta\lambda) = \Delta\lambda_{\text{meas}} - \sqrt{\Delta\lambda_{\text{meas}}^2 - \Delta\lambda_{\text{mono}}^2} \tag{4.21}$$

$$= 3.20\,\text{nm} - \sqrt{(3.20\,\text{nm})^2 - (0.54\,\text{nm})^2} \tag{4.22}$$

$$= 0.05\,\text{nm}, \tag{4.23}$$

where $\Delta\lambda_{\text{meas}}$ is the measured spectral resolution. This means that the value for the spectral resolution is, in a worst case approximation, overestimated by 0.05 nm. Since the center wavelength accuracy of the monochromator is within 0.1 nm, the error is not negligible.

To quantify the impact of these errors, we use two test scenes, see Appendix A. From the measured angular and spectral resolutions of each pixel, we derive the amount of potential overestimation of the resolution and create two artificial sensors with Gaussian RFs—one with the same resolution as measured and one corrected for the overestimation.

We then sample test scene 1 and test scene 2 with both sensors and compare the results. Test scene 1 has an artificial checkerboard pattern, while test scene 2 is based on natural spectra with solar and atmospheric features. For test scene 1, the pixels with the largest errors of up to 1.4 % are located in the center of the detector, where the spectral and spatial resolution width are also the shortest, see Fig. 4.16a. For test scene 2, the errors are up to

0.6 % at the location of a oxygen absorption band in channel 95, see Fig. 4.16b. Again, the maximum error is in the center of the detector, where the resolution widths are the shortest. Toward the detector edges, the errors decrease to values below 0.3 % due to the increasing resolution widths. For all other channels, the errors are below 0.2 %, which are therefore negligible.

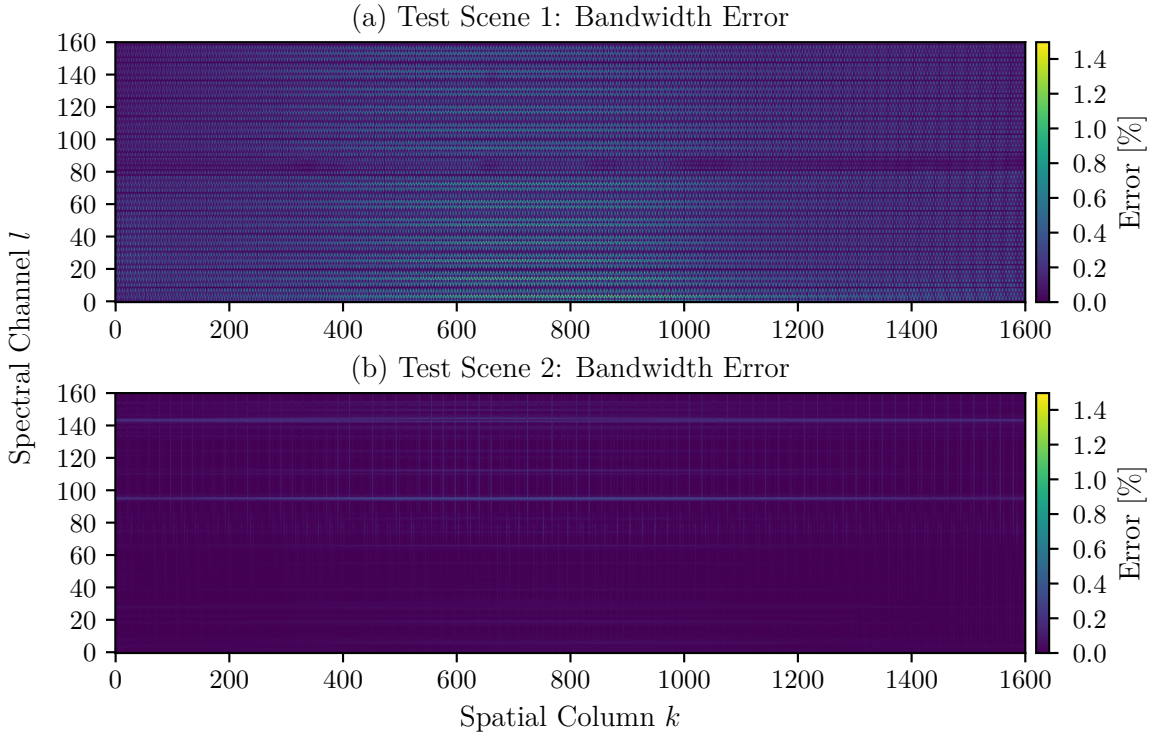

Figure 4.16: Approximation of the errors caused by the finite band and line widths of the calibration sources. (a) The maximum error of 1.4 % for test scene 1 is the reached in the center of the detector, where the spatial and spectral resolution widths are the shortest. (b) For test scene 2, the maximum error with 0.6 % occurs in channel 95, where a oxygen absorption band is located. For the other channels, the errors are below 0.2 % and therefore in a negligible range.

4.9.3 Error of Spectral Response Function Interpolation

The interpolation of the SRFs that are not measured is based on the assumption that they do not change significantly between the reference SRFs. Of course, no interpolation is perfect. For this reason, we investigate the interpolation error in this section. Since we measure the SRFs from the center channels with high spatial density, we can use the data from one of these channels to get an approximation of the interpolation error for channels, which are measured with lower density. We use channel 102, as it is the highest channel number of the area which is scanned with high spatial density and since this channel is not affected by the distortions caused by the edge of the spectral filter. In this channel, the SRFs of 1102 pixels are measured with 127 different wavelength scans, see Fig. 4.8. From these measurements we use the SRFs of 127 pixels at 15 scan locations where the SRFs of the other detector channels are measured. The results are depicted in Fig. 4.17. The largest difference in the

center wavelength is 0.08 nm at spatial column 1100. The resolution diverges up to 0.15 nm at spatial column 33, while the difference is not bigger than ±0.05 nm at the remaining geometric pixels.

The interpolated and the measured SRFs in spatial column 1100 and spatial column 33 of spectral channel 102 are shown in Fig. 4.18. As can be seen, for both locations, the interpolation errors are below the error due to a 0.1 nm shift of SRFs. Since these are the SRFs with the largest center wavelength and resolution error, respectively, the interpolation errors of the other SRFs is considerably smaller.

To check the influence of the error on actual measurements, we use two test scenes, see Appendix. A. We shift the center wavelengths of SRFs in each spatial column by the residuals from Fig. 4.17a. Both test scenes are convolved with the shifted and the original SRFs. An approximation of the interpolation error is derived by comparing the results of shifted and original SRFs convolution. The absolute relative error of test scene 1, which is a kind of a worst-case scenario, is up to 5 %, see Fig. 4.19a. For test scene 2, which is a more realistic case, the absolute relative error is below 3 %, see Fig. 4.19b. This error is mostly present in channel 142, where the water vapor absorption is strongest. For the remaining channels, the error is mostly negligible.

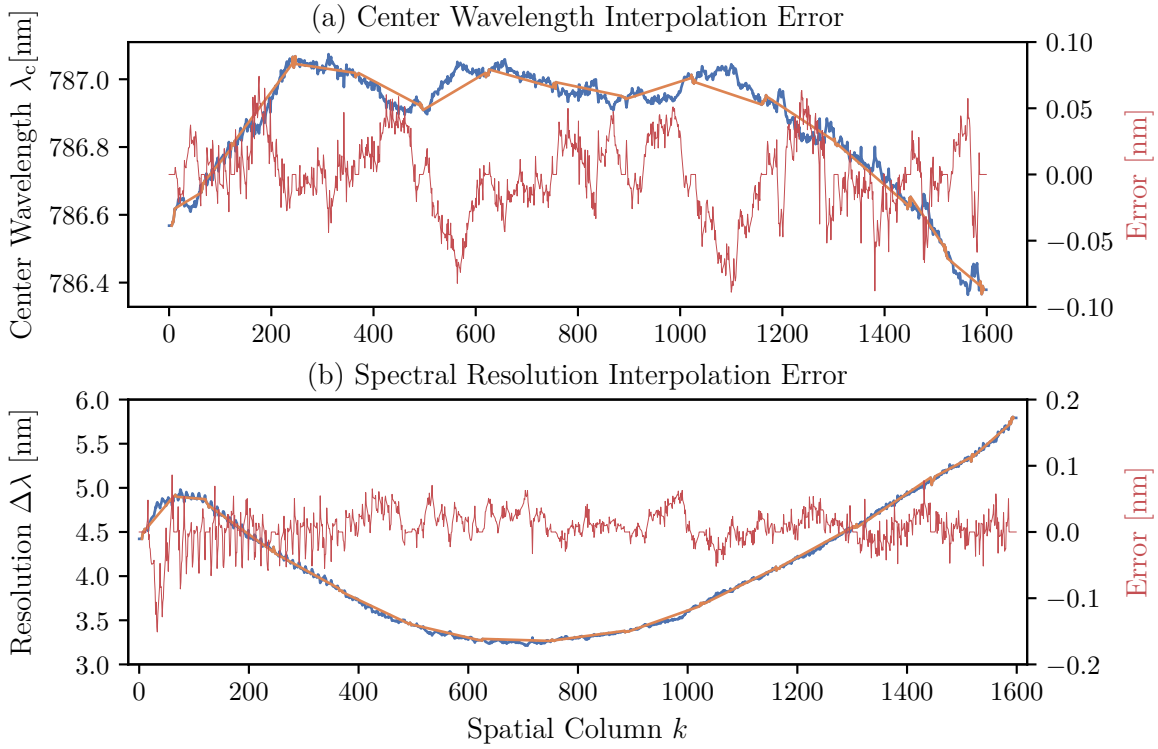

Figure 4.17: Difference (red) of the measurements of 1102 pixels at 127 different illuminations angles (blue) and measurements of 128 pixels at 15 different illumination angles (orange). Missing values are linearly interpolated. (a) Center wavelengths (b) Resolution.

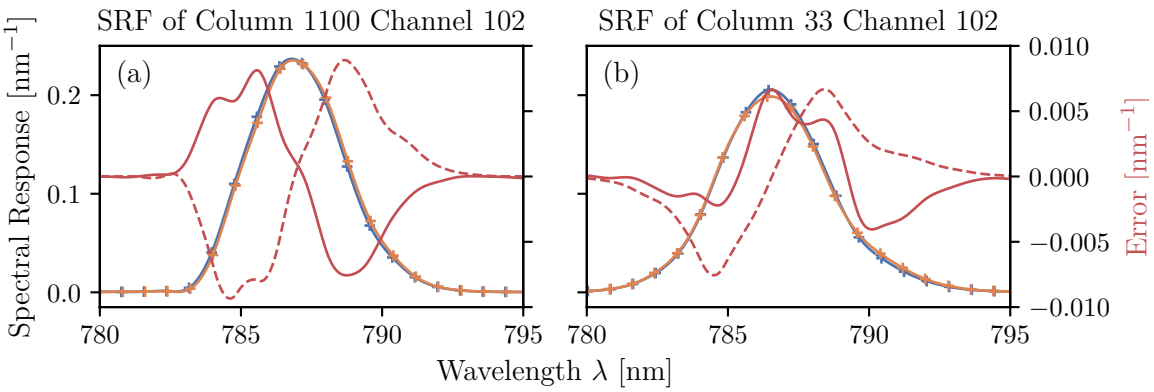

Figure 4.18: Error (red solid) of interpolated SRF (blue) with respect to measured SRF (orange). For comparison, the error for a 1 nm shift of the measured SRF is shown (red dashed). (a) Measured and interpolated SRFs of spatial column 1100 of spectral channel 102. This is the column with the largest center wavelength error, see Fig. 4.17a. (b) Measured and interpolated SRFs of spatial column 33 of spectral channel 102. This is the pixel with the largest resolution error, see Fig. 4.17b.

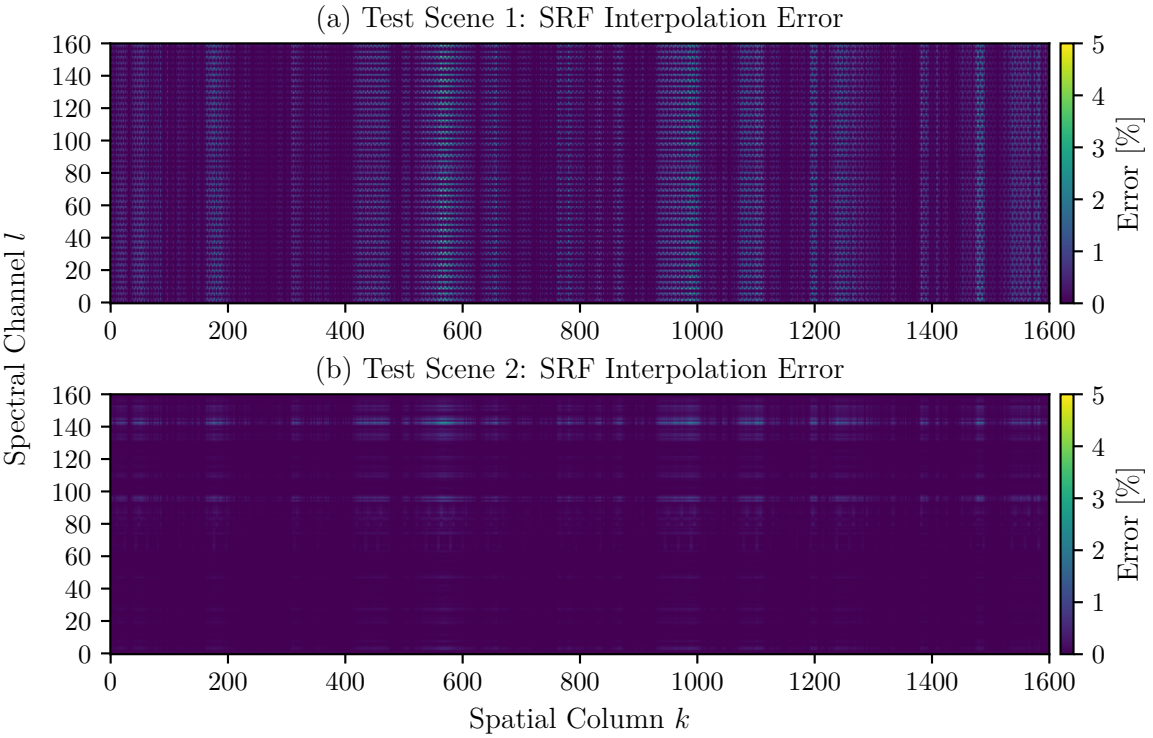

Figure 4.19: Approximation of the errors caused by the SRF interpolation by comparing test scene 1 and test scene 2.

4.9.4 Improvements over Gaussian Response Function Model

As we discussed before, Gaussian normal distribution functions are often used to describe the shape of ARFs and SRFs. In the past, this was also the model of choice for the HySpex instrument [12]. To quantify possible errors, we use test scene 1 and test scene 2, see Appendix A. Each scene is convolved with cubic spline as well as Gaussian-based PRFs using Eq. (2.21) with the slight modification that the along-track angle α is not resolved because the scenes are constant in the along-track direction.

The absolute relative error is up to 96 % for test scene 1, see Fig. 4.20b. The bigger discrepancy of the Gaussian model is especially visible at the location of the filter edge between channel 70 and 90. For test scene 2, the errors are smaller, as the scene is more natural and does not have such big gradients as scene 1 does, see Fig. 4.20b. The errors below channel 60 are smaller than 1 %. At the filter edge, they increase to 5 %. For higher channels, the big gradients between the different spectra cause errors up to 20 %.

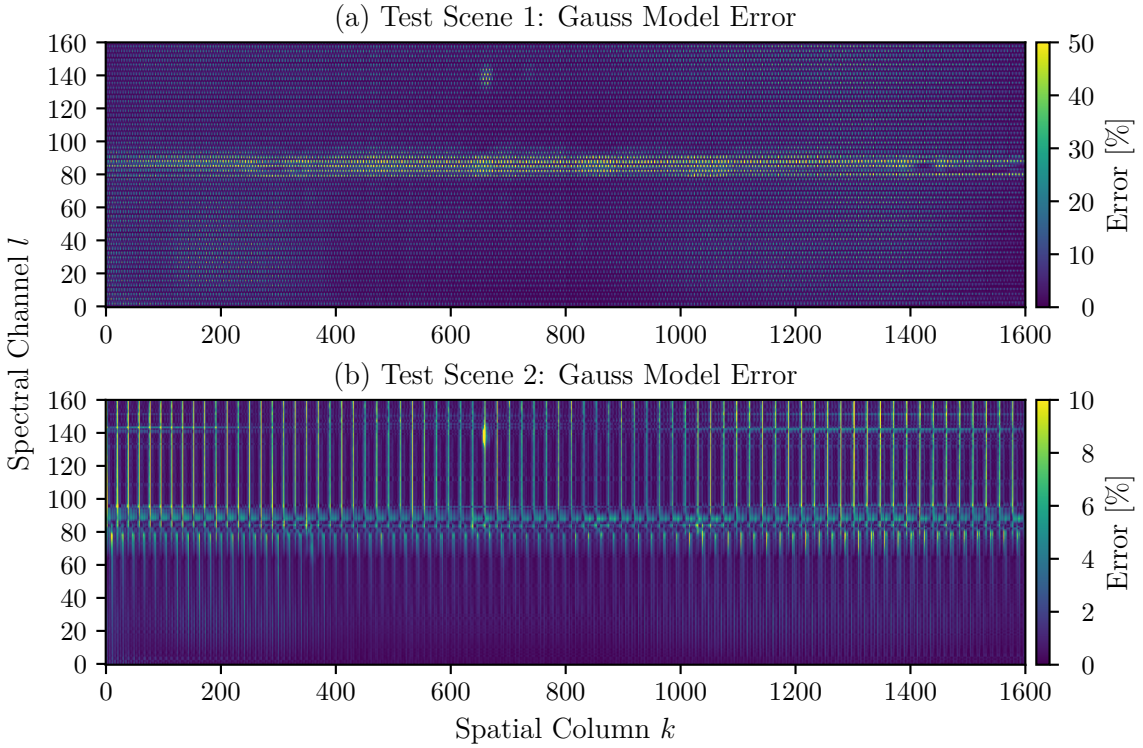

Figure 4.20: Absolute relative error of Gaussian normal distribution based response functions to cubic spline model. Please note the different scales. (a) Errors for test scene 1. The errors are up to 96 % (the scale is truncated at 0.5 for better visualization). The biggest errors are at the location of the filter edge between channels 70 and 90. (b) Errors for test scene 2. The errors below channel 60 are under 1 %, while they increase to 5 % at the filter edge location. Above the this area the high gradients between the different spectra causes errors of up to 20 % (truncated scale).

4.9.5 Spatial and Spectral Calibration Uncertainty

We can now specify the uncertainties of the ARF and SRF models demand by calibration measurements. Due to the uncertainty of the folding mirror angle, see Sec. 4.2, we specify the angle accuracy also with 0.006 mrad ($k = 2$) which is approximately 2 % of the smallest measured resolution width. The uncertainty of the spectral calibration is 0.15 nm ($k = 2$), mostly caused by the interpolation errors and the monochromator uncertainty.

4.10 Summary

- A collimator setup with a slit as target is used to measure the across-track ARFs.
- The SRFs are measured with a monochromator setup. Due to the limited output intensity of the monochromator, only a few spatial columns can be illuminated simultaneously.
- The center wavelength, bandwidth and relative radiometric output power of the monochromator are calibrated. For the center wavelength calibration, an echelle grating wavelength meter is used with a method we developed to traceably calibrate a monochromator with arbitrary sampling distances. The center wavelength calibration is traceable to spectral line lamps with an uncertainty of 0.1 nm ($k = 2$).
- The relative radiometric monochromator calibration is used to correct the measured SRFs for the wavelength dependent monochromator output intensity.
- For the measured ARFs and SRFs, no analytical function could be found that describes these functions for every pixel without introducing systematic errors. We interpolate therefore with a cubic spline between the measured sampling points to derive a model for the ARFs and SRFs. Simulations show that the uncertainty of the cubic spline interpolation model is negligible for the chosen sampling distances.
- The SRFs of a subset of detector pixels are measured due to the limited monochromator output intensity and time constraints. Unmeasured SRFs are interpolated. We developed a novel method to interpolate the entire shape of the SRFs, not only the two main parameters, which are conventionally the center wavelength and the FWHM.
- Validating the interpolation shows that the error of the interpolation is less than the error of a 0.1 nm shift. Simulations show that the maximum radiometric error caused by the interpolation is 3 % in the water vapor absorption band at channel 142.
- The uncertainties of the ARF models are 0.006 mrad ($k = 2$), which is approximately 2 % of the smallest measured resolution width.
- Due to the limited accuracy of the interpolation, the wavelength uncertainty is specified by 0.15 nm ($k = 2$), which is approximately 5 % of the smallest measured resolution width.
- The keystone is up to 0.16 mrad (0.33 pixel) towards the edges of the detector.
- The across-track angular resolution is between 0.28 mrad and 0.50 mrad.
- The SRFs between spectral channel 75 and 90 ($\sim$690 nm and $\sim$745 nm) are asymmetrically deformed due to the edge of a spectral filter that covers the upper detector half. The SRF shapes in this region rapidly change within a few pixels.
- The smile effect is up to 0.5 nm (0.15 pixel) outside of the deformed region and more than 1.4 nm (0.42 pixel) at the right detector edge in the deformed region.
- The spectral resolution width is between 3.2 nm and 6.3 nm outside of the deformed region and increases up to 10 nm in the deformed region.

- The PRFs are derived from the across-track ARFs and the SRFs, assuming these are orthogonally independent.
- Errors caused by the finite width of the collimator target are negligible while the monochromator bandwidth causes errors of up to 0.6 % in the oxygen absorption band in channel 95.
- Errors between Gaussian normal distribution based RF models and the introduced spline model are up to 20 % at steep changes in a synthetic test scene based on natural spectra.

5

Radiometric Calibration

Contents

5.1 Introduction 84
5.2 Methods 84
5.3 Results 90
5.4 Summary 94

5.1 Introduction

The purpose of the radiometric calibration measurement is to determine the radiometric calibration coefficients R that are used to convert raw data to spectral radiance.

We use for the radiometric calibration a secondary standard called RASTA, which was developed in cooperation with DLR and PTB [49–52]. Since RASTA has relatively low output power and can only cover a small FoV, it was designed to calibrate a transfer spectroradiometer. The spectroradiometer itself then calibrates an integrating sphere which can cover the complete FoV of an instrument. Of course the uncertainties of the spectroradiometer add to the radiometric calibration. We therefore calibrate the center pixels of the HySpex instrument directly with RASTA. An integrating sphere is then only used for the relative calibration of all pixels, a procedure called flat fielding. To derive the calibration coefficients, the calibration spectrum of the standard needs to be resampled to the sensor responses. This is usually done by interpolating the spectrum at an instrument's center wavelengths. However, this is only accurate to a certain extent, compared to convolving the spectrum with the instrument's SRFs. In the following, we will therefore also examine possible errors of these procedures.

In addition, we discuss the polarization sensitivity calibration. The polarization sensitivity calibration of our HySpex VNIR-1600 is published in [19]. However, the formula used to determine the polarization sensitivity P gives wrong results. We use therefore Eq. (2.34) to derive the polarization sensitivity of each pixel. To measure the polarization sensitivity, we use a wire grid polarizer that has a high degree of polarization over the whole spectral range of the instrument.

5.2 Methods

For the calibration, we use a 0/45 lamp-plaque setup. In this configuration, a lamp irradiates a diffusely scattering plaque under an incident angle of 0° to the normal of the plaque. The reference is then the radiance emitted at 45°.

Hence, any instrument calibrated with this setup must be placed under an angle of 45° with the FoV facing toward the center of the plaque. Airborne push-broom imaging spectrometers usually have an FoV that is too large fulfill these requirements. However, the IFoVs of the center pixels can usually be covered by the plaque. The remaining pixels can then be calibrated relatively to the center pixels, a procedure commonly known as flat fielding.

In the following, all photo signals are corrected for dark as well as offset signal and all other detector effects, see chapter 3.

5.2.1 Radiometric Calibration using Spectral Response Functions

The calibration coefficients R_i can be derived according to Eq. (2.31). Since the emitted radiance can be assumed to be uniform within the IFoV of a pixel, Eq. (2.31) simplifies to

$$R_{k=\text{center},l} = \frac{S^{\text{ph,ref}}_{k=\text{center},l}}{t_{\text{int}} \int_0^\infty \text{SRF}_{k=\text{center},l}(\lambda) L^{\text{ref}}_\lambda(\lambda)\, \text{d}\lambda}, \tag{5.1}$$

where k is a pixels spatial column and l is the spectral channel number. $S^{\text{ph,ref}}_{k=\text{center},l}$ is the photon signal of the center pixels.

We derive then the calibration of the flat field source radiance with the center pixels as

$$L^{\text{ff}}_l = \frac{S^{\text{ph,ff}}_{\text{center},l}}{t^{\text{ff}}_{\text{int}} R_{\text{center},l}}, \tag{5.2}$$

where, L^{ff}_l is the flat field source radiance at wavelengths $\lambda_{\text{center},l}$ and $S^{\text{ph,ff}}_{\text{center},l}$ is the resulting photo signal. Assuming a smooth spectrum of the flat field source radiance, we can define an interpolation function $L^{\text{ff}}_\lambda(\lambda)$. The radiometric calibration coefficient of each pixel is then

$$R_{kl} = \frac{S^{\text{ph,ff}}_{kl}}{t_{\text{int}} \int_0^\infty \text{SRF}_{kl}(\lambda) L^{\text{ff}}_\lambda(\lambda)\, \text{d}\lambda}. \tag{5.3}$$

5.2.2 Conventional Radiometric Calibration Approach

Often, the reference radiance is just linearly interpolated at the center wavelengths λ_{c} of the SRFs instead by sampling it with the instrument's SRF:

$$R^{\text{approx}}_{\text{center},l} = \frac{S^{\text{ph}}_{\text{center},l}}{t_{\text{int}} L^{\text{ref}}_\lambda(\lambda_{\text{center},l})}. \tag{5.4}$$

The remaining pixels areas are then relatively calibrated with a uniform light source such as an integrating sphere. A naive approach for deriving the flat field ff would be to divide the signal S^{ff}_{kl} of all pixels of a channel by the signal of the center pixel $S^{\text{ff}}_{\text{center},c}$. The radiometric calibration coefficient is then

$$R^{\text{approx}}_{kl} = \frac{S^{\text{ph,ff}}_{kl}}{S^{\text{ph,ff}}_{\text{center},l}} R^{\text{approx}}_{\text{center},l}. \tag{5.5}$$

However, this neglects smile and SRF differences within one channel.

5.2.3 Center Pixel Calibration

As spectral radiance normal, we use a 0/45 lamp-plaque setup called RASTA. RASTA is an existing setup and was developed by DLR and PTB and has self-monitoring capabilities [49–52]. The setup works as follows, see Fig. 5.1: A lamp irradiates a diffusely scattering

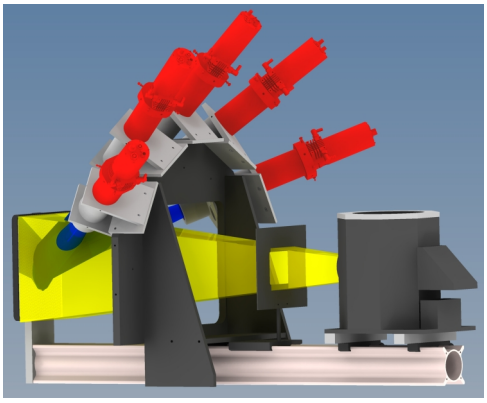

Figure 5.1: Mechanical setup of RASTA. A lamp illuminates a diffuse reflecting plaque, while the radiance is monitored by five radiometers (red) where each covers a different spectral range.

plaque, which is calibrated for a scattering angle of 45° to the normal angle of the plaque. Since the plaque is not a perfect Lambertian reflector, the sensor to calibrate must be placed with a viewing angle of 45° toward the plaque. According to the calibration certificate of the plaque, errors of up to 0.5 % are expected for viewing angles that differ by 2°. At the same time, the acceptance cone of the sensor must be aligned to the center of the plaque. Five additional radiometers are positioned around the plaque. Each radiometer covers a different part of the emitted spectrum. This allows the setup to be monitored and for determining possible drifts of the lamp, the plaque or the radiometers.

RASTA's calibration curve with its uncertainty is depicted in Fig. 5.2. The uncertainty is mainly caused by the temperature uncertainty of the radiance normal that was used by PTB to calibrate RASTA. Hence, a strong correlation of the uncertainties is assumed [80].

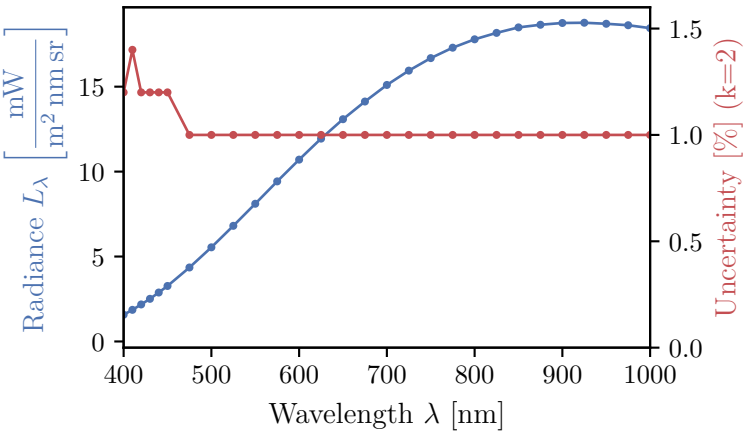

Figure 5.2: Radiance (blue) of RASTA with uncertainties (red). The radiance rises from 2.8 $\mathrm{mW/m^2\,nm\,sr}$ at 400 nm to 33.4 $\mathrm{mW/m^2\,nm\,sr}$ at 925 nm, while the uncertainty is between 1.0 % and 1.4 % ($k = 2$). The radiance is calibrated every 25 nm for most parts of the spectrum.

We place the HySpex VNIR-1600 in front on the plaque. The center pixels are aligned to the plaque center with a viewing angle of 45°. A series of 1000 reference frames are taken with an integration time of 120 ms. At this integration time, smear effect is negligible, see

Sec. 3.7. Since the HySpex instrument has a total FoV of approximately 34.5°, Bidirectional Reflectance Distribution Function (BRDF) effects are no longer negligible. Hence, only the radiometric coefficients R of the center pixels can be derived. After covering the lamp, the same number of frames are taken to measure the background signal.

We correct the acquired data for non-linearity effects and subtract the background signal. The radiometric calibration coefficients of the center pixels are then calculated with Eq. (5.3) and for comparison also with Eq. (5.5).

5.2.4 Interpolation Method

RASTA's calibrated spectral radiance is sampled from 350 nm to 450 nm every 10 nm and from 450 nm to 2500 nm every 25 nm. To obtain the continuous spectral radiance $L_{\lambda}^{mathrmref}$ that is required for Eqs. (5.1), (5.3) and (5.4), we need to interpolate the discrete sampled calibration data. This can be done, since the lamp spectrum has a smooth shape close to a Planck curve [81]. The accuracy of the interpolation has of course an influence on the calculated radiometric calibration coefficients. We therefore investigate the errors introduced by linear and cubic spline interpolation to determine which method is the most appropriate. As the test spectrum we use a Planck curve at a temperature of 3000 K. We sample the curve at the same wavelengths that the RASTA's calibration curve is sampled. After interpolating between the sampling points, we compare the result of the linear and cubic spline interpolation with the Planck curve. The results in Fig. 5.3 show that the maximum error of 0.03 % of the cubic spline interpolation is negligible, while the linear interpolation introduces significant errors of up to 0.4 %. For this reason, we use cubic splines to interpolate the calibration radiation of RASTA.

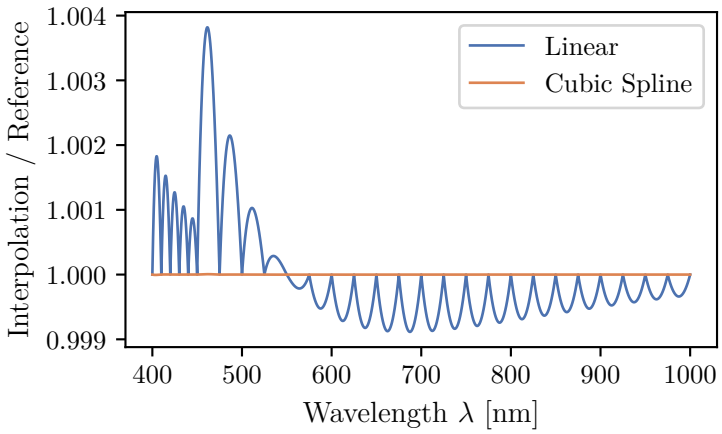

Figure 5.3: Errors of linear respectively cubic spline interpolation with respect to the reference Planck spectrum at a temperature of 3100 K. The spectrum is interpolated between the wavelengths with which RASTA's calibration curve is sampled. It can be seen that the linear interpolation introduces errors of up to 0.4 %, while the errors of the cubic spline interpolation are with ≤0.03 % negligible.

5.2.5 Flat Field Calibration

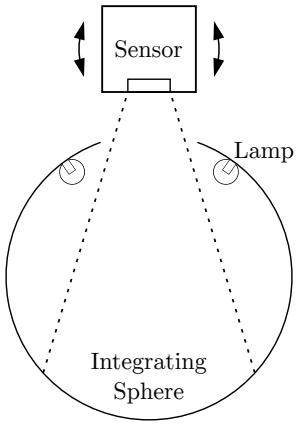

Figure 5.4: Flat fielding measurement setup. The imaging spectrometer under investigation is mounted on a rotary stage positioned on top of an integrating sphere. The integrating sphere is illuminated by lamps mounted in the upper hemisphere. The instrument is rotated along its across-track angle so that each geometric line measures the same spot in the center of the sphere.

As mentioned before, with RASTA, only a subset of pixels can be calibrated directly. We therefore use an integrating sphere to simultaneously illuminate all pixels and to perform a relative calibration. The sphere is illuminated by a number of lamps mounted in the upper hemisphere. The instrument under investigation is placed on top of the integrating sphere so that the complete FoV is covered by the radiance field of the sphere. Additionally, it is ensured that the light emitted by the lamps is at least diffusely scattered once by the sphere's surface before it is coupled into the instrument. Usually, the flat fielding is performed by measuring the radiance field of the integrating sphere once. Since the imaging spectrometers for remote sensing are focused on infinity, different pixels receive light from different parts of the sphere's background. Non-uniformities of the background can introduce a systematic error.

To avoid background non-uniformity errors, we therefore modify the classical approach and rotate the instrument over its across-track angle, so that each spatial column measures the same spot of the sphere. The instrument is rotated from a starting position where the entire FoV is outside of the sphere's exit port to an end position that is also outside of the port. We continuously record frames during the scanning motion. The rotation speed and the frame rate are adjusted so that a sufficient amount of frames of the same spot size in the center of the exit port are recorded. We chose an integration time of 20 000 μs so that systematic errors due to smearing are below 0.25 %, see Sec. 3.6.2.

The recorded data is corrected for background signal and non-linearity effects as well as stray light. For each pixel, we determine the frames that measured the radiance field within the exit port. This is done by identifying the frames that received at least 95 % of the maximum signal as

$$S_{ij}^{\text{port}} = S_{ij} \text{ for } S_{ij} \geq 0.95 \max_{j}(S_{ij}), \tag{5.6}$$

where j is the frame index and i is the pixel index. From S_{ij}^{port}, we use 800 frames in the center of the array and calculate the average ($S[\bar{x}yz]$) to derive the flat field signal $S_i^{\text{ph,ff}}$ of

pixel i, which yields

$$S_i^{\mathrm{ph,ff}} = \sum_{j_{\mathrm{center}}-400}^{j_{\mathrm{center}}+400} S_{ij}^{\mathrm{port}}, \tag{5.7}$$

where j_{center} is the center index of S_{ij}^{port}.

5.2.6 Monte Carlo Simulation

We perform Monte Carlo simulations to determine the uncertainty of the radiometric calibration. The following steps are repeated for 1000 times:

- Randomize RASTA calibration curve with Gaussian normal distribution. Since a high correlation of the sampling points of the RASTA spectrum is assumed, we multiply their uncertainties with the same random value that ranges from -1 to 1. The result is added to the values of the sampling points.

- Perform cubic spline interpolation of RASTA spectrum with a sampling distance of 0.01 nm.

- Randomize SRF sampling points with Gaussian normal distributions for a wavelength uncertainty of 0.015 nm and radiometric uncertainty, see Sec. 4. Additionally, to account for SRF interpolation errors, we add an uncertainty of 0.1 nm with a flat distribution. The radiometric uncertainty is calculated from the standard deviation of the averaged frames. The sampling points are randomized with a Gaussian distribution before the cubic spline interpolation.

- Perform cubic spline interpolation on SRF sampling points and normalize SRF integrals to unity.

- Randomize averaged RASTA measurement with Gaussian normal distribution with standard deviation of averaged frames devided by the number of frames.

- Add uncertainty of detector temperature to RASTA measurements, see Sec. 3.4.

- Sample the interpolated RASTA spectrum with the center SRF and calculate radiometric calibration coefficient analog to Eq. (5.3).

- Randomize flat field measurements with Gaussian normal distribution with standard deviation of averaged frames devided by number of frames.

- Determine integrating sphere radiance, according to Eq. (5.2).

- Interpolate integrating sphere radiance with a sampling distance of 0.01 nm.

- Derive radiometric calibration coefficient for all detector pixels analog to Eq. (5.3).

5.2.7 Polarization Sensitivity Measurements

We measure the polarization sensitivity with the same approach published in [13]. A wire grid polarizer mounted on a rotary stage is placed in front of an integrating sphere. The polarizer has a polarization of $p > 99.99\,\%$ and is aligned parallel to the slit of the imaging spectrometer. The imaging spectrometer is "looking" through the polarizer into the integrating sphere, which is illuminated by halogen lamps. We change the rotation angle from 0° to 360° and record every 15° 200 frames. Since the aperture of the rotary stage with polarizer cannot cover the entire instrument FoV, we repeat these measurement at five different across-track angles by rotation the imaging spectrometer.

The signals of each pixel are averaged $S[\bar{x}yz]$ and corrected for the detector effects discussed in chapter 3. We determine the parameters $R^{\mathrm{p}} \cdot L^{\mathrm{s}}$ and $R^{\mathrm{up}} \cdot L^{\mathrm{s}}$ and γ by fitting Eq. (2.33) on the data points of each pixel. With Eq. (2.34) we derive the polarization sensitivity P. Finally, the data sets with different viewing angles are stitched together to a complete polarization array.

5.3 Results

5.3.1 Potential Sampling Errors

As aforementioned, the radiometric response of each pixel can be calculated according to either Sec. 5.2.1 or Sec. 5.2.2, where the former provides a more accurate solution.

The first part, which distinguishes both methods, is that the calibration spectrum is either interpolated at the center wavelengths or convolved with the SRFs of the instrument. The difference between the results for both methods is shown in Fig. 5.5. It can be seen that there is a difference of up to 0.25 % at the center channel, which is caused by the asymmetric shape of the SRFs. This indicates that for systems with symmetric response functions, the error is negligible when the calibration spectrum is interpolated at the center wavelengths.

The next difference is the relative radiometric calibration (flat fielding) method, i.e. the calibration of the remaining pixels relative to the calibrated center pixels. This can be done by either assuming that the SRFs of a channel are constant using Eq. (5.5) or by using the more accurate method using Eqs. (5.2) and (5.3). We use the same $R_{\mathrm{center},c}$ in Eqs. (5.2) and (5.5) to directly compare both approaches. The different outcome of both equation is shown in Fig. 5.6a. An error of up to 0.7 % is introduced by assuming that a channel's SRFs are constant.

The total difference of both methods is depicted in Fig. 5.6b. An error of up to 0.9 % is introduced if the approach from Sec. 5.2.2 is used.

5.3.2 Radiometric Calibration Results

The detector temperature during the RASTA measurements was 32 °C. We use this value as reference temperature T_{ref} in Eq. (3.6). Hence, every signal to which the temperature

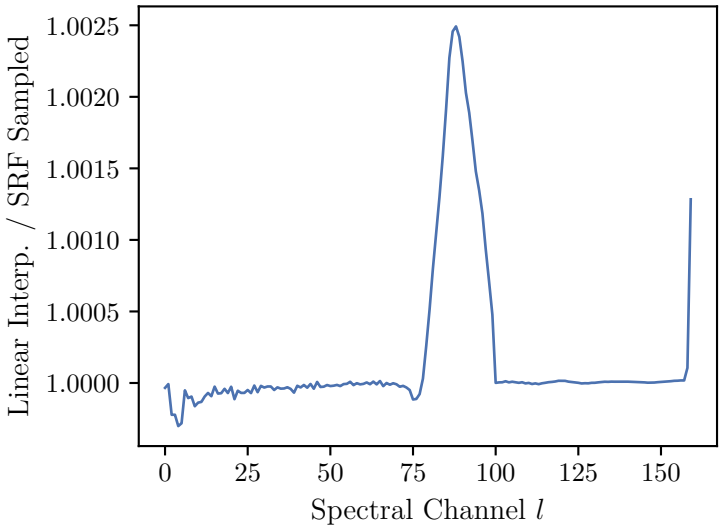

Figure 5.5: Ratio between the spectral radiance of RASTA, linearly sampled with the center wavelengths and convolved with the SRFs of spatial column 800 of the HySpex instrument. The difference of up to 0.25 % that is visible at the center channels is caused by the asymmetric shape of the SRFs there.

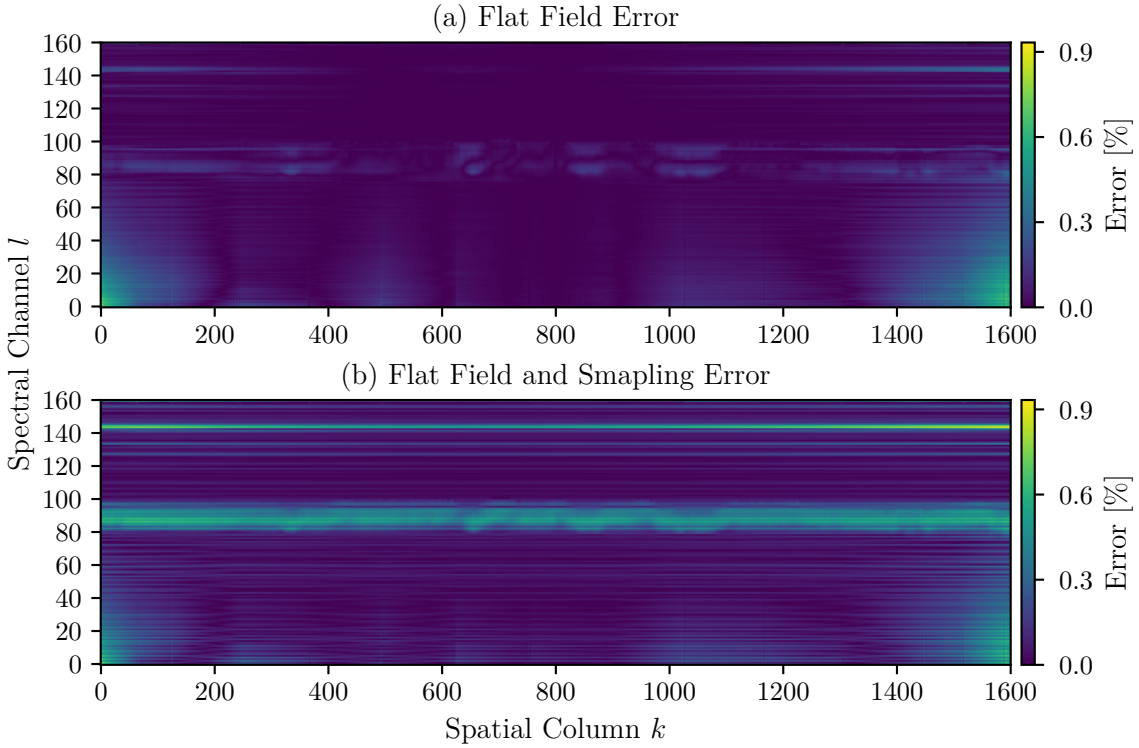

Figure 5.6: (a) Potential errors of flat fielding measurements if difference of spectral response functions in one spectral channel are not considered. (b) Potential errors of (a) with sampling errors as shown in Fig. 5.5.

correction is applied is corrected to the temperature at radiometric calibration.

The radiometric response is shown in Fig. 5.7. The maximum response is between 500 nm and 600 nm, while it drops to significant lower values toward the lower and higher wavelengths. Between channel 70 and 90, the influence of the edge of the order sorting filter is visible, compare Sec. 4.7.2. Over the whole spectral range the minimum response is approximately 70 % of the maximum response. The relative radiometric response is depicted in Fig. 5.8. It can be seen that the response on the left detector half is up to 30 % higher than on the right half and drops to 70 % of the mean response toward the left and right detector edges.

Surprisingly, the uncertainty derived by the Monte Carlo simulation is almost identical to uncertainty of the RASTA calibration, see Fig. 5.7. This indicates that the wavelength uncertainty of the SRF sampling points is completely negligible. Also, the temperature uncertainty has a minor influence on the result of the radiometric calibration, which is visible in slightly increased uncertainty toward higher channel numbers, see Fig. 5.7. Additionally, the flat distribution of the temperature uncertainty has a negligible effect on the distribution of the data from the Monte Carlo simulation and can still be assumed to be normally distributed. Due to aging of RASTA's calibration lamp and possible misalignment of the HySpex instrument, we add an additional uncertainty of 0.5 %. Considering this additional uncertainties, we specify the uncertainty of the radiometric calibration with 2 % ($k = 2$).

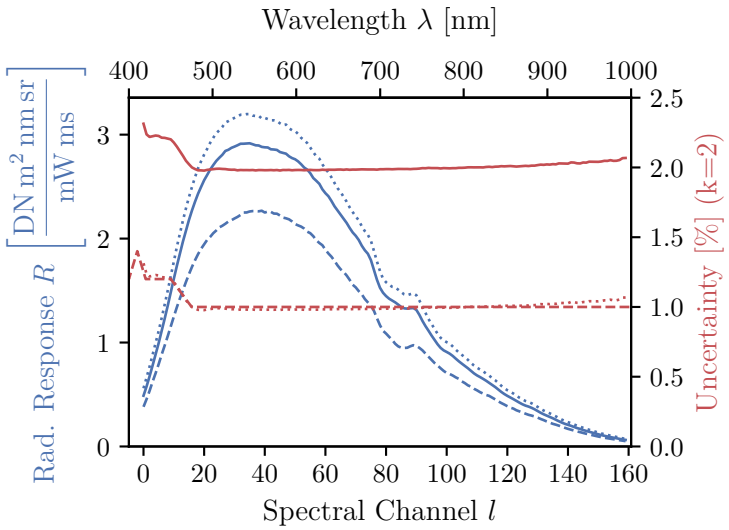

Figure 5.7: (blue solid) Radiometric response averaged over all spatial columns. (blue dashed) Maximum radiometric response. (blue dotted) Minimum radiometric response. (red dotted) Uncertainty of radiometric response averaged over all spatial columns, as determined with the Monte Carlo simulation. (red solid) Uncertainty of (red dotted) plus a potential error of 0.5 % due to lamp aging and alignment errors. An overall uncertainty of 2 % ($k = 2$) can be assumed. (red dashed) Uncertainty of RASTA calibration.

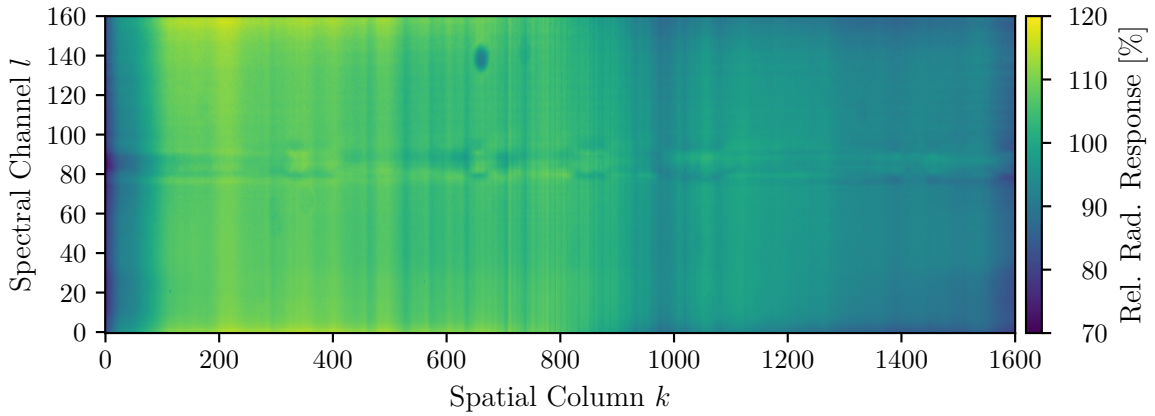

Figure 5.8: Relative radiometric response. Each channel is referenced to its mean value. The response on the left detector half is up to 30 % higher than on the right half and drops to 70 % of the mean response towards the left and right detector edges.

5.3.3 Polarization Sensitivity Results

The results of the polarization measurements are shown in Fig. 5.9. As it can be seen, the polarization sensitivity ranges from 0 % to a maximum value of 6.8 %. The polarization sensitivity is vertical to the slit for channel number below 60 and changes it orientation rapidly by 90° above channel 60.

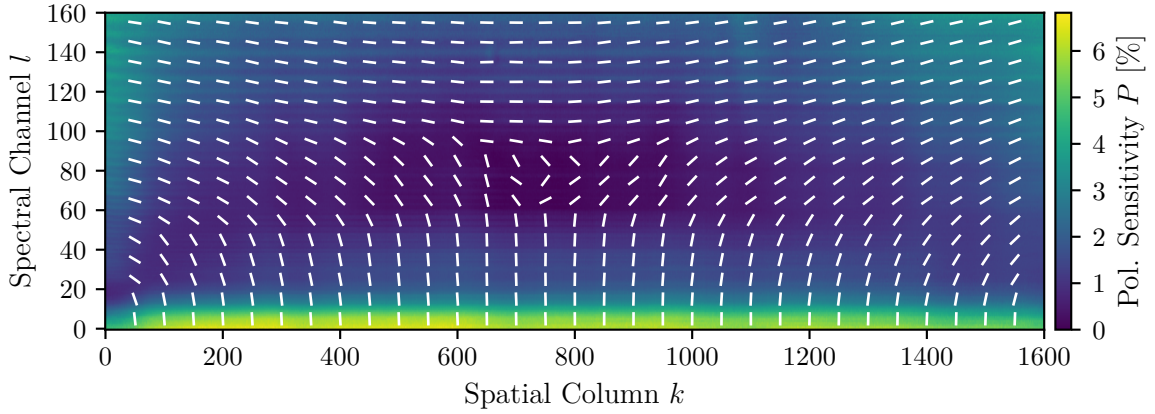

Figure 5.9: Polarization sensitivity of each pixel and orientation of the maximum polarization sensitivity relative to the HySpex VNIR-1600 slit (white lines).

5.4 Summary

- For the radiometric calibration, we use the secondary radiometric standard RASTA, which consists of a diffusely scattering plaque illuminated with a lamp. The calibration uncertainty of RASTA is approximately 1 % ($k = 2$) over the spectral range from 400 nm to 1000 nm.
- The calibrated radiance field of RASTA has a limited area and solid angle. Hence, only the center pixels of imaging spectrometers can be directly calibrated.
- A second calibration step is required to calibrate all pixels relative to the center pixels. For this purpose, we use an integrating sphere.
- The calibration data of RASTA is sampled with a sampling distance of 25 nm over most of the spectral range. We investigated the influence of linear and cubic spline interpolation of the sampling points using a Planck curve similar to the RASTA spectrum. The linear interpolation introduces systematic errors of up to 0.4 % while the error of the spline interpolation is negligible.
- We investigated two data evaluation methods. The first is a classical approach, where the calibration spectrum of the radiometric standard is interpolated at the center wavelengths and for the relative calibration of all pixels constant channel SRFs are assumed. With the second method, the sampling of the calibration spectrum and the relative pixel calibration takes the SRF shapes into account. The first method introduces systematic errors of up to 0.9 %.
- We use Monte Carlo simulations to determine the uncertainty of the radiometric calibration. Uncertainties due to detector temperature and spectral calibration are negligible compared to RASTA's uncertainties.
- Accounting for uncertainties due to lamp aging and alignment errors of the instrument on RASTA, we calculated an absolute radiometric uncertainty of 2 % ($k = 2$).
- The polarization sensitivity ranges from 0 % to 6.8 % and is below 2 % for most parts of the detector.

6

Transformation of Geometric and Spectral Pixel Properties

Contents

6.1 Introduction 96
6.2 Pixel Response Function Transformation 96
6.3 Transformation Matrix Constraints 98
6.4 Uncertainty Propagation 98
6.5 Regularization Matrix 99
6.6 Virtual Sensors 99
6.7 Generation of Transformation Matrices 101
6.8 Performance Tests 104
6.9 Summary 111

6.1 Introduction

As we have seen in chapter 4, the HySpex instrument suffers from optical distortions like smile, keystone and non-uniform shapes and resolutions of the response functions that change within a few pixels. Although we can assign to each pixel its distinct properties, it makes using such data for further analysis complicated and cumbersome. Many algorithms cannot handle pixel individual response functions and typical methods like Fourier analysis cannot be applied on such data. Therefore, the response functions are often assumed to be constant, which in turn leads to errors in data processing.

In this chapter, we propose a novel method that allows sensor A images to be transformed into images with properties of a sensor B considering pixel-specific image properties. This is performed by applying a transformation matrix on sensor A images that maps every pixel of sensor B to the set of pixels of sensor A. Sensor B can either be a distortion-free version of sensor A or another instrument. The latter allows comparing images acquired with different sensors. The method is basically a generalization of the well-known Wiener deconvolution for sensors that exhibit a rapid pixel-to-pixel variation of geometric or spectral responsivity. Though developed for correcting image distortions in imaging spectrometers, the presented algorithm is very general in nature. In fact, it should be applicable to almost any ground-based, air- and spaceborne camera and imaging spectrometer. In the following, we give an overview of the necessary equations to correct optical distortions. A mathematical in-depth analysis of the method can be found in [82].

Although our method can deal with three-dimensional PRFs, we do not perform a transformation of the along-track ARF, since every image is smeared in along-track direction due to sensor movement. The degree of smearing is dependent on the speed in along-track direction, target distance, frame rate, and other movements of the instrument. Hence, this would introduce a new level of complexity. However, such effects are usually treated during geometric processing, which is typically performed after the calibration process.

6.2 Pixel Response Function Transformation

Based on Eq. (2.21), the process of acquiring a radiometrically calibrated image L_i^A of spectral radiance L_λ with a sensor A that has the PRFs f_i^A and M pixels can be expressed as

$$L_i^A = \int_0^{2\pi} \int_0^{\infty} f_i^A(\beta, \lambda) L_\lambda(\beta, \lambda) \, \mathrm{d}\lambda \, \mathrm{d}\beta, \qquad i = 1, \ldots, M, \tag{6.1}$$

where i is the continuous counting pixel index over all instrument pixels (spectral and spatial). In the same way, the image L_j^B of a sensor B with PRFs f_j^B and M' pixels of the same spectral radiance L_λ is

$$L_j^B = \int_0^{2\pi} \int_0^{\infty} f_j^B(\beta, \lambda) L_\lambda(\beta, \lambda) \, \mathrm{d}\lambda \, \mathrm{d}\beta, \qquad j = 1, \ldots, M'. \tag{6.2}$$

For the further formalism we introduces the vectors

$$\boldsymbol{L}^A := \left(L_1^A, \ldots, L_M^A\right)^T \tag{6.3}$$

$$\boldsymbol{L}^B := \left(L_1^B, \ldots, L_{M'}^B\right)^T. \tag{6.4}$$

The objective is now to convert images $\boldsymbol{L}^A$ of sensor A into images $\boldsymbol{L}^B$ of sensor B. For this purpose we use a transformation matrix $\boldsymbol{K}$ that is applied on $\boldsymbol{L}^A$ by

$$\boldsymbol{L}^B = \boldsymbol{K} \cdot \boldsymbol{L}^A. \tag{6.5}$$

As it can be seen, the matrix $\boldsymbol{K}$ maps each pixel of sensor A individually to the set of pixels of sensor B. Of course such a matrix can only exist if the PRFs f^B of sensor B overlap with the response functions f^A of sensor A.

In a contiguously sampled sensor A the adjacent PRFs overlap. Hence, each pixel has a certain relationship to the other pixels of the sensor. This relationship is the cross-correlation. The cross-correlation matrix of sensor A and itself is

$$\boldsymbol{C}_{ii'}^{AA} = \int_0^{2\pi} \int_0^{\infty} f_i^A(\beta, \lambda) f_{i'}^A(\beta, \lambda) \, \mathrm{d}\lambda \, \mathrm{d}\beta. \tag{6.6}$$

The pixels of sensor B also correlate with pixels of sensor A, given that they have overlapping properties. The cross-correlation matrix of sensor B and A is

$$\boldsymbol{C}_{ji}^{\mathrm{BA}} = \int_0^{2\pi} \int_0^{\infty} f_j^B(\beta, \lambda) f_i^A(\beta, \lambda) \, \mathrm{d}\lambda \, \mathrm{d}\beta. \tag{6.7}$$

Any transformation of sensor A image vectors $\boldsymbol{L}^A$ to sensor B image vectors $\boldsymbol{L}^B$ involves also a transformation of the cross-correlation matrix $\boldsymbol{C}^{AA}$ to $\boldsymbol{C}^{BA}$. An formal derivation of this argument can be found in [82]. Consequently, if we apply the transformation matrix $\boldsymbol{K}$ on the cross-correlation matrix $\boldsymbol{C}^{AA}$ we obtain the cross-correlation matrix $\boldsymbol{C}^{BA}$:

$$\boldsymbol{C}^{BA} = \boldsymbol{K}\boldsymbol{C}^{AA}. \tag{6.8}$$

Hence, we can derive $\boldsymbol{K}$ from the inversion of Eq. (6.8), which yields

$$\hat{\boldsymbol{K}} = \arg\min_{\boldsymbol{K}} \left\{ \left\| \boldsymbol{K}\, \boldsymbol{C}^{AA} - \boldsymbol{C}^{BA} \right\|_2^2 \right\}, \tag{6.9}$$

where $\hat{\boldsymbol{K}}$ symbolises the least squares estimator for the matrix $\boldsymbol{K}$ and $\|\cdot\|_2$ is the Euclidean norm.

Unfortunately, this problem tends to be ill-posed, which means that the solutions of $\boldsymbol{K}$ are ambiguous. By assuming a certain degree of "smoothness" of the PRFs we can add a

Tikhonov regularization term [83–86] to the equation, which yields

$$\hat{\boldsymbol{K}} = \arg\min_{\boldsymbol{K}} \left\{ \left\| \boldsymbol{K}\,\boldsymbol{C}^{AA} - \boldsymbol{C}^{BA} \right\|_2^2 + \mu^2 \|\boldsymbol{K}\boldsymbol{\Gamma}\|_2^2 \right\} \tag{6.10}$$

$$= \boldsymbol{C}^{BA}\,\boldsymbol{C}^{AA} \left(\boldsymbol{C}^{AA}\boldsymbol{C}^{AA} + \mu^2 \boldsymbol{\Gamma}^\dagger \boldsymbol{\Gamma} \right)^{-1}. \tag{6.11}$$

where $\hat{\boldsymbol{K}}$ symbolizes the least square estimation of $\boldsymbol{K}$, $\boldsymbol{\Gamma}$ is the Tikhonov matrix, and μ is the regularization parameter. Both can be chosen to tune the balance between the data fidelity and the penalization. Please note that the equation can be solved independently for each row of $\hat{\boldsymbol{K}}$ and $\boldsymbol{C}^{BA}$ and therefore also for each pixel of sensor B.

6.3 Transformation Matrix Constraints

As discussed in Sec. 2.5, the PRFs are normalized. The normalization condition Eq. (2.20) can be used to infer a constraint on the rows of the kernel matrix $\boldsymbol{K}$. Assuming a homogeneous, spectrally flat illumination $\left(L_\lambda(\beta,\lambda) = L^{\text{flat}} = \text{const.}\right)$ on both sensors, we obtain the signals

$$L_i^A = L_\lambda^{\text{flat}} \tag{6.12}$$

$$L_j^B = L_\lambda^{\text{flat}}. \tag{6.13}$$

Insertion into Eq. (6.5) immediately leads to

$$\sum_{i=1}^{M} K_{ji} = 1. \tag{6.14}$$

In other words, the sum over each row of the transformation matrix $\boldsymbol{K}$ has to be unity. This constraint can be used to normalize the kernel to suppress numerical artifacts.

6.4 Uncertainty Propagation

If we interpret the measurement $\boldsymbol{L}^A$ as random variable with expectation value $E\left[\boldsymbol{L}^A\right] = \bar{\boldsymbol{L}}^A$ and covariance matrix

$$\Sigma_{ii'}^A = E\left[\left(L_i^A - \bar{L}_i^A \right) \left(L_{i'}^A - \bar{L}_{i'}^A \right) \right] \tag{6.15}$$

then $\boldsymbol{L}^B$ is also a random variable with expectation value, i.e. mean, $E\left[\boldsymbol{L}^B\right] = \boldsymbol{K} \cdot \bar{\boldsymbol{L}}^A$ and covariance matrix

$$\boldsymbol{\Sigma}^B = \boldsymbol{K}\boldsymbol{\Sigma}^A\boldsymbol{K}^T. \tag{6.16}$$

Eq (6.16) can be used to propagate the uncertainties of measurement $\boldsymbol{L}^A$ to measurement $\boldsymbol{L}^B$.

6.5 Regularization Matrix

Following [62], we chose a second order differential operator as basis for the regularization matrix $\mathbf{\Gamma}$. The equivalent operator $\boldsymbol{d}$ for the discrete convolution of a two-dimensional image is

$$\boldsymbol{d} = \begin{bmatrix} 0 & -1 & 0 \\ -1 & 4 & -1 \\ 0 & -1 & 0 \end{bmatrix}. \tag{6.17}$$

The second-order differential operator $\boldsymbol{d}$ penalizes high frequencies. We choose this operator since we can assume that the PRF cross-correlation matrices $\boldsymbol{C}^{AA}$ and $\boldsymbol{C}^{BA}$ and therefore also the transformation matrix $\boldsymbol{K}$ have a certain degree of "smoothness."

The $\boldsymbol{d}$ operator translates to matrix representation by

$$\mathbf{\Gamma}_{ii'} = \begin{cases} -1 & \text{for } i = i' - M_\mathrm{z} \\ -1 & \text{for } i = i' - 1 \neq kM_\mathrm{z} \\ 4 & \text{for } i = i' \\ -1 & \text{for } i = i' + 1 \neq kM_\mathrm{z} + 1 \\ -1 & \text{for } i = i' + M_\mathrm{z} \\ 0 & \text{else} \end{cases}, \tag{6.18}$$

where M_z is the number of spectral channels. The expressions $i'-1 \neq kM_\mathrm{z}$ and $i'+1 \neq kM_\mathrm{z}+1$ are necessary to account for row switching. Otherwise, the most left pixel of a row in the 2D-image would regularize the first pixels of the next row and vice versa.

6.6 Virtual Sensors

With the proposed method, we can convert images into data of virtual sensors with desired parameters. To test the performance of the algorithm, we specify three virtual sensors with PRFs $f^B(\beta, \lambda)$ that use Gaussian functions h, see Eq. (3.18), for the angular and spectral responses

$$f^B_{kl}(\beta, \lambda) = h(\beta, \beta^B_{\mathrm{c}_k}, \Delta\beta^B_k) h(\lambda, \lambda^B_{\mathrm{c,l}}, \Delta\lambda^B_l), \tag{6.19}$$

Table 6.1: Overview of the virtual sensors that are used for testing the transformation algorithm.

Virtual Sensor	1	2	3
Source Sensor	HySpex VNIR	HySpex VNIR	Interpolated from HySpex VNIR
Spectral Range λ_c [nm]	417.4 to 993.4	417.40 to 993.4 linear	417.4 to 993.4 linear
Spectral Res. $\Delta\lambda$ [nm]	4.1 to 6.7	5.0	5.0
Spatial Range β_c[mrad]	-287.1 to 313.3	-287.1 to 313.3	-287.1 to 313.3
Spatial Res. $\Delta\beta$ [mrad]	0.32 to 0.60	0.87	0.87
Spatial Columns M_y	1600	1600	3200
Spectral Channels M_z	160	160	320

where $\Delta\beta^B$ and $\Delta\lambda^B$ are the spectral and geometric resolution interpreted as the FWHMs and β_c^B and λ_c^B are the center angle and center wavelength, respectively. We use Gaussians since these functions are often used to describe the response functions of imaging spectrometers and Gaussian response functions are completely described by a center and a FWHM value. The three virtual sensors have the following properties:

- Virtual sensor 1:
  The source sensor is the HySpex VNIR-1600, represented by its PRFs f^A. As parameters for Eq. (6.19) we calculate the mean center wavelength and mean resolution of each channel by

$$\lambda_{\mathrm{c},l}^B = \frac{1}{M_\mathrm{y}} \sum_{k=1}^{M_\mathrm{y}} \lambda_{\mathrm{c},kl}^A, \tag{6.20}$$

$$\Delta\lambda_l^B = \frac{1}{M_\mathrm{y}} \sum_{k=1}^{M_\mathrm{y}} \Delta\lambda_{kl}^A, \tag{6.21}$$

  where M_y is the number of spatial columns. The result is an individual Gaussian SRF for each channel where the smile and the resolution differences are corrected. In the same manner, we derive the across-track center angle and resolution by

$$\beta_{\mathrm{c},k}^B = \frac{1}{M_\mathrm{z}} \sum_{l=1}^{M_\mathrm{z}} \beta_{\mathrm{c},kl}^A, \tag{6.22}$$

$$\Delta\beta_k = \frac{1}{M_\mathrm{z}} \sum_{l=1}^{M_\mathrm{z}} \Delta\beta_{kl}^A, \tag{6.23}$$

  resulting in individual Gaussian ARFs for each spatial column with corrected keystone and resolution differences.

- Virtual sensor 2:
  As for virtual sensor 1, the source sensor is the HySpex VNIR-1600. Virtual sensor 2 is a trade-off between minimizing resampling errors and preserving resolution. The resolution respectively FWHM of all virtual SRFs is $\Delta\lambda^B = 5\,\mathrm{nm}$, while the center wavelength of each spectral channel is constant, changing linearly from channel 0 to 159 from 417.4 nm to 993.4 nm:

$$\lambda_{\mathrm{c},l}^B = 417.4\,\mathrm{nm} + \frac{576.0\,\mathrm{nm}}{160}\, l. \tag{6.24}$$

  Since the angular range deviates strongly from a linear distribution, we use the center angles of channel 80 of the real sensor as the center angles for all other elements of the same spatial column:

$$\beta_{\mathrm{c},k}^B = \beta_{\mathrm{c},kl=80}^A. \tag{6.25}$$

  As the HySpex VNIR-1600 along-track resolution width is twice of the across-track resolution width [11, 12], we decide to double the across-track resolution width as well. Thus, the target angular resolution is $\Delta\beta^A = 0.87\,\mathrm{mrad}$.

- Virtual sensor 3:

In this case, the source sensor is an artificial sensor with twice as many spatial columns and spectral channels as the HySpex VNIR-1600, totaling four times more detector elements. The additional PRFs are interpolated from the PRFs of the HySpex instrument, resulting in identical geometric and spectral resolution but a doubled spectral and spatial sampling. This resembles a sensor which is at the time of writing purchased by DLR and which has the same optics as the HySpex VNIR-1600 but a different detector with higher pixel density. Besides the higher pixel count and therefore doubled sampling ratio, the virtual target sensor has the same properties as virtual sensor 2.

An overview of these three virtual sensors is given in Table 6.1.

6.7 Generation of Transformation Matrices

Before determining the cross-correlations, we calculate the discrete representations of the response functions with the trapezoidal rule. Since this process may introduce additional noise, i.e., the integral of the discrete responses differ slightly from the actual integral, we normalize the results to unity. Then for each virtual sensor, the cross-correlation matrices $\boldsymbol{C}^{\mathrm{AA}}$ and $\boldsymbol{C}^{\mathrm{BA}}$ are calculated according to Eq. (6.6) and (6.7), respectively.

To limit the computation time and memory usage, we define subkernels for each pixel of sensor B. The two-dimensional representation $\boldsymbol{K}^{sub}$ of a subkernel of pixel j of sensor B is defined as

$$K_{jkl}^{sub} = \begin{bmatrix} K_{j1} & \cdots & K_{j(M_{\mathrm{z}})} \\ \vdots & \ddots & \vdots \\ K_{j[(M_{\mathrm{y}}-1)M_{\mathrm{z}}+1]+1} & \cdots & K_{j(M_{\mathrm{y}}M_{\mathrm{z}})} \end{bmatrix}. \tag{6.26}$$

We limit the size of the subkernels for test sensor 1 and 2 to 19 spatial columns $\times$ 31 spectral channels and for test sensor 3 to 21 $\times$ 43 pixels. This can be done due to the limited extend of the PRFs. In the same manner, the extent of C^{AA} and C^{BA} is limited. These cropped matrices are then used to solve the linear equation system individually for each sensor B pixel using Eq. (6.11). The use of subkernels becomes especially necessary for instruments that have a large number of pixels. For instance, in case of the HySpex VNIR-1600 the cross-correlation matrix $\boldsymbol{C}^{AA}$ would otherwise consist of $(1600 \times 160)^2$ elements.

We use a regularization parameter of $\mu^2 = 10^{-11}$. The parameter is found by trial and error, i.e., using the process we describe in Sec. 6.8 and by minimizing the errors between transformed and target image. It turns out that for our cases, the exact value has a minor impact on the result, as the calculated transformation matrix is not very sensitive to the parameter when it is changed by one order of magnitude. For a similar operation, the same was reported in [56]. The value for μ seems to be quite small. Although setting $\mu^2 = 0$ leads to a suitable solution for most pixels, the calculation of a significant amount of subkernels fails.

Since the simulated camera is radiometric calibrated, i.e., the integrals of the PRFs are normalized to unity, we apply Eq. (6.14) on the transformation matrix $\boldsymbol{K}$. This reduces errors introduced by the finite accuracy of the numerical calculations.

Figure 6.1 shows the results of the matrices $\boldsymbol{C}^{\mathrm{AA}}$, $\boldsymbol{C}^{\mathrm{BA}}$ and $\boldsymbol{K}$ of virtual sensor 1 in a two-dimensional representation, compare Eq. (6.26). The higher the values of the center pixels of the cross-correlations matrix $\boldsymbol{C}^{\mathrm{AA}}$, the sharper is image A. The highest value has the pixel at spatial column $k = 755$ spectral channel $l = 50$ (755, 50), which is located where the spectral and spatial resolution is very high compared to other detector areas, compare Fig. 4.12 and Fig. 4.10. The other pixels are located at positions where the influence of the order sorting filter appears, see Sec. 4.7.2. The impact of the filter is visible at pixel (755, 80), which causes increased correlations along the spectral axis, due to the broadened SRFs. More apparent is the influence at pixel (1390, 80), where many pixels have an increased correlation along the spectral axis.

The virtual sensor 1 and HySpex cross-correlations $\boldsymbol{C}^{\mathrm{BA}}$ of pixels (755, 50) and (755, 80) show a lower value for the center pixels while the correlations along the spectral axis are increased. This is caused by the reduction of spectral resolution from 3.3 nm to 4.2 nm for pixel (755, 50) and 4.5 nm to 5.2 nm for pixel (755, 80). Effects of the displacement of the PRFs by -0.1 nm respectively -0.2 nm are barely visible in the depiction. At pixel (1390, 80) the spectral resolution width is decreased from 6.2 nm to 5.2 nm while the PRF is displaced by 0.5 nm along the spectral axis. This is indicated by the increased correlation of the channel below the reference channel. The asymmetric shape along the spectral axis of the cross-correlations $\boldsymbol{C}^{\mathrm{BA}}$ at pixel (755, 80), and especially pixel (1390, 80) are caused by the asymmetric shape of the SRFs in this area of detector. For all cross-correlations, the change of the spatial parameters are negligible.

The transformation kernel of pixel (755, 50) shows a bit of a broadening along the spectral axis, which is caused by the decreased spectral resolution. The same is true for pixel (755, 80). Both kernels have elements with values slightly below 0, which is caused by the spectral shift. For pixel (1390, 80) the shape is more complex, due to the shift along the spectral axis by 0.5 nm and the sharpening of spectral resolution, i.e., reduction of the resolution width. The displacement and the sharpening are also the reason for the negative values of several kernel elements.

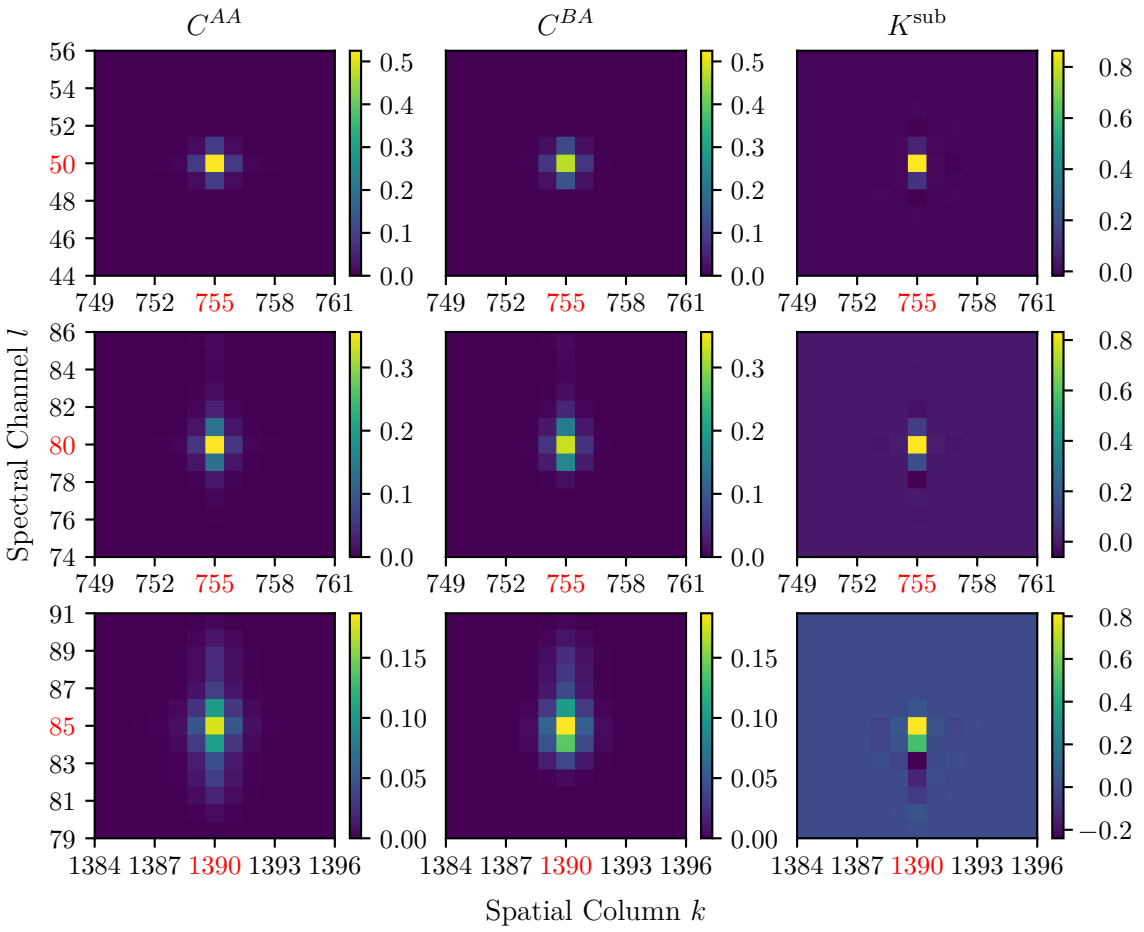

Figure 6.1: Cross-correlations of three different pixels of the HySpex VNIR-1600 and itself C^{AA} (left column) and virtual sensor 1 and HySpex VNIR-1600 C^{BA} (center column). The corresponding transformation subkernels K^{sub} are also shown (right column). The numbers given in red are denoting the coordinates of the references pixels of sensor A. For pixel (755, 50) [755, 80] {1390, 88} the spectral resolution width changes from (3.3 nm) [4.5 nm] {6.2 nm} to (4.2 nm) [5.2 nm] {5.2 nm} and the PRF is displaced by (−0.1 nm) [−0.2 nm] {0.5 nm}.

6.8 Performance Tests

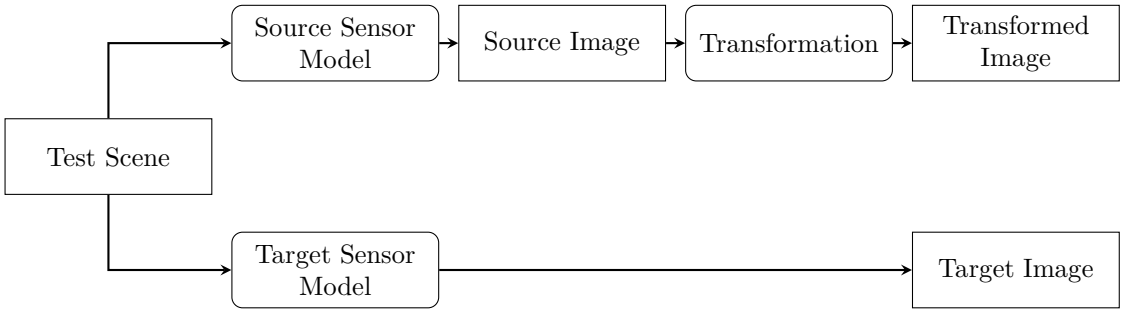

Figure 6.2: Method of performance comparison. A test scene is sampled with the PRFs of the source and the target sensor creating the source and target image, respectively. The source image is then transformed to an image with properties close the target image. Finally, the transformed and target image are compared.

To check the performance of the algorithm, we use the procedure visualized in Fig. 6.2. Test scenes 1 and 2 defined in Appendix A are sampled with the PRFs of the A sensors and with the PRFs of the virtual B sensors that we defined in Sec. 6.6 using Eqs. (6.1) and (6.2). The source images are then converted to the three virtual sensors by applying the according transformation matrices following Eq. 6.5. Additionally, a conversion to the center angles and wavelengths of sensor 1 is performed by cubic spline interpolations, which is the originally used method for keystone and smile correction in DLR's HySpex VNIR-1600 calibration software [12]. Of course, with the spline interpolation the resolution of the PRFs is not altered in a defined way. Hence, we perform the cubic spline interpolation only for sensor 1, where the angular and spectral resolution is the average of each spatial column and spectral channel, respectively. For the other sensors, the results would be significantly worse. We end up with four test cases, namely each test scene sampled with A sensor PRFs transformed to images of:

a) Virtual sensor 1 using cubic spline interpolation

b) Virtual sensor 1 using a transformation matrix

c) Virtual sensor 2 using a transformation matrix

d) Virtual sensor 3 using a transformation matrix

To judge the quality of the transformed images, we use the the Root Mean Square Relative Error (RMSRE) [54], which is defined as

$$\mathrm{RMSRE} = \sqrt{\frac{1}{M'}\sum_{j=1}^{M'}\left(\frac{L_j^B - L_j^{A\to B}}{L_j^B}\right)^2}, \tag{6.27}$$

where $L_j^{A\to B}$ is the transformed image.

6.8.1 Results for Test Scene 1

The checkerboard pattern of test scene 1 is a very unnatural composition and challenges every algorithm, see Appendix A.1. Although it is very unlikely that such a pattern will occur in reality, it can provide useful information about the performance of the algorithms.

In case a), the RMSRE is 12.2 %, see Fig. 6.3a. The relative errors are not normally distributed and not centered to 0. However, the absolute errors (not shown) are centered to 0 and have a symmetric Gaussian shape. In Fig. 6.4a the two-dimensional representations of the relative errors are depicted. The influence of the edge of the order sorting filter is visible between channel 70 and 90, which deforms the SRFs of these channels, see Sec. 4.7.2.

Using a transformation matrix for the same target sensor—case b)—results in smaller errors that have a more symmetrical distortion with a RMSRE of 7.5 %, see Fig. 6.3b. Remarkable are the smaller errors at the location of the filter edge, see Fig. 6.4b. We assume that this is due to the higher SSR in this area.

In case c), the results are better than for case b), with a RMSRE of 1.9 %, see Fig. 6.3c. The errors are quite evenly distributed over the detector area and the influence of the filter edge is barley visible, see Fig. 6.4c.

With a RMSRE of 0.4 %, the best results are obtained in case d), see Fig. 6.3d. The source and target sensors here have the same resolution as in case c) but twice as many spatial and spectral pixels, respectively. The remaining errors are located next to the right detector edge where the spectral resolution widths are the highest due to the distortions caused by the filter edge, see Fig. 6.4d.

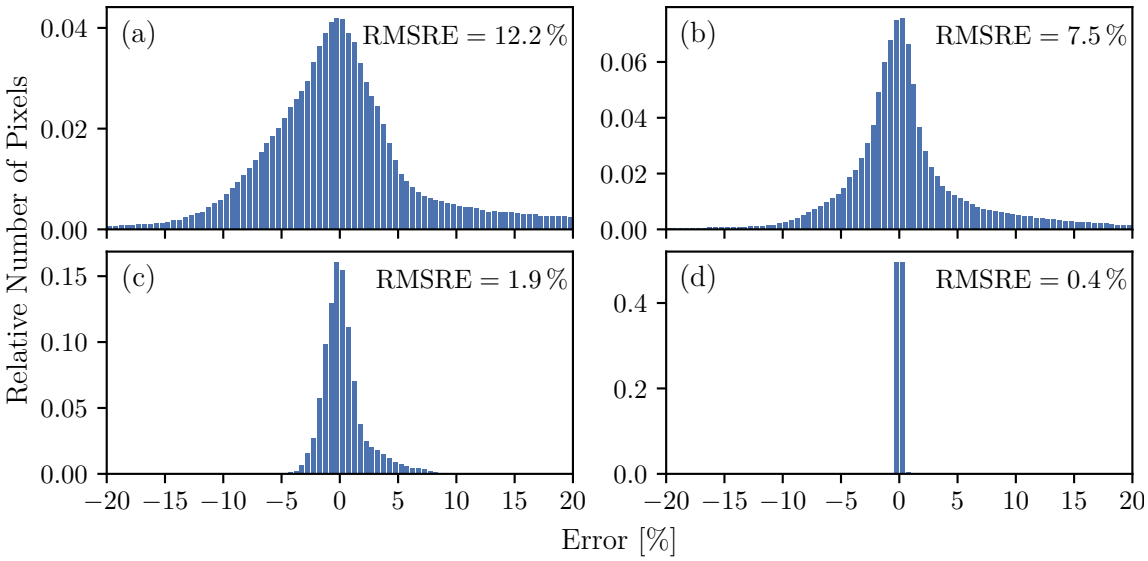

Figure 6.3: Error distributions of transformed image with respect to the target image for test scene 1. In the histograms, each bin is 0.5 % wide.

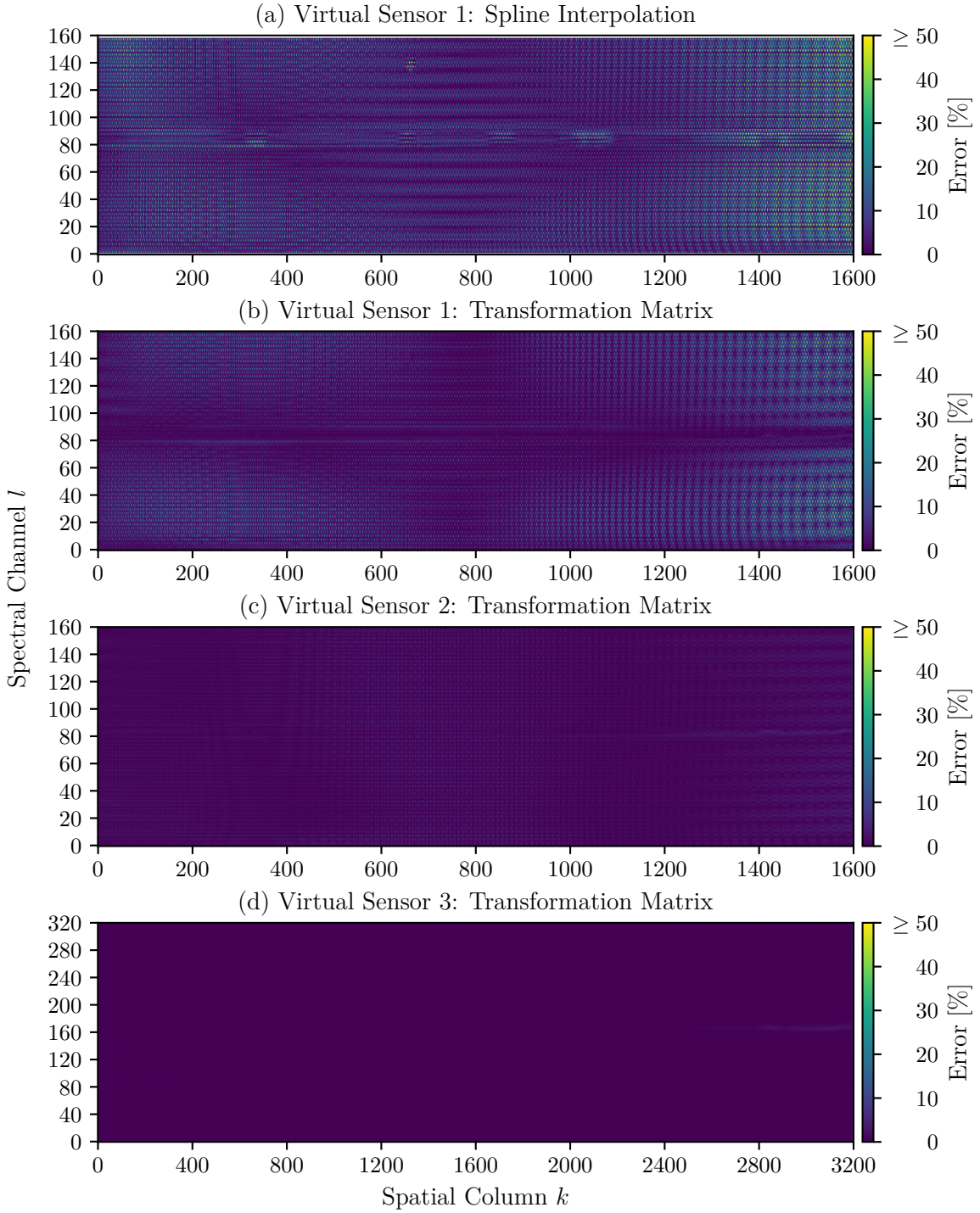

Figure 6.4: Errors of transformed images with respect to the target images for test scene 1. The labels correspond to the test cases. (a) Transformation with spline interpolation. (b) to (d) Transformation with transformation matrix.

6.8.2 Results for Test Scene 2

Test scene 2 is composed of four spectra that resemble a more realistic scenario than test scene 1 does, see Appendix A.2.

In case a), the RMSRE is 2.5 %, see Fig. 6.5a. The largest errors are at the joints between the different spectra, at the oxygen, and the water vapor absorption bands at channel 96 and 143, respectively, see Fig. 6.6a. Just as for test scene 1, the influence of the distorted SRFs at the center channels is visible.

In case b), the RMSRE is 1.6 %, see Fig. 6.5b. As for test scene 1, the performance of the transformation matrix is again better than that of plain cubic spline interpolation. At the spectral filter edge location, the errors are much lower than with cubic spline interpolation, see Fig. 6.6b. Again, the biggest errors are at the transition between two adjacent spectral regions and at the water vapor absorption band at channel 143.

The RMSRE in case c) is 0.8 %, see Fig. 6.5c. Although there are still some errors visible at pixels where two different spectra join, the biggest errors are now at the location of the lowest spectral resolution of the HySpex VNIR-1600 and at the location of the water vapor absorption band, see Fig. 6.6c.

The best performance is achieved—as for scene 1—in case d). The RMSRE with 0.3 % is lower as in case c), see Fig. 6.5d. Almost 75 % of the converted pixels are in an range of ±0.1 % compared to the reference image. The errors at the spatial columns where the different spectra join are almost gone, see Fig. 6.6d. It can be seen that the remaining errors are still located at the edge of the order sorting filter.

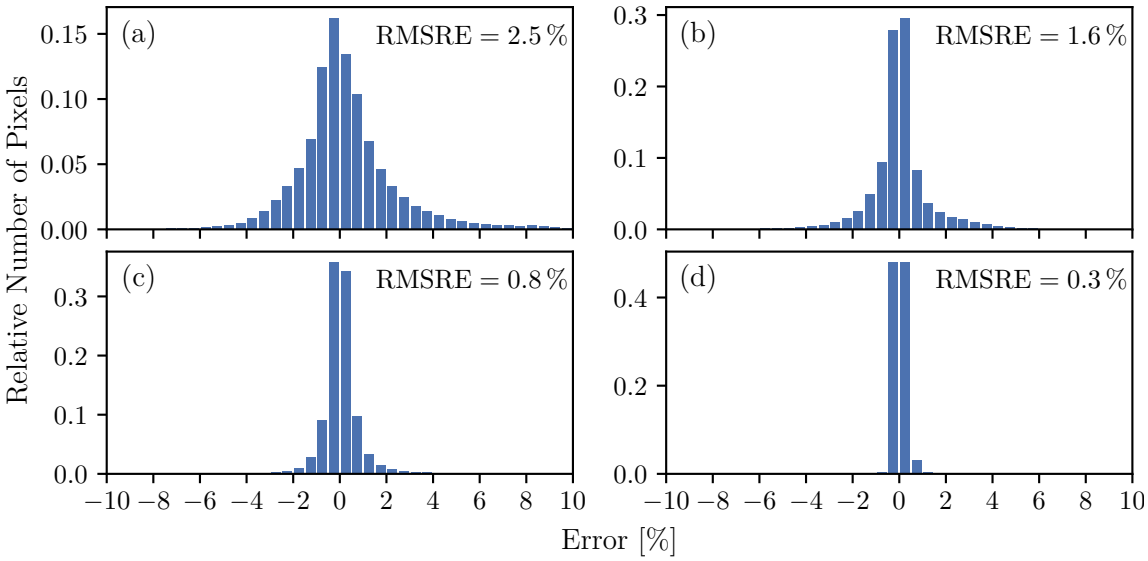

Figure 6.5: Error distributions of transformed images with respect to the target images for test scene 2. In the histograms, each bin is 0.5 % wide.

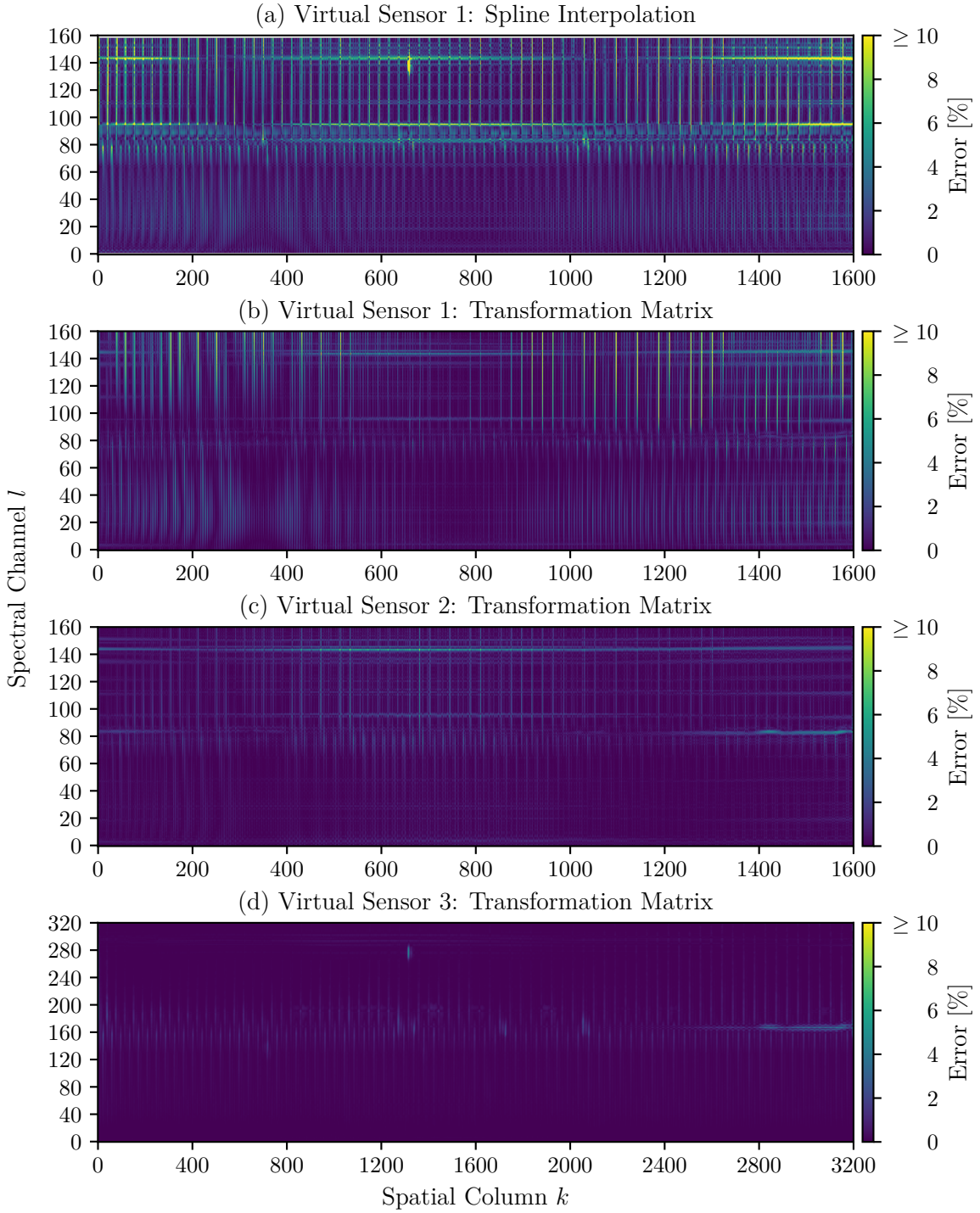

Figure 6.6: Errors of transformed images with respect to the target images for test scene 2. The labels correspond to the test cases. (a) Transformation with spline interpolation. (b) to (d) Transformation with transformation matrix.

6.8.3 Overall Results

In case a), the worst performance is achieved, as the cubic spline interpolation only treats the smile and keystone and neglects—in contrast to the transformation matrix used in case b)—the shape of the PRFs. Although the results in case b) with the transformation matrix method are substantially better than the spline interpolation, a significant error remains. This is mostly caused by the fact that the Nyquist–Shannon sampling theorem is violated [70, 71, 87], as the original system has sampling ratios close to one, see Fig. 4.10 and Fig. 4.12. Additionally, using the average resolution along spatial columns and spectral channels as parameters for the target sensor means that approximately 50 % of the image elements are sharpened, which is an ill-posed problem. In case c), the best result for the HySpex VNIR-1600 are obtained. Decreasing the resolution to 0.87 mrad results in sampling ratios of approximately two for most pixels, values that are close to the Nyquist sampling rate. Along the spectral axis this is not achieved, since the target resolution is 5 nm and some pixels have a resolution of up to 10 nm and are therefore sharpened. The best performance can be expected from a sensor with sampling ratios of greater 2, like in case d). With the exception of the detector locations where the PRFs are sharpened, which is the case for pixels between channel 70 and 90, transformation results are obtained with negligible uncertainties.

6.8.4 Impact on Noise

As we have discussed before, the covariance of a transformed image can be calculated with Eq. (6.16) from the covariance of the sensor A image. Assuming that the noise of the reference sensor is independent between pixels, we can calculate the relative noise of sensor B compared to sensor A by replacing $\boldsymbol{\Sigma}^A$ in Eq. (6.16) with the identity matrix $\boldsymbol{I}_M$:

$$\boldsymbol{\Sigma}^B = \boldsymbol{K}\boldsymbol{I}_M\boldsymbol{K}^T$$

The variances are on the diagonal of the covariance matrix $\boldsymbol{\Sigma}^B$. The relative change of variance and standard deviation compared to the original image is shown in Fig. 6.7. It can be seen that the noise of virtual sensor 1 images does not change considerably. This is due to the fact that the spatial and spectral resolutions are the means of each spatial column and spectral channel, respectively, and are therefore close to the original sensor.

With virtual sensor 2, the noise is almost halved, except at the location of the order sorting filter edge. This is caused by the sharpening of the SRFs in this region, while the resolution width is increased at the other parts of the detector.

The noise of virtual sensor 3 images is below 30 % of the noise of the reference sensor images. This is caused by the higher pixel count compared to virtual sensor 2. Again, the noise level is increased between channels 70 and 90.

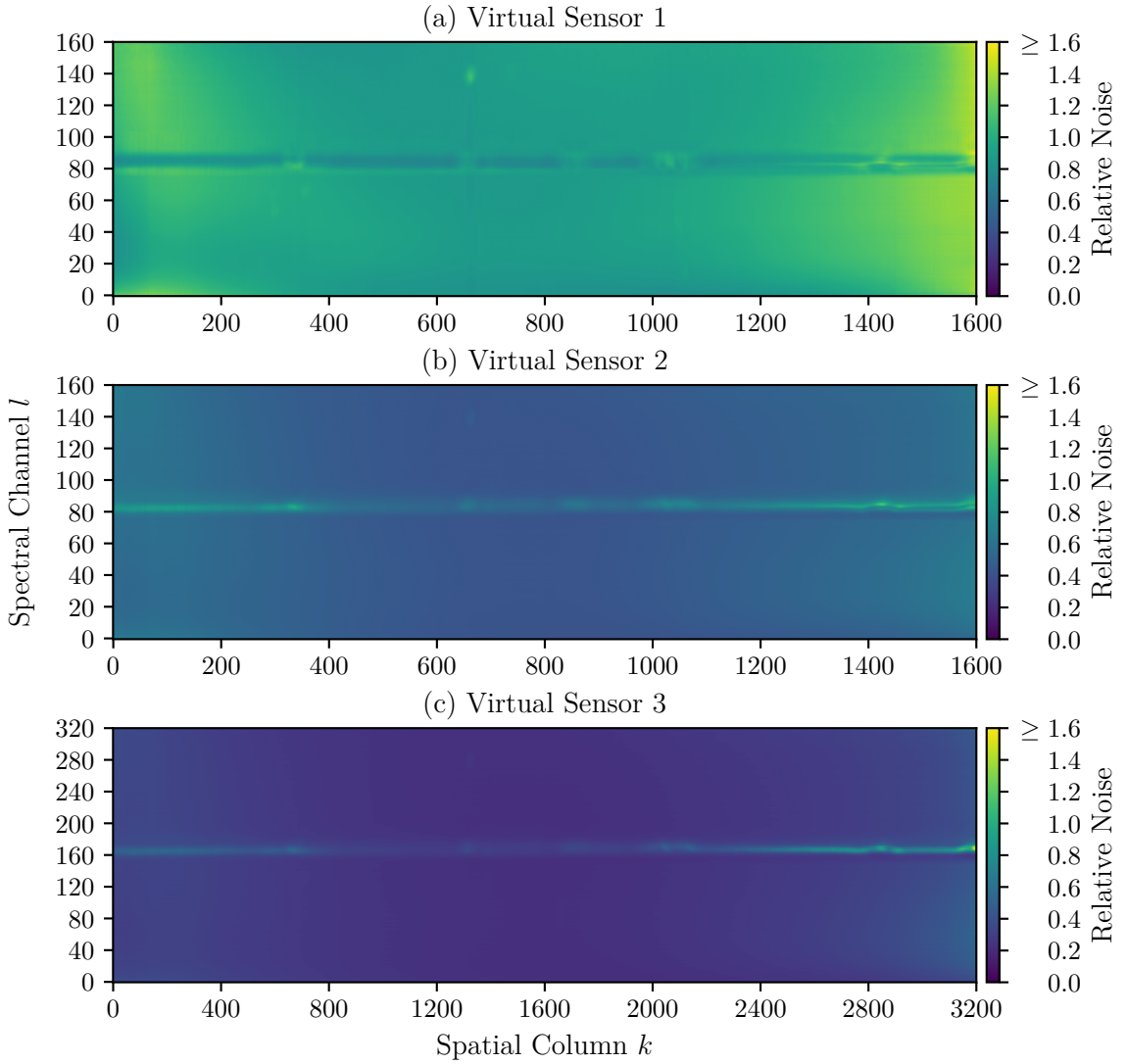

Figure 6.7: Relative noise levels of transformed images compared to the source images. (a) Virtual sensor 1: The noise is quite similar with higher values at ares of decreased PRF resolution widths and lower values at areas of increased resolution widths. (b) Virtual sensor 2: Approximately halved noise level. (c) Virtual sensor 3: Noise level below 30 % at most parts of the detector.

6.9 Summary

- We proposed a novel method for transforming images acquired with an optical imaging sensor A into images with properties of a sensors B.
- Our method can handle highly non-uniform geometric and spectral pixel properties, which are different for every pixel. This is an unique feature.
- Sensor B can be a synthetic system with "idealized" imaging properties without imaging distortions or a real instrument with known system parameters. In the first case, this enables processing methods that required uniform pixel properties, such as Fourier analysis. In the latter case, the method can be used to make images of different instruments comparable.
- The core idea of the method is to apply a linear transformation matrix on sensor A images that maps every pixel of sensor B to the set of pixels of sensor A. This matrix is derived from two cross-correlation matrices: Sensor A and itself, and sensor B and sensor A.
- Since this problem tends to be ill-posed, we assume smooth response functions and use Tikhonov regularization to suppress high frequencies. It turns out that the derived transformation matrix has a low sensitivity to the regularization parameter, which can be varied within an order of magnitude without causing significant changes.
- The transformation matrix needs to be calculated only once and can then be applied to images with low computational cost.
- The covariance of the transformed image can be easily calculated from the covariance matrix of the reference image.
- We performed simulations with three virtual sensors with which we sample two synthetic test scenes. Two virtual sensor have as reference the HySpex VNIR-1600 instrument. A third reference sensor is an interpolated version of the HySpex instrument with twice as much spatial columns and spectral channels but with identical spatial and spectral resolutions. This system is sampled above the Nyquist rate.
- Compared to the previously used cubic spline interpolation for smile and keystone correction, the new approach shows significantly better performance. The errors are up to six times smaller for the HySpex VNIR-1600 instrument.
- The simulations show that images of systems that are sampled above the Nyquist rate can be transformed without significant errors as long as the resolution width is not reduced.
- In certain cases, the noise level can be reduced considerably compared to the reference image, e.g., to a level below 30 % for one of the simulated systems. For the HySpex VNIR-1600, the noise level can be halved when it's data is transformed to one of the virtual sensors.

7

Summary, Conclusion, and Outlook

Contents

7.1 Summary and Description of Calibration Chain 114
7.2 Conclusion 119
7.3 Outlook 120

7.1 Summary and Description of Calibration Chain

The final result of this work is the traceable calibration chain for the HySpex VNIR-1600 instrument, which is depicted in Fig. 7.1, with the main sources of uncertainties, see Table 7.1. Since the chain follows the structure of this work, we discuss each processing step to summarize the results.

The input in the calibration chain are individual frames of raw sensor signals. We derived the noise characteristics of the raw data using the Photon Transfer Curve (PTC) method. The signal dependent noise ranges from 6.4 DN to 46.6 DN ($k = 2$). This leads to a peak SNR of 176, which means that the noise is $\geq$1.14 % ($k = 2$) of the signal.

At first, effects related to the detector are corrected, by subtracting the offset signal, which is caused by an electronic offset from the raw signal. The dark signal does not need to be corrected, since the dark signal is $\ll$0.1 DN in the typical integration time range. Otherwise, the dark signal would have to be considered for the signal non-linearity correction. The offset signal differs between the "left" (spatial column 0 - 799) and the "right" detector half (spatial column 800 - 1599). This is caused by the different readout electronics of both halves. The offset signal is stable with an uncertainty of <0.1 DN.

Non-linearity correction is performed in the next step. We discovered that the signal non-linearity depends on the channel and the detector half and is up to 15 % for the right half. It was measured with a newly developed setup called BALIS that works based on the light-addition method. The setup provides high radiance levels through the Visible and Near-InfraRed (VNIR) region and does not introduce significant systematic errors. We enhanced the light-addition method to allow the calibration with smaller signal level distances than conventionally possible. Investigating the integration time non-linearity, we discovered that the actual integration time has an offset of 25 μs. Additionally, the set integration time between 3500 μs and 8900 μs differ of up to 0.5 % from the actual values. To correct these effects, the integration time is adjusted to the correct values. Validation measurements show that the signal and integration time non-linearities are corrected with uncertainties of $\leq$0.1 %.

After the non-linearity, the smear effect would be corrected. The smear effect is caused by leakage of charge carriers into other pixels during electronic readout along the spectral axis and is common for CCD detectors. Since the readout time is fixed, the effect is more prominent at shorter integration times. Hence, we characterized the effect at integration times shorter than 1000 μs with a high radiance monochromatic light source to obtain a sufficient signal. Unfortunately, the smear effect randomly changes between at least three different patterns after restarting the HySpex acquisition software. Currently, it is not clear what causes this random behavior. Hence, this correction step is not performed at the time of this writing. We therefore recommend using the instrument with integration times greater than 10 ms to reduce smearing errors. However, we developed a method to separate stray light from the smear effect, so that the effect can be characterized if the source of the random behavior is found.

The next processing step involves the correction of radiometric responsivity changes with the detector temperature. The CCD detector of the HySpex instrument is a silicon semiconductor

that has a temperature dependent responsivity. The effect is wavelength dependent with a responsivity change of up to 0.6 %/K. To measure this effect, we placed the switched-off instrument in front of an illuminated integrating sphere. After power-on, the change in responsivity was measured until thermal stabilization. Since the detector temperature sensor has a resolution of only 1 K the accuracy of the correction is limited to 0.3 % in the worst case.

The correction of stray light is performed as it is published in [18]. It is the only major aspect that we did not cover in this thesis. The measurements were performed at PTB using the Pulsed Laser for Advanced Characterization Of Spectroradiometers (PLACOS) setup. Unfortunately, the uncertainties of the stray light correction are currently unknown.

For correcting optical distortions the spectral and spatial parameters of an instrument need to be known. Knowledge of the spectral properties is also required for the radiometric calibration of the data.

To measure the spatial proprieties we placed a broadband light source in front of a slit, which was guided via a collimator and a rotary mirror to the sensor aperture. By moving the mirror, the image of the slit was scanned over the detector. Since the whole spectral range of the instrument is covered, each ARF is measured. A cubic spline model was used to model the across-track ARFs of each pixel. The accuracy of the ARF model is 0.006 mrad ($k = 2$), which is 2 % of the smallest ARF resolution width.

With a monochromator setup, the spectral properties of the imaging spectrometer were determined. We calibrated the center wavelength, bandwidth, and relative radiometric output power of the monochromator. The center wavelength calibration was performed with an echelle grating wavelength meter. For this purpose, we have developed a method that allows arbitrary sampling distances of the monochromator wavelength. This is not possible with conventional approaches, which use spectral line lamps directly with a monochromator. The calibration of the wavelength meter itself is traceable to a physical standard in the form of spectral line lamps.

With the monochromator setup, we scan over the wavelength range of the imaging spectrometer to determine its SRFs. The relative radiometric calibration of the monochromator was applied to correct the measured data for the wavelength-dependent monochromator output intensity. Since we could not find an analytical model for the SRFs, we use the measured sampling points as a lookup table and interpolate these with cubic splines in order to have continuously differentiable curves. Because of the limited output radiance of the setup, only a few spatial columns could be illuminated simultaneously. Therefore and due to time constraints, only a limited number of SRFs were measured directly. Consequently, we developed a method to interpolate the response function shapes from the cubic spline models. The results show that at the center channels the SRF shapes are asymmetrically deformed and broadened. This is caused by the edge of a spectral filter, which is mounted on top of the detector to suppress higher diffraction orders of the diffraction grating of the imaging spectrometer. The SRFs shapes change within few spectral channels and spatial columns. We therefore measured the SRFs in the affected detector area at considerably more spatial positions. The error of the SRF model is 0.15 nm ($k = 2$), which is 3 % of the

smallest SRF resolution width.

We derive the PRFs from the ARFs and the SRFs by assuming that they are orthogonal. To judge the accuracy improvement of the cubic spline model based PRFs compared to Gaussian response functions, we compared images sampled with both methods. The conventional Gaussian response model causes systematic errors of up to 20 % in a synthetic test scene based on natural spectra.

For the absolute radiometric calibration, we use the derived SRFs to sample the calibration spectrum of a radiometric standard. The standard has an uncertainty of approximately 1 % ($k = 2$) with a sampling distance of 10 nm to 25 nm. Our tests with a Planck curve similar to the calibration spectrum show that a cubic spline interpolation of the sampling points leads to negligible errors of $\leq$0.03 %. In contrast to conventional methods, we sampled the interpolated calibration spectrum with SRFs. Additionally, the SRFs were also used for the relative spectral calibration. Neglecting the effect of the SRFs for the absolute and relative spectral calibration leads to systematic errors of up to 0.9 %, which are now corrected. To determine the uncertainty of the radiometric calibration, we preformed Monte Carlo simulations. With the results from the Monte Carlo simulations and accounting for additional uncertainty sources, the uncertainty of the radiometric calibration is 2 % ($k = 2$).

Additionally, we investigated the polarization sensitivity of each pixel. For this purpose, we placed a wire-grid polarization filter in front of an integrating sphere. By rotating the filter in discrete steps, we obtained the polarization sensitivity. It ranges from 0 % to 5.2 % for channel 5 and below while being less than 2 % for most parts of the detector.

The product after these processing steps is calibrated at-aperture radiance to whose values individual ARF and a SRF can be assigned.

Obviously, individual geometric and spectral pixel properties make dealing with the data in further processing steps quite complicated. Many algorithms cannot handle pixel-individual response functions and typical methods like Fourier analysis cannot be applied on such data. For this reason, we developed a novel method which allows the transformation of pixel-individual ARFs and SRFs. The spatial and spectral properties of images acquired with a source instrument can be transformed into images with properties from a target instrument with uniform pixel properties. In contrast to existing methods, the response function shapes of each pixel are manipulated individually. In case of the HySpex VNIR-1600 instrument, this is required due to rapid changes of response function shapes at the location of the spectral filter edge. We discussed the mathematical background as well as the propagation of uncertainties of the method. The accuracy of the method depends on the resolution and sampling distance of the source and the target instruments. We use the method to transform HySpex data to smile- and keystone-free images with uniform Gaussian ARFs and SRFs. A test with a scene based on natural spectra leads to errors of 1.6 % ($k = 2$). In comparison, when using cubic spline interpolation to correct smile and keystone distortion, the error is 5 %. For instruments with oversampled response functions, the errors of the method are smaller. As a further result of the transformation, the noise of the target image is reduced to approximately 50 % of the source image noise.

The product after this processing step is at-aperture radiance with homogeneous Gaussian

Table 7.1: Overview of uncertainties of the HySpex VNIR-1600 instrument after calibration.

Parameter	Uncertainty ($k = 2$)	Comment
Noise	6.4 DN to 46.6 DN (≥1.14 %)	Signal dependent
Noise (after distortion correction)	2.6 DN to 18.8 DN (≥0.46 %)	Signal dependent
Offset signal correction	<0.1 %	Negligible
Non-linearity correction t_{int}	<0.1 %	Negligible
Non-linearity correction signal	<0.1 %	Negligible
Smear	Unknown	Scene dependent
Temperature correction	0.0 % to 0.3 %	Channel dependent
Stray light	Unknown	Scene dependent
Spectral calibration	0.15 nm	
Spectral calibration stability	Unknown	
Angular calibration	0.006 mrad	Negligible
Angular calibration stability	Unknown	
Radiometric calibration	2 %	
Polarization	≤ 6.8 %	Scene dependent
Distortion correction	1.6 %	For test scene 2

ARFs and SRFs.

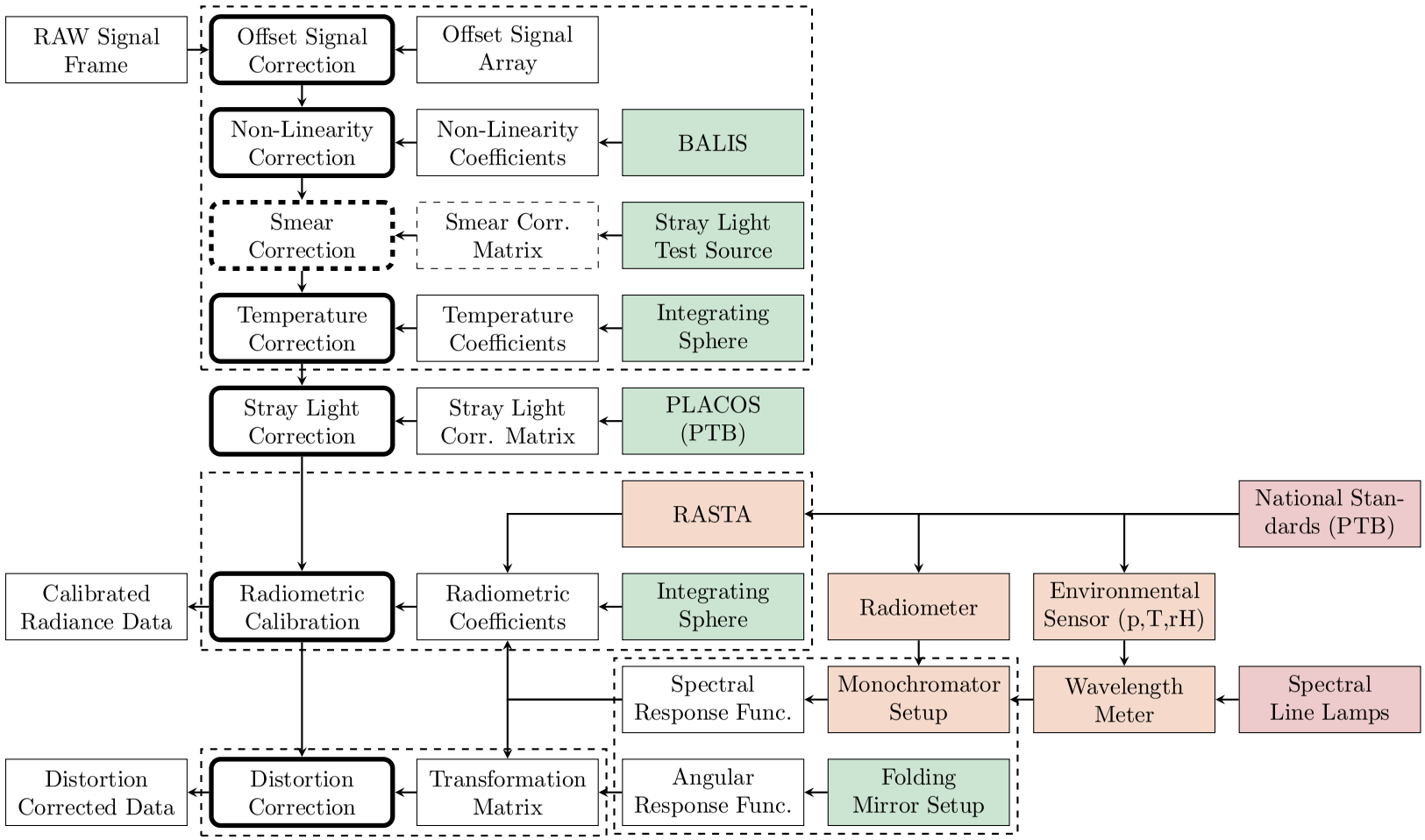

Figure 7.1: Structure and traceability of the calibration processor developed for DLR's HySpex VNIR-1600. RAW signal is converted step by step by different correction processes (second column). Every process needs some sort of calibration data (third column). The calibration data is either based on secondary standards (orange) that are traceable to primary standards (red) or on combinations of measurement methods and setups (green). The dashed boxes indicate the different topics covered in the different chapters in this work. The smear correction is currently not part of the processor, since no smear correction matrix could be determined due to the non-deterministic system behavior.

7.2 Conclusion

This thesis is the result of many laboratory measurements, research and development work. It provides a comprehensive overview of the issues and the challenges that come with calibrating push-broom imaging spectrometers. The developed methods, setups and software will benefit other instruments that are calibrated in DLR's Calibration Home Base (CHB) or in other calibration laboratories.

Overall, the calibration of the HySpex VNIR-1600 instrument, which we used to demonstrate our methods, is significantly improved. The correction of temperature effects is now part of the processing chain. This significantly reduces the measurement uncertainty, which would be dominated by this effect in many instrument channels. In the worst case of a measured in-flight detector temperature of 9° and a detector reference temperature of 32°, the uncorrected systematic error is up to 7 %.

Also, the non-linearity effects are corrected with uncertainties of <0.1 %. The derived linearity is based only on the method and has no over external decencies, such as the linearity of reference radiometers. This has the advantage that validity of the results can be easily checked with the calibration data itself.

The improved spatial and spectral calibration have significant impact in the reduction of systematic measurement errors. The Gaussian response function model previously used for the HySpex VNIR-1600 leads to significant errors, The Gaussian response function model previously used for the HySpex VNIR-1600 leads to significant errors, especially at steep jumps in the measured scenes. The cubic spline-based model that is now used is very general, so that it can be applied for any instrument.

The radiometric calibration is also improved, since systematic errors in the calibration process were able to be identified and eliminated. Further, we can now provide the polarization sensitivity of each pixel. Although the uncertainty due to polarization sensitivity seems to dominate with up to 6.8 %, it must be considered that this is only the case for completely polarized scenes. A lower degree of scene polarization causes obviously fewer errors. Although the scene polarization is usually unknown, assumptions can be made for estimating the polarization uncertainty.

The icing on the cake is definitely the transformation algorithm we have developed in the context of this thesis. Relatively inexpensive imaging spectrometers could provide data comparable to much more costly instruments. In particular instruments that are sufficiently oversampled can benefit from the method. This could lead to a paradigm change in instrument design, where the specifications for ARF and SRF uniformity as well as smile and keystone can be relaxed. Additionally, the method can be used to make data of different instruments comparable, which can be used for cross-calibration, for example. It is possible to provide data products with optimized geometric, spectral, and noise properties depending on the application. The method is not limited to push-broom imaging spectrometers. In fact, it should be applicable to almost any ground-based, air- and spaceborne camera and imaging spectrometer.

7.3 Outlook

Overall, this work a big step toward the Système International d'unités (SI) traceability of data products acquired with imaging spectrometers. As mentioned earlier, there are still aspects remaining which need to be considered to create a completely traceable at-aperture radiance data product.

The calibration of the temperature effects needs to be validated and it would be desirable to cover a wider temperature range. For this purpose, a thermal chamber or box could be used. Such a box was recently built in the context of the CHB and used to calibrate a number of fiber-coupled, non-imaging spectrometers. For calibrating imaging spectrometers, however, some adaptations are necessary because the light from a stable light source must be guided to an instrument aperture from outside the box.

One effect that has a major impact on the measurement uncertainty is the random behavior of the smear effect we discovered for the HySpex VNIR-1600. Further measurements and discussion with the instrument and detector manufacturer are needed to get to the bottom of this problem. We could not find any reports that mention such a random behavior in other detectors and instruments. It is therefore very likely that other detectors do not suffer from this type of problem.

Another aspect that remains is the in-flight validation of the angular and spectral calibration. Methods could be adapted that use atmospheric absorption features to determine spectral shift [40, 55, 88–91]. The angular calibration can be validated by using bright next to dark surfaces [92–94]. Some in-flight measurements with spectral line lamps have been made recently. Unfortunately, we could not cover this experiment in this thesis, and evaluating this data right now is an open topic.

Since stray light manifests in the tails of the PRFs, correcting stray light could be included in the transformation process. This has the advantage that inconsistencies between PRF transformation and stray light correction can be avoided and that the same propagation of uncertainties method can be used.

As the time of writing of this thesis, DLR has received an upgrade of the HySpex VNIR-1600 instrument. The new instrument has a similar optical layout but has a new detector with 3200 spatial columns and 700 spectral channels on the same area as the HySpex VNIR-1600 detector. Since the slit size is unchanged, an Spectral Sampling Ration (SSR) of greater four is expected. This drastically reduces the errors after PRF transformation, as our simulations show. Of course, all other calibration methods shown in this thesis need to be performed with this new instrument.

It would also be desirable to provide not only the uncertainty of single pixels in imaging spectrometer data but also their covariances. Providing these together with the three-dimensional imaging spectrometer data array would be very uneconomical or even impossible, since its size would be the squared number of array elements. Other techniques are conceivable, such as clever calculation of the covariance between certain pixels from a set of variances and correlations along different axes of the data array.

List of Symbols

α	Along-track angle
$\bar{L}$	Expectation value of sampled radiance L
β	Across-track angle
β_c	Across-track center angle
$\Delta\beta$	Across-track angular resolution
$\Delta\lambda$	Bandwidth/spectral resolution
$\delta\lambda$	Spectral step width/spectral sampling interval
δ	Dirac delta peak
ε	Deviation from linearity
η	Quantum efficiency
Γ	Tikhonov matrix
γ	Polarization angle parallel to instrument entrance slit
γ_0	Polarization angle for which S^ph is maximal
λ	Wavelength
λ_c	Center wavelength
$\|\cdot\|_2$	Euclidean norm
$\boldsymbol{\Sigma}$	Covariance matrix
$\boldsymbol{C}^{AA}$	Cross-correlation matrix of sensor A and itself
$\boldsymbol{C}^{BA}$	Cross-correlation matrix of sensor B and sensor A
$\boldsymbol{d}$	Two-dimensional second order differential operator
$\boldsymbol{K}$	Transformation matrix
$\boldsymbol{K}^\mathrm{sub}$	Subkernel of transformation matrix $\boldsymbol{K}$
$\boldsymbol{I}_M$	Identity matrix with $M \times M$ elements
μ	Regularization parameter
σ_d	Dark current noise
σ_ph	Photon shot noise
σ_Q	Quantization noise
σ_r	Read noise
σ_tot	Total instrument noise
$\sqcap$	Boxcar function

τ	Optical transmission function
ζ^{S}	Signal non-linearity
ζ_{D}	Potential well non-linearity
ζ_{gD}	Combined ADC and potential well non-linearity
ζ_{g}	ADC non-linearity
ζ_{t}	Integration time non-linearity
A	Area
A_{d}	Detector area
A_{e}	Entrance aperture area
c	Speed of light
C_T	Temperature coefficient
D	Detector model
E	Expectation
E	Irradiance
e	Error
e^{spline}	Spline model error
e_{nl}	Non-linearity error
f	Pixel response function
f_{ε}	Deviation from linearity function
f_{FWHM}	FWHM function dependent on signal
$f_{\zeta j}$	Signal non-linearity function
g	Gain
h	Gaussian function
h	Planck's constant
I	Current
I^{d}	Dark current
I^{ph}	Photo current
k	Coverage factor
k	Spatial column index
l	Spectral channel index
L^{A}	Radiance sample with sensor A

L^{B}	Radiance sample with sensor B
L^{s}	Sampled radiance
L_λ	Spectral radiance
$L_\lambda^{\mathrm{flat}}$	Flat spectral radiance field
L_{a}	Excitation a
L_{b}	Excitation b
L_{mono}	Relative monochromator spectrum
M	Number of sensor A pixels
m	Number of matching values
M'	Number of sensor B pixels
M_{y}	Number of spatial columns
M_{z}	Number of spectral channels
n	Number of signal levels
N^{nl}	Non-linear potential well fill level
N^{d}	Number of electrons
N^{o}	Electronic offset electrons
N^{ph}	Number of electrons
O	Optical system model
P	Polarization sensitivity
p	Degree of polarization
R	Radiometric response
r	Response
R^{p}	Radiometric response to polarized light
R^{up}	Radiometric response to unpolarized light
S	Signal
S^{nl}	Non-linear signal
S^{smear}	Smear signal
S^{d}	Dark signal
S^{lin}	Linear signal
S^{ph}	Photo signal
T	Temperature

t_{int}	Boxcar function
$t_{\mathrm{int}}^{\mathrm{set}}$	Set integration time
u	Uncertainty
u_{calib}	Calibration uncertainty
V^{ph}	Photo signal factor
V^{smear}	Smear factor
w	Weights
x	Detector and data array axis corresponding to the along-track direction
x'	Object plane axis corresponding to the along-track direction
y	Detector and data array axis corresponding to the across-track direction
y'	Object plane axis corresponding to the across-track direction
z	Data array axis corresponding to wavelength
z'	Axis perpendicular to the object plane, facing away from the sensor

List of Abbreviations

ADC Analog Digital Converter

APEX Airborne Prism EXperiment

ASI Angular Sampling Interval

ASR Angular Sampling Ration

ARF Angular Response Function

BALIS Broadband Attenuable LIght Source

BRDF Bidirectional Reflectance Distribution Function

CCD Charge Coupled Device

CHB Calibration Home Base

DC Dark Current

DLR Deutsches Zentrum für Luft- und Raumfahrt

DN Digital Numbers

ESA European Space Agency

FoV Field of View

FPA Focal Plane Array

FWHM Full Width at Half Maximum

GWU GWU-Lasertechnik Vertriebsges.mbH

GUM Guide to the Expression of Uncertainty in Measurement

IFoV Instantaneous Field of View

ND Neutral Density

NIST National Institute of Standards and Technology

OAPM Off-Axis Parabolic Mirror

PLACOS Pulsed Laser for Advanced Characterization Of Spectroradiometers

PRF Pixel Response Function

PSF Point Spread Function

PTB Physikalisch-Technische Bundesanstalt

PTC Photon Transfer Curve

RASTA Radiometric Standard

RF Response Function

RMSRE Root Mean Square Relative Error

SI Système International d'unités

SIRCUS Spectral Irradiance and Radiance Responsivity Calibrations using Uniform Sources

SNR Signal to Noise Ratio

SRF Spectral Response Function

SLTS Stray Light Test Source

SSI Spectral Sampling Interval

SSR Spectral Sampling Ration

WM Wavelength Meter

VNIR Visible and Near-InfraRed

VIM International Vocabulary of Metrology

List of Figures

1.1 Imaging spectrometers HySpex VNIR-1600 (a) and HySpex SWIR-320m-e (b) installed on a gyro-stabilized mount in a DLR aircraft. 11

2.1 Principle setup of push-broom imaging spectrometers. An objective optics creates an intermediate image from which a slit cuts out a line. This line is a collimated and the spectral components are split perpendicularly to the slit by a dispersing element. Finally, a focusing optics images the collimated and spectrally dispersed beam a Focal Plane Array (FPA). By moving the instrument along x' and continuous data acquisition a three dimensional data array is generated. Figure taken from [67]. 14
2.2 Push-broom imaging spectrometer geometry. A sensor platform, here represented by an aircraft, moves along the x'-axis in along-track direction. The instrument's Field of View (FoV) spans along the y'-axis in across-track direction, with α and β denoting the angular coordinates parallel and perpendicular to the FoV, respectively. The ground pixel area is the area of one geometric line covered during the acquisition of one frame. Please note that in reality the pixel footprints do not have a rectangular shape. Original figure taken from [67]. 15
2.3 Conversion of radiance to digital numbers for a signal location in a scene. Figure taken from [2]. 16
2.4 Slice through an angular axis of a PSF which is the signal created by a point source. The orange dots indicate the signal of each pixel while the blue curves are the PRFs. As it can be seen, the pixel signal corresponds to the value of the PRFs at the intersection which the point source. 19
2.5 Smile and keystone distortions as well as change of PSF resolution shown on idealized FPA grids. Each circle is the FWHM of a PSF. (a) Smile: Change of center wavelength in one channel with spatial position. (b) Keystone: Change of center angle with wavelength. (c) Resolution: Change of spectral and spatial resolution with detector position. (d) Combination of these effects. Figure inspired by [2]. 21
2.6 Example of a Spectral Response Function (SRF) with semi logarithmic representation. Although the response at three times of the FWHM from the center is below 0.01 %/nm, the sum of the response outside of these borders accounts for 2.5 % of the total response. 22
2.7 Example of signal normalized by integration time $S^{\mathrm{ph}}/t_{\mathrm{int}}$ dependent on the polarization angle of the measured radiance L^{s}. The radiometric response R is logically split in a polarization-dependent response R^{p} and polarization independent response R^{up}. γ_0 is the angle of the maximum sensitivity relative to the instrument slit. Figure inspired by [13]. 23

3.1 Offset signal of all pixels for the left (a) and right (b) detector halves. It can be seen that the offset signal level on the right side is with approximately 24 DN 5 DN higher than on the left detector half with 19 DN. The offset signal increases towards the left and right detector edges. 29

3.2 Read noise, which is the standard deviation of the offset signal. A minor difference between the left and the right detector halves is visible. 29
3.3 PTC of pixel in column 1200 channel 110. (blue) Standard deviation as function of wavelength. For signals over 4000 DN, the noise starts dropping to 0, since more and more of the random signals are saturated. (orange) Fit of Eq. (2.47) on values below 4000 DN. 31
3.4 Average gain over each channel of the left and right detector half. The standard deviation over the averaged gain values is below 6×10^{-4} DN. 31
3.5 (blue) Change of detector sensitivity with temperature. The sensitivity ranges from -0.4 to 0.6 %/K. (red) The uncertainty of the temperature correction is the absolute value of the half coefficient, since the temperature only resolved at a 1 K resolution. 33
3.6 Example of a perfect linear (blue) and a non-linear response (orange). The deviation from linearity ε is determined between dedicated signal levels. While, for instance, $\varepsilon(\mathrm{C}, \mathrm{D})$ describes the relation between levels C and D, a statement about the relation between the levels B and D can be derived from the combination of $\varepsilon(\mathrm{B}, \mathrm{C})$ and $\varepsilon(\mathrm{C}, \mathrm{D})$. 35
3.7 Deviation from non-linearity ε (blue) and from these derived the non-linearity factors ζ^{S} (orange). The actual non-linearity function ζ_{actual} (green) is shown for comparison. 36
3.8 Additional data sets are added to fill the gaps shown in Fig. 3.7. Same colors correspond to the same data set. The initially from the ε values derived non-linearity factors ζ^{S} are not matched to each other. By matching these data sets $\zeta^{\mathrm{S,matched}}$ is derived. 37
3.9 Broadband Attenuable LIght Source (BALIS) for non-linearity measurements. The light of two identical lamp configurations is coupled into an integrating sphere. Each lamp configuration consists of a collimating lens, a beam shutter, an adjustable iris shutter, and a focusing lens. The sensor under investigation is placed in front of a third port. We make sure that the area in the FoV is illuminated with light that is diffusely scattered at least once from other parts of the sphere. 38
3.10 Closeup of signal level C of Fig. 3.6, which is the mean of signal levels C_a and C_b. Hence, the sum of C_a and C_b is the signal level D. As it can be seen, although both values diff by 1.5 % from C, no significant error between actual and calculated signal level is introduced. 39
3.11 Error caused by signal level change due beam shutter position of the other lamp configuration. The relative intensity is related to the iris setting. No significant error is introduced for relative intensities below 0.95. 40
3.12 Deviation from linearity values ε of channel 80 of the left and right detector half. The in general larger values of the right side indicate a higher non-linearity. 43
3.13 Deviations from linearity for both detector halves of selected channels and the averaged values. The legend indicates the channel number. A clear dependence of the non-linearity on the channel number is observable. Please note that both plots are differently scaled, since the non-linearity is on the right detector side much higher. 43

3.14 Normalized ratios for integration time and signal. (a) A constant integration time offset and smear causes a non-linear relation ship between integration time and signal. The smaller the integration time, the bigger the error. (b) With removed integration time offset and smear effect, systematic differences between set and actual integration times are visible in the range of 3500 to 8900 μs. 45

3.15 (a) Signal of a lamp measurement normalized to the integration time. (b) Errors caused by the smear effect for different integration times. Since the smear effect changes randomly after restarting the HySpex software, the errors cannot be corrected. 48

3.16 Stray Light Test Source (SLTS) and CHB collimator setup: Light from a plasma light source is guided via an optical fiber to a collimating Off-Axis Parabolic Mirror (OAPM). For safety reasons, a long pass filter suppresses light below 350 nm. A set of ND filters and a set of bandpass filters are used to control the output power and output wavelength of the SLTS, respectively. Each filter set is arranged in a filter wheel. From here, the beam is coupled into another optical fiber. Two OAPM and a collimator guide the beam over a folding mirror to the sensor. Moving and rotating the folding mirror changes the across-track illumination angle and allows illumination of different spatial columns. 49

3.17 The Smear V^{smear} and photo signal factor V^{ph} for channel 147. A jump of the smear factor is visible between channel 78 and 80. Another jump is visible in front of the illuminated area, which has a smear factor of zero. The photo signal factor shows the peak at the illuminated pixels. 51

3.18 Measurements for a bandpass filter with a center wavelength of 900 nm and a bandwidth of 40 nm. Although the measurements are performed with the same instrument settings and illumination level, three different smear pattern occur after restarting the HySpex software. 51

3.19 Non-linearities for integration times ranging from 5000 to 340 000 μs. The uncorrected (solid) ratios of the left (blue) and right (orange) detector halves show strong non-linearities. The for non-linearity corrected results (dashed) are within the specified target uncertainty (black). (a) Results for channel 0. For better visibility, we shifted the blue curve upwards. (b) Results for channel 60. The signal levels are higher than for channel 0 due to the lamp spectrum and the instrument responsivity. Please note the different axes scales. 52

4.1 Geometric characterization setup. A lamp illuminates a slit from which the optical beam is guided via a collimator and a folding mirror to the aperture of an imaging spectrometer. The result is an image of the slit on the detector array. Moving and rotating the mirror changes the angle of incidence, the slit image on the detector to be displaced. 57

4.2 Setup for calibrating spectral properties of imaging spectrometers. The emitted light from a monochromator is coupled into a multi-mode fiber. Since the light has a certain bandwidth with changing wavelength over the exit port, a mode scrambler is used to mix the modes in the fiber to create an uniform output spectrum. A fiber-to-fiber (F to F) coupler provides a modular interface to which a second fiber is connected that leads to a collimating mirror. The collimated beam is guided over a folding mirror to the imaging spectrometer. 58
4.3 Residuals of monochromator calibration (blue) and validation measurements utilizing the former calibration (orange) for all three gratings. A sinusoidal pattern can be seen in the calibration measurements, caused by the worm gear of the grating turret. The pattern vanishes completely in the validation measurements. 60
4.4 Results of bandwidth measurements for a monochromator slit width of 0.15 mm. Only the wavelength ranges of the grating that are used for the instrument characterization are given. For grating 1, the bandwidth declines from approx. 0.54 nm at an emitted wavelength 404 nm to 0.48 nm at 600 nm. For grating 2, the bandwidth changes from 0.51 nm at 550 nm to 0.43 nm for wavelengths longer than 900 nm. 61
4.5 Calibrated radiometric response (blue) and uncertainties (red) of the radiometer used for the radiometric calibration of the spectral characterization setup. 62
4.6 Radiometric calibration results of the spectral characterization setup. (blue) Relative spectral intensity for grating 1 with order sorting filter 1. (orange) Relative spectral intensity for grating 2 with order sorting filter 2. (red) Uncertainties for both data sets. 63
4.7 Maximum intensities of each channel of geometric line 755 for each wavelength scan. Different scans are necessary to either optimize the SNR or to address the change of the monochromator's order sorting filter between scan 2 (orange) and 3 (green). 64
4.8 Coordinates of pixels from which the SRF is measured. Missing SRFs are later interpolated. 65
4.9 SRF measurement of column 755 channel 40. The response curves from scan range 2 (orange) and scan range 3 (blue) the 2 DN line (green) and the noise level (red) are depicted. The range 2 scan is not complete for this pixel as it did not go below the 2 DN line at the right side of the maximum. 66
4.10 Results of the across-track geometric calibration of the HySpex instrument: (a) Center angles of each pixel referenced on the mean angle of each spatial column, illustrating the keystone effect. The effect is almost non-existent for the center pixels while it increases to displacements of up to 0.17 mrad. (b) Across-track resolution of each pixel. (c) Across-track Angular Sampling Interval (ASI), which is the distance of the center angles of adjacent pixels along the geometric axis. While the resolution of most pixels is approximately 0.50 mrad and better, it decreases to 0.77 mrad at the upper left of the detector. (d) Across-track Angular Sampling Ration (ASR), which is the resolution divided by the sampling interval. 69

4.11 ARFs of selected pixels of the HySpex instrument. For comparison, the dotted lines represent Gaussian functions that are fitted to the data points. (a) and (b) ARFs in column 755 to 758 of channel 50 and channel 80 respectively. They overlap at levels below 50 % of their maximum, which indicates a fill factor below 100 % and that the image sharpness is not limited by the optical system but by the detector. (c) ARFs in columns 1390 to 1393 of channel 85. Although less sharp compared to the ARFs of (a) and (b) the overlapping values are also below 50 %. (d) ARFs in column 100 to 103 of channel 140. The overlapping values are above 50 %, indicating that the image sharpness is limited by the optical system. 70

4.12 Results of the HySpex wavelength calibration. (a) Center wavelength of each spatial column in a spectral channel referenced on the mean of all channels of one spatial column, illustrating the Smile effect. (b) Spectral resolution of each detector pixel. (c) Spectral Sampling Interval (SSI), which is the distance of the center wavelengths of adjacent pixels. (d) Spectral Sampling Ration (SSR), which is the resolution divided by the sampling ratio. In all Figures the effect of the edge of a spectral filter placed at the upper detector half is visible between channel 70 and 90. 71

4.13 SRFs of selected pixels of the HySpex instrument. For comparison, the dotted lines represent Gaussian functions that are fitted to the data points. (a) SRFs of channels 50 to 53 of spatial column 755. The SRFs have a triangular shape and a 3.2 nm resolution. (b) SRFs of channels 80 to 83 of spatial column 755. The edge of the spectral filter causes distortions which leads to a asymmetric SRFs shape. (c) SRFs of channels 80 to 87 of spatial column 1390. 72

4.14 Examples of three PRFs constructed from the ARFs and SRFs measurement results. (left) PRF of pixel 755 channel 50. (center) PRF of pixel 755 channel 80. (right) PRF of pixel 1390 channel 80. Please note the different scales on the color axis. Since the integral of PRFs are normalized to one, higher values of the two-dimensional curves correspond to a high resolution. 72

4.15 Error between cubic spline interpolation and Gaussian function with a FWHM of 3.2 nm when the function is sampled with 0.8 nm. (blue) Residuals when sampling function is not shifted. (orange and green) Range of errors. (red) Standard deviation. 74

4.16 Approximation of the errors caused by the finite band and line widths of the calibration sources. (a) The maximum error of 1.4 % for test scene 1 is the reached in the center of the detector, where the spatial and spectral resolution widths are the shortest. (b) For test scene 2, the maximum error with 0.6 % occurs in channel 95, where a oxygen absorption band is located. For the other channels, the errors are below 0.2 % and therefore in a negligible range. 76

4.17 Difference (red) of the measurements of 1102 pixels at 127 different illuminations angles (blue) and measurements of 128 pixels at 15 different illumination angles (orange). Missing values are linearly interpolated. (a) Center wavelengths (b) Resolution. 77

4.18 Error (red solid) of interpolated SRF (blue) with respect to measured SRF (orange). For comparison, the error for a 1 nm shift of the measured SRF is shown (red dashed). (a) Measured and interpolated SRFs of spatial column 1100 of spectral channel 102. This is the column with the largest center wavelength error, see Fig. 4.17a. (b) Measured and interpolated SRFs of spatial column 33 of spectral channel 102. This is the pixel with the largest resolution error, see Fig. 4.17b. 78

4.19 Approximation of the errors caused by the SRF interpolation by comparing test scene 1 and test scene 2. 78

4.20 Absolute relative error of Gaussian normal distribution based response functions to cubic spline model. Please note the different scales. (a) Errors for test scene 1. The errors are up to 96 % (the scale is truncated at 0.5 for better visualization). The biggest errors are at the location of the filter edge between channels 70 and 90. (b) Errors for test scene 2. The errors below channel 60 are under 1 %, while they increase to 5 % at the filter edge location. Above the this area the high gradients between the different spectra causes errors of up to 20 % (truncated scale). 79

5.1 Mechanical setup of RASTA. A lamp illuminates a diffuse reflecting plaque, while the radiance is monitored by five radiometers (red) where each covers a different spectral range. 86

5.2 Radiance (blue) of RASTA with uncertainties (red). The radiance rises from 2.8 $\mathrm{mW/m^2\,nm\,sr}$ at 400 nm to 33.4 $\mathrm{mW/m^2\,nm\,sr}$ at 925 nm, while the uncertainty is between 1.0 % and 1.4 % ($k = 2$). The radiance is calibrated every 25 nm for most parts of the spectrum. 86

5.3 Errors of linear respectively cubic spline interpolation with respect to the reference Planck spectrum at a temperature of 3100 K. The spectrum is interpolated between the wavelengths with which RASTA's calibration curve is sampled. It can be seen that the linear interpolation introduces errors of up to 0.4 %, while the errors of the cubic spline interpolation are with $\leq$0.03 % negligible. 87

5.4 Flat fielding measurement setup. The imaging spectrometer under investigation is mounted on a rotary stage positioned on top of an integrating sphere. The integrating sphere is illuminated by lamps mounted in the upper hemisphere. The instrument is rotated along its across-track angle so that each geometric line measures the same spot in the center of the sphere. . . . 88

5.5 Ratio between the spectral radiance of RASTA, linearly sampled with the center wavelengths and convolved with the SRFs of spatial column 800 of the HySpex instrument. The difference of up to 0.25 % that is visible at the center channels is caused by the asymmetric shape of the SRFs there. 91

5.6 (a) Potential errors of flat fielding measurements if difference of spectral response functions in one spectral channel are not considered. (b) Potential errors of (a) with sampling errors as shown in Fig. 5.5. 91

5.7 (blue solid) Radiometric response averaged over all spatial columns. (blue dashed) Maximum radiometric response. (blue dotted) Minimum radiometric response. (red dotted) Uncertainty of radiometric response averaged over all spatial columns, as determined with the Monte Carlo simulation. (red solid) Uncertainty of (red dotted) plus a potential error of 0.5 % due to lamp aging and alignment errors. An overall uncertainty of 2 % ($k = 2$) can be assumed. (red dashed) Uncertainty of RASTA calibration. 92

5.8 Relative radiometric response. Each channel is referenced to its mean value. The response on the left detector half is up to 30 % higher than on the right half and drops to 70 % of the mean response towards the left and right detector edges. 93

5.9 Polarization sensitivity of each pixel and orientation of the maximum polarization sensitivity relative to the HySpex VNIR-1600 slit (white lines). 93

6.1 Cross-correlations of three different pixels of the HySpex VNIR-1600 and itself C^{AA} (left column) and virtual sensor 1 and HySpex VNIR-1600 C^{BA} (center column). The corresponding transformation subkernels K^{sub} are also shown (right column). The numbers given in red are denoting the coordinates of the references pixels of sensor A. For pixel (755, 50) [755, 80] {1390, 88} the spectral resolution width changes from (3.3 nm) [4.5 nm] {6.2 nm} to (4.2 nm) [5.2 nm] {5.2 nm} and the PRF is displaced by (−0.1 nm) [−0.2 nm] {0.5 nm}. 103

6.2 Method of performance comparison. A test scene is sampled with the PRFs of the source and the target sensor creating the source and target image, respectively. The source image is then transformed to an image with properties close the target image. Finally, the transformed and target image are compared. 104

6.3 Error distributions of transformed image with respect to the target image for test scene 1. In the histograms, each bin is 0.5 % wide. 105

6.4 Errors of transformed images with respect to the target images for test scene 1. The labels correspond to the test cases. (a) Transformation with spline interpolation. (b) to (d) Transformation with transformation matrix. 106

6.5 Error distributions of transformed images with respect to the target images for test scene 2. In the histograms, each bin is 0.5 % wide. 107

6.6 Errors of transformed images with respect to the target images for test scene 2. The labels correspond to the test cases. (a) Transformation with spline interpolation. (b) to (d) Transformation with transformation matrix. 108

6.7 Relative noise levels of transformed images compared to the source images. (a) Virtual sensor 1: The noise is quite similar with higher values at ares of decreased PRF resolution widths and lower values at areas of increased resolution widths. (b) Virtual sensor 2: Approximately halved noise level. (c) Virtual sensor 3: Noise level below 30 % at most parts of the detector. . . 110

7.1 Structure and traceability of the calibration processor developed for DLR's HySpex VNIR-1600. RAW signal is converted step by step by different correction processes (second column). Every process needs some sort of calibration data (third column). The calibration data is either based on secondary standards (orange) that are traceable to primary standards (red) or on combinations of measurement methods and setups (green). The dashed boxes indicate the different topics covered in the different chapters in this work. The smear correction is currently not part of the processor, since no smear correction matrix could be determined due to the non-deterministic system behavior. 118

A.1 Test scene 1 extending from $-0.32\,\mathrm{rad}$ to $0.32\,\mathrm{rad}$ and from $400\,\mathrm{nm}$ to $1040\,\mathrm{nm}$: (a) Checker board pattern with radiance levels ranging from $0.1\,\mathrm{W\,m^{-2}\,nm^{-1}\,sr^{-1}}$ to $1.0\,\mathrm{W\,m^{-2}\,nm^{-1}\,sr^{-1}}$. (b) Along the spectral z-axis each pattern is $10\,\mathrm{nm}$ wide with a sampling of $0.2\,\mathrm{nm}$. (c) Along the across-track y-axis each pattern is $0.1\,\mathrm{rad}$ with a sampling of $0.02\,\mathrm{mrad}$. . . . 146

A.2 Test scene 2 extending from $-0.32\,\mathrm{rad}$ to $0.32\,\mathrm{rad}$ and from $400\,\mathrm{nm}$ to $1040\,\mathrm{nm}$: (a) Simulated spectra of solar irradiance scattered and aborted by atmosphere and four different surface types. The spectra are sampled every $0.2\,\mathrm{nm}$. (b) Along the across-track y-axis the spectra are repeatably stacked, with a spectrum extending over $2\,\mathrm{mrad}$ and a sampling of $0.02\,\mathrm{mrad}$. (c) Appearance of the scene to the human eye. The letters correspond to the first letters of the surface material. 147

B.1 Spherical coordinate system used in this thesis. Original figure taken from [96]. 149

List of Tables

1.1 Specifications of the HySpex VNIR-1600 airborne imaging spectrometer used in this work. 11

3.1 Relative output intensities of both lamp configurations. The values are adjusted by tuning the iris shutter. 41
3.2 Measurement sequence for each linearity deviation ε. The background is acquired with the first measurement step. Steps 2 and 3 are used to measure the radiance emitted by lamps a and b, respectively. In the last step the sum of both lamp radiances is measured. 41
3.3 Integration time settings for measuring integration time-dependent non-linearity. The light sources is kept stable during each scan and between scan 2 and 3. Between each measurement step, a data take with an integration time of $t_{\mathrm{int,ref}}$ is performed. 44
3.4 SLTS measurement settings. 50

4.1 Specifications of the three installed gratings and the corresponding measurement parameters. λ_{min}, λ_{max} and $\delta\lambda$ are the start, the end and the step width of the measurements, respectively. 59
4.2 Wavelength settings for the SRF measurements. We chose the number of spatial positions at which we perform the wavelength scans, so that the SRFs can be accurately interpolated later. Regions where the SRFs change quicker with the spatial column are therefore scanned with higher spatial density. For this reason, scan 4 is performed at 117 spatial positions which all other scans are performed at 15 positions. 64

6.1 Overview of the virtual sensors that are used for testing the transformation algorithm. 99

7.1 Overview of uncertainties of the HySpex VNIR-1600 instrument after calibration. 117

Bibliography

[1] Michael E. Schaepman, Susan L. Ustin, Antonio J. Plaza, Thomas H. Painter, Jochem Verrelst, and Shunlin Liang. "Earth System Science Related Imaging Spectroscopy-An Assessment". In: *Remote Sensing of Environment* 113 (2009), S123–S137. DOI: 10.1016/j.rse.2009.03.001.

[2] D.G. Manolakis, R.B. Lockwood, and T.W. Cooley. *Hyperspectral Imaging Remote Sensing: Physics, Sensors, and Algorithms*. Cambridge University Press, 2016. ISBN: 9781107083660.

[3] Robert O. Green. "Spectral Calibration Requirement for Earth-Looking Imaging Spectrometers in the Solar-Reflected Spectrum". In: *Applied Optics* 37.4 (1998), p. 683. DOI: 10.1364/ao.37.000683.

[4] Daniel Schläpfer, Jens Nieke, and Klaus I. Itten. "Spatial Psf Nonuniformity Effects in Airborne Pushbroom Imaging Spectrometry Data". In: *IEEE Transactions on Geoscience and Remote Sensing* 45.2 (2007), pp. 458–468. DOI: 10.1109/tgrs.2006.886182.

[5] Jens Nieke, Daniel Schläpfer, Francesco Dell'Endice, Jason Brazile, and Klaus I. Itten. "Uniformity of Imaging Spectrometry Data Products". In: *IEEE Transactions on Geoscience and Remote Sensing* 46.10 (2008), pp. 3326–3336. DOI: 10.1109/tgrs.2008.918764.

[6] Joseph Meola. "Examining the impact of spectral uncertainty on hyperspectral data exploitation". In: *Algorithms and Technologies for Multispectral, Hyperspectral, and Ultraspectral Imagery XXIV*. Vol. 10644. Proc. SPIE. May 2018, pp. 164–175. DOI: 10.1117/12.2303725.

[7] Rupert Müller, Manfred Lehner, Peter Reinartz, and Manfred Schroeder. "Evaluation Of Spacebore and Airboren Line Scanner Images using a Generic Ortho Image Processor". In: ed. by C. Heipke, K. Jacobsen, and M. Gerke. Vol. XXXVI. IAPRS. 2005.

[8] Pantazis Z. Mouroulis. "Low-distortion imaging spectrometer designs utilizing convex gratings". In: *International Optical Design Conference 1998*. Vol. 3482. Proc. SPIE. Sept. 1998, pp. 594–601. DOI: 10.1117/12.322062.

[9] Pantazis Z. Mouroulis. "Spectral and spatial uniformity in pushbroom imaging spectrometers". In: *Imaging Spectrometry V*. Vol. 3753. Proc. SPIE. Oct. 1999, pp. 133–141. DOI: 10.1117/12.366313.

[10] Pantazis Mouroulis, Robert O. Green, and Thomas G. Chrien. "Design of Pushbroom Imaging Spectrometers for Optimum Recovery of Spectroscopic and Spatial Information". In: *Applied Optics* 39.13 (2000), p. 2210. DOI: 10.1364/ao.39.002210.

[11] Andreas Baumgartner, Peter Gege, Claas Köhler, Karim Lenhard, and Thomas Schwarzmaier. "Characterisation methods for the hyperspectral sensor HySpex at DLR's calibration home base". In: *Sensors, Systems, and Next-Generation Satellites XVI*. Vol. 8533. Proc. SPIE. Nov. 2012, pp. 371–378. DOI: 10.1117/12.974664.

[12] Karim Lenhard, Andreas Baumgartner, and Thomas Schwarzmaier. "Independent Laboratory Characterization of Neo HySpex Imaging Spectrometers VNIR-1600 and SWIR-320m-e". In: *IEEE Transactions on Geoscience and Remote Sensing* 53.4 (2015), pp. 1828–1841. DOI: 10.1109/tgrs.2014.2349737.

[13] Florian Ewald, Tobias Kölling, Andreas Baumgartner, Tobias Zinner, and Bernhard Mayer. "Design and Characterization of specMACS, a Multipurpose Hyperspectral Cloud and Sky Imager". In: *Atmospheric Measurement Techniques* 9.5 (2016), pp. 2015–2042. DOI: 10.5194/amt-9-2015-2016.

[14] Robert O Green, Michael L Eastwood, Charles M Sarture, Thomas G Chrien, Mikael Aronsson, Bruce J Chippendale, Jessica A Faust, Betina E Pavri, Christopher J Chovit, Manuel Solis, Martin R Olah, and Orlesa Williams. "Imaging Spectroscopy and the Airborne Visible/infrared Imaging Spectrometer (AVIRIS)". In: *Remote Sensing of Environment* 65.3 (1998), pp. 227–248. DOI: 10.1016/s0034-4257(98)00064-9.

[15] J.S. Pearlman, P.S. Barry, C.C. Segal, J. Shepanski, D. Beiso, and S.L. Carman. "Hyperion, a Space-Based Imaging Spectrometer". In: *IEEE Transactions on Geoscience and Remote Sensing* 41.6 (2003), pp. 1160–1173. DOI: 10.1109/tgrs.2003.815018.

[16] Nathan Leisso, Thomas Kampe, and Bryan Karpowicz. "Calibration of the National Ecological Observatory Network's airborne imaging spectrometers". In: *2014 IEEE Geoscience and Remote Sensing Symposium*. July 2014, pp. 2625–2628. DOI: 10.1109/igarss.2014.6947012.

[17] Michael E. Schaepman, Michael Jehle, Andreas Hueni, Petra D'Odorico, Alexander Damm, Jürg Weyermann, Fabian D. Schneider, Valérie Laurent, Christoph Popp, Felix C. Seidel, Karim Lenhard, Peter Gege, Christoph Küchler, Jason Brazile, Peter Kohler, Lieve De Vos, Koen Meuleman, Roland Meynart, Daniel Schläpfer, Mathias Kneubühler, and Klaus I. Itten. "Advanced Radiometry Measurements and Earth Science Applications With the Airborne Prism Experiment (APEX)". In: *Remote Sensing of Environment* 158 (2015), pp. 207–219. DOI: 10.1016/j.rse.2014.11.014.

[18] Karim Lenhard, Andreas Baumgartner, Peter Gege, Saulius Nevas, Stefan Nowy, and Armin Sperling. "Impact of Improved Calibration of a Neo HySpex VNIR-1600 Sensor on Remote Sensing of Water Depth". In: *IEEE Transactions on Geoscience and Remote Sensing* 53.11 (2015), pp. 6085–6098. DOI: 10.1109/tgrs.2015.2431743.

[19] Karim Lenhard. "Improving the Calibration of Airborne Hyperspectral Sensors for Earth Observation". PhD thesis. June 2015. DOI: 10.5167/UZH-121434.

[20] Richard A. M. Lee, Christopher W. O'Dell, Debra Wunch, Coleen M. Roehl, Gregory B. Osterman, Jean-Francois Blavier, Robert Rosenberg, Lars Chapsky, Christian Frankenberg, Sarah L. Hunyadi-Lay, Brendan M. Fisher, David M. Rider, David Crisp, and Randy Pollock. "Preflight Spectral Calibration of the Orbiting Carbon Observatory 2". In: *IEEE Transactions on Geoscience and Remote Sensing* 55.5 (2017), pp. 2499–2508. DOI: 10.1109/tgrs.2016.2645614.

[21] Robert Rosenberg, Stephen Maxwell, B. Carol Johnson, Lars Chapsky, Richard A. M. Lee, and Randy Pollock. "Preflight Radiometric Calibration of Orbiting Carbon Observatory 2". In: *IEEE Transactions on Geoscience and Remote Sensing* 55.4 (2017), pp. 1994–2006. DOI: 10.1109/tgrs.2016.2634023.

[22] Quintus Kleipool, Antje Ludewig, Ljubiša Babić, Rolf Bartstra, Remco Braak, Werner Dierssen, Pieter-Jan Dewitte, Pepijn Kenter, Robin Landzaat, Jonatan Leloux, Erwin Loots, Peter Meijering, Emiel van der Plas, Nico Rozemeijer, Dinand Schepers, Daniel Schiavini, Joost Smeets, Giuseppe Vacanti, Frank Vonk, and Pepijn Veefkind. "Pre-Launch Calibration Results of the Tropomi Payload On-Board the Sentinel-5 Precursor Satellite". In: *Atmospheric Measurement Techniques* 11.12 (2018), pp. 6439–6479. DOI: 10.5194/amt-11-6439-2018.

[23] Richard M. van Hees, Paul J. J. Tol, Sidney Cadot, Matthijs Krijger, Stefan T. Persijn, Tim A. van Kempen, Ralph Snel, Ilse Aben, and Ruud W. M. Hoogeveen. "Determination of the Tropomi-Swir Instrument Spectral Response Function". In: *Atmospheric Measurement Techniques* 11.7 (2018), pp. 3917–3933. DOI: 10.5194/amt-11-3917-2018.

[24] Ilse Sebastian, David Krutz, Andreas Eckardt, Holger Venus, Ingo Walter, Burghardt Günther, Michael Neidhardt, Ralf Reulke, Rupert Müller, Mathias Uhlig, Sandra Müller, Thomas Peschel, Simone Arloth, Matthias Lieder, and Friedrich Schrandt. "On-ground calibration of DESIS: DLR's Earth sensing imaging spectrometer for the International Space Station (ISS)". In: *Optical Sensing and Detection V*. Ed. by Francis Berghmans and Anna G. Mignani. Vol. 10680. Proc. SPIE. International Society for Optics and Photonics. 2018, pp. 1–12. DOI: 10.1117/12.2307188.

[25] John W. Chapman, David R. Thompson, Mark C. Helmlinger, Brian D. Bue, Robert O. Green, Michael L. Eastwood, Sven Geier, Winston Olson-Duvall, and Sarah R. Lundeen. "Spectral and Radiometric Calibration of the Next Generation Airborne Visible Infrared Spectrometer (AVIRIS-NG)". In: *Remote Sensing* 11.18 (2019), p. 2129. DOI: 10.3390/rs11182129.

[26] James R. Janesick. *Photon Transfer*. SPIE, 2007. DOI: 10.1117/3.725073.

[27] EMVA 1288 Working group. *EMVA Standard 1288*. Dec. 2016.

[28] Saber G. R. Salim, Nigel P. Fox, Evangelos Theocharous, Tong Sun, and Kenneth T. V. Grattan. "Temperature and Nonlinearity Corrections for a Photodiode Array Spectrometer Used in the Field". In: *Applied Optics* 50.6 (2011), p. 866. DOI: 10.1364/ao.50.000866.

[29] Andreas Hueni and Agnieszka Bialek. "Cause, Effect, and Correction of Field Spectroradiometer Interchannel Radiometric Steps". In: *IEEE Journal of Selected Topics in Applied Earth Observations and Remote Sensing* 10.4 (2017), pp. 1542–1551. DOI: 10.1109/jstars.2016.2625043.

[30] Terrence H. Hemmer and Todd L. Westphal. "Lessons learned in the postprocessing of field spectroradiometric data covering the 0.4-2.5-μm wavelength region". In: *Algorithms for Multispectral, Hyperspectral, and Ultraspectral Imagery VI*. Vol. 4049. Proc. SPIE. Aug. 2000, pp. 249–260. DOI: 10.1117/12.410347.

[31] Toomas Kübarsepp, Atte Haapalinna, Petri Kärhä, and Erkki Ikonen. "Nonlinearity Measurements of Silicon Photodetectors". In: *Applied Optics* 37.13 (1998), p. 2716. DOI: 10.1364/ao.37.002716.

[32] L P Boivin. "Automated Absolute and Relative Spectral Linearity Measurements on Photovoltaic Detectors". In: *Metrologia* 30.4 (1993), pp. 355–360. DOI: 10.1088/0026-1394/30/4/025.

[33] Bernd Tabbert and Alexander O. Goushcha. "Linearity of the Photocurrent Response with Light Intensity". In: *2006 IEEE Nuclear Science Symposium Conference Record, for Silicon PIN Photodiode Array*. 2006, pp. 1060–1063. DOI: 10.1109/nssmic.2006.356029.

[34] Mark F. Larsen. "Temperature-Dependent Linearity Calibration for the Spirit III Radiometer". In: *Optical Engineering* 36.11 (1997), p. 2956. DOI: 10.1117/1.601536.

[35] C. L. Sanders. "A Photocell Linearity Tester". In: *Applied Optics* 1.3 (1962), p. 207. DOI: 10.1364/ao.1.000207.

[36] Klaus D. Mielenz and Ken L. Eckerle. "Spectrophotometer Linearity Testing Using the Double-Aperture Method". In: *Applied Optics* 11.10 (1972), p. 2294. DOI: 10.1364/ao.11.002294.

[37] William Gallery and Nathan Leisso. *NEON Algorithm Theoretical Basis Document: NEON Imaging Spectrometer (NIS) Level 1B Calibrated Radiance*. Tech. rep. NEON, 2014.

[38] Steven W. Brown, George P. Eppeldauer, and Keith R. Lykke. "Facility for Spectral Irradiance and Radiance Responsivity Calibrations Using Uniform Sources". In: *Applied Optics* 45.32 (2006), p. 8218. DOI: 10.1364/ao.45.008218.

[39] Thomas G. Chrien, Robert O. Green, and Michael L. Eastwood. "Accuracy of the spectral and radiometric laboratory calibration of the Airborne Visible/Infrared Imaging Spectrometer (AVIRIS". In: *Imaging Spectroscopy of the Terrestrial Environment*. Vol. 1298. Proc. SPIE. Sept. 1990, pp. 37–49. DOI: 10.1117/12.21334.

[40] Gerrit Kuhlmann, Andreas Hueni, Alexander Damm, and Dominik Brunner. "An Algorithm for In-Flight Spectral Calibration of Imaging Spectrometers". In: *Remote Sensing* 8.12 (2016), p. 1017. DOI: 10.3390/rs8121017.

[41] Jason O. Day, Christopher W. O'Dell, Randy Pollock, Carol J. Bruegge, David Rider, David Crisp, and Charles E. Miller. "Preflight Spectral Calibration of the Orbiting Carbon Observatory". In: *IEEE Transactions on Geoscience and Remote Sensing* 49.7 (2011), pp. 2793–2801. DOI: 10.1109/tgrs.2011.2107745.

[42] Kang Sun, Xiong Liu, Caroline R. Nowlan, Zhaonan Cai, Kelly Chance, Christian Frankenberg, Richard A. M. Lee, Randy Pollock, Robert Rosenberg, and David Crisp. "Characterization of the Oco-2 Instrument Line Shape Functions Using On-Orbit Solar Measurements". In: *Atmospheric Measurement Techniques* 10.3 (2017), pp. 939–953. DOI: 10.5194/amt-10-939-2017.

[43] Peter Gege, Jochen Fries, Peter Haschberger, Paul Schötz, Horst Schwarzer, Peter Strobl, Birgit Suhr, Gerd Ulbrich, and Willem Jan Vreeling. "Calibration Facility for Airborne Imaging

Spectrometers". In: *ISPRS Journal of Photogrammetry and Remote Sensing* 64.4 (2009), pp. 387–397. DOI: 10.1016/j.isprsjprs.2009.01.006.

[44] DLR Remote Sensing Technology Institute. "The Calibration Home Base for Imaging Spectrometers". In: *Journal of large-scale research facilities* 2 (2016), A82. DOI: 10.17815/jlsrf-2-137.

[45] Stuart F. Biggar, Kurtis J. Thome, Ronald B. Lockwood, and Steven Miller. "VNIR transfer radiometer for validation of calibration sources for hyperspectral sensors". In: *Earth Observing Systems XII*. Vol. 6677. Proc. SPIE. Sept. 2007, pp. 347–355. DOI: 10.1117/12.740231.

[46] Nik Anderson, Kurt Thome, Stuart Biggar, and Jeffrey S. Czapla-Myers. "Design and validation of a transfer radiometer". In: *Earth Observing Systems XIII*. Vol. 7081. Proc. SPIE. Aug. 2008, pp. 30–37. DOI: 10.1117/12.795478.

[47] R.U. Datla, J.P. Rice, K.R. Lykke, B.C. Johnson, J.J. Butler, and X. Xiong. "Best Practice Guidelines for Pre-Launch Characterization and Calibration of Instruments for Passive Optical Remote Sensing". In: *Journal of Research of the National Institute of Standards and Technology* 116.2 (2011), p. 621. DOI: 10.6028/jres.116.009.

[48] Howard W. Yoon and Raghu N.Kacker. *Guidelines for Radiometric Calibration of Electro-Optical Instruments for Remote Sensing*. Tech. rep. 157. Gaithersburg, MD: National Institute of Standards and Technology, May 2015. DOI: 10.6028/nist.hb.157.

[49] T. Schwarzmaier, A. Baumgartner, P. Gege, C. Köhler, and K. Lenhard. "The Radiance Standard RASTA of DLR's calibration facility for airborne imaging spectrometers". In: *Sensors, Systems, and Next-Generation Satellites XVI*. Vol. 8533. Proc. SPIE. Nov. 2012, pp. 431–436. DOI: 10.1117/12.974599.

[50] Thomas Schwarzmaier, Andreas Baumgartner, Peter Gege, Claas Köhler, and Karim Lenhard. "DLR's New Traceable Radiance Standard RASTA". In: *IGARSS 2012*. 2012, pp. 1–4.

[51] D. R. Taubert, J. Hollandt, P. Sperfeld, S. Pape, A. Höpe, K.-O. Hauer, P. Gege, T. Schwarzmaier, K. Lenhard, and A. Baumgartner. "Providing radiometric traceability for the calibration home base of DLR by PTB". In: vol. 1531. 1. 2013, pp. 376–379. DOI: 10.1063/1.4804785.

[52] D.R. Taubert, J. Hollandt, C. Monte, Peter Gege, Thomas Schwarzmaier, Karim Lenhard, and Andreas Baumgartner. "Absolute radiometric characterization of the transfer radiometer unit of RASTA in the UV, VIS and NIR spectral range". In: *SPIE Remote Sensing*. Proc. SPIE. Sept. 2013.

[53] Xavier Ceamanos and Sylvain Doute. "Spectral Smile Correction of CRISM/MRO Hyperspectral Images". In: *IEEE Transactions on Geoscience and Remote Sensing* 48.11 (2010), pp. 3951–3959. DOI: 10.1109/tgrs.2010.2064326.

[54] Huijie Zhao, Guorui Jia, and Na Li. "Transformation From Hyperspectral Radiance Data To Data of Other Sensors Based on Spectral Superresolution". In: *IEEE Transactions on Geoscience and Remote Sensing* 48.11 (2010), pp. 3903–3912. DOI: 10.1109/tgrs.2010.2068302.

[55] Guorui Jia, Andreas Hueni, Michael E. Schaepman, and Huijie Zhao. "Detection and Correction of Spectral Shift Effects for the Airborne Prism Experiment". In: *IEEE Transactions on Geoscience and Remote Sensing* 55.11 (2017), pp. 6666–6679. DOI: 10.1109/tgrs.2017.2731399.

[56] Saulius Nevas, Gerd Wübbeler, Armin Sperling, Clemens Elster, and Annette Teuber. "Simultaneous Correction of Bandpass and Stray-Light Effects in Array Spectroradiometer Data". In: *Metrologia* 49.2 (2012), S43–S47. DOI: 10.1088/0026-1394/49/2/s43.

[57] D. M. Bramich. "A New Algorithm for Difference Image Analysis". In: *Monthly Notices of the Royal Astronomical Society: Letters* 386.1 (2008), pp. L77–L81. DOI: 10.1111/j.1745-3933.2008.00464.x.

[58] Karl D. Gordon, Charles W. Engelbracht, George H. Rieke, K. A. Misselt, J.-D. T. Smith, and Jr. Robert C. Kennicutt. "The Behavior of the Aromatic Features in M101 H II Regions:

Evidence for Dust Processing". In: *The Astrophysical Journal* 682.1 (2008), pp. 336–354. DOI: 10.1086/589567.

[59] T. Darnell, E. Bertin, M. Gower, C. Ngeow, S. Desai, J. J. Mohr, D. Adams, G. E. Daues, M. Gower, C. Ngeow, S. Desai, C. Beldica, M. Freemon, H. Lin, E. H. Neilsen, D. Tucker, L. A. N. da Costa, L. Martelli, R. L. C. Ogando, M. Jarvis, and E. Sheldon. "The Dark Energy Survey Data Management System: The Coaddition Pipeline and PSF Homogenization". In: *Astronomical Data Analysis Software and Systems XVIII*. Vol. 411. Astronomical Society of the Pacific Conference Series. 2009, pp. 18–21.

[60] E. Bertin. "Automated Morphometry with SExtractor and PSFEx". In: *Astronomical Data Analysis Software and Systems XX*. Vol. 442. Astronomical Society of the Pacific Conference Series. 2011, pp. 435–438.

[61] S. Desai, R. Armstrong, J. J. Mohr, D. R. Semler, J. Liu, E. Bertin, S. S. Allam, W. A. Barkhouse, G. Bazin, E. J. Buckley-Geer, M. C. Cooper, S. M. Hansen, F. W. High, H. Lin, Y.-T. Lin, C.-C. Ngeow, A. Rest, J. Song, D. Tucker, and A. Zenteno. "The Blanco Cosmology Survey: Data Acquisition, Processing, Calibration, Quality Diagnostics, and Data Release". In: *The Astrophysical Journal* 757.1 (2012), p. 83. DOI: 10.1088/0004-637x/757/1/83.

[62] A. Boucaud, M. Bocchio, A. Abergel, F. Orieux, H. Dole, and M. A. Hadj-Youcef. "Convolution Kernels for Multi-Wavelength Imaging". In: *Astronomy & Astrophysics* 596 (2016), A63. DOI: 10.1051/0004-6361/201629080.

[63] BIPM, IEC, IFCC, ILAC, IUPAC, IUPAP, ISO, OIML. *The international vocabulary of metrology—basic and general concepts and associated terms (VIM)*. 3rd ed. JCGM 200:2012. 2012.

[64] BIPM, IEC, IFCC, ILAC, IUPAC, IUPAP, ISO, OIML. *Evaluation of measurement data — Guide to the expression of uncertainty in measurement (GUM)*. 1st ed. JCGM 100:2008. 2008.

[65] DLR Remote Sensing Technology Institute. "Airborne Imaging Spectrometer Hyspex". In: *Journal of large-scale research facilities JLSRF* 2 (2016), A93. DOI: 10.17815/jlsrf-2-151.

[66] *Manual Adimec-1600m Adimec-1620m rev 1.3*. Adimec Advanced Image Systems B.V. Eindhoven, The Netherlands, Sept. 2006.

[67] Gary A. Shaw and Hsiao-hua K. Burke. "Spectral Imaging for Remote Sensing". In: *LINCOLN LABORATORY JOURNAL* 14.1 (2003), pp. 3–28.

[68] Y.P. Varshni. "Temperature Dependence of the Energy Gap in Semiconductors". In: *Physica* 34.1 (1967), pp. 149–154. DOI: 10.1016/0031-8914(67)90062-6.

[69] Thierry P. Appourchaux, Didier D. E. Martin, and Udo Telljohann. "Temperature dependence of silicon photodiode quantum efficiency: theoretical and experimental results". In: *Physics and Simulation of Optoelectronic Devices*. Vol. 1679. Proc. SPIE. July 1992, pp. 200–211. DOI: 10.1117/12.60488.

[70] H. Nyquist. "Certain Topics in Telegraph Transmission Theory". In: *Transactions of the American Institute of Electrical Engineers* 47.2 (1928), pp. 617–644. DOI: 10.1109/t-aiee.1928.5055024.

[71] C.E. Shannon. "Communication in the Presence of Noise". In: *Proceedings of the IRE* 37.1 (1949), pp. 10–21. DOI: 10.1109/jrproc.1949.232969.

[72] Bernd Jähne. *Digital Image Processing*. Springer-Verlag, 2005. DOI: 10.1007/3-540-27563-0.

[73] Luchang Li, Mengting Li, Zhaoning Zhang, and Zhen-Li Huang. "Assessing Low-Light Cameras With Photon Transfer Curve Method". In: *Journal of Innovative Optical Health Sciences* 09.03 (2016), p. 1630008. DOI: 10.1142/s1793545816300081.

[74] Hamamatsu. *Opto-semiconductor Handbook*. Hamamatsu, 2014.

[75] Adimec. *CCD versus CMOS: blooming and smear performance*. URL: https://www.adimec.com/ccd-versus-cmos-blooming-and-smear-performance/ (visited on 06/16/2020).

[76] Yuqin Zong, Steven W. Brown, B. Carol Johnson, Keith R. Lykke, and Yoshi Ohno. "Simple Spectral Stray Light Correction Method for Array Spectroradiometers". In: *Applied Optics* 45.6 (2006), p. 1111. DOI: 10.1364/ao.45.001111.

[77] Malte Kretz. “Design and construction of a light source setup for stray light measurements in array spectrometers”. MA thesis. KIT Karlsruhe, Jan. 2018.

[78] Charles Thomas Pope and Andreas Baumgartner. “Light source for stray light characterisation of EnMAP spectrometers”. In: *Sensors, Systems, and Next-Generation Satellites XXIII*. Vol. 11151. Proc. SPIE. Oct. 2019, pp. 452–459. DOI: 10.1117/12.2531264.

[79] Andreas Baumgartner. “Grating Monochromator Wavelength Calibration Using an Echelle Grating Wavelength Meter”. In: *Optics Express* 27.10 (2019), p. 13596. DOI: 10.1364/oe.27.013596.

[80] Dieter Richard Taubert. personal communication. May 2020.

[81] Max Planck. “Zur Theorie Des Gesetzes Der Energieverteilung Im Normalspectrum”. In: *Verhandlungen der Deutschen Physikalischen Gesellschaft* 2 (1900), pp. 237–245. DOI: 10.1002/phbl.19480040404.

[82] Andreas Baumgartner and Claas Henning Köhler. “Transformation of point spread functions on an individual pixel scale”. In: *Optics Express* 28.26 (2020), pp. 38682–38697. DOI: 10.1364/oe.409626.

[83] Andrey N. Tikhonov. “Solution of incorrectly formulated problems and the regularization method”. In: *Soviet Math. Dokl.* 4 (1963), pp. 1035–1038.

[84] Andrey N. Tikhonov. “Regularization of incorrectly posed problems”. In: *Soviet Math. Dokl.* 4 (1963), pp. 1624–1627.

[85] Andrey N. Tikhonov and Vasiliy Y. Arsenin. *Solutions of ill-posed problems*. Washington, D.C.: John Wiley & Sons, New York: V. H. Winston & Sons, 1977. ISBN: 0470991240.

[86] Adrian Doicu, Thomas Trautmann, and Franz Schreier. *Numerical regularization for atmospheric inverse problems*. Berlin London: Springer, 2010. ISBN: 9783642054389.

[87] Kelly Chance, Thomas P. Kurosu, and Christopher E. Sioris. “Undersampling Correction for Array Detector-Based Satellite Spectrometers”. In: *Applied Optics* 44.7 (2005), p. 1296. DOI: 10.1364/ao.44.001296.

[88] Bo-Cai Gao, Marcos J. Montes, and Curtiss O. Davis. “Refinement of Wavelength Calibrations of Hyperspectral Imaging Data Using a Spectrum-Matching Technique”. In: *Remote Sensing of Environment* 90.4 (2004), pp. 424–433. DOI: 10.1016/j.rse.2003.09.002.

[89] Luis Guanter, Rudolf Richter, and José Moreno. “Spectral Calibration of Hyperspectral Imagery Using Atmospheric Absorption Features”. In: *Applied Optics* 45.10 (2006), p. 2360. DOI: 10.1364/ao.45.002360.

[90] Robert A Neville, Lixin Sun, and Karl Staenz. “Spectral calibration of imaging spectrometers by atmospheric absorption feature matching”. In: *Canadian Journal of Remote Sensing* 34.sup1 (2008), S29–S42. DOI: 10.5589/m07-072.

[91] Rudolf Richter, Daniel Schläpfer, and Andreas Müller. “Operational Atmospheric Correction for Imaging Spectrometers Accounting for the Smile Effect”. In: *IEEE Transactions on Geoscience and Remote Sensing* 49.5 (2011), pp. 1772–1780. DOI: 10.1109/tgrs.2010.2089799.

[92] Robert Ryan, Braxton Baldridge, Robert A Schowengerdt, Taeyoung Choi, Dennis L Helder, and Slawomir Blonski. “IKONOS Spatial Resolution and Image Interpretability Characterization”. In: *Remote Sensing of Environment* 88.1-2 (2003), pp. 37–52. DOI: 10.1016/j.rse.2003.07.006.

[93] Françoise Viallefont-Robinet and Dominique Léger. “Improvement of the Edge Method for On-Orbit MTF Measurement”. In: *Optics Express* 18.4 (2010), p. 3531. DOI: 10.1364/oe.18.003531.

[94] Chong Fan, Guanda Li, and Chao Tao. “Slant Edge Method for Point Spread Function Estimation”. In: *Applied Optics* 54.13 (2015), p. 4097. DOI: 10.1364/ao.54.004097.

[95] A. Berk, P. Conforti, R. Kennett, T. Perkins, F. Hawes, and J. van den Bosch. “MODTRAN® 6: A major upgrade of the MODTRAN® radiative transfer code”. In: *6th Workshop on Hyperspectral Image and Signal Processing: Evolution in Remote Sensing (WHISPERS)*. June 2014, pp. 1–4. DOI: 10.1109/whispers.2014.8077573.

[96] Wikimedia Commons. *Kugelkoordinaten: Definition*. File: Kugelkoord-def.svg. 2015. URL: https://commons.wikimedia.org/w/index.php?title=File:Kugelkoord-def.svg (visited on 06/05/2020).

Appendix A

Test Scenes

The synthetic scenes are two-dimensional data sets with an angular sampling of 0.02 mrad, extending from -0.32 rad to 0.32 rad and a spectral sampling of 0.2 nm extending from 400 nm to 1040 nm.

A.1 Test Scene 1

Synthetic test scene 1 consists of a checkerboard pattern with an angular width of 0.1 rad and a spectral width of 10 nm, see Fig. A.1. The bright patches have a radiance of $1.0\,\mathrm{W\,m^{-2}\,nm^{-1}\,sr^{-1}}$ and the dark patches of $0.1\,\mathrm{W\,m^{-2}\,nm^{-1}\,sr^{-1}}$.

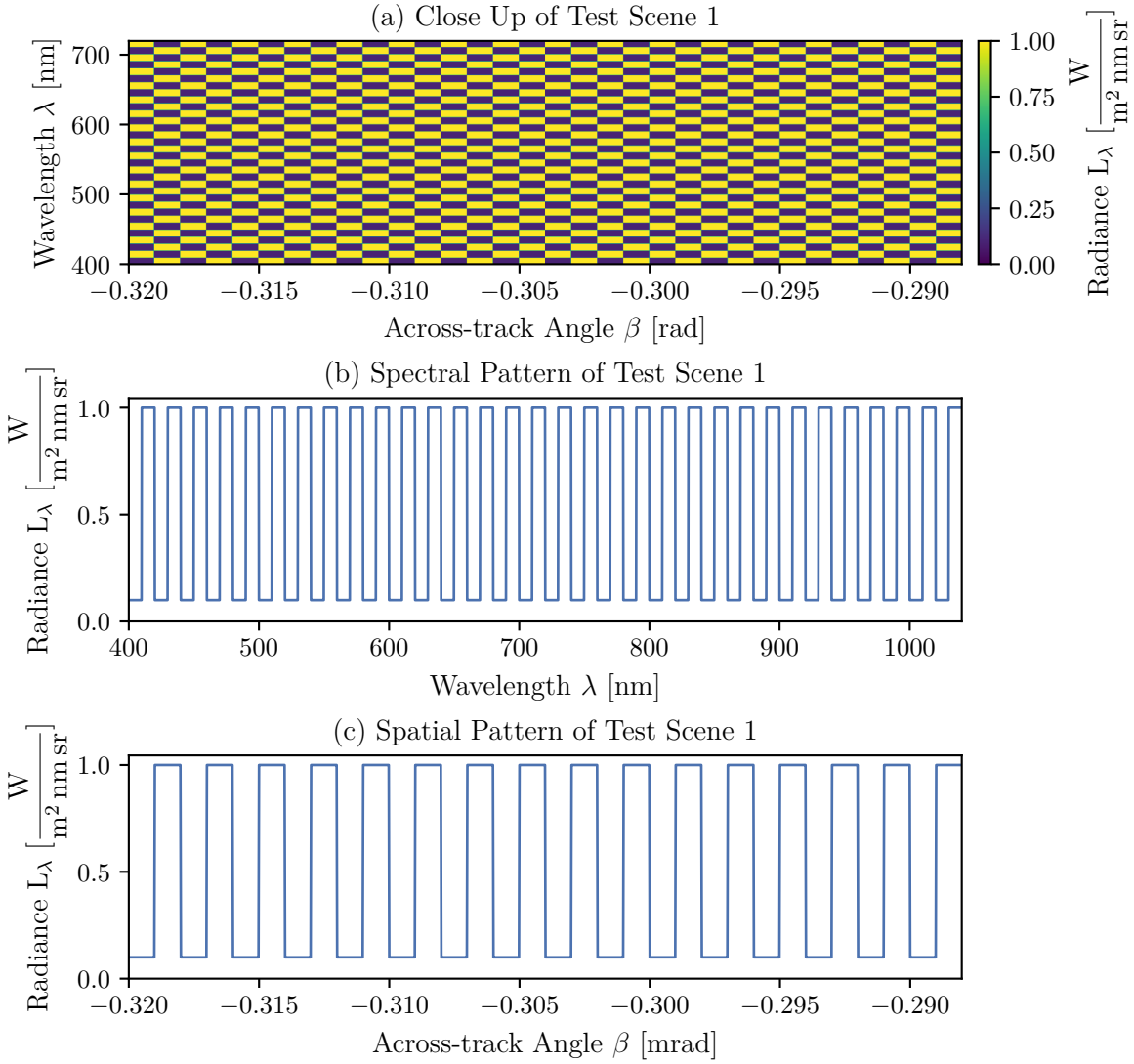

Figure A.1: Test scene 1 extending from −0.32 rad to 0.32 rad and from 400 nm to 1040 nm: (a) Checker board pattern with radiance levels ranging from $0.1\,\mathrm{W\,m^{-2}\,nm^{-1}\,sr^{-1}}$ to $1.0\,\mathrm{W\,m^{-2}\,nm^{-1}\,sr^{-1}}$. (b) Along the spectral z-axis each pattern is 10 nm wide with a sampling of 0.2 nm. (c) Along the across-track y-axis each pattern is 0.1 rad with a sampling of 0.02 mrad.

A.2 Test Scene 2

Synthetic test scene 2 consists of synthetic radiances that are simulated with MODTRAN [95]. Each radiance is the simulation of the solar irradiance scattered and refracted by a surface and atmosphere. Four different surface types are used, which are supplied with MODTRAN: Urban, Tundra, Forest Mixed, and Grassland, see Fig. A.2a. These radiances are stacked along the across-track y-axis and changed in periodic manner, see Fig. A.2b. This makes it possible to evaluate the effect of rapidly changing surface types, which is normally the case in remote sensing scenes.

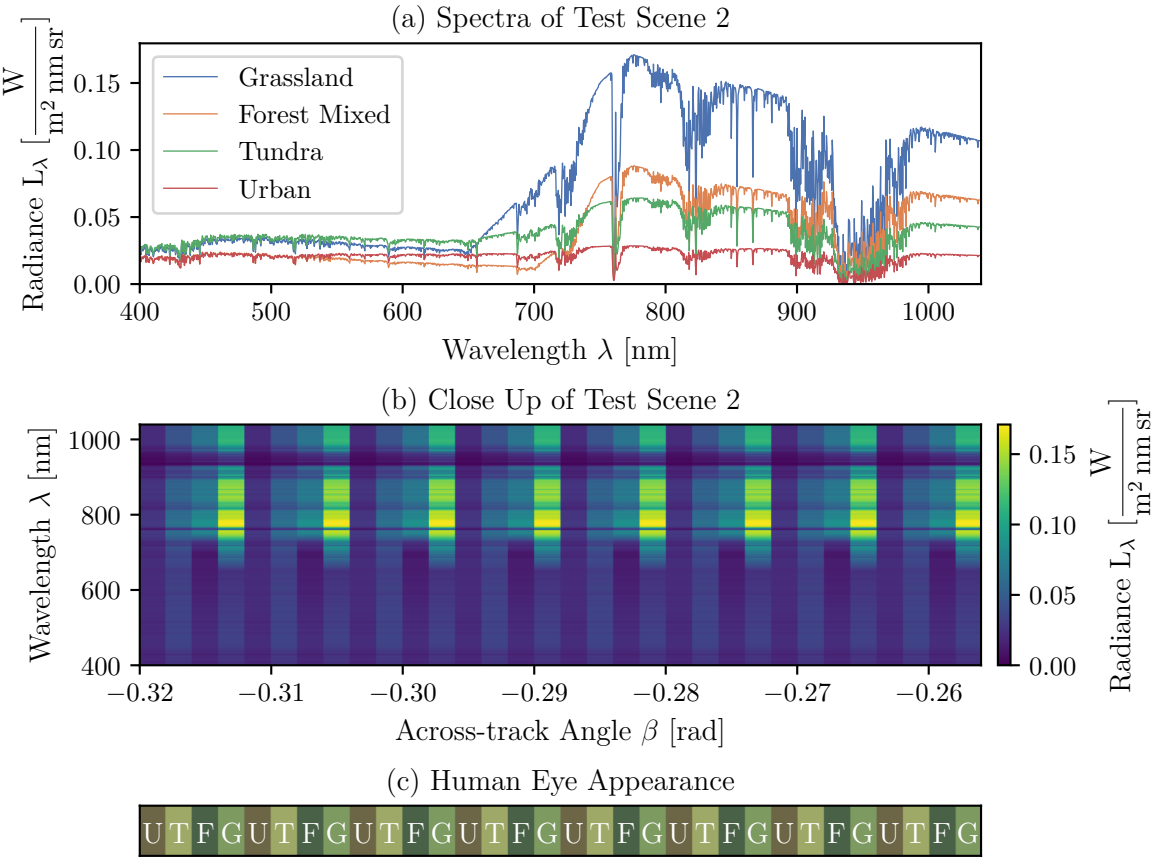

Figure A.2: Test scene 2 extending from −0.32 rad to 0.32 rad and from 400 nm to 1040 nm: (a) Simulated spectra of solar irradiance scattered and aborted by atmosphere and four different surface types. The spectra are sampled every 0.2 nm. (b) Along the across-track y-axis the spectra are repeatably stacked, with a spectrum extending over 2 mrad and a sampling of 0.02 mrad. (c) Appearance of the scene to the human eye. The letters correspond to the first letters of the surface material.

Appendix B

Spherical Coordinate System

In this thesis, we use a spherical coordinate system as it is depicted in Fig. B.1. The axis is identical to those shown in Fig. 2.2. Hence, the z'-axis is oriented downward. Please note that the polar angle θ and the azimuth angle ϕ do not follow classical conventions. We have chosen the coordinate system in this way to ease integration of the solid angle over the typical FoVs of imaging spectrometers as we will show in the following.

To convert the spherical to Cartesian coordinates, the following equations can be used:

$$x' = r\cos\theta \tag{B.1}$$

$$y' = r\sin\theta\cos\phi \tag{B.2}$$

$$z' = r\sin\theta\sin\phi, \tag{B.3}$$

where r is the radial distance with $r \in [0, \infty)$, $\theta \in [0, \pi]$, and $\phi \in [0, 2\pi)$.

Following these definitions, the across-track angle β is identical to the azimuth angle ϕ:

$$\beta = \phi. \tag{B.4}$$

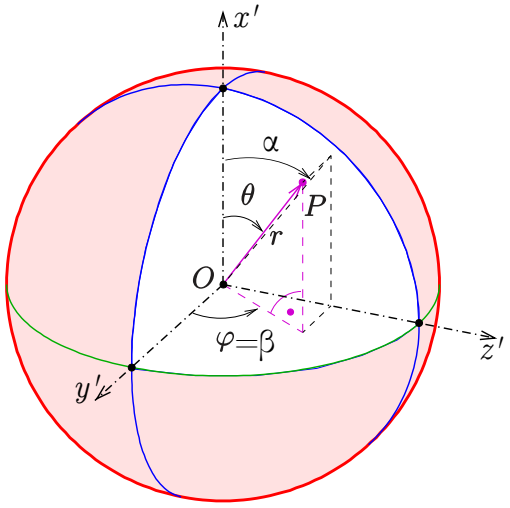

Figure B.1: Spherical coordinate system used in this thesis. Original figure taken from [96].

For the along-track angle α the following is true:

$$\tan\alpha = \frac{z'}{x'} \tag{B.5}$$

$$= \frac{\sin\theta\sin\phi}{\cos\theta} \tag{B.6}$$

$$= \tan\theta\sin\phi \tag{B.7}$$

$$= \tan\theta\sin\beta. \tag{B.8}$$

The polar angle θ is then

$$\theta = \arctan\frac{\tan\alpha}{\sin\beta}. \tag{B.9}$$

The integral over the half hemisphere is defined as

$$\Omega = \int_{2\pi} \sin\theta\,\mathrm{d}^2\omega. \tag{B.10}$$

Inserting Eq. (B.9) into Eq. (B.10) allows us to perform the same operation in therms of the along-track and across-track angle:

$$\Omega = \int_{2\pi} \sin\arctan\frac{\tan\alpha}{\sin\beta}\,\mathrm{d}^2\omega. \tag{B.11}$$

For imaging spectrometers which a small along-track FoV ($\alpha \approx \pi/2$) the equation can be simplified to

$$\Omega = \int_{\Omega_{\mathrm{FOV}}} \sin\arctan\frac{\tan\alpha}{\sin\beta}\,\mathrm{d}^2\omega \approx \int_{\Omega_{\mathrm{FOV}}} \mathrm{d}^2\omega, \tag{B.12}$$

where Ω_{FOV} is the instrument's FoV.

Appendix C

Related Publications

Peer-Review Articles

1. Andreas Baumgartner and Claas Henning Köhler. "Transformation of point spread functions on an individual pixel scale". In: *Optics Express* 28.26 (2020), pp. 38682–38697. DOI: 10.1364/oe.409626

2. Linda Forster, Meinhard Seefeldner, Andreas Baumgartner, Tobias Kölling, and Bernhard Mayer. "Ice Crystal Characterization in Cirrus Clouds II: Radiometric Characterization of HaloCam for the Quantitative Analysis of Halo Displays". In: *Atmospheric Measurement Techniques* 13.7 (2020), pp. 3977–3991. DOI: 10.5194/amt-13-3977-2020

3. Andreas Baumgartner. "Grating Monochromator Wavelength Calibration Using an Echelle Grating Wavelength Meter". In: *Optics Express* 27.10 (2019), p. 13596. DOI: 10.1364/oe.27.013596

4. Florian Ewald, Tobias Kölling, Andreas Baumgartner, Tobias Zinner, and Bernhard Mayer. "Design and Characterization of specMACS, a Multipurpose Hyperspectral Cloud and Sky Imager". In: *Atmospheric Measurement Techniques* 9.5 (2016), pp. 2015–2042. DOI: 10.5194/amt-9-2015-2016

5. Karim Lenhard, Andreas Baumgartner, Peter Gege, Saulius Nevas, Stefan Nowy, and Armin Sperling. "Impact of Improved Calibration of a Neo HySpex VNIR-1600 Sensor on Remote Sensing of Water Depth". In: *IEEE Transactions on Geoscience and Remote Sensing* 53.11 (2015), pp. 6085–6098. DOI: 10.1109/tgrs.2015.2431743

6. Karim Lenhard, Andreas Baumgartner, and Thomas Schwarzmaier. "Independent Laboratory Characterization of Neo HySpex Imaging Spectrometers VNIR-1600 and SWIR-320m-e". In: *IEEE Transactions on Geoscience and Remote Sensing* 53.4 (2015), pp. 1828–1841. DOI: 10.1109/tgrs.2014.2349737

7. Michael Jehle, Andreas Hueni, Karim Lenhard, Andreas Baumgartner, and Michael E. Schaepman. "Detection and Correction of Radiance Variations During Spectral Calibration in Apex". In: *IEEE Geoscience and Remote Sensing Letters* 12.5 (2015), pp. 1023–1027. DOI: 10.1109/lgrs.2014.2374358

8. Andreas Hueni, Karim Lenhard, Andreas Baumgartner, and Michael E. Schaepman. "Airborne Prism Experiment Calibration Information System". In: *IEEE Transactions on Geoscience and Remote Sensing* 51.11 (2013), pp. 5169–5180. DOI: 10.1109/tgrs.2013.2246575

Patents

9. Andreas Baumgartner "Ermitteln einer radiometrischen Inhomogenität bzw. Homogenität einer flächigen Strahlungsverteilung",
DE Patent 102,013,106,571, 2013

Other Articles

10. DLR Remote Sensing Technology Institute. "The Calibration Home Base for Imaging Spectrometers". In: *Journal of large-scale research facilities* 2 (2016), A82. DOI: 10.17815/jlsrf-2-137

Conference Contributions

11. Kevin Alonso, Martin Bachmann, Andreas Baumgartner, Emiliano Carmona, Sebastian Fischer, Birgit Gerasch, Martin Habermeyer, Hans-Peter Honold, Harald Krawczyk, Maximilian Langheinrich, Martin Mücke, Miguel Figueiredo Vaz Pato, Raquel de los Reyes, Mathias Schneider, Peter Schwind, Tobias Storch, and Richard Wachter. "EnMAP - Calibration and Validation Activities". In: *NASA SBG Cal/Val Workshop*. NASA SBG Cal/Val Workshop. July 2020

12. Charles Thomas Pope and Andreas Baumgartner. "Light source for stray light characterisation of EnMAP spectrometers". In: *Sensors, Systems, and Next-Generation Satellites XXIII*. vol. 11151. Proc. SPIE. Oct. 2019, pp. 452–459. DOI: 10.1117/12.2531264

13. Mathias Schneider, Andreas Baumgartner, Peter Schwind, Emiliano Carmona, and Tobias Storch. "Differences and Similarities in the Processing of Airborne and Spaceborne Hyperspectral Data Shown on HySpex and EnMap Processing Chains". In: *IGARSS 2019 - 2019 IEEE International Geoscience and Remote Sensing Symposium* (July 2019). DOI: 10.1109/igarss.2019.8898527

14. Stefanie Holzwarth, Nicole Pinnel, Martin Bachmann, Mathias Schneider, Claas Henning Köhler, Andreas Baumgartner, and Daniel Schläpfer. "Optimized Processing of Airborne Hyperspectral Data for Forest Studies". In: *WHISPERS 2018, 9th Workshop on Hyperspectral and Signal Processing: Evolution in Remote Sensing*. Oct. 2018

15. Andreas Baumgartner. "Matching Pixel Response Functions in Imaging Spectrometers". In: *FIDUCEO Workshop*. Apr. 2018

16. Andreas Baumgartner and Thomas Schwarzmaier. "Traceable Radiometric Calibration of the German Imaging Spectrometer Satellite Mission EnMAP". in: *CALCON Technical Meeting*. Aug. 2017

17. Claas Henning Köhler, Andreas Baumgartner, and Johannes Brachmann. "EnMAP related Cal/Val Activities of the User Service OpAiRS". in: *ICARE 2017*. July 2017

18. Florian Ewald, Tobias Kölling, Andreas Baumgartner, Tobias Zinner, and Bernhard Mayer. "Characterization and airborne deployment of specMACS, a multipurpose hyperspectral cloud and sky imager". In: Optical Society of America, 2016, HM2E.3. DOI: 10.1364/hise.2016.hm2e.3

19. Johannes F. S. Brachmann, Andreas Baumgartner, and Karim Lenhard. "Calibration procedures for imaging spectrometers: improving data quality from satellite missions to UAV campaigns". In: *Sensors, Systems, and Next-Generation Satellites XX*. vol. 10000. Proc. SPIE. Oct. 2016, pp. 1–12. DOI: 10.1117/12.2240076

20. Johannes Felix Simon Brachmann, Andreas Baumgartner, and Karim Lenhard. "The Calibration Home Base for Imaging Spectrometers: Present Activities in an Overview". In: *Onera-DLR ODAS Symposium 2016*. June 2016, pp. 1–8

21. Karim Lenhard, Andreas Baumgartner, Saulius Nevas, Stefan Nowy, and Armin Sperling. "Improvements to the calibration of a NEO HySpex VNIR-1600 sensor". In: *EARSeL 2015*. Apr. 2015

22. Saulius Nevas, Stefan Nowy, Armin Sperling, Karim Lenhard, and Andreas Baumgartner. "Stray light characterisation of a hyperspectral spectrometer for airborne remote sensing applications". In: *NEWRAD 2014*. June 2014, pp. 53–54

23. Peter Gege, Andreas Baumgartner, Karim Lenhard, and Thomas Schwarzmaier. "Recent developments at DLR's Calibration Home Base". In: *Challenges in the inland water remote sensing - future sensors, improved processing methods*. Apr. 2014

24. T. Schwarzmaier, A. Baumgartner, P. Gege, and K. Lenhard. "Calibration of a monochromator using a lambdameter". In: *Sensors, Systems, and Next-Generation Satellites XVII*. vol. 8889. Proc. SPIE. Oct. 2013, pp. 222–227. DOI: 10.1117/12.2028670

25. D.R. Taubert, J. Hollandt, C. Monte, Peter Gege, Thomas Schwarzmaier, Karim Lenhard, and Andreas Baumgartner. "Absolute radiometric characterization of the transfer radiometer unit of RASTA in the UV, VIS and NIR spectral range". In: *SPIE Remote Sensing*. Proc. SPIE. Sept. 2013

26. Andreas Baumgartner. "Characterization of integrating sphere homogeneity with an uncalibrated imaging spectrometer". In: *2013 5th Workshop on Hyperspectral Image and Signal Processing: Evolution in Remote Sensing (WHISPERS)*. June 2013, pp. 1–4. DOI: 10.1109/whispers.2013.8080735

27. D. R. Taubert, J. Hollandt, P. Sperfeld, S. Pape, A. Höpe, K.-O. Hauer, P. Gege, T. Schwarzmaier, K. Lenhard, and A. Baumgartner. "Providing radiometric traceability for the calibration home base of DLR by PTB". in: vol. 1531. 1. 2013, pp. 376–379. DOI: 10.1063/1.4804785

28. Andreas Baumgartner, Peter Gege, Claas Köhler, Karim Lenhard, and Thomas Schwarzmaier. "Characterisation methods for the hyperspectral sensor HySpex at DLR's calibration home base". In: *Sensors, Systems, and Next-Generation Satellites XVI*. vol. 8533. Proc. SPIE. Nov. 2012, pp. 371–378. DOI: 10.1117/12.974664

29. T. Schwarzmaier, A. Baumgartner, P. Gege, C. Köhler, and K. Lenhard. “The Radiance Standard RASTA of DLR’s calibration facility for airborne imaging spectrometers”. In: *Sensors, Systems, and Next-Generation Satellites XVI*. vol. 8533. Proc. SPIE. Nov. 2012, pp. 431–436. DOI: 10.1117/12.974599

30. Karim Lenhard, Andreas Baumgartner, Peter Gege, Claas Köhler, and Thomas Schwarzmaier. “Characterization of DLR’s EnMAP simulator”. In: *International Radiation Symposium 2012*. Aug. 2012

31. Karim Lenhard, Andreas Baumgartner, Peter Gege, Claas Köhler, and Thomas Schwarzmaier. “Independent laboratory characterization of NEO HySpex VNIR-1600 and NEO HySpex SWIR-320m-e hyperspectral imagers”. In: *IGARSS 2012*. July 2012, pp. 1–3

32. Karim Lenhard, Andreas Baumgartner, Claas Köhler, and Thomas Schwarzmaier. “Ein Kalibrierlabor für Hyperspektralsensoren”. In: *Fachgruppe Messtechnik*. Mar. 2012

33. Thomas Schwarzmaier, Andreas Baumgartner, Peter Gege, Claas Köhler, and Karim Lenhard. “DLR’s New Traceable Radiance Standard RASTA”. in: *IGARSS 2012*. 2012, pp. 1–4

34. Karim Lenhard and Andreas Baumgartner. “Estimation of radiometric uncertainty after smile correction”. In: *ESA Hyperspectral Workshop 2010*. 2010, pp. 1–5